Modelling of Ground Vibration from Underground Railways

A dissertation submitted to the University of Cambridge
for the degree of Doctor of Philosophy

by

James Alexander Forrest
Pembroke College

June 1999

to my parents

PREFACE

The work described in this dissertation was carried out at the Cambridge University Engineering Department between October 1995 and May 1999. The project was suggested by Dr Hugh Hunt, who also acted as my research supervisor. I wish to thank him for his enthusiastic encouragement and knowledgeable guidance in all aspects of the work presented here. I would also like to thank Professor David Newland, who acted as my supervisor for part of my first year and maintained a keen interest in the project throughout.

The field measurements would not have been possible without the assistance of Mr Hugh Kenyon and Mr Adam Webb of Tiflex Ltd, who arranged access to the underground railway tunnel, and also helped with the measurements on site. I am also grateful to Mr David Miller in the Mechanics Lab, who helped to get the measuring equipment in order.

I am grateful for the generous financial support of the Cambridge Commonwealth Trust and the Overseas Research Students Awards scheme during the course of my studies in Cambridge.

Lastly, I would like to thank my colleagues in the Workshop Flats and the South Wing, who have helped make the research student experience an enjoyable one.

I declare that, except for commonly understood and accepted ideas or where specific reference has been made to the work of others, this dissertation is the result of my own work and includes nothing which is the outcome of work done in collaboration. This dissertation is approximately 52,200 words in length and contains 89 figures.

James Forrest

Cambridge, June 1999

SUMMARY

Vibration generated by underground railways is an increasingly significant problem in densely populated urban areas. One popular method used to reduce vibration transmitted into nearby buildings is floating-slab track, whereby a concrete slab supporting the two rails is isolated from the tunnel invert typically by means of rubber bearings or steel springs.

This dissertation is concerned with the often disappointing performance of floating-slab track in reducing ground vibration propagated from railways in tunnels. Vibration levels in the soil surrounding the tunnel are investigated using analytical models, which allow relatively fast computation times to be realised. The tunnel is considered as a thin cylindrical shell of infinite length, surrounded by a viscoelastic continuum of infinite extent to model the soil. The equations of motion for the tunnel and soil are solved in a modal wavenumber-frequency domain. Three different infinitely long track models are considered: a simple slab beam in bending only, a slab beam in bending and torsion, and a full track comprising a rail beam and slab beam. These are coupled to the tunnel by a spatial convolution method, the slab bearings being represented as an elastic layer. Excitation by random roughness-displacement inputs between a series of train axle masses and the rail beam of the full track model is considered. A separate approach utilises a repeating-unit method to create infinitely long double-beam models of the track alone, allowing the effect of various parameters on total force transmitted to the foundation to be examined. Some aspects of the dynamic behaviour of floating-slab track have been observed experimentally by means of impulse tests performed in a railway tunnel.

The various wave-propagation effects in the three-dimensional track-tunnel-soil system give results which cannot be predicted with the simple mass-spring models commonly used in the design of railway track for isolation of vibration. These results suggest that insertion-loss predictions greater than 6dB are in most cases exaggerated and that the technique of floating the track slab may in fact cause increased transmission of vibration under certain conditions.

CONTENTS

Chapter 1

INTRODUCTION

The purpose of this chapter is to describe the reasons for doing research on the *Modelling of Ground Vibration from Underground Railways*, to set out the objectives of such research, and to give a brief outline of the chapters following this introduction.

1.1 Motivation for the Research

This dissertation investigates the generation of ground vibration from underground railways. The transmission of ground vibration into nearby buildings has become a topic of great importance, as many underground railways operate in densely-populated urban areas around the world in both residential and commercial zones. Indeed, traffic-generated vibration and noise is currently a European Union priority area for research.

At a time when people's tolerance of environmental disturbances such as noise and vibration is decreasing, the understanding of the vibration-generation mechanisms in underground railways is vital. The cost of taking vibration-isolation measures means that calculations of their effectiveness must be correct. There is therefore a need for detailed and accurate models of the total system comprising the track, tunnel, soil and buildings.

1.2 Objectives of the Research

The scope of this dissertation is the source of the ground vibration, that is, the underground railway itself. In particular, it is concerned with the vibration-isolation performance of floating-slab track, whereby a concrete slab supporting the two rails is isolated from the tunnel invert by means of resilient bearings. The dissertation focuses on the interactions between systems where the vibration wavelengths are comparable to system dimensions. The frequency range of interest for vibration from urban railways is approximately 20Hz to 100Hz; with a speed of about 200m/s, shear waves in the ground will have a wavelength of 4m at 50Hz, the middle of this range. This wavelength is of the order of the spacing of train axles, the tunnel diameter, and the distance from the tunnel to building foundations; modelling is therefore difficult because interaction between these entities cannot be ignored.

There are three objectives for the research undertaken. The primary objective is to create a structurally correct mathematical model of the track, tunnel and soil, which takes into account the major dynamic characteristics of the three-dimensional system. Current design methods are based on simplistic lumped-parameter models, whose accuracy is somewhat dubious; better design tools are needed. However, a disadvantage of more detailed models is the computation time required to generate results by computer, especially with numerical techniques such as finite-element (FE) analysis. To be useful as a design tool for making informed choices about various vibration-isolation options, any mathematical model must be able to be implemented as a relatively fast-running program on a standard personal computer. Thus the aim is to create a mathematical model based as much as possible on analytical methods, so that closed-form solutions can be used to speed up computation for a particular set of parameters.

A second objective is to test the hypothesis that floating-slab track is not always an effective means of vibration control. Given that measurement of the performance of floating-slab track is almost impossible, the analytical models developed in this dissertation are used to evaluate its performance computationally. The reader is directed to Section 5.3 for a discussion of this issue and to Figures 5.35 to 5.38 in particular, which show how poor the vibration-isolation performance of floating-slab track can be.

A third objective is to provide analytical results which could be used as part of a validation process for an FE (or other numerical) model of an underground railway. Although analytical methods can give much insight into a general problem – because the factors contributing to the overall behaviour are explicitly apparent – they are usually limited to a small set of soluble cases. Thus it can be difficult to apply an analytical approach to a specific situation and a numerical method must then be used instead. Once validated, a numerical model could easily be adapted to deal with the complexities of individual sites.

1.3 Outline of the Dissertation

This dissertation falls into three sections: a review of previous work, theoretical modelling of the underground railway, and field vibration measurements.

Chapter 2 gives a literature review of previous research on the dynamics of different types of railway track, the prediction of ground vibration from surface and underground railways, and experimental measurements of railway-induced noise and vibration. This allows the identification of new areas which can be addressed by the current work, thus providing a starting point for the theoretical modelling.

Chapter 3 considers the modelling of floating-slab railway track, based on the theory of beams on elastic foundations. A repeating-unit method is used to construct track models, and the effects of various parameters are investigated. Chapter 4 looks at modelling a tunnel surrounded by soil, using cylindrical shell theory for the tunnel and elastic continuum theory for the soil. The solution is developed in a modal wavenumber-frequency domain, the familiar time-harmonic response being obtained by a sum of modes and inverse Fourier transformation from the wavenumber to space domain. Chapter 5 considers the problem of joining tunnel and track models together, to give a complete model of the underground railway. The joining is formulated as a convolution of frequency-response functions in space, which is implemented by multiplication in the wavenumber domain. The complete model allows the calculation of power spectral densities and RMS levels of soil vibration around the tunnel when a train is running through it.

Chapter 6 describes some field measurements carried out using impulse-hammer tests inside an underground railway tunnel. Although no measurements could be made in the soil or on its surface, several useful observations regarding the dynamic behaviour of the track and tunnel can be made. These are compared qualitatively to results from the combined models of Chapter 5, allowing some degree of validation.

Overall conclusions and suggestions for further development of the work presented in this dissertation are given in Chapter 7.

Chapter 2

LITERATURE REVIEW

This chapter reviews previous work relevant to the current problem. This includes the impact of train-induced ground vibration, the design and analysis of railway tracks, methods for predicting the propagation of ground vibration, and measurements of ground vibration.

2.1 Impact of Ground Vibration

The effects of vibrations on buildings and their occupants have been summarised by many researchers, for example Kraemer [111], Hunt [89], Cryer [38] and Ng [146]. People experience vibration transmitted into buildings as both vibratory motion and re-radiated noise caused by vibrating surfaces. Grootenhuis [78] states that the problem frequency range for groundborne vibration transmitted from underground railways is 15Hz to 200Hz. Similar figures are given by Greer and Manning [77]: 30Hz to 250Hz for re-radiated sound and 1Hz to 80Hz for perceptible vibration. Data in Heckl et al [82] shows that peak levels occur in the range 40Hz to 80Hz. The levels induced in buildings by transmitted ground vibration are nevertheless relatively low (slamming a door can cause higher levels).

The ORE review [152] notes that structural damage is only likely above vibration levels at which people feel unsafe (the “coefficient of human safety” principle). Such levels occur during earthquakes and are much higher than those due to traffic-induced ground vibration; occasionally building damage has been attributed to ground vibration due to sources such as nearby pile driving. The effect is thus one of discomfort and annoyance for a building’s occupants rather

than of structural damage. However, people often overestimate the levels of vibration subjectively, *thinking* damage is occurring because they are being annoyed [152]. Vibration in buildings can also upset sensitive equipment [89].

A survey of surface railway noise and vibration by Knall [107] found that people's reactions to noise correlate closely to sound pressure level, but vary widely for a given vibration level, and that perceived annoyance and discomfort depend on the number of statistical events exceeding threshold levels, rather than how often trains run. Öhrström [154] found that people living near railway lines have a 10dB(A) lower tolerance to noise when there is simultaneous strong transmitted vibration exceeding 2 mm/s. Howarth and Griffin conducted tests of simulated railway noise and vibration on human subjects, to quantify how more trains per hour at lower vibration levels result in equal annoyance [87], and to quantify the equivalence between sound exposure level and vibration dose level to determine equal annoyance with differing proportions of simultaneous noise and vibration [88].

Zach and Rutishauser [204] give acceptable vibration limits ranging from 0.2 mm/s (for quiet residential buildings at night) to 0.4 mm/s (for noisy residential buildings in the day), with corresponding limits in sound pressure levels from 25dB(A) to 40dB(A). Acceptable sinusoidal vibration levels for various living and working areas are codified in standards such as BS 6472:1992 [24], and depend on many factors, including the duration and frequency of transient vibrations, the usage of the buildings and the time of day. Tolerance to early morning and evening trains is less [152]. However, there are no standards as yet on assessing the source, although an ISO committee (ISO/TC 108/SC 2/WG 8) is currently considering the prediction of groundborne vibration from underground railways.

2.2 Railway Track

The design of railway track is enormously varied. There are also many approaches to modelling its dynamic behaviour.

2.2.1 Track Designs

Many aspects of the design of railway track are discussed in the book by Esveld [50]. Surface railway track is usually "ballasted", the traditional form with rails which rest on a bed of coarse crushed rock, the ballast. However, due to settlement and degradation with use, ballasted track requires much maintenance, an operation carried out less easily underground than above. This led in the 1960s to the introduction of non-ballasted tracks mounted directly onto concrete slabs. Slab track is several times more expensive to construct and radiates more sound than ballasted track, but requires much less maintenance (Henn [84]).

Many different track designs have been proposed to reduce the transmission of vibration and sound and several are described in the ORE report [151], with vibration-isolation performance gauged by a simple mass-on-a-spring argument. Resilient rubber elements can be used in both ballasted and non-ballasted tracks: rail or baseplate pads, sleeper pads, and ballast mats, in order of effectiveness. Special non-ballasted track constructions fall into several groups. Rail mountings based on conical rubber elements include the Clouth system in Hamburg, the Cologne Egg (see also Braitsch [21]), and the shear-transmitting element described by Ando et al [5]. Sleeper-mounting systems include the Paris metro STEDEF system of twin-block concrete sleepers mounted in rubber "boots" (see also Duval [47]).

Floating-slab tracks mount the rail-supporting concrete slab on resilient bearings of rubber, glass fibre or steel springs, to give a large isolated mass and hence low natural frequency with theoretically large reductions in vibration transmission. Designs utilising short pre-cast slab sections include the Toronto "double-sleeper" (slabs 1.5m long), the Eisenmann track in Munich and Frankfurt (3.4m long) and the New York subway (7m long), while the British VIPACT system supports a continuous slab. A very large isolated mass can be achieved with composite track consisting of a floating concrete tray containing ballasted track. Examples include the Üderstadt track in Cologne, and the Barbican (two tracks on one deck) and Piccadilly Line (single-track deck) systems in London.

Vibration counter-measures in railways have generally been developed by trial and error, with the most effective also the most expensive. Damping of low frequencies (2 to 30Hz) involves considerable expense and is difficult to achieve [151].

Singal [164] discusses the design of non-ballasted track, including structural and electrical considerations. In particular, the goal of using very soft railpads and slab bearings in floating-slab track to maximise reduction of noise and vibration conflicts with the requirement for the track to be rigid enough for safety and stability, as noted also by Grootenhuis [78] and Wilson et al [191]. In practice a compromise has to be made between vibration isolation and other track requirements.

2.2.2 Simplified Track Analysis

As mentioned above, design predictions of track vibration-isolation performance have usually been based on a simple lumped mass-spring argument. Using this approach, Zach and Rutishauser [204] claim that a 25dB reduction in transmitted vibration at 50Hz can be achieved by using a floating-slab track with an 8-9Hz natural frequency. Wettschureck and Kurze [188] define a decibel "insertion loss" for ballast mats in underground railways using a one-dimensional impedance model. This assumes that the ballast mat is a simple spring and the tunnel is rigid; with this and measurements they claim a 20dB reduction of tunnel wall vibration.

Similarly large reductions are predicted by Wettschureck [186, 187] for ballast mats in railway tracks above ground and on bridges, and by Isaksson [95], who uses the impedance model of [188] combined with statistical energy analysis for ballast mats on bridges. Wilson et al [191] predict high reductions above 20Hz for a floating-slab track designed for a 14-16Hz natural frequency, but their measurements on the surface above the railway tunnel indicate only a modest reduction of 7dB above 31.5Hz. A lumped-parameter approach for underground railway track is also advocated by Capponi and Murray [28].

The pitfalls of this simplistic design approach are highlighted by Greer and Manning [77], who note that a lumped-parameter model on a rigid foundation is perhaps sufficient for a tunnel in hard-rock ground, but that more sophisticated approaches such as finite-element models are required otherwise. To complicate matters, there is no standard definition of insertion loss – an in-specification isolation performance can become out-of-specification with a change of definition.

2.2.3 Beam Models of Track

Hetényi [85] states that an Euler beam on a continuous elastic foundation was first analysed by Winkler in 1867 in order to investigate railway track behaviour, and discusses several similar models. Variations on the basic Winkler beam have been widely used to model railway track, but the context has nearly always been ballasted track with the emphasis on track behaviour rather than ground vibration. Kerr [106] gives design curves for determining an empirical stiffness per unit length for use in the Winkler model through rail deflections measured under known axle loads.

Cai et al [26] conduct a free-vibration analysis of a track modelled as a rail beam supported via springs on discrete crosswise sleeper beams, which rest on Winkler foundations. The track is composed of a number of single-span units characterised by an exact dynamic-stiffness approach. Cai and Raymond [25] extend this model by including an axial rail force to simulate thermal forces, and a varying sleeper Winkler stiffness to represent uneven ballast compaction. The transverse response to both deterministic and random loading of an axially pre-loaded, Timoshenko beam on an elastic foundation is determined by Chang [30].

Mead and Yaman [134] calculate the harmonic response of infinite beams on simple, transverse elastic, and general elastic periodic supports. A propagation constant determines the reaction forces under the periodic structure's two semi-infinite halves lying either side of the loaded span. Nordborg [147, 148] applies the same idea to a rail beam on periodic sleeper-beam supports to determine its forced response as a linear combination of the free-vibration solutions. Ballast properties are determined by fitting experimental data to the model. A similar model is used by Dalenbring [40] to ascertain the vertical rail motion with different experimentally determined railpad stiffnesses.

A beam model of floating-slab track is used by Samavedam and Cross [163] to evaluate vibration isolation. The model is like a double Winkler beam, comprising an infinite rail beam on railpad springs resting on an infinite slab beam on bearing springs. The tunnel floor is assumed to be rigid compared to the slab bearings (however, a halfspace is proposed to represent the tunnel floor for non-floating slab). Infinite double-beam periodic structures are used by Forrest [61] to model the rails supported on continuous and discrete floating slabs.

To use models like these, appropriate properties for the resilient elements must be specified. Melke and Switaiski [139] describe some of the problems in performing tests to determine the static and dynamic stiffnesses and loss factor of such elements. Gade and Wismer [68] summarise the various viscoelastic constitutive laws which can be used and describe a "non-resonant" method for measuring complex stiffness. Thompson et al [172] describe another method and note that the stiffness of viscoelastic materials like railpads depends on the preload, temperature, frequency, strain magnitude and strain history. Based on laboratory measurements of elastomeric materials used in railways, Castellani et al [29] propose an interpretative model with separate terms for strain-rate dependent stiffness, hysteretic dissipation and viscous dissipation. Dalenbring [40] notes that the stiffness of an individual pad depends on a "form factor", the ratio of loaded surface to free surface. Fenander [53] uses measurements to propose a fractional derivative model of dissipation in railpads; however, the response of a beam track model using this law shows no significant differences to that of one using standard viscous damping [54].

2.2.4 Beams with Moving Loads

Patil [155] determines the response of a harmonically loaded Winkler beam when a mass is applied suddenly. Duffy [46] extends this to a moving mass, finding that resonance is lowered by an increase of velocity as well as increased mass, and examines changes in the waves at and above critical speed. A time-domain finite-element (FE) approach is used by Chang and Liu [31] to find the response of a non-linear beam on an elastic foundation to a mass on a spring traversing it with constant velocity or acceleration.

Much work on moving loads has also been done in the context of simply-supported beams modelling bridge-type structures. Blejwas et al [16] use a time-stepping method to treat the two cases of a smooth mass traversing a smooth beam and an idealised vehicle (mass-spring-mass) traversing a rigid sinusoidal surface. Esmailzadeh and Ghorashi [49] use an approximate modal solution to find the response of a simply supported beam traversed by a partially distributed mass moving at constant velocity, showing that very large displacements develop above the critical speed. The midspan response to a sequence of loads with time-varying velocity, whose arrival

times are a Poissonian random process, is investigated by Zibdeh and Rackwitz [206]. Yang et al [198] provide an analytical solution for a simply supported beam traversed by a train, by superimposing the results for two sets of equally spaced loads, one set for the front wheels of each bogie assembly, the other for the back wheels.

A more complicated structure is treated by Wang and Lin [183], who use a modal solution to investigate a multispan Timoshenko beam excited by a random load moving at constant velocity. Belotserkovskiy [12] examines a harmonic force moving along infinite periodic structures representing railway track. The structures are beams on various continuous or discrete foundations, with the periodicity arising from rail joints (low-frequency effects) or sleeper spacing (high-frequency effects). Since urban trains travel at speeds much less than the critical speeds of waves in tracks, the movement of loads would only have to be considered explicitly when this type of parametric excitation is important.

2.2.5 Train-Track Interaction

Detailed treatment of railway vehicle dynamics is given by Garg and Dukkipati [69]. The concern is with the vehicle and not the effect on track response; many degrees of freedom are considered, in more than one plane, as are trains of more than one vehicle. Fujimoto et al [67] consider the effect of track irregularities on the dynamics of high-speed trains. Fröhling [64] investigates low-frequency vehicle-track interaction by means of track-profile inputs to an eleven degree-of-freedom vehicle model, in order to determine forces for use in a settlement law for ballasted track. Zhai and Cai [205] describe a ten degree-of-freedom vehicle model excited by wheel-rail irregularities on a track represented by an infinite beam on discrete mass-spring supports.

Research into rail corrugation and other damage has produced many vehicle-track interaction models. Grassie et al [76] model ballasted track with infinite beams on a Winkler foundation, on a continuous two-layer support incorporating sleeper mass, and on discrete supports including sleeper masses. Their concern is the effect on track dynamics of a train, modelled as a wheel mass on a Hertzian contact spring (see Johnson [98] for Hertzian contact), traversing the short-pitch (40-80mm wavelength) rail corrugations responsible for “roaring rails”. The two-layer

model is extended by Grassie and Cox [75] to cope with unsupported sleepers by setting a section of the ballast layer to have zero stiffness and damping, with parameters determined from impulse responses of a test track with hung sleepers. Grassie [74] generalises the model to treat any non-sinusoidal rail-wheel roughness, and compares predicted contact force and rail-seat moment (which influences cracking of concrete sleepers) to measurements.

Lucas [122] uses a rail beam supported on discrete sleeper beams and springs to examine ballast settlement due to impulsive forces from rail dips as well as wheels traversing rail corrugation. Clark et al [35] use a similar model, with theoretical and experimental results showing that the Hertzian contact does not significantly affect track dynamics below 750Hz. Hemplemann et al [83] investigate the wheelset and track modes thought to be responsible for corrugation by means of a more complicated rail model comprising a combination of beam, plate and rod dynamics and supported on rigid-body sleepers with railpad and ballast springs. A similarly complex rail, with a rail-head beam in bending and torsion and plates for the foot and web, resting on uniformly distributed support, is used by Bhaskar et al [13, 14] in conjunction with a detailed conformal contact model to understand corrugation generation.

Minimisation of the dynamic forces causing track damage is investigated by Dahlberg et al [39] using measured sleeper and railpad parameters in a model comprising sleeper beams supporting a rail beam traversed by a single wheel, with excitation provided by a wheel flat and rail joints. Dalenbring [40] and Nordborg [147, 148] determine the response of their periodic track structures to both parametric and rail-wheel roughness excitation. A beam on discrete supports, excited by a lumped-mass wheelset with Hertzian contact is analysed by Ishida et al [96] to determine track behaviour with high-speed trains. Oscarsson and Dahlberg [153] consider a similar structure using FE methods.

Vehicle-bridge interaction has also been studied. Courage and van Staalduinen [37] consider a multi-vehicle train running on an elevated railway track modelled in nine sections, each comprising a rail beam mounted via railpad springs on a viaduct beam. Rail roughness and out-of-round wheels provide the excitation. Bridge response to road vehicles traversing road surface roughness has been considered by Wang and Huang [184] for cable-stayed bridges modelled by two-dimensional FE beam elements, by Waarts and Courage [182] using a horizontal mesh of FE

beams to determine dynamic amplification factors for parts of steel bridges, and by Boudjelal et al [19] using a more complicated FE bridge model composed of plate and beam elements to determine response with both two- and three-dimensional vehicle models.

While parametric excitation such as sleeper spacing is easy to define, quantifying rail roughness profiles is more difficult. Frederich [62] defines a formula for the power-spectral density (PSD) of track-geometry irregularity, based on fitting curves to measured data from many sources. The PSD is of the same form for irregularity in different track dimensions (height, alignment, track width etc), and gives more weight to longer irregularity wavelengths. Fröhling [63] uses this formula to characterise measured South African track geometry. Ford [60] uses measured rail surface profiles directly as input to a simple mass-spring vehicle model to determine rail forces. Some of the problems encountered in measuring track geometry are discussed by Yoshimura et al [199], who describe a "restored waveform" method to correct track irregularities as they are measured.

2.2.6 Other Models of Railway Track

More realistic track models consider the non-rigidity of the underlying soil. Ono and Yamada [150] use a standard infinite rail beam on mass-spring sleepers, but the ballast and roadbed are considered elastic with an assumed pressure distribution acting over increasing area with depth. Responses to rail-joint and wheel-flat impulses, and to rail-wheel roughness demonstrate that waves propagate down into the roadbed, as well as along the track as in a Winkler model.

Several researchers have investigated track dynamics using finite elements to model beam tracks on non-rigid subgrades. Luo et al [123] simulate the infinite soil under the track with a finite FE mesh with rigid boundary conditions; the soil mesh is made large enough that waves cannot return from the boundaries within the time considered. Sadeghi and Kohoutek [162] use a plane-strain FE model of the soil with viscous absorbing boundaries to determine the dynamic-stiffness of the foundation for use in a beam track model. Esveld et al [51] determine the response of a paved-in tramway with a discrete-element model of its different concrete slab, asphalt and soil layers. Triantafyllidis and Prange [176, 177] look at high-speed train energy loss associated with train-track interaction through a rail beam on rigid footings resting on a halfspace

represented by a boundary-element formulation. An asymmetric rail deflection line occurs due to Doppler effects as the train speed approaches the subsoil's surface-wave velocity. Auersch [8] uses a similar approach but with a layered soil, to compare predicted and measured dynamic axle loads and displacement magnitudes.

Clearly soil interaction has important effects on track dynamics. To model the soil realistically requires an understanding of wave propagation in solids and the methods available to deal with it, which is the subject of the next section.

2.3 Prediction of Ground Vibration

The soil through which ground vibration propagates from a railway can be conceptualised as a halfspace, a semi-infinite solid bounded only by the plane formed by its surface. For deeply buried vibration sources, such as many underground railways, soil can be conceptualised as an infinite solid if only local effects are of interest.

2.3.1 Wave Propagation in Solids

Achenbach [1] and Graff [73] give solutions to many problems of wave propagation in elastic solids, noting the seminal contributions made between 1880 and 1910 by Rayleigh, Lamb and Love. Achenbach [1] describes the different types of waves that can occur in an elastic solid, and Gutowski and Dym [80] also provide a summary applied to ground vibration. In the bulk medium, longitudinal pressure waves (P-waves) and transverse shear waves (S-waves) can exist. Other types can arise at interfaces: Rayleigh waves (non-dispersive waves propagating along a free surface with in-plane longitudinal and transverse components); Stoneley waves (surface waves confined to the neighbourhood of the interface between two halfspaces of different materials); and Love waves (dispersive interface waves with motion perpendicular to the interface). Of the three wave types occurring in a uniform halfspace, P-waves travel fastest (so are also known as primary waves because they arrive first), S-waves are slower (so are also known as secondary waves), and Rayleigh waves are slowest.

Analytical solutions for the surface motion of an elastic homogeneous isotropic halfspace subject to concentrated point and line loads at and below the surface are derived in Lamb [118]

in the form of integral equations and summarised in [1, 52, 73, 159]. For a point load, Rayleigh waves propagate outwards across the surface with a circular wavefront, while S- and P-waves propagate outwards and downwards with a hemispherical wavefront; for a line load, the wavefronts are a straight-line and a cylindrical surface respectively. Thus Rayleigh-wave magnitudes are reduced much less by the effects of geometric spreading. Many books [73, 98, 159] quote the Miller and Pursey partition of energy between the different wave types in a halfspace loaded by a disc as 67% Rayleigh waves, 26% shear waves and 7% pressure waves. These two factors suggest that the surface response of a halfspace is always dominated by Rayleigh waves at large distances from the load. However, Wolf [192] shows that a high proportion of energy goes into Rayleigh waves only at low dimensionless frequencies (angular frequency by disc radius on S-wave speed), that is, for low frequency or small disc area (tending to a point load). At higher dimensionless frequencies, the Rayleigh-wave contribution is no more than 10%, with most energy (60% to 80%) going into P-waves and the remainder into S-waves.

Stresses and displacements induced by various loading conditions in an infinite elastic solid are derived by Eason et al [48]. Pekeris and Lifson [156] determine the surface motion of a halfspace to a buried pulse. Energy radiated from a spherical source in an infinite elastic medium is considered in Rudnicki [160]. Wave propagation in layered media is treated in Ewing et al [52]. Much of the work on wave motion in elastic media has been prompted by foundation analysis, a good summary of which is given in Karabalis and Beskos [105]. Analytical approaches can be found in Richart et al [159], beginning with oscillations of footings resting on a halfspace and finishing with vibrations of rigid foundations supported by piles. Wolf [192] describes cone models (for circular foundations) and wedge models (for strip foundations) which spread downwards with an angle determined by wave propagation considerations.

2.3.2 Absorbing Boundaries for Finite Models of Infinite Media

The interaction of complex structures with soil which is not necessarily homogeneous is often analytically intractable. An approximate numerical approach such as the finite-element method (FEM) or finite-difference method (FDM) must then be used. Using such a method gives a finite model whose boundaries reflect waves rather than transmit them as does the infinite soil. Thus

boundary conditions which absorb incident waves are required. Lysmer and Kuhlemeyer [124] were among the first to propose one, the "standard viscous boundary", equivalent to arrays of normal and tangential dashpots applied to the artificial boundary of a two-dimensional model to absorb P- and S-waves. White et al [189] alter the definition of absorption efficiency to define the optimal dashpot coefficients as functions of Poisson's ratio, giving the "unified viscous boundary".

Deeks and Randolph [42] extend the viscous boundary to plane-strain axisymmetric FE models. By considering travelling cylindrical waves, they develop boundaries consisting of parallel springs and dashpots to absorb S-waves, and springs, dashpots and masses to absorb P-waves. Similar mechanical systems as boundaries are proposed by Kallivokas et al [104], using the two-dimensional wave equation in the domain exterior to that being modelled as a prototype situation. Sochacki [167] uses the two-dimensional wave equation to find exact boundary conditions which absorb S- and P-waves, then derives approximate versions to use in FDM. Peng and Toksöz [157] describe optimal absorbing boundaries for modelling three-dimensional elastic wave propagation by FDM. Wolf and Song [196] develop a doubly asymptotic multi-directional boundary, of which the viscous boundary is a special case. Degrande and De Roeck [43, 44] formulate and demonstrate a frequency-dependent absorbing boundary condition for modelling soil as a saturated poroelastic medium. An absorbing boundary exact in the FE sense is determined by Wolf and Song [195] through the geometric similarity of an arbitrary excavation in a halfspace with an infinitesimal layer of finite elements of known properties to one without the layer.

Another approach to absorbing boundaries is to use "infinite" elements, such as the two-dimensional ones of Chow and Smith [33], the axisymmetric and three-dimensional frequency-domain ones of Medina and Penzien [135] capable of transmitting Rayleigh, shear and pressure waves, or the axisymmetric ones of Yun and Kim [203] for a layered halfspace. Infinite elements are the same as normal finite elements except for the infinity of the element domain [203]. The shape functions have an exponential term which ensures that they decay to zero at large distances [33]. Infinite elements are now included in the standard element libraries of commercial FE packages such as ABAQUS.

A popular way to represent the unbounded soil medium is the boundary-element method (BEM), described in Karabalis and Beskos [105] and Wolf and Darbre [193]. BEM uses fundamental solutions (Green's functions) of the medium's governing equations to generate integral equations relating the boundary displacements and tractions. These equations can be used in a time-integration scheme or to determine a dynamic-stiffness relation for the soil. Only the boundary has to be discretised – the exterior region remains a continuum, automatically taking care of the radiation condition. Other work on soil-structure interaction using the BEM approach includes Aubry and Clouteau [6] and Aubry et al [7] (layered soils); Wolf and Darbre [194] and Takemiya et al [170] (shallow foundations); and Lo [121] (piled foundations). A variation described in Wolf and Darbre [193] is to determine the dynamic-stiffness matrix of an embedded foundation as the difference of those for the halfspace (determined exactly) and the excavated part (determined by FEM). These examples are concerned with determining the dynamics of a structure which interacts with soil, rather than investigating ground vibration propagation.

2.3.3 Estimation Methods for Groundborne Vibration Transmission

Empirical or semi-empirical models are often used in practice to predict ground vibration from surface railways, especially when it is difficult to determine appropriate parameters for use in a more complex theoretical model. Considering a road or a railway as a line source, Gutowski and Dym [80] propose an exponential law of decay with distance from the line, with the coefficient of decay determined from actual measurements. Melke and Kraemer [138] advocate the use of transfer functions measured between various parts of a railway-soil system to formulate more informed transmission laws. Fujikake [65, 66] describes a prediction procedure based on taking the track and ballast as single-degree-of-freedom systems and modelling the soil transmission path as a band-pass filter approximating the measured transfer function between the railway and observation point. Measured ground transfer functions are also used by Yoshioka and Ashiya [201] to examine the effect of changes in the rolling stock on ground vibration. The model can be a simple product of attenuation factors for the various parts of the transmission path, derived from large databases of measurements from many sites, as in Madhus, Bessason and Hårvik

[125]. A simplified measurement-based propagation law is also described in Ackva and Niedermeyer [2].

Prediction of ground vibration from underground railways has also often relied on empirical means. An approach based on transmission factors gleaned from a database of over 3000 measurements from various sites is utilised by Hood et al [86]. Other methods, such as those in Kraemer [111] and Melke [137], rely on semi-empirical transmission laws in conjunction with impedances derived from simplified lumped-parameter models of the track and the receiving building. Trochides [178] compares laboratory measurements on a scaled-down tunnel-soil-building system to predictions from approximate impedance models combined with SEA.

2.3.4 Models for Ground Vibration from Surface Railways

Analytical methods can be applied to surface ground vibration. Alabi [3] presents a parametric study of train-induced ground vibration based on the motion of a uniform halfspace loaded by an oblique moving force. Jones and Petyt investigate ground vibration from railways through strip loads acting on a halfspace [101], on an elastic layer on a rigid foundation [102], and on an elastic layer on a halfspace [103]. A detailed analysis of wave propagation in layered soils is used by Auersch [9] with measurements to produce a simplified prediction scheme.

Hunt [90, 91] models the vibration at a distance from a surface roadway by considering the vehicle inputs on the road as a series of random point loads and using Lamb's [118] far-field halfspace responses, which assume dominance of Rayleigh waves. This model fitted vibration measured near busy roadways quite well. The same approach is used by Hao and Ang [81]. Ng [146] uses similar ideas in constructing a beam-on-halfspace model of a surface railway track to compare to vibration measurements, but in this case an approximate near-field halfspace response is needed to couple the infinite track beam to it. Ford [59] uses a superposition of Rayleigh-wave propagation induced by a series of axle loads to show that the ground response is dominated by frequencies near the sleeper-passing frequency. Krylov and Ferguson [117] assume that the quasi-static deflected shape of the railway track under an axle load provides a point-force input to the halfspace as it passes through a sleeper, and sum the responses due to the many simultaneous sleeper inputs of a moving train by a Green's function approach. Ground

vibration can be reduced by careful selection of sleeper and axle spacings [59, 117]. Krylov [114, 115] uses this model to predict a ground-vibration "boom" when trains exceed the soil's Rayleigh-wave speed; trans-Rayleigh conditions of high-speed trains on very soft soils have been observed in western Sweden to increase ground vibration levels tenfold [116]. Measurements of ground vibration from heavy freight trains are compared to a model comprising an infinite rail beam on discrete mass-spring sleepers resting on a three-dimensional layered medium by Jones [99] (with other simpler models) and Jones and Block [100].

FEM has been much used to model surface railway ground vibration. Girardi and Recchia [72] investigate the influence of sleeper type and ballast depth on ground response by means of a detailed FE track and vehicle model supported on a three-dimensional layered medium representing the ballast and subsoil, comparing results to under-track measurements. Yoshioka [200] uses a two-dimensional FE model with viscous boundaries to calculate the vibration propagation through the cross-section of a railway embankment on layered soil. Takemiya [169] uses a "2.5-dimensional" FE track-embankment cross-section resting on a halfspace represented by BEM to quantify the effect of a wave-impeding block (WIB) in the embankment under moving track loads. Takemiya and Goda [171] extend this to a layered halfspace. Peplow et al [158] use BEM to evaluate the performance of a WIB in uniform and layered halfspaces. A three-dimensional FEM-BEM treatment of a railway comprising two rail beams on rigid sleeper footings on a halfspace is given in Mohammadi and Karabalis [140]. Yang and Hung [197] examine the effect of filled and open vibration-screening trenches near a railway line by means of a two-dimensional FE model bounded by infinite elements. Madhus et al [126] use a substructuring method to model the response of layered soil under an FE track model, finding that stiff tracks give lower ground vibration close to the track but have little effect at large distances, where the total load rather than its distribution is important.

2.3.5 Models for Ground Vibration from Underground Railways

An analytical methodology for calculating ground-vibration propagation using tunnel and building models of infinite length to simplify solution is presented by Hunt [93]. Balendra et al [11] use a substructure technique, based on consideration of the two-dimensional wave equation,

to create a cross-sectional model of a rigid tunnel and a rigid strip foundation embedded in a viscoelastic halfspace. Kostarev [109] represents an underground tunnel as an acoustic waveguide in a halfspace, implemented by defining a variation in wavespeed with depth. Krylov [113] applies earlier work [117] on surface railways by assuming that the tunnel diameter is much smaller than the wavelength of low-frequency propagated waves, so that each sleeper in an underground track can be construed as a point load buried in a halfspace. Guan and Moore [79] treat the interaction between two deep side-by-side circular tunnels by solving the three-dimensional wave equations for two cylindrical cavities in an unbounded medium.

Underground railway tunnels of circular cross-section are analogous to buried pipes. Singh et al [165] model a seismically loaded pipe using the axisymmetric response of an orthotropic cylindrical shell buried in an infinite medium subject to an axially travelling pressure wave. The thick-shell theory used in [165] is compared to thin-shell theory in [166]. Köpke [110] applies the thick-shell approach of Gazis [70, 71] to a "pipe in a pipe", the inside pipe representing a buried pipeline and the outside one, of infinite outer diameter, representing the surrounding soil. The solution is general, but the results only consider the driving-point response of the pipe based on the translation mode of the pipe cross-section. Hunt and May [94] include several circumferential modes of Köpke's solution to calculate soil responses around a simply loaded railway tunnel.

Numerical models include the two-dimensional plane-strain FE model of Balendra et al [10], which represents the cross-section of a Singaporean subway-soil-building system and utilises a viscous boundary. The tunnel and soil are modelled with solid elements, the multi-storey building as a framework of beam elements. Chua et al [34] use this model to calculate the vibration reduction effected by soft railpads and floating-slab track, construing the train input as a line load determined from a lumped-mass model of wheel and track. Rücker and Said [161] use a similar model bounded with boundary elements to determine the effect of an open vibration-screening trench between tunnel and building, and of a stiff plate on the ground surface. Thornely-Taylor [173] applies FDM to such a cross-sectional representation to predict vibration levels at specific sites. However, such two-dimensional models ignore the longitudinal dynamics of the track and tunnel.

2.3.6 Building Vibration and Isolation

Attempts to shield buildings from groundborne vibration have been made by placing wave barriers such as walls or trenches in the ground. The ORE report [151] states that maximum attenuation occurs when the ground cuts are arranged perpendicular to the direction of incidence and when the impedance of the ground is significantly smaller than that of the cut. High frequencies are more effectively damped than low frequencies, as wavelengths longer than the barrier depth just go around it. Massarch [129] describes the use of gas cushions to stabilise isolating trenches and so allow greater depths.

Another approach is to mount the building on steel springs or laminated rubber bearings. Some case studies of base isolation near or above railways are discussed in Commins et al [36], Manning [128], and Anderson [4]. Although it is acknowledged that the actual structural dynamics are more complex, all idealise the building as a one-degree-of-freedom mass on a spring in order to select bearings to give a low natural frequency and hence theoretically large vibration reductions, just as in floating-slab track design. Manufacturers of base-isolation springs also work on the mass-spring assumption (see Jaquet and Heiland [97]). However, Newland and Hunt [145] show that even a simple model of an elastic concrete column mounted on a pile via a resilient bearing has many resonances rather than the single one of a mass-spring model. This is borne out by their measurements of transmissibility at a pile cap excited by passing underground trains.

Chouw [32] examines the effect of a WIB placed directly under a frame model of a building on rigid footings supported by an FEM-BEM foundation. Field tests of this WIB are described in Forchap and Verbic [58]. Cryer [38] (see also Hunt [92]) constructs a two-dimensional periodic building model of infinite horizontal extent by repeating a portal-frame unit of beams. This infinite model was found to predict vibration levels in actual buildings much better than a finite model. The portal-frame units are described by the direct dynamic-stiffness approach given in Langley [119], and repeated by Floquet's theorem as described by Mead [130, 131, 132]. A comprehensive summary of analytical methods applicable to periodic structures can be found in Mead [133].

2.4 Measurement of Railway-Induced Vibration and Noise

There have been several studies of vibration and noise produced by actual railways, apart from those already mentioned in conjunction with theoretical modelling. Koch [108] gives some measurements taken near a surface high-speed railway line, which show that soil-surface velocity has an approximately reciprocal relationship to distance from the track. Lineside levels due to heavy freight trains are discussed by Dawn [41], with a maximum response apparent when the sleeper-passage frequency coincides with the resonance of the total vehicle on the track. Measurements obtained at three different surface railway sites by Volberg [180] show decay with distance from the track following a simple power law. Capponi [27] presents measurements of attenuation between the rail foot and tunnel wall in the Milan underground, which show that ballasted tracks achieve the least attenuation and heavy floating-slab tracks the most. A similar, later study is detailed by Bocciolone et al [18]. Bovey [20] describes an impact method using a drop hammer to determine the transfer functions between various parts of the track and between the tunnel and the soil surface in the London Underground. Heckl et al [82] discuss the mechanisms of railway-induced structural vibration in relation to some typical data. Okumura and Kuno [149] apply statistical analysis to railway noise and vibration data obtained from a multitude of sites in an urban area.

2.5 Conclusions

Many types of non-ballasted track have been devised for reducing vibration transmission from underground railways. Beams on continuous and discrete foundations developed from the original Winkler beam have been widely used to investigate the dynamics of ballasted track, but design for vibration isolation using resilient elements has been based on simple mass-spring models. In any case, the ultimately rigid foundations of these models mean that soil vibration cannot be determined directly.

Prediction of ground-vibration transmission from railways is often done in practice with estimation procedures based wholly or largely on empirical data. More sophisticated approaches are based on analytical methods for wave propagation in soil, which give direct insight, or

numerical methods like FEM-BEM, which can deal with the complexities of specific sites. However, there will always be the problem of selecting appropriate parameter values when absolute quantitative predictions are desired.

Ground vibration from surface (generally ballasted) railways has been treated with detailed models which often include track dynamics and are sometimes three-dimensional. However, models of underground railways have either not considered tunnel dynamics fully or have only been two-dimensional. None have included detailed track models. There is thus a need to develop a detailed three-dimensional underground-railway model that includes the dynamics of the train, the track, the tunnel and the soil. An analytical approach would give insight into the physics involved, as well as allow the comparative effectiveness of vibration-isolation measures to be gauged. In addition, it would be computationally fast compared to an approach such as FEM-BEM. This is a gap this dissertation aims to fill.

Chapter 3

MODELLING TRACKS

Traditional railway track consists of the two steel rails fastened to sleepers (once wooden, now often concrete) laid crosswise at intervals of about 0.6m, the sleepers supported on a bed of ballast (crushed stone of large particle diameter). When the first underground railways were built about a century ago, ballasted track was naturally used. However, ballast shifts and settles due to repeated train passage and so needs constant maintenance to keep the track in good repair, an activity which is not as easy to carry out on underground railway lines as on surface ones. Thus underground tracks were introduced where the rails are directly fastened to a concrete slab cast in the tunnel invert. Such a track design requires much less maintenance, although it is still uneconomic in comparison to ballasted track for the much longer mainline surface routes. Nevertheless, a major drawback of directly fixed track is that it leads to higher levels of ground vibration and noise generation, since ballast absorbs quite a lot of the energy imparted to it, while concrete is much less damped. This has led, beginning in the 1960s, to the popularity of a design known as *floating-slab track* for underground railways, whereby the concrete track slab is mounted on resilient bearings, or "floats" above the tunnel invert, in an effort to provide a degree of vibration isolation to the tunnel and surrounding soil.

The typical arrangement of a floating-slab track (FST) in a tunnel is shown in Figure 3.1. Only one tunnel with its track is shown; in the London Underground there are usually two tunnels in close proximity, one for each direction of travel. The two rails are mounted via rail pads and rail fasteners onto a massive concrete slab, which in turn rests on slab bearings

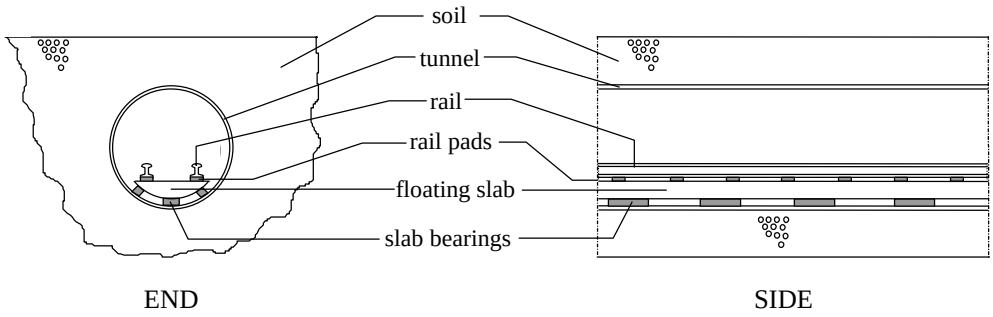

Figure 3.1: Underground railway layout showing the components of floating-slab track.

supported by the tunnel invert. The slab may be cast in-situ, resulting in a continuous length of concrete, or may be constructed of a number of discrete pre-cast sections laid end to end. The rail pads are rubber and protect the concrete against cracking, as well as reduce the amount of noise generated. The slab bearings can be rubber blocks or steel springs, or can be replaced by a continuous sheet of rubber under the slab. Their purpose, in conjunction with the track slab, is to provide vibration isolation to the tunnel invert from the track. The vibration-isolation performance is usually assessed on the basis of simple lumped mass-spring models, where isolation is predicted to occur above some designed low natural frequency. However, such an approach ignores important dynamic effects due to the structure of the track, tunnel and soil. As a starting point for investigation of these effects the track alone can be considered.

3.1 Modelling of Floating-Slab Track with Beams

The three-dimensional underground railway track shown in Figure 3.1 can be thought of as a two-dimensional model consisting of an infinite beam, representing the two rails, mounted on another infinite beam, representing the slab. This is shown in Figure 3.2(a). An infinite track length is reasonable, as real railways are very long. The elastic layers between the two beams represent the rail pads and the slab bearings. The foundation is considered rigid. This is an extension of a simple beam on an elastic foundation (Winkler beam). The lower beam may be

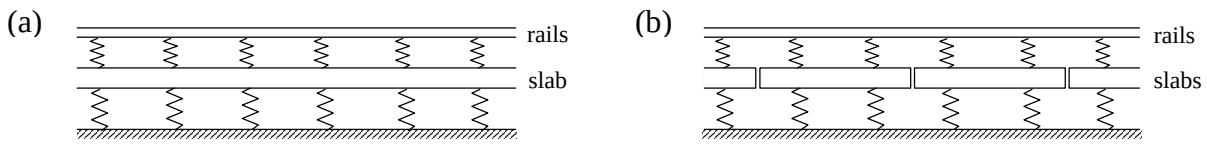

Figure 3.2: Double-beam models of floating-slab track with (a) a continuous slab (cast in-situ) and (b) discrete slabs (pre-cast sections).

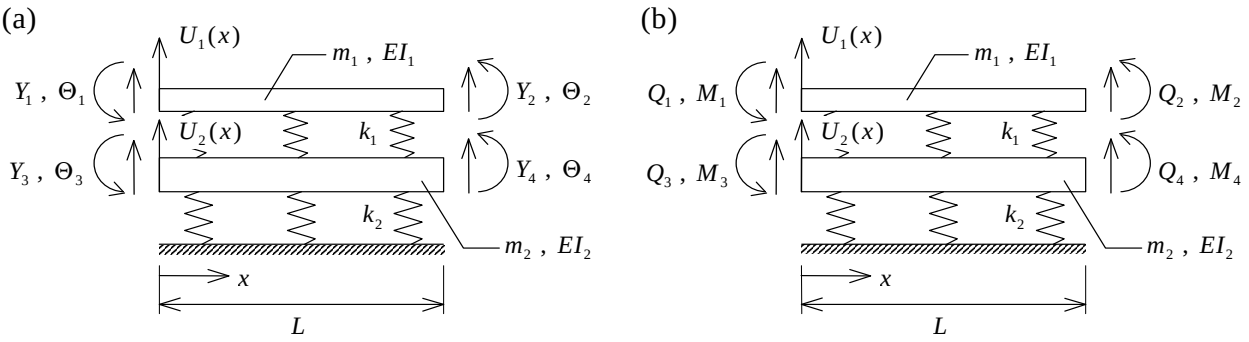

Figure 3.3: Double-beam unit showing (a) the displacements *Y* and rotations Θ and (b) the shear forces *Q* and bending moments *M* at the ends of the unit.

divided into finite sections to model discrete slabs, as in Figure 3.2(b).

Either of the two models given in Figure 3.2 can be thought of as being constructed of an infinite number of finite-length double-beam units. For continuous slab track, both the top and bottom beams of the unit are joined end-to-end; for discrete slab track, only the top beams are joined. Such a double beam unit is depicted in Figure 3.3. Euler beam theory (see Meirovitch [136] or Newland [143]) gives the equation of motion for the displacement $u(x,t)$ of a beam in bending as

$$m\frac{\partial^2 u}{\partial t^2} + EI\frac{\partial^4 u}{\partial x^4} = f(x,t) \tag{3.1}$$

where *m* is the mass per unit length and *EI* the bending stiffness (*E* Young's modulus, *I* second moment of area) of the beam, and $f(x,t)$ is the distributed force per unit length acting on the beam. For the top beam, the force is $f(x,t) = -k_1 u_1 + k_1 u_2$, and for the bottom beam, $f(x,t) = k_1 u_1 - (k_1 + k_2)u_2$, so that the coupled equations of motion for the top and bottom beams can be written as a 2×2 matrix system

$$\mathbf{u}^{\mathrm{IV}} + \begin{bmatrix} m_1/EI_1 & 0 \\ 0 & m_2/EI_2 \end{bmatrix}\ddot{\mathbf{u}} + \begin{bmatrix} k_1/EI_1 & -k_1/EI_1 \\ -k_1/EI_2 & (k_1+k_2)/EI_2 \end{bmatrix}\mathbf{u} = \mathbf{0} \tag{3.2}$$

where **u** is the vector of displacements $\{u_1 \quad u_2\}^{\mathrm{T}}$ of the top and bottom beams, and *k* is stiffness per unit length, with subscript 1 denoting the top beam, subscript 2 the bottom. The numeral IV indicates the fourth derivative with respect to distance *x* and dot indicates differentiation with respect to time *t*. The effects of damping can be included by making the material parameters complex once the problem is in the frequency domain. This is possible through the

correspondence principle, whereby the real parameters of an elastic problem can be replaced by complex ones to model the equivalent viscoelastic problem (see Bland [15] for example).

Substitution of the harmonic solution $\mathbf{u} = \mathbf{U}(x)e^{i\omega t}$ into (3.2) yields

$$\begin{aligned} \mathbf{U}^{\mathrm{IV}} &= \begin{bmatrix} (m_1\omega^2 - k_1)/EI_1 & k_1/EI_1 \\ k_1/EI_2 & (m_2\omega^2 - k_1 - k_2)/EI_2 \end{bmatrix}\mathbf{U} \\ &= [\mathbf{B}]\mathbf{U} \end{aligned} \tag{3.3}$$

where ω is angular frequency. Substitution of an exponential solution of the form $\mathbf{U} = \mathbf{V}e^{\alpha x}$ in (3.3) results in an eigenvalue problem in [**B**], with eigenvalues α^4 and eigenvectors **V**. The two eigenvalues ${\alpha_1}^4$ and ${\alpha_2}^4$ yield four roots each, which together with the two eigenvectors $\mathbf{V}_1$ and $\mathbf{V}_2$ allow the general solution for the displacement of the beam to be written as

$$\begin{aligned} \mathbf{U} = (Ae^{\alpha_1 x} + Be^{i\alpha_1 x} + Ce^{-\alpha_1 x} + De^{-i\alpha_1 x})\mathbf{V}_1 \; + \\ (Ee^{\alpha_2 x} + Fe^{i\alpha_2 x} + Ge^{-\alpha_2 x} + He^{-i\alpha_2 x})\mathbf{V}_2 \end{aligned} \tag{3.4}$$

where *A*, *B*, *C*, *D*, *E*, *F*, *G* and *H* are arbitrary coefficients. The four roots of an eigenvalue are of equal magnitude but separated in the complex plane by a phase difference of $\pi/2$ from one to the next; thus all roots can be obtained from one by successive multiplication by *i*, as in (3.4). This can easily be seen by considering an eigenvalue in polar form as $\alpha^4 = re^{i(\theta+2n\pi)}$, and applying De Moivre's theorem to obtain the roots as $\alpha = \sqrt[4]{r}.e^{i(\theta/4+n\pi/2)}$. Hence there are two roots with negative real part, corresponding to solutions which decay with increasing *x*, and two with positive real part, corresponding to growing solutions. The position of a root in the complex plane determines whether the root corresponds to localised or travelling waves at a given frequency. If (3.4) were to be solved for a double beam with infinite extent in the positive *x*-direction excited at $x = 0$, then the growing solutions would be ignored, because the response must tend towards zero at infinity.

The dynamic stiffness matrix (DSM) relating the generalised forces (forces and moments) to the generalised displacements (displacements and rotations) at the beam ends can be obtained from the general boundary conditions at $x = 0$ and $x = L$, giving eight equations relating the end displacements to the eight coefficients in (3.4), and eight equations relating the end forces to the coefficients. The boundary conditions for the top beam are (see Figure 3.3)

$$
\begin{aligned}
U_1\big|_{x=0} &= Y_1 & U_1\big|_{x=L} &= Y_2 \\
\frac{dU_1}{dx}\bigg|_{x=0} &= \Theta_1 & \frac{dU_1}{dx}\bigg|_{x=L} &= \Theta_2 \\
\frac{d^2U_1}{dx^2}\bigg|_{x=0} &= \frac{-M_1}{EI_1} & \frac{d^2U_1}{dx^2}\bigg|_{x=L} &= \frac{M_2}{EI_1} \\
\frac{d^3U_1}{dx^3}\bigg|_{x=0} &= \frac{Q_1}{EI_1} & \frac{d^3U_1}{dx^3}\bigg|_{x=L} &= \frac{-Q_2}{EI_1}
\end{aligned}
\tag{3.5}
$$

with the boundary conditions for the bottom beam the same, but with U_2 and EI_2 replacing U_1 and EI_1, and subscripts 3 and 4 instead of 1 and 2 everywhere else. By substituting the displacements (3.4) into the boundary conditions (3.5), the sixteen equations can be rendered in matrix form as

$$\mathbf{Y} = [\mathbf{M}]\mathbf{A} \quad \text{and} \quad \mathbf{Q} = [\mathbf{N}]\mathbf{A} \tag{3.6}$$

where $\mathbf{Y} = \{Y_1 \quad \Theta_1 \quad Y_3 \quad \Theta_3 \quad Y_2 \quad \Theta_2 \quad Y_4 \quad \Theta_4\}^{\mathrm{T}}$ is the vector of all end displacements (including rotations), $\mathbf{Q} = \{Q_1 \quad M_1 \quad Q_3 \quad M_3 \quad Q_2 \quad M_2 \quad Q_4 \quad M_4\}^{\mathrm{T}}$ is the vector of all end forces (including moments), and $\mathbf{A} = \{A \quad B \quad C \quad D \quad E \quad F \quad G \quad H\}^{\mathrm{T}}$ is the vector of the coefficients in (3.4). The elements of [**M**] and [**N**] are given in Appendix A. By eliminating the coefficients **A** from the 8x8 system of (3.6), the DSM [**K**] of the double-beam unit is found from

$$\mathbf{Q} = [\mathbf{N}][\mathbf{M}]^{-1}\mathbf{Y} = [\mathbf{K}]\mathbf{Y} \tag{3.7}$$

at a particular frequency ω.

3.2 The Repeating-Unit Method

The full, infinitely long track structure is simply an infinite series of repeated double-beam units added end to end. The unit DSM derived in the previous section can be used to obtain the DSM for a semi-infinite track as described below, then two semi-infinite tracks can be joined at their free ends to yield the infinite track model.

3.2.1 Determination of the DSM for an Infinite Structure

The semi-infinite structure shown in Figure 3.4 illustrates the principle of the repeating-unit method. The objective is to obtain the DSM for the semi-infinite structure; it is clear that adding

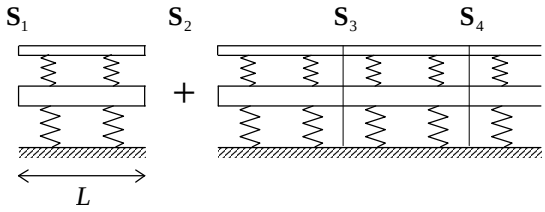

Figure 3.4: Addition of one more repeating unit to a semi-infinite double-beam model, showing the states **S** of the left-hand ends of the units.

one more unit to such a structure will not change its DSM. The method used here is that employed by Cryer [38] to model buildings as infinite structures of beam elements. This in turn is based on the transfer-matrix methods described by Mead [130, 131, 132] and Livesley [120].

The unit's DSM [**K**] is used to generate the transfer matrix [**T**], which relates the *state* of displacement and force $\mathbf{S} = \{\mathbf{Y}^{\mathrm{T}} \;\; \mathbf{Q}^{\mathrm{T}}\}^{\mathrm{T}}$ at the *left-hand* end of a unit to the *state* at the *left-hand* end of the previous unit. The DSM matrix equation (3.7) can be partitioned between the forces and displacements at the left and right ends of the unit. Given no external forces acting on the semi-infinite structure except at the free end, compatibility conditions require that the displacements at the right-hand end of the j^{th} unit are equal to the displacements at the left-hand end of the $(j+1)^{\mathrm{th}}$ unit, while equilibrium requires that forces are equal and opposite. Partitioning (3.7) and substituting the equilibrium conditions gives

$$\begin{Bmatrix} \mathbf{Q}_j^l \\ \mathbf{Q}_j^r \end{Bmatrix} = \begin{Bmatrix} \mathbf{Q}_j^l \\ -\mathbf{Q}_{j+1}^l \end{Bmatrix} = \begin{bmatrix} [\mathbf{K}_{ll}] & [\mathbf{K}_{lr}] \\ [\mathbf{K}_{rl}] & [\mathbf{K}_{rr}] \end{bmatrix} \begin{Bmatrix} \mathbf{Y}_j^l \\ \mathbf{Y}_j^r \end{Bmatrix} = \begin{bmatrix} [\mathbf{K}_{ll}] & [\mathbf{K}_{lr}] \\ [\mathbf{K}_{rl}] & [\mathbf{K}_{rr}] \end{bmatrix} \begin{Bmatrix} \mathbf{Y}_j^l \\ \mathbf{Y}_{j+1}^l \end{Bmatrix} \tag{3.8}$$

where the sub/superscripts of *l* and *r* refer to the left-hand and right-hand ends of a unit respectively. Rearrangement of (3.8) results in the relationship

$$\begin{Bmatrix} \mathbf{Y}_{j+1}^l \\ \mathbf{Q}_{j+1}^l \end{Bmatrix} = \begin{bmatrix} -[\mathbf{K}_{lr}]^{-1}[\mathbf{K}_{ll}] & [\mathbf{K}_{lr}]^{-1} \\ [\mathbf{K}_{rr}][\mathbf{K}_{lr}]^{-1}[\mathbf{K}_{ll}] - [\mathbf{K}_{rl}] & -[\mathbf{K}_{rr}][\mathbf{K}_{lr}]^{-1} \end{bmatrix} \begin{Bmatrix} \mathbf{Y}_j^l \\ \mathbf{Q}_j^l \end{Bmatrix} = [\mathbf{T}] \begin{Bmatrix} \mathbf{Y}_j^l \\ \mathbf{Q}_j^l \end{Bmatrix} \tag{3.9}$$

between the state $\mathbf{S}_{j+1}$ and the state $\mathbf{S}_j$.

The crux of the method is that states propagate along the structure unchanged except in amplitude and phase. If the complex amplitude-modifying factor is λ, then from the j^{th} unit to the $(j+1)^{\mathrm{th}}$ unit

$$\mathbf{S}_{j+1} = [\mathbf{T}]\mathbf{S}_j \quad \text{and} \quad \mathbf{S}_{j+1} = \lambda \mathbf{S}_j \tag{3.10}$$

which is an eigenvalue problem in [**T**] with eigenvalues λ and eigenvectors $\mathbf{S}_j$. Equation (3.10) is a statement of Floquet's theorem (see Ferrari [55]). For the model of Figure 3.2(a) with a

continuous slab beam, both the top and bottom beams are joined from unit to unit, so that [**T**] is an 8×8 matrix and there are eight eigenvalues, essentially four from each beam. Four of these have $|\lambda| < 1$, corresponding to decaying solutions as x increases, and four have $|\lambda| > 1$, corresponding to growing solutions. Since for excitation at the free end the response must vanish as $x \to \infty$, only the four decaying solutions are used to obtain the DSM.

Any state of the free end can be expressed as a linear combination of the four eigenvectors with $|\lambda| < 1$. If the coefficients for each eigenvector contribution are written as a vector $\mathbf{C} = \{C_1 \quad C_2 \quad C_3 \quad C_4\}^{\mathrm{T}}$, and the end state and four eigenvectors split between displacements and forces, then

$$\begin{aligned} \mathbf{Y}_1 &= [\overline{\mathbf{Y}}_1 \quad \overline{\mathbf{Y}}_2 \quad \overline{\mathbf{Y}}_3 \quad \overline{\mathbf{Y}}_4]\mathbf{C} \quad &= [\overline{\mathbf{Y}}]\mathbf{C} \\ \mathbf{Q}_1 &= [\overline{\mathbf{Q}}_1 \quad \overline{\mathbf{Q}}_2 \quad \overline{\mathbf{Q}}_3 \quad \overline{\mathbf{Q}}_4]\mathbf{C} \quad &= [\overline{\mathbf{Q}}]\mathbf{C} \end{aligned} \tag{3.11}$$

where the overbar indicates eigenvector quantities. Equations (3.11) can be used to eliminate **C** to obtain the 4×4 DSM $[\mathbf{K}_\infty]$ of the semi-infinite structure from

$$\mathbf{Q}_1 = [\overline{\mathbf{Q}}][\overline{\mathbf{Y}}]^{-1}\mathbf{Y}_1 = [\mathbf{K}_\infty]\mathbf{Y}_1 \tag{3.12}$$

The dynamics of the semi-infinite structure have now been condensed to a relationship between the forces and displacements at the free end. Obtaining $[\mathbf{K}_\infty]$ in this way involves one computational step, whereas an analogous solution for a finite structure – adding units together until convergence is reached – requires many iterations.

For the model of Figure 3.2(b) with discrete slab beams, the DSM of the repeating unit is extracted from [**K**] in (3.7) to relate only the top beam's forces and displacements, given that the end forces on the bottom beam must be zero if those ends remain free. Hence [**T**] is 4×4. When the repeating unit process is applied to this new DSM, there will be only four eigenvectors, two having $|\lambda| < 1$, and thus only two eigenvectors will appear in (3.11), resulting in a 2×2 $[\mathbf{K}_\infty]$.

The DSM for a semi-infinite structure extending to the left can be obtained by a similar argument to the proceeding one. Alternatively, it can be obtained directly by symmetry from the DSM for the structure extending to the right, by changing the sign of the off-diagonal elements relating the free-end forces and rotations, and the free-end moments and displacements. The DSM for an infinite structure can be obtained by adding the DSMs for two semi-infinite structures, one extending to the left, the other to the right.

3.2.2 Adding Axle Masses to the Model

Masses can be placed on the rail beam to represent the unsprung mass of axle-wheel assemblies of a train of infinite length running on the track, as shown in Figure 3.5. The DSM for the new infinite model is obtained by applying the repeating-unit method to a double-beam unit with a lumped mass m_a added to one end. The inertia force introduced by this mass is $-m_a\omega^2 Y_1$ added to Q_1, or $-m_a\omega^2 Y_2$ added to Q_2, depending on which end the mass is situated at. Therefore the new unit's DSM is created simply by adding a $-m_a\omega^2$ term to the appropriate main diagonal element of the original double-beam unit's DSM [**K**] in (3.7). The DSM for the case of a force input at the middle of an infinite track with axle masses, Figure 3.5(a), is relatively simple to obtain: the DSMs for the left and right semi-infinite structures are both calculated from units with masses *all* at the left-hand end (or *all* at the right-hand end).

A more useful and realistic model for simulating roughness and other irregularities of the rail-wheel contact is to use a displacement input δ between the centre axle-wheel mass and rail beam, as shown in Figure 3.5(b). This time the right semi-infinite structure is based on units with axle masses all on the right-hand end, while the left is based on units with left-hand masses, so that the middle of the resulting infinite track structure has no axle mass. The centre mass is added to the structure with a harmonic roughness displacement $\delta = \Delta e^{i\omega t}$ interposed. This displacement can be thought of as the variation about the mean of the roughness. Suppose there are no external inputs except the roughness displacement. If Y_a is the displacement of the new mass in the frequency domain, then the interaction force acting on it must be equal to $-m_a\omega^2 Y_a$; an equal and opposite interaction force acts on the rail beam directly below the mass, so that $Q_1 - m_a\omega^2 Y_a = 0$, while the other forces acting at the centre are zero. These forces

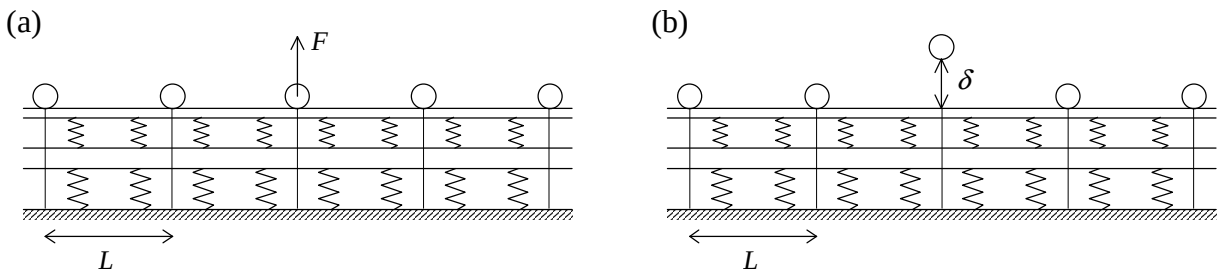

Figure 3.5: Infinite track model with an infinite series of axle-wheel masses added to the rail beam, excited by (a) a force at one mass (b) a displacement input between one mass and the rail beam.

$\mathbf{Q}_1 = \{Q_1 \quad M_1 \quad Q_3 \quad M_3\}^{\mathrm{T}}$ are defined by (3.12) in terms of the centre displacements $\mathbf{Y}_1 = \{Y_1 \quad \Theta_1 \quad Y_3 \quad \Theta_3\}^{\mathrm{T}}$. The additional condition that the difference between the axle-mass and rail displacements must be equal to the roughness input, $Y_a - Y_1 = \Delta$, is required for the five unknown displacement components to be found. Putting all of this together yields the matrix equation

$$\begin{bmatrix} k_{11} & k_{12} & k_{13} & k_{14} & -m_a\omega^2 \\ k_{21} & k_{22} & k_{23} & k_{24} & 0 \\ k_{31} & k_{32} & k_{33} & k_{34} & 0 \\ k_{41} & k_{42} & k_{43} & k_{44} & 0 \\ -1 & 0 & 0 & 0 & 1 \end{bmatrix} \begin{Bmatrix} Y_1 \\ \Theta_1 \\ Y_3 \\ \Theta_3 \\ Y_a \end{Bmatrix} = \begin{Bmatrix} 0 \\ 0 \\ 0 \\ 0 \\ \Delta \end{Bmatrix} \tag{3.13}$$

where the k_{ij} are the elements of the DSM $[\mathbf{K}_\infty]$ of the *infinite* track structure with axle masses but no mass in the middle. A 4×4 $[\mathbf{K}_\infty]$, which corresponds to a continuous slab beam, is used in (3.13); in the discrete-slab case it would be 2×2 since only the rail beams are joined. Note that the new system of equations is of dimension one greater than the original DSM $[\mathbf{K}_\infty]$, because a new independent displacement component Y_a has been introduced.

3.3 Transmitted Force

As an initial point of comparison between different configurations of FST, the total force transmitted into the ground for a given input can be considered. Via its wheels, a train provides several inputs to the track simultaneously, but this case of multiple inputs is best developed by first considering the transmitted force due to a single input acting on the track.

3.3.1 Transmitted Force for a Single Input

Each infinitesimal element *dx* of the lower beam of a unit will provide an increment in transmitted force of $dF_u = k_2 U_2 dx$, as shown in Figure 3.6(a). The force transmitted from the unit onto the foundation will be the integral of these increments over the length of the unit, from $x = 0$ to $x = L$. The bottom-beam displacement U_2 is given by the second row of matrix equation (3.4), so that

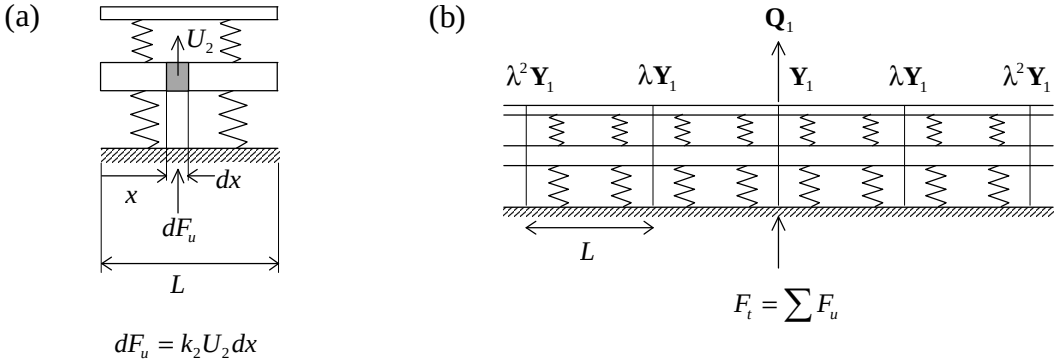

Figure 3.6: (a) Transmitted-force increment for a single double-beam unit. (b) Transmitted force for the whole structure, showing how an eigenvector displacement propagates away from the loading point.

$$\begin{aligned} F_u &= k_2 \int_0^L U_2 dx \\ &= k_2 V_{12} \left(\frac{A(e^{\alpha_1 L} - 1) - C(e^{-\alpha_1 L} - 1)}{\alpha_1} + \frac{B(e^{i\alpha_1 L} - 1) - D(e^{-i\alpha_1 L} - 1)}{i\alpha_1} \right) \\ &+ k_2 V_{22} \left(\frac{E(e^{\alpha_2 L} - 1) - F(e^{-\alpha_2 L} - 1)}{\alpha_2} + \frac{G(e^{i\alpha_2 L} - 1) - H(e^{-i\alpha_2 L} - 1)}{i\alpha_2} \right) \end{aligned} \tag{3.14}$$

for a single unit, where the eigenvectors are defined by $\mathbf{V}_1 = \{V_{11} \quad V_{12}\}^{\mathrm{T}}$ and $\mathbf{V}_2 = \{V_{21} \quad V_{22}\}^{\mathrm{T}}$. The coefficients **A** can be found using the end displacements **Y** of the unit and the matrix [**M**] in (3.6).

The total force transmitted from the whole track to the foundation is obtained by considering the infinite track model shown in Figure 3.6(b). The response at the load point $\mathbf{Y}_1$ to applied input excitation $\mathbf{Q}_1$ can be found from the infinite model's DSM (created from two semi-infinite models' DSMs).

The transmitted force F_u under any unit can be calculated by (3.14) if the end displacements **Y** are known. The displacements are a linear combination of the eigenvectors $\overline{\mathbf{Y}}_j$ according to (3.11), and from (3.10) each eigenvector decays from unit to unit by a factor of λ_j. If the displacement at the excitation point corresponds to one of the four eigenvectors $\overline{\mathbf{Y}}_j$, the end displacements are $\mathbf{Y} = \{\overline{\mathbf{Y}}_j^{\mathrm{T}} \quad \lambda_j \overline{\mathbf{Y}}_j^{\mathrm{T}}\}^{\mathrm{T}}$ for the first unit to the right, $\{\lambda_j \overline{\mathbf{Y}}_j^{\mathrm{T}} \quad \lambda_j^{\,2} \overline{\mathbf{Y}}_j^{\mathrm{T}}\}^{\mathrm{T}}$ for the second, $\{\lambda_j^{\,2} \overline{\mathbf{Y}}_j^{\mathrm{T}} \quad \lambda_j^{\,3} \overline{\mathbf{Y}}_j^{\mathrm{T}}\}^{\mathrm{T}}$ for the third and so on. Equation (3.6) then gives the coefficients for each unit as **A**, $\lambda_j \mathbf{A}$, $\lambda_j^{\,2} \mathbf{A}$ and so on. Hence from (3.14) the transmitted force of one unit will be that of the previous unit multiplied by λ_j. Denoting the transmitted force for the first

unit due to the j^{th} eigenvector as $\overline{F}_{uj}$, the total transmitted force under the right-hand semi-infinite structure, summing over all the units to infinity, is a geometric series (recall $|\lambda_j| < 1$)

$$\overline{F}_{uj} + \lambda_j \overline{F}_{uj} + \lambda_j{}^2 \overline{F}_{uj} + \lambda_j{}^3 \overline{F}_{uj} + \ldots = \frac{\overline{F}_{uj}}{1-\lambda_j} \tag{3.15}$$

A linear combination of the eigenvector contributions (3.15) according to the proportions **C**, calculated from (3.11), gives the total transmitted force for the right half of the track model for any input $\mathbf{Q}_1$. The total transmitted force F_t for the whole structure will be twice this value by symmetry. Thus

$$F_t = 2 \cdot \left(\frac{C_1 \overline{F}_{u1}}{1-\lambda_1} + \frac{C_2 \overline{F}_{u2}}{1-\lambda_2} + \frac{C_3 \overline{F}_{u3}}{1-\lambda_3} + \frac{C_4 \overline{F}_{u4}}{1-\lambda_4} \right) \tag{3.16}$$

for the continuous slab model; the discrete slab model would have only the first two terms. If the input $\mathbf{Q}_1$ is a unit harmonic force acting on the rail, (3.16) gives the transfer function F_t/F of total transmitted force to input force.

The concept of total transmitted force adds together all the increments of force without regard for spatial disposition. This gives a valid picture for an observer at a distance from the track which is large compared to the length over which transmitted force is produced: all transmitted force increments then appear to act at a single point. This is known as St Venant's principle. In practice, however, track displacement involves travelling waves, so that an observer can never be far enough away for the transmitted force to be considered as coming from a point source. The transmitted-force approach is therefore only useful for comparisons between track configurations.

3.3.2 Transmitted Force for Multiple Inputs

Figure 3.7 shows the case of an infinite series of force inputs acting on the rail beam, to represent the passage of a train of infinite length. The inputs are separated by the unit length *L*, and have equal magnitude with a phase difference of ϕ from one to the next to account for the time delay between forces from successive wheels of the train. The superposition of an infinite number of single-load cases, shifted in phase and space, gives the result for the transmitted force.

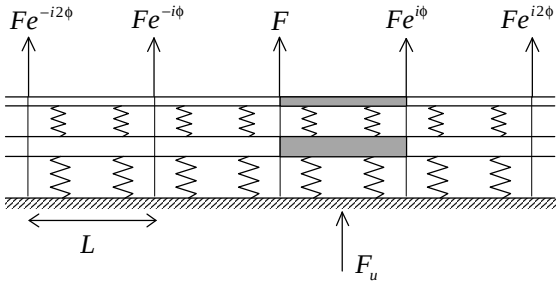

Figure 3.7: Transmitted force for a single unit in an infinite FST model excited by multiple phased inputs applied at the unit junctions.

The unit between the loads F and $Fe^{i\phi}$ in Figure 3.7 has contributions to its transmitted force from the loads to its left and the loads to its right. The number of units that a particular load is from the unit under consideration determines the quantity of that load's contribution as a power of λ_j. Adding these two sets of contributions for one eigenvector of the model gives a sum of two geometric series

$$\begin{aligned} &\overline{F}_{uj} + \lambda_j e^{-i\phi}\overline{F}_{uj} + \lambda_j{}^2 e^{-i2\phi}\overline{F}_{uj} + \lambda_j{}^3 e^{-i3\phi}\overline{F}_{uj} + \ldots \\ &+ e^{i\phi}\overline{F}_{uj} + \lambda_j e^{i2\phi}\overline{F}_{uj} + \lambda_j{}^2 e^{i3\phi}\overline{F}_{uj} + \lambda_j{}^3 e^{i4\phi}\overline{F}_{uj} + \ldots \\ &= \frac{\overline{F}_{uj}}{1-\lambda_j e^{-i\phi}} + \frac{e^{i\phi}\overline{F}_{uj}}{1-\lambda_j e^{i\phi}} \end{aligned} \tag{3.17}$$

where $\overline{F}_{uj}$ is an eigenvector contribution to the transmitted force under the first unit to the right of the load when the infinite track model is excited by the single load F. The transmitted force F_u for the unit is the linear combination of the eigenvector contributions

$$\begin{aligned} F_u = &\left(\frac{C_1\overline{F}_{u1}}{1-\lambda_1 e^{-i\phi}} + \frac{C_2\overline{F}_{u2}}{1-\lambda_2 e^{-i\phi}} + \frac{C_3\overline{F}_{u3}}{1-\lambda_3 e^{-i\phi}} + \frac{C_4\overline{F}_{u4}}{1-\lambda_4 e^{-i\phi}}\right) \\ &+ e^{i\phi}.\left(\frac{C_1\overline{F}_{u1}}{1-\lambda_1 e^{i\phi}} + \frac{C_2\overline{F}_{u2}}{1-\lambda_2 e^{i\phi}} + \frac{C_3\overline{F}_{u3}}{1-\lambda_3 e^{i\phi}} + \frac{C_4\overline{F}_{u4}}{1-\lambda_4 e^{i\phi}}\right) \end{aligned} \tag{3.18}$$

for the continuous slab model. The discrete slab model result would have only two eigenvector components instead of four.

For the next unit to the right of that considered, the series in (3.17) is multiplied by $e^{i\phi}$. Hence F_u in (3.18) is also multiplied by $e^{i\phi}$; for each successive unit to the right, the result is repeatedly multiplied by this phase-shifting factor. With a factor of $e^{-i\phi}$ the same is true for the units to the left. The total transmitted force summed over all units is then $F_u \sum_{n=-\infty}^{\infty} e^{in\phi}$. The total input force for a series of phased unit harmonic inputs is $\sum_{n=-\infty}^{\infty} e^{in\phi}$. The transfer function of total

transmitted force to total input force $F_t/\Sigma F$ is therefore the same as the unit transmitted force F_u given in (3.18).

3.4 Results

The package Matlab was used to investigate the behaviour of infinite FST models based on the double beam unit developed in the previous section. The parameters used are given in Table 3.1.

Rail Beam	Slab Beam
$m_1 = 100\,\mathrm{kg/m}$	$m_2 = 3500\,\mathrm{kg/m}$
$EI_1 = 10\times10^6\ \mathrm{Pa.m^4}$	$EI_2 = 1430\times10^6\ \mathrm{Pa.m^4}$
$k_1 = 40\times10^6\ \mathrm{N/m^2}$	$k_2 = 50\times10^6\ \mathrm{N/m^2}$
$\zeta_1 = 0.5\times10^{-3}\ \mathrm{s}$	$\zeta_2 = 1\times10^{-3}\ \mathrm{s}$

Table 3.1: Parameter values used for the double-beam track model.

The rail beam's parameters are for two rails together. The damping is viscous such that the real stiffnesses written as *k* in (3.3), the equations of motion in the frequency domain, are replaced by complex stiffnesses $k^* = k(1+i\omega\zeta)$. The parameters above are based on typical values for FST, but the value of the rail-support stiffness k_1 has been reduced by an order of magnitude to make the resonance of the rail on the rail pads fall below 200Hz, the maximum frequency which will be considered.

With the parameters given, the maximum unit length *L* which could be treated was about 14m. This is because the elements of [**M**] and [**N**] of (3.6), upon which the unit DSM [**K**] depends, contain exponential terms whose exponents are both positive and negative products of *L* and the roots α_1 and α_2 (see Appendix A). Thus as *L* increases, [**M**] and [**N**] start containing elements both very large and very small. The accuracy of matrix inverses calculated numerically is adversely affected when the difference in order of magnitude between the largest and smallest matrix elements becomes too great for the computational precision used. To ensure the numerical accuracy of the transfer matrix [**T**] of (3.9), which involves inverses of submatrices of [**K**], some scheme of row and column normalisation would have to be used for larger values of *L*.

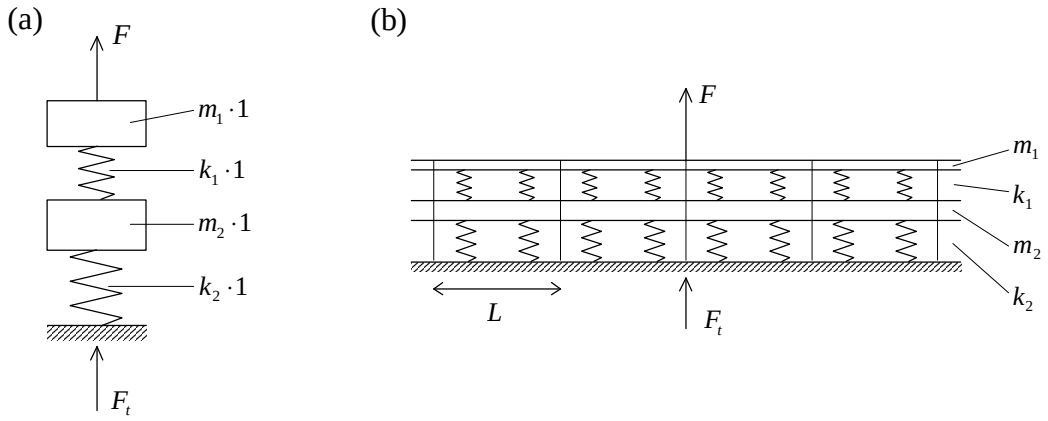

Figure 3.8: Total transmitted force for (a) a double mass-spring system compared to that for (b) a double-beam model. The parameters for (a) are equivalent to one metre of FST.

The first comparison is of total transmitted force for beam models with continuous and discrete slabs to the double-mass-spring system shown in Figure 3.8. The transfer function of transmitted force for the double mass can be shown to be

$$\frac{F_t}{F} = \frac{k_1 k_2}{(m_1\omega^2 - k_1)(m_2\omega^2 - k_2) - k_1 m_1 \omega^2} \tag{3.19}$$

where the masses m and stiffnesses k are given values equivalent to some length of the FST, say one metre.

Figure 3.9 shows the transfer function of total transmitted force for the double mass and for FST models of varying slab length including continuous slab, calculated from (3.16) and (3.19). The numerical results are identical for all the models. There is a peak at about 20Hz for the resonance of the slab on the slab bearings, and a broad peak at about 100Hz for the resonance of the rails on the rail pads. These resonances mark the onset of travelling waves in the respective beams. It seems that slab length has no effect on transmitted force and that FST can be accurately represented by simple lumped-parameter mass-spring models. It is interesting to note that calculating the total transmitted force for a single Winkler beam, by starting from (3.1) to determine its displacement and then using integration as in (3.14) to obtain the total force, gives an identical analytical result as an equivalent single mass-spring system.

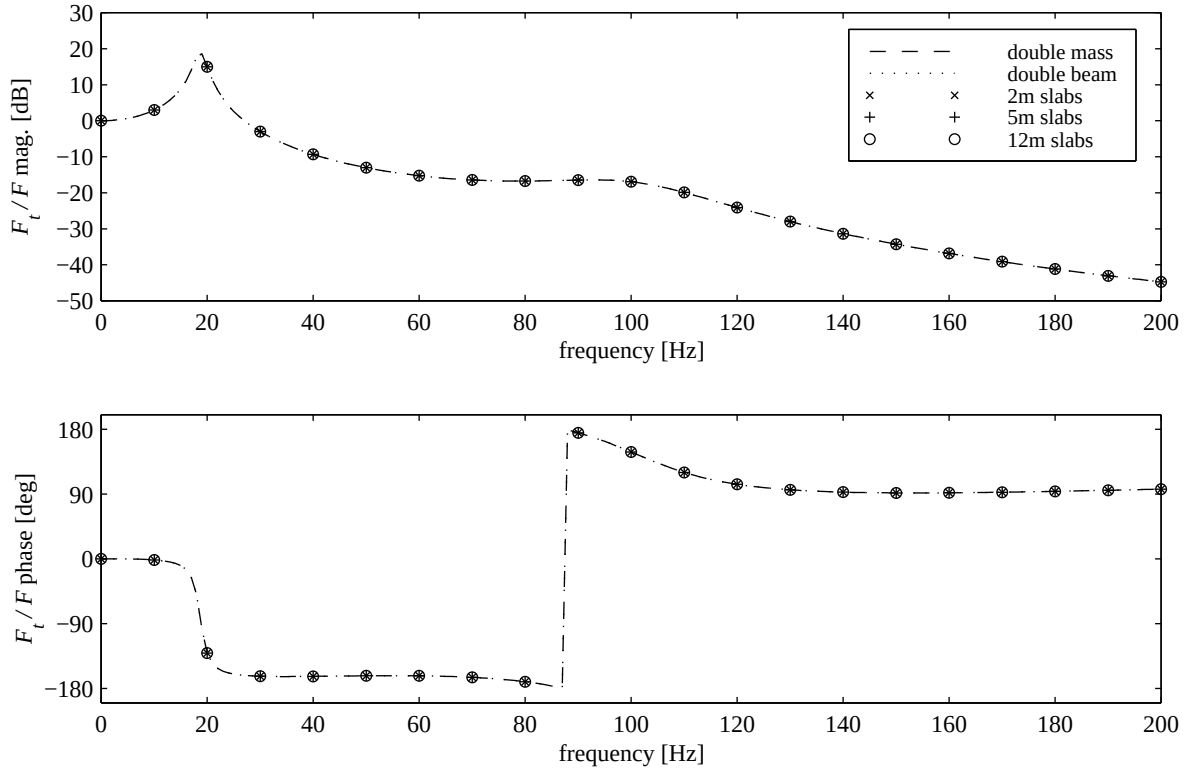

Figure 3.9: Transfer function of total transmitted force due to a single force on the rail beam, calculated using different FST models, and compared to that for a double mass-spring model.

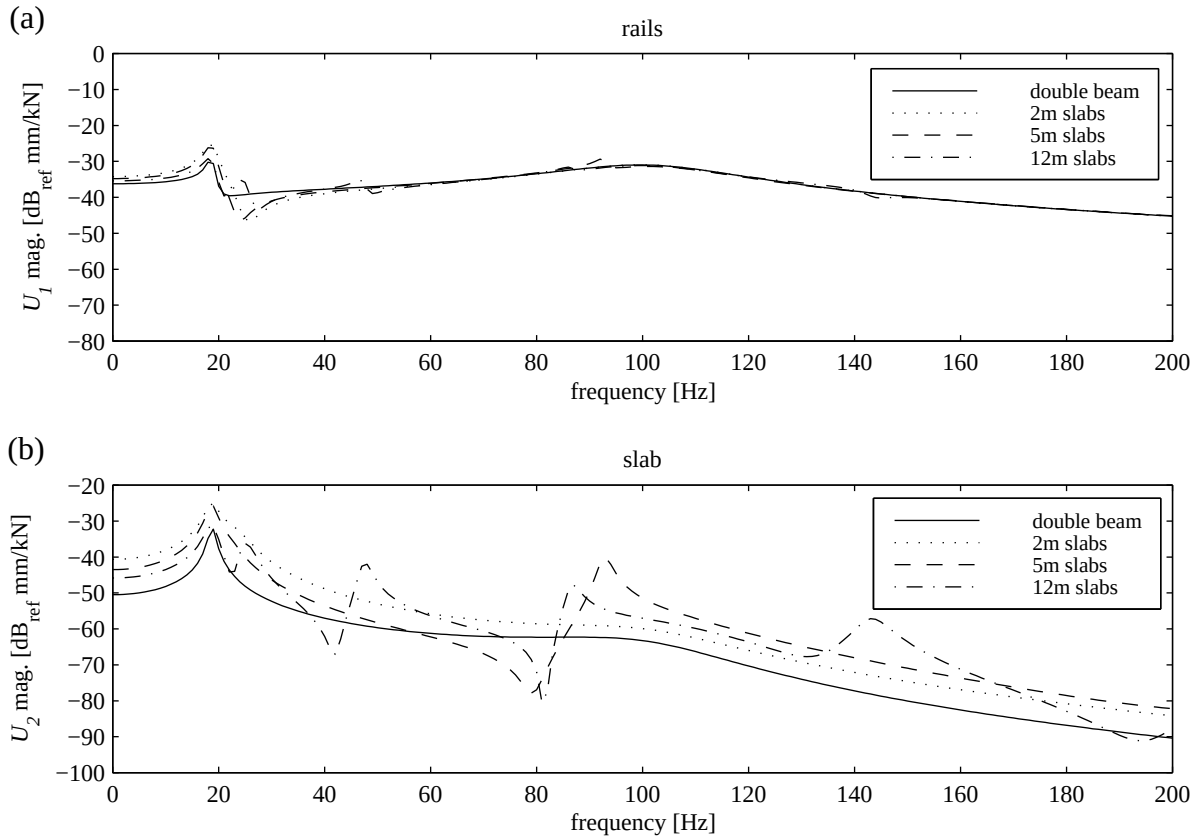

Figure 3.10: Responses at the loaded joint of (a) the top beam and (b) the bottom beam for an infinite FST model with a unit harmonic load applied to the rail beam.

A more subtle picture emerges when the displacement response is examined. Figure 3.10 gives the responses of the top and bottom beams at the loading point for different slab lengths. The bottom beam displacement determines the transmitted force. Discrete slab beams introduce a larger resonant response of the slab on its bearings at 20Hz and a number of new resonances after this point compared to the continuous double-beam model's response, which follows the same general shape as the total transmitted force curve. The breaks in the slab beams reflect travelling waves, preventing energy from propagating away from the loading point through the slab. Thus the response at slab resonance is greater and standing waves can be set up in the discrete slabs, resulting in the further resonances seen. Longer discrete slabs allow standing waves to form at lower frequencies: the 12m slabs result in four extra resonances below 200Hz, but the 2m slabs are too short for any standing waves to occur in this frequency range. Discrete slabs markedly change the response of the slab near the applied load, and thus also the local increment of transmitted force. Because energy is prevented from propagating down the structure, the responses away from the load will be less than with continuous slab. These changes in local effects would be important for an observer (or building foundation) close to the

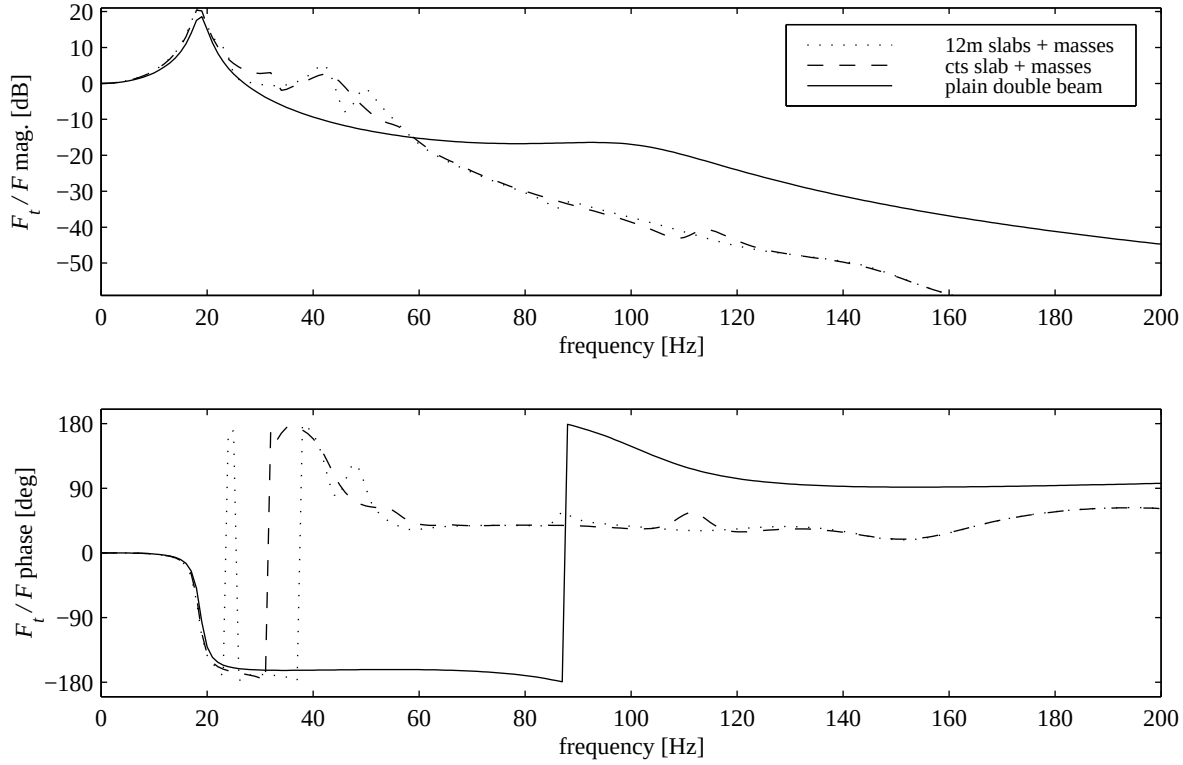

Figure 3.11: Transfer function of total transmitted force for discrete- and continuous-slab FST models once 500kg axle masses at 12m spacing are added to the rail beam, with the double-beam result as a reference.

track, where the concept of total transmitted force breaks down because the force transmitted to the foundation cannot be construed as acting at a single point.

A train of infinite length running on the track can be represented by placing axle masses on the rail beam, as described in Section 3.2 and shown in Figure 3.5(a) with a single force input. Figure 3.11 gives the total transmitted force for the model with added masses excited by a force at one of the masses. It can be seen that now there is a difference between the results for continuous and discrete slab beams. The added mass has also reduced the resonant frequency of the top beam. Figure 3.12 shows the effect on total transmitted force of changing the value and spacing of the masses for a continuous-slab track, so that slab length does not change with mass spacing. The mass value, not the spacing between masses, changes the top beam resonance. This indicates that each mass interacts with some characteristic length of the beam, as shown in Figure 3.13, rather than there being some averaging effect of mass over the whole beam. The spacing between masses only has an effect at higher frequencies, above 100Hz, after the onset of

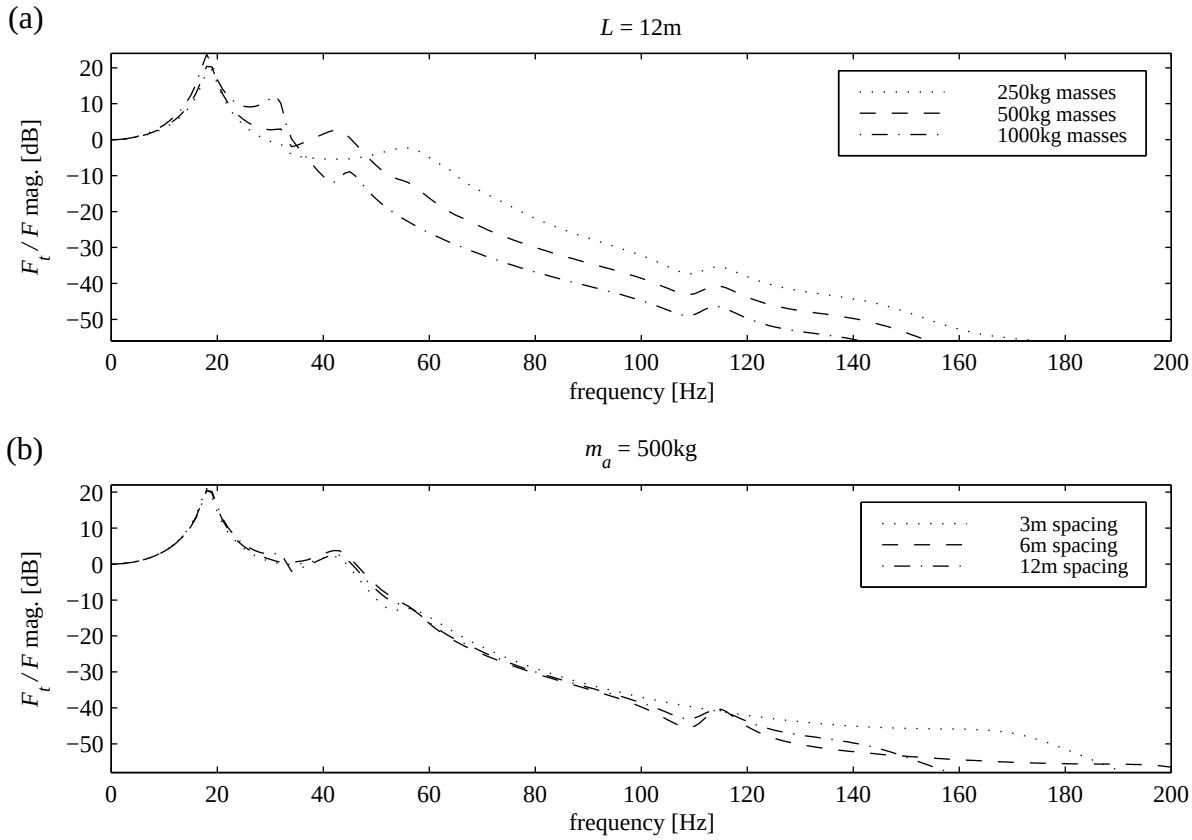

Figure 3.12: Magnitude of the transfer function of total transmitted force for the continuous-slab FST model with axle masses on the rail beam for (a) varying mass at 12m spacing and (b) varying spacing of 500kg masses.

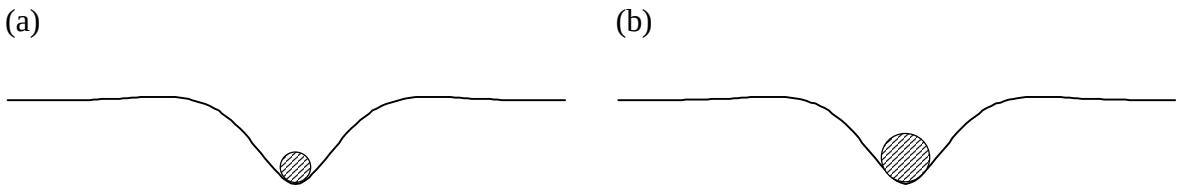

Figure 3.13: Schematics showing that (a) a smaller axle mass interacts with the same shaped "deflection bowl" of rail as (b) a larger axle mass, below the frequency of travelling waves in the rail beam. The shape is that of the static deflection of a 20m section of an infinite rail beam on springs with properties as given in Table 3.1 (vertical scale highly exaggerated).

travelling waves in the top beam itself. For real railpad stiffnesses an order of magnitude higher than that used here, the cut-on frequency of travelling waves would be of the order of 300Hz, so that these higher-frequency effects would not be visible in the frequency range considered.

The total transmitted force for phased force inputs at all the axle-wheel masses can be calculated from (3.18). For an axle spacing of L and a train speed of v, the time delay between axles is L/v so that the phase difference is given by $\phi = \omega L/v$. The frequency ω determines the wavelength of the irregularity in the rail-wheel interface for a given spacing and speed.

Figure 3.14 shows the total transmitted force for this model with $v = 24\text{m/s}$. With a frequency range upto 200Hz, irregularity wavelengths decreasing from infinite to 0.12m are being simulated. The transfer function shows a series of resonances and deep antiresonances at a spacing of 2Hz from peak to peak. The resonances result when all the masses move up and down together in phase. This occurs when a whole multiple of the excitation wavelength corresponds to the axle spacing of 12m, as depicted in Figure 3.15(a), implying frequency intervals of 2Hz as observed. Similarly, the antiresonances occur when each mass is moving in antiphase compared to its two neighbours, as depicted in Figure 3.15(b). The shape traced by the peaks of the 2Hz resonances is similar to the curves in Figures 3.11 and 3.12 for a single load.

The more realistic model using a roughness displacement input δ between one of the axle-wheel masses and the rail beam, shown in Figure 3.5(b), has dynamics given by equation (3.14). Once the displacements $\mathbf{Y}_1$ of the model are calculated, all the previously developed results for transmitted force hold. Figure 3.16 gives the response of the model to phased displacement inputs at all the axle-wheel masses for the same parameters as the case with phased force inputs. The series of resonances and anti-resonances at 2Hz intervals appear again as expected. Note,

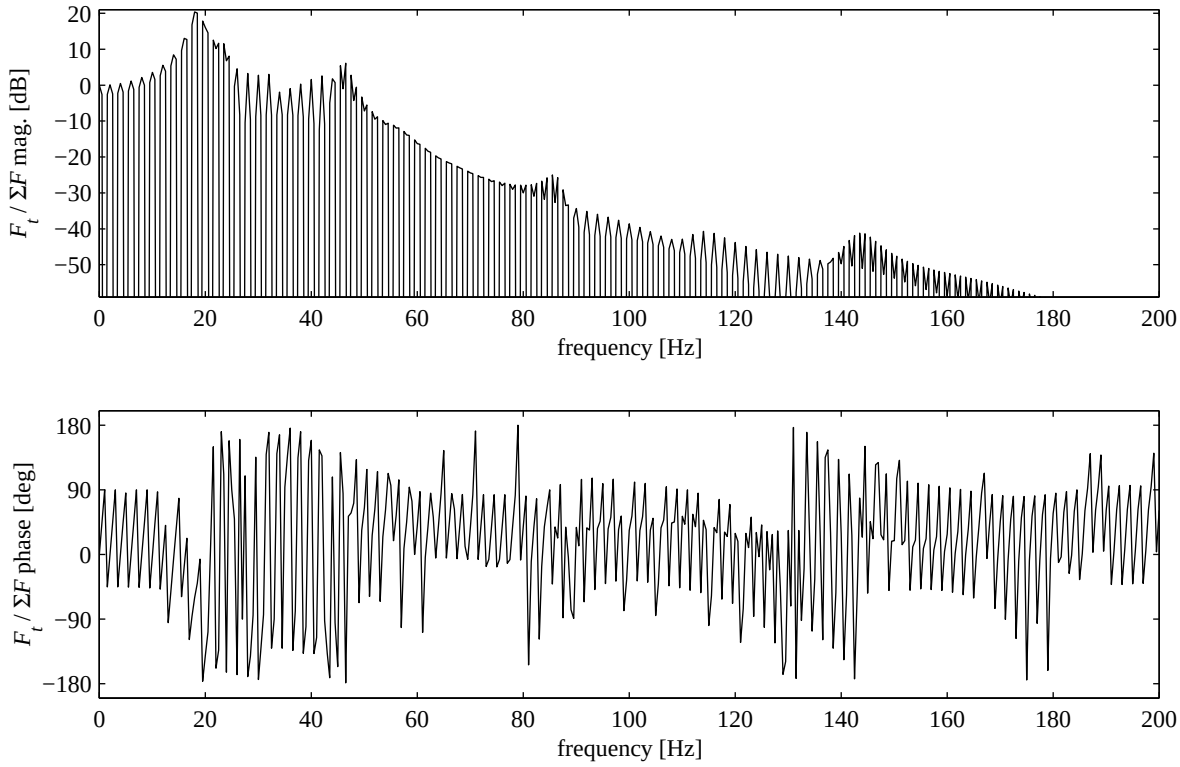

Figure 3.14: Transfer function of total transmitted force for phased input forces at 500kg axle masses with 12m spacing on the continuous-slab FST model. Train speed 24m/s.

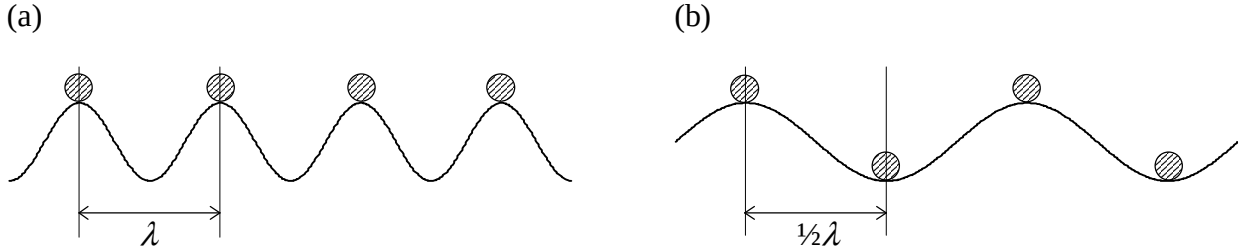

Figure 3.15: Schematics showing the relationship of irregularity wavelength λ and axle-mass positions for (a) resonances in total transmitted force (masses in phase), and (b) antiresonances in total transmitted force (alternate masses in antiphase), at the lowest frequencies (largest wavelengths) these first occur.

however, that displacement inputs give significant transmitted force at the higher-frequency end of the FRF of transmitted force, where the FRF for force inputs (Figure 3.14) is highly attenuated.

The regular series of resonances seen in Figures 3.14 and 3.16 are due to an effect known as wheelbase filtering in the field of vehicle-road interaction. For a varied distribution of motor-vehicle speeds and axle spacings as would be expected on a typical busy roadway, the effect of wheelbase filtering is smoothed out and is thus unimportant in calculating the ground-vibration response near the road by means of random process theory (see Hunt [90, 91]). In a real railway

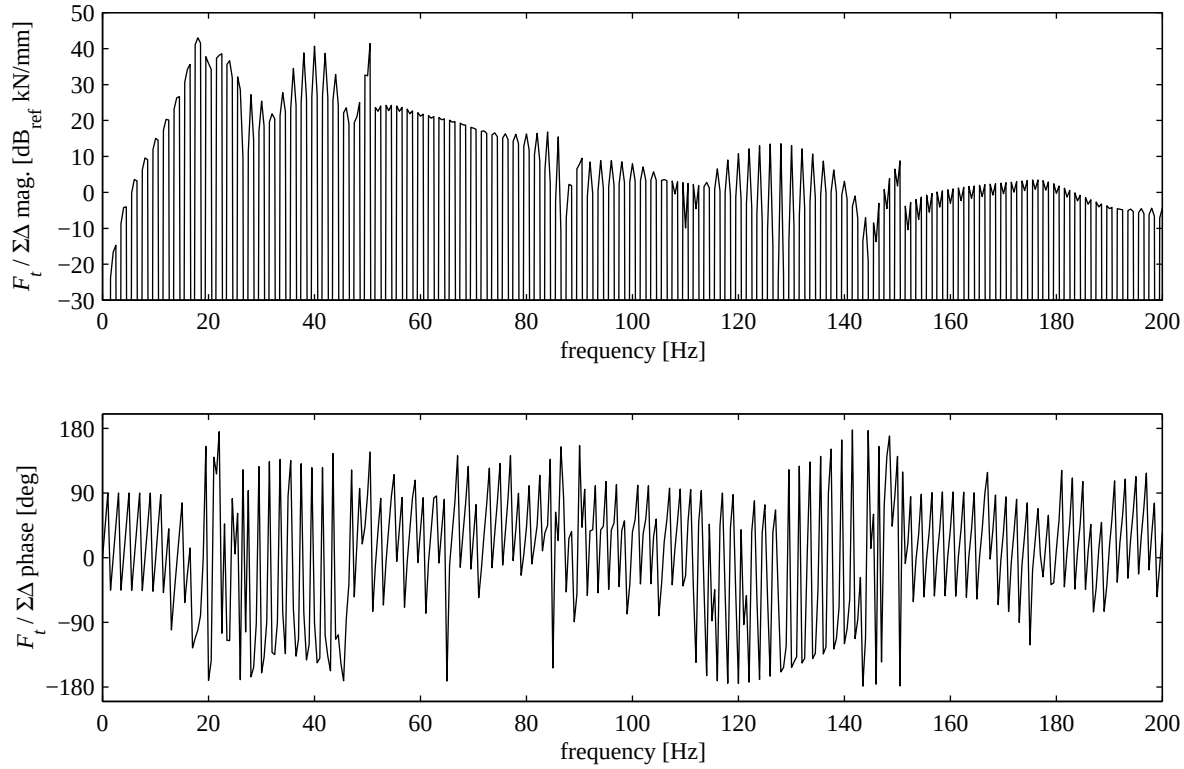

Figure 3.16: Transfer function of total transmitted force for phased displacement inputs at 500kg axle masses with 12m spacing on the continuous-slab FST model. Train speed 24m/s.

vehicle-track system, there will be slight random variations in the spacing between the axles, which means that the sharp resonances in Figures 3.14 and 3.16 will be smoothed out to some extent, but not as completely as for a busy roadway. However, the repeating-unit method does not lend itself easily to the treatment of varied axle spacing, because the transfer-matrix approach assumes units of precisely the same length. Thus a different method would be needed to model axle spacing with some degree of inherent randomness.

3.5 Conclusions

Although at first glance it seems that FST is well modelled by a simple double mass-spring system when transmitted force is considered, closer inspection using double-beam models of infinite length reveals otherwise. In particular, the slab length has a significant effect on the displacement response and hence on the local contribution of force transmitted onto the foundation. With masses added to the model to represent axle-wheel assemblies of a train, the total transmitted force for a single force input can be partially explained by the dynamics of an axle-wheel mass on a characteristic length of rail. However, when multiple, phased inputs of

force or displacement are used to model rail-wheel irregularities, a series of resonances due to axle spacing appear, which cannot be explained with simpler models. Nevertheless, the concept of total transmitted force is limited, despite increasingly more complex models, because of the way all force increments are summed without regard to spatial distribution. Most importantly, the models considered so far have assumed a rigid foundation, so nothing can be said about vibration levels in the soil surrounding the tunnel. The dynamics of the tunnel and the soil need to be addressed.

Chapter 4

MODELLING THE TUNNEL

As described at the beginning of Chapter 3, the track in an underground railway is supported by the invert of the tunnel, which is surrounded by soil (see Figure 3.1). The dynamics of the track were investigated by considering the tunnel as a rigid foundation. However, it is reasonable to expect that different tunnel designs and soil conditions will influence the effectiveness of underground railway tracks designed for vibration isolation, particularly if the "stiffness" of the tunnel invert is not so high as to be effectively rigid in comparison to the various track elements between the rail and the invert. In addition to this, the only sure measure of a track design's vibration-isolation performance is the level of vibration resulting in the soil around the tunnel when a train runs on that track. For these reasons, a mathematical model of the underground railway system needs to include the effects of the tunnel and soil dynamics.

Underground railway tunnels can be of rectangular or circular cross-section. Rectangular cross-sections result from the construction method known as "cut-and-cover", where a trench is excavated, the tunnel lining put in place, then the whole covered to ground level. This method is used for shallow tunnels (a few metres underground), or as a run-in from the surface for deeper tunnels. Circular cross-sections result from boring tunnels at greater depths. A tunnel of circular cross-section will be considered in this chapter.

The tunnel is conceptualised as an infinitely long cylindrical tube surrounded by soil of infinite radial extent. If the tunnel wall is thin compared to its radius, cylindrical shell theory can be used to model the tunnel's response. The infinite soil can be treated by use of the wave

equations for an elastic continuum, formulated in cylindrical coordinates. The analytical solutions for these two components of the physical model are coupled together through the use of appropriate stress and displacement boundary conditions. Despite the absence of a free soil surface, useful results concerning the propagation of vibration into the soil near the tunnel – where building foundations are located – can be obtained. The results for the motion of the tunnel and surrounding soil can then be combined with a track model (the subject of Chapter 5) to improve upon the understanding gained from the track models with rigid foundation considered in Chapter 3.

4.1 Cylindrical Shell Equations

The linear equations of motion for a general thin shell made of linear elastic, homogeneous, isotropic material are given by Volmir [181] and reproduced in Appendix B. For the special case of a thin cylindrical shell, shown in Figure 4.1(a), Volmir's equations can be substantially simplified. In this case they are the same as the static equations of Flügge [57] with the addition of inertia terms. Each of the three equations represents dynamic equilibrium in one of the three principal directions. Equilibrium in the longitudinal direction x gives

$$\begin{aligned} & a\frac{\partial^2 u}{\partial x^2} + \frac{(1-\nu)}{2a}\frac{\partial^2 u}{\partial \theta^2} + \frac{(1+\nu)}{2}\frac{\partial^2 v}{\partial x \partial \theta} - \nu\frac{\partial w}{\partial x} \\ & + \frac{h^2}{12}\left[\frac{(1-\nu)}{2a^3}\frac{\partial^2 u}{\partial \theta^2} + \frac{\partial^3 w}{\partial x^3} - \frac{(1-\nu)}{2a^2}\frac{\partial^3 w}{\partial x \partial \theta^2}\right] \\ & + a\frac{(1-\nu^2)}{Eh}q_x - \rho a\frac{(1-\nu^2)}{E}\frac{\partial^2 u}{\partial t^2} = 0 \end{aligned} \tag{4.1}$$

equilibrium in the tangential direction y gives

$$\begin{aligned} & \frac{(1+\nu)}{2}\frac{\partial^2 u}{\partial x \partial \theta} + a\frac{(1-\nu)}{2}\frac{\partial^2 v}{\partial x^2} + \frac{1}{a}\frac{\partial^2 v}{\partial \theta^2} - \frac{1}{a}\frac{\partial w}{\partial \theta} \\ & + \frac{h^2}{12}\left[\frac{3(1-\nu)}{2a}\frac{\partial^2 v}{\partial x^2} + \frac{(3-\nu)}{2a}\frac{\partial^3 w}{\partial x^2 \partial \theta}\right] \\ & + a\frac{(1-\nu^2)}{Eh}q_y - \rho a\frac{(1-\nu^2)}{E}\frac{\partial^2 v}{\partial t^2} = 0 \end{aligned} \tag{4.2}$$

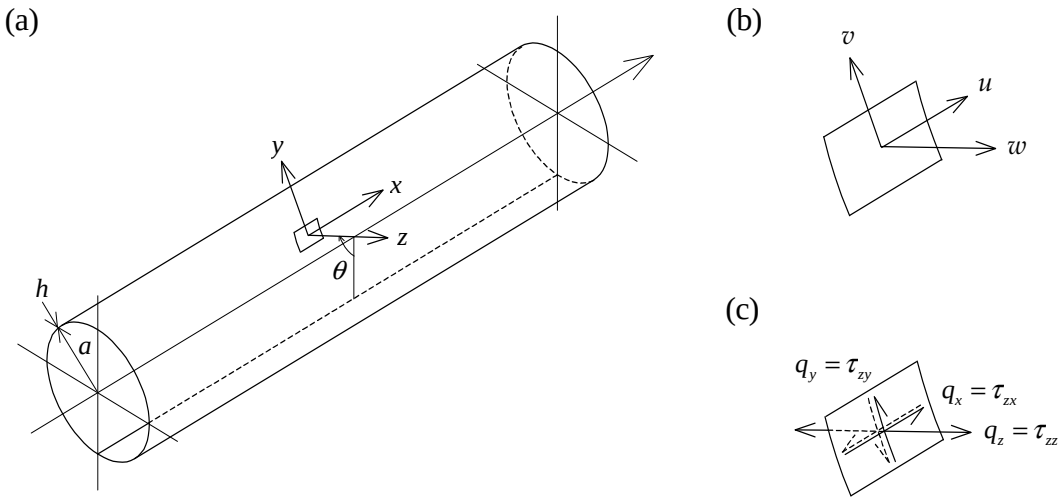

Figure 4.1: Coordinate system used for the thin-walled cylindrical-shell theory, showing (a) the principle directions for a typical element in the shell, (b) the corresponding displacement components and (c) the corresponding surface stress components. To model a railway tunnel, the length of the cylindrical shell is taken as infinite.

and equilibrium in the radial direction *z* gives

$$\begin{aligned} &\nu\frac{\partial u}{\partial x} + \frac{1}{a}\frac{\partial v}{\partial \theta} - \frac{1}{a}w - \frac{h^2}{12}\left[a\frac{\partial^4 w}{\partial x^4} + \frac{2}{a}\frac{\partial^4 w}{\partial x^2 \partial \theta^2} + \frac{1}{a^3}\frac{\partial^4 w}{\partial \theta^4}\right] \\ &- \frac{h^2}{12}\left[\frac{\partial^3 u}{\partial x^3} - \frac{(1-\nu)}{2a^2}\frac{\partial^3 u}{\partial x \partial \theta^2} + \frac{(3-\nu)}{2a}\frac{\partial^3 v}{\partial x^2 \partial \theta} + \frac{1}{a^3}w + \frac{2}{a^3}\frac{\partial^2 w}{\partial \theta^2}\right] \\ &+ a\frac{(1-\nu^2)}{Eh}q_z - \rho a\frac{(1-\nu^2)}{E}\frac{\partial^2 w}{\partial t^2} = 0 \end{aligned} \tag{4.3}$$

where *u*, *v* and *w* are the displacement components in directions *x*, *y* and *z* respectively and varying with time *t*, *a* is the radius of the shell, and *h* is its thickness. The shell material has Young's modulus *E*, Poisson's ratio ν, and density ρ. The effects of material damping can be included by using complex material parameters in the frequency domain. The net applied loading is usually represented by stress components acting on the inside surface of the shell: two shear tractions q_x and q_y, and one normal stress q_z. More precisely, these are the net stresses acting, the differences between the inside and outside values of the surface stresses τ_{zx}, τ_{zy} and τ_{zz} respectively. The displacement and stress components are shown in Figure 4.1(b) and (c).

The terms in (4.1) to (4.3) which are multiplied by the factor $h^2/12$ represent the contribution of bending effects to the displacements, while those without represent the contribution of membrane effects. Use of the simplified static cylindrical shell theory of Timoshenko and Woinowsky-Krieger [175] results in the loss of the bending terms in (4.1) and

(4.2), and of the second bracket of bending terms in (4.3). However, while also giving this simplified theory, Flügge [57] notes that such gross simplifications have been made as to make the resulting equations next to useless.

If the loading applied to an infinitely long cylindrical shell comprises stress components which are harmonic in both space and time, of the form

$$\begin{aligned} q_x(x,t) &= \tilde{Q}_{xn} \cos n\theta . e^{i(\omega t + \xi x)} \\ q_y(x,t) &= \tilde{Q}_{yn} \sin n\theta . e^{i(\omega t + \xi x)} \\ q_z(x,t) &= \tilde{Q}_{zn} \cos n\theta . e^{i(\omega t + \xi x)} \end{aligned} \tag{4.4}$$

and hence separable in time t, space x and angular position θ, then the equations of motion (4.1) to (4.3) are satisfied by the similarly harmonic displacement components

$$\begin{aligned} u(x,t) &= \tilde{U}_n \cos n\theta . e^{i(\omega t + \xi x)} \\ v(x,t) &= \tilde{V}_n \sin n\theta . e^{i(\omega t + \xi x)} \\ w(x,t) &= \tilde{W}_n \cos n\theta . e^{i(\omega t + \xi x)} \end{aligned} \tag{4.5}$$

where ω is angular frequency, ξ is angular wavenumber, n is a positive integer, while the tilde on the uppercase coefficients $\tilde{Q}_{xn}$, $\tilde{Q}_{yn}$, $\tilde{Q}_{zn}$, $\tilde{U}_n$, $\tilde{V}_n$ and $\tilde{W}_n$ indicate that they are in the wavenumber domain as well as the frequency domain. The spatial exponential term $e^{i\xi x}$ arises because of the cylindrical shell's infinite longitudinal extent; if it was of finite length L, then these exponentials would be replaced by terms like $\sin(m\pi x/L)$ or $\cos(m\pi x/L)$ – with the choice depending on the end conditions – where m is a positive integer. The trigonometric terms represent ring modes of the cylindrical cross-section and are chosen so that the displacements are symmetric about $\theta = 0$, the downward vertical. Figure 4.2 shows these ring modes as they relate to the three displacement components u, v and w. The modes are composed of an integer number n of waves developed around the circumference. Hence for the in-plane flexural modes of Figure 4.2(a), which are associated with radial displacement w, $n = 0$ corresponds to an expansion or "breathing" mode, $n = 1$ corresponds to one full wave or translation of the cross-section, $n = 2$ corresponds to two full waves or a squashed cross-section, and so on. The ring modes for the tangential displacement v are the in-plane extensional modes of Figure 4.2(b), while those for the longitudinal displacement u are the out-of-plane flexural modes of Figure 4.2(c).

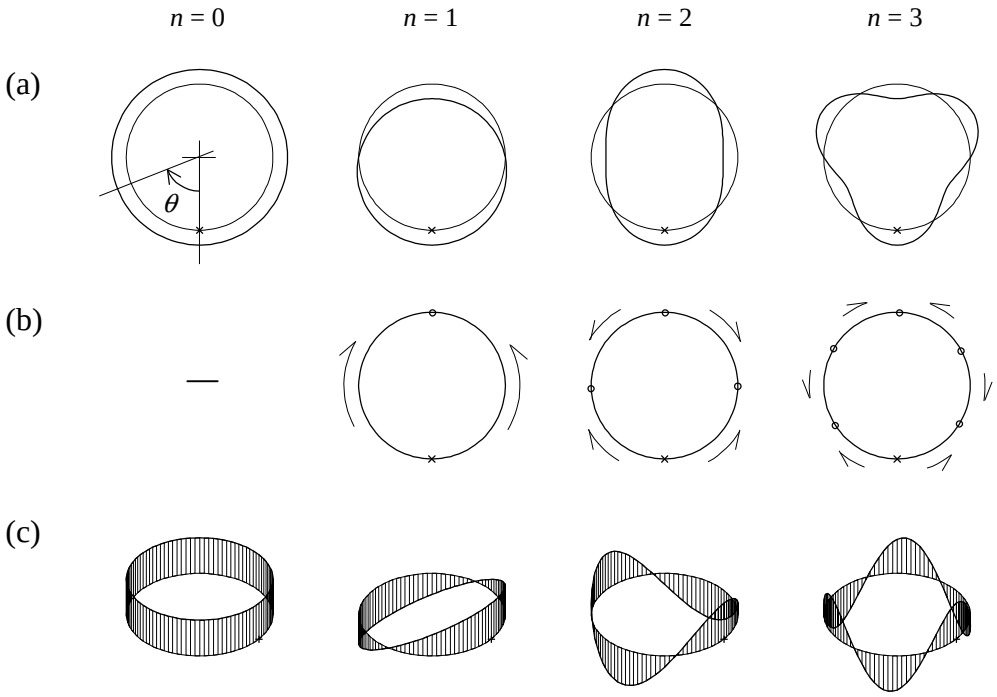

Figure 4.2: (a) In-plane flexural ring modes, varying as $\cos n\theta$ and corresponding to radial displacement w; (b) in-plane extensional ring modes, varying as $\sin n\theta$ and corresponding to tangential displacement v; and (c) out-of-plane flexural ring modes, varying as $\cos n\theta$ and corresponding to displacement u, for different values of circumferential modenumber n. The $\theta = 0$ points are marked with small crosses on the undeformed ring shapes, while the small circles in (b) mark the additional nodal points on the ring's circumference.

Substitution of the stresses (4.4) and displacements (4.5) into equations (4.1) to (4.3) and putting all three equations into matrix form yields

$$[\mathbf{A}] \begin{Bmatrix} \tilde{U}_n \\ \tilde{V}_n \\ \tilde{W}_n \end{Bmatrix} = \frac{-a(1-\nu^2)}{Eh} \begin{Bmatrix} \tilde{Q}_{xn} \\ \tilde{Q}_{yn} \\ \tilde{Q}_{zn} \end{Bmatrix} \tag{4.6}$$

where [**A**] is a matrix of coefficients whose elements are given in Appendix B. If the stresses $\tilde{\mathbf{Q}} = \{\tilde{Q}_{xn} \quad \tilde{Q}_{yn} \quad \tilde{Q}_{zn}\}^{\mathrm{T}}$ are such that they represent some kind of unit loading condition, then the displacements $\tilde{\mathbf{U}} = \{\tilde{U}_n \quad \tilde{V}_n \quad \tilde{W}_n\}^{\mathrm{T}}$ represent the displacement frequency-response functions (FRFs) in the wavenumber domain for a particular circumferential mode n. The actual stresses and displacements will in general be linear combinations of the modal quantities.

4.2 Elastic Continuum Equations

The soil surrounding the tunnel is modelled as a three-dimensional, homogeneous, isotropic elastic solid in the form of a thick-walled cylinder with an inner diameter equal to the diameter of the tunnel, and an outer diameter of infinite extent, as shown in Figure 4.3(a). The solution for the motion of this cylinder follows the method employed by Gazis [70] to investigate the modes of thick-walled cylindrical shells and developed further by Köpke [110] to model the dynamics of buried undersea pipelines.

The wave equation describing motion within a three-dimensional, homogeneous, isotropic, elastic, solid medium is derived by Graff [73] and is

$$(\lambda+\mu)\nabla\nabla\cdot\mathbf{u} + \mu\nabla^2\mathbf{u} + \rho\mathbf{f} = \rho\frac{\partial^2\mathbf{u}}{\partial t^2} \tag{4.7}$$

where **u** is the displacement vector, **f** the vector of body forces, t is time, $\lambda = 2\nu G/(1-2\nu)$ and $\mu = E/2(\nu+1) = G$ are Lamé's elastic constants (where G is shear modulus, E Young's modulus, and ν Poisson's ratio) for the medium, and ρ is the medium's density. In this case, the only body forces acting are due to gravity; but since the desired solution is for vibration about an

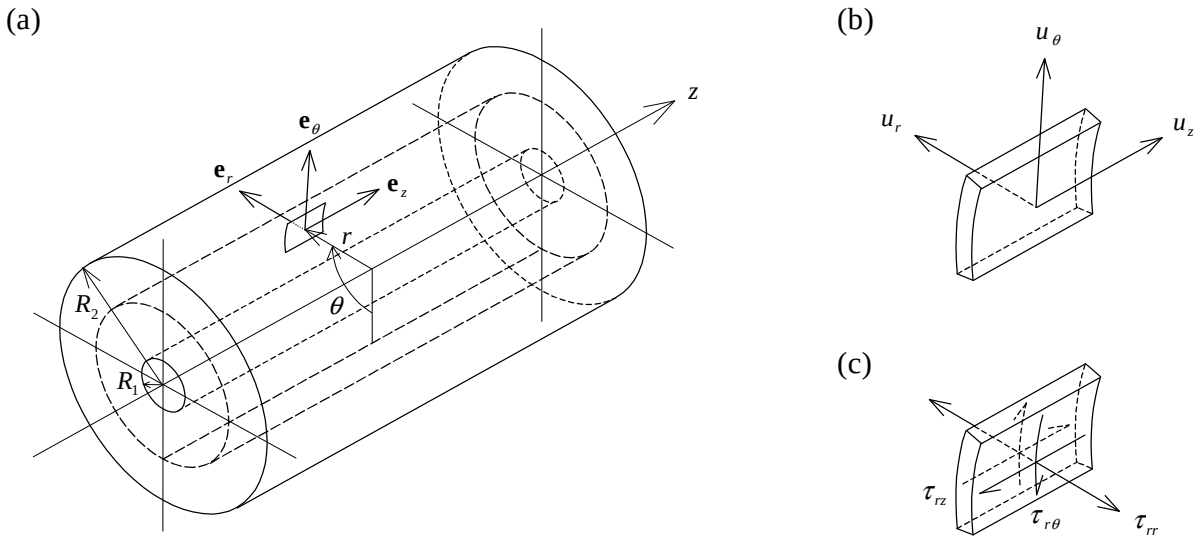

Figure 4.3: Coordinate system used for the theory of an elastic continuum with cylindrical geometry, showing (a) the principle directions with their unit vectors for a typical element on a cylindrical surface of radius r within the bulk medium, (b) the corresponding displacement components and (c) the corresponding cylindrical-surface stress components (stresses acting on the edges of the element are not shown). To model the soil surrounding a railway tunnel, the inner radius is set to $R_1 = a$ to match the cylindrical shell of Figure 4.1, the outer radius is made infinite $R_2 \to \infty$, and the length of the cylinder is taken as infinite.

equilibrium position, they are ignored and **f** is correspondingly set to zero. The problem has cylindrical geometry, so the cylindrical coordinate system will be used. The coordinate, displacement and stress directions are given in Figure 4.3. Note that this system is different from that used for the analysis of the cylindrical shell in the previous section, with *z* now denoting the longitudinal coordinate.

The wave equation (4.7) can be solved by making use of the scalar and vector potentials – Lamé's potentials – which describe the field transformation

$$\begin{aligned} \mathbf{u} &= \nabla\phi + \nabla\times\mathbf{H} \\ \text{with } \nabla\cdot\mathbf{H} &= F(\mathbf{r},t) \end{aligned} \tag{4.8}$$

where **r** is the position vector (r, θ, z). The scalar function $F(\mathbf{r},t)$ is arbitrary, due to the *gauge invariance* of the transformation. The property of gauge invariance essentially means that the displacement field is not altered by the choice of the potentials used to describe it (see Morse and Feshbach [141]). Usually **H** is defined by $\nabla\cdot\mathbf{H}=0$ for convenience, but the arbitrary nature of $F(\mathbf{r},t)$ will be useful for the current problem.

The displacement equations (4.7) are satisfied if the potentials satisfy

$$\begin{aligned} \nabla^2\phi &= \frac{1}{c_1^{\,2}}\frac{\partial^2\phi}{\partial t^2} \\ \text{and } \nabla^2\mathbf{H} &= \frac{1}{c_2^{\,2}}\frac{\partial^2\mathbf{H}}{\partial t^2} \end{aligned} \tag{4.9}$$

where $c_1=\sqrt{(\lambda+2\mu)/\rho}$ is the speed of pressure waves in the medium and $c_2=\sqrt{\mu/\rho}$ the speed of shear waves. Since there are no surfaces or interfaces in the bulk medium, only these two types of waves can exist. For cylindrical coordinates, the Laplacians in (4.9) are given by [73]

$$\begin{aligned} \nabla^2\phi &= \frac{1}{r}\frac{\partial\phi}{\partial r} + \frac{\partial^2\phi}{\partial r^2} + \frac{1}{r^2}\frac{\partial^2\phi}{\partial\theta^2} + \frac{\partial^2\phi}{\partial z^2} \\ \nabla^2\mathbf{H} &= \left(\nabla^2 H_r - \frac{H_r}{r^2} - \frac{2}{r^2}\frac{\partial H_\theta}{\partial\theta}\right)\mathbf{e}_r + \left(\nabla^2 H_\theta - \frac{H_\theta}{r^2} + \frac{2}{r^2}\frac{\partial H_r}{\partial\theta}\right)\mathbf{e}_\theta + \nabla^2 H_z\mathbf{e}_z \end{aligned} \tag{4.10}$$

where $\mathbf{e}_r$, $\mathbf{e}_\theta$ and $\mathbf{e}_z$ are unit vectors in the principal directions of the cylindrical coordinate system, shown in Figure 4.3(a), and H_r, H_θ and H_z are the components of **H**.

From (4.8), the displacement components can be written out as

$$
\begin{aligned}
u_r &= \frac{\partial \phi}{\partial r} + \frac{1}{r}\frac{\partial H_z}{\partial \theta} - \frac{\partial H_\theta}{\partial z} \\
u_\theta &= \frac{1}{r}\frac{\partial \phi}{\partial \theta} + \frac{\partial H_r}{\partial z} - \frac{\partial H_z}{\partial r} \\
u_z &= \frac{\partial \phi}{\partial z} + \frac{1}{r}\frac{\partial (r H_\theta)}{\partial r} - \frac{1}{r}\frac{\partial H_r}{\partial \theta}
\end{aligned}
\tag{4.11}
$$

The components of stress τ_{jk} are given by the general stress-strain relation of Hooke's law, and are (see Timoshenko and Goodier [174])

$$
\begin{aligned}
\tau_{rr} &= (\lambda + 2\mu)\varepsilon_{rr} + \lambda\varepsilon_{\theta\theta} + \lambda\varepsilon_{zz} \\
\tau_{\theta\theta} &= \lambda\varepsilon_{rr} + (\lambda + 2\mu)\varepsilon_{\theta\theta} + \lambda\varepsilon_{zz} \\
\tau_{zz} &= \lambda\varepsilon_{rr} + \lambda\varepsilon_{\theta\theta} + (\lambda + 2\mu)\varepsilon_{zz} \\
\tau_{r\theta} &= 2\mu\varepsilon_{r\theta} = \tau_{\theta r} \\
\tau_{rz} &= 2\mu\varepsilon_{rz} = \tau_{zr} \\
\tau_{\theta z} &= 2\mu\varepsilon_{\theta z} = \tau_{z\theta}
\end{aligned}
\tag{4.12}
$$

where the standard convention for designating stress directions is used (a stress is considered positive if its direction and the direction of the normal to the surface it acts upon are either both positive or both negative with respect to the coordinate system). Hooke's law is valid for linear-elastic materials. If some damping is introduced into the material, so that it becomes viscoelastic, the stress-strain relations (4.12) are still valid for low damping and the small magnitudes of vibration considered here. However, when viscoelastic materials are subjected to large loads and displacements, more comprehensive stress-strain relations involving strain rates apply (see Bland [15] or Flügge [56]). The components of strain ε_{jk} are defined in cylindrical coordinates by [73]

$$
\begin{aligned}
&\varepsilon_{rr} = \frac{\partial u_r}{\partial r}, \quad \varepsilon_{\theta\theta} = \frac{1}{r}\frac{\partial u_\theta}{\partial \theta} + \frac{u_r}{r}, \quad \varepsilon_{zz} = \frac{\partial u_z}{\partial z}, \\
&\varepsilon_{r\theta} = \frac{1}{2}\left(\frac{1}{r}\frac{\partial u_r}{\partial \theta} + \frac{\partial u_\theta}{\partial r} - \frac{u_\theta}{r}\right), \quad \varepsilon_{\theta z} = \frac{1}{2}\left(\frac{\partial u_\theta}{\partial z} + \frac{1}{r}\frac{\partial u_z}{\partial \theta}\right), \\
&\varepsilon_{rz} = \frac{1}{2}\left(\frac{\partial u_r}{\partial z} + \frac{\partial u_z}{\partial r}\right)
\end{aligned}
\tag{4.13}
$$

Equations (4.7) to (4.13) supply enough information to solve for the displacement and stress components. To solve, solutions for the potentials in the wave equations (4.9), separable in the three space variables *r*, θ and *z*, and the time variable *t*, of the following form are assumed.

$$\begin{aligned} \phi &= f(r)\cos n\theta.e^{i(\omega t+\xi z)} \\ H_r &= g_r(r)\sin n\theta.e^{i(\omega t+\xi z)} \\ H_\theta &= g_\theta(r)\cos n\theta.e^{i(\omega t+\xi z)} \\ H_z &= g_z(r)\sin n\theta.e^{i(\omega t+\xi z)} \end{aligned} \tag{4.14}$$

These represent harmonic solutions in the same way as those used in the cylindrical shell analysis, but now there is also variation with radius *r* governed by the functions *f*, g_r, g_θ and g_z (which also vary with ω, ξ and *n*). Substitution of solutions (4.14) into equations (4.9) making use of definitions (4.10) and considering each component of the equation in **H** in turn results in the four differential equations

$$\begin{aligned} & r^2 f'' + rf' - \left[\left(\xi^2 - \frac{\omega^2}{{c_1}^2}\right)r^2 + n^2\right]f = 0 \\ & r^2 g_r'' + rg_r' - \left[\left(\xi^2 - \frac{\omega^2}{{c_2}^2}\right)r^2 + n^2 + 1\right]g_r + 2ng_\theta = 0 \\ & r^2 g_\theta'' + rg_\theta' - \left[\left(\xi^2 - \frac{\omega^2}{{c_2}^2}\right)r^2 + n^2 + 1\right]g_\theta + 2ng_r = 0 \\ & r^2 g_z'' + rg_z' - \left[\left(\xi^2 - \frac{\omega^2}{{c_2}^2}\right)r^2 + n^2\right]g_z = 0 \end{aligned} \tag{4.15}$$

where prime denotes differentiation with respect to *r*.

The first and fourth of equations (4.15) are modified Bessel equations of order *n* (see Kreyszig [112] for an introduction and Watson [185] for more detail), and thus have solutions based on modified Bessel functions of order *n*. However, the second and third equations require further manipulation before a solution can be found. Here the property of gauge invariance becomes useful: one of the functions g_r, g_θ or g_z can be set arbitrarily without any loss of generality [70]. Choosing $g_r = -g_\theta$ and substituting into the second equation of (4.15) gives

$$r^2 g_r'' + rg_r' - \left[\left(\xi^2 - \frac{\omega^2}{{c_2}^2}\right)r^2 + (n+1)^2\right]g_r = 0 \tag{4.16}$$

which is a modified Bessel equation of order $(n+1)$.

Hence solutions for the functions *f*, g_r, g_θ and g_z can be deduced from equations (4.15) and (4.16) in the form of linear combinations of modified Bessel functions as

$$\begin{aligned} f &= AI_n(\alpha r) + BK_n(\alpha r) \\ g_r &= -g_\theta = A_r I_{n+1}(\beta r) + B_r K_{n+1}(\beta r) \\ g_z &= A_z I_n(\beta r) + B_z K_n(\beta r) \end{aligned} \tag{4.17}$$

where $\alpha^2 = \xi^2 - \omega^2/c_1^{\,2}$ and $\beta^2 = \xi^2 - \omega^2/c_2^{\,2}$, and I_n and K_n are modified Bessel functions of respectively the first and second kinds, of order *n*. The coefficients *A, B,* A_r, B_r, A_z and B_z are arbitrary, to be determined from boundary conditions.

The displacements and stresses can be found in terms of the functions given by (4.17) by substituting the expressions for the potentials (4.14) into equations (4.11), recalling that $g_r = -g_\theta$. This gives the displacements as

$$\begin{aligned} u_r &= \left[f' + \frac{n}{r} g_z + i\xi g_r \right] \cos n\theta . e^{i(\omega t + \xi z)} \\ u_\theta &= \left[-\frac{n}{r} f + i\xi g_r - g_z' \right] \sin n\theta . e^{i(\omega t + \xi z)} \\ u_z &= \left[i\xi f - \frac{(n+1)}{r} g_r - g_r' \right] \cos n\theta . e^{i(\omega t + \xi z)} \end{aligned} \tag{4.18}$$

The stresses can be determined from (4.12) by using the strain definitions (4.13) with the displacements (4.18) above. Of the six components of stress, the three which act on cylindrical surfaces of the model (τ_{rr}, $\tau_{r\theta}$ and τ_{rz}) are the most important in the current consideration, because they are involved with the boundary conditions, while the remaining three components ($\tau_{\theta\theta}$, $\tau_{\theta z}$ and τ_{zz}) are internal stresses. The surface stresses are given by

$$\begin{aligned} \tau_{rr} &= \left[(\lambda + 2\mu) f'' + \frac{\lambda}{r} f' - \lambda\left(\frac{n^2}{r^2} + \xi^2 \right) f + 2\mu i\xi g_r' + 2\mu \frac{n}{r} g_z' \right. \\ &\qquad \left. - 2\mu \frac{n}{r^2} g_z \right] \cos n\theta . e^{i(\omega t + \xi z)} \\ \tau_{r\theta} &= \left[-2\mu \frac{n}{r} f' + 2\mu \frac{n}{r^2} f + \mu i\xi g_r' - \mu i\xi \frac{(n+1)}{r} g_r - \mu g_z'' \right. \\ &\qquad \left. + \frac{\mu}{r} g_z' - \mu \frac{n^2}{r^2} g_z \right] \sin n\theta . e^{i(\omega t + \xi z)} \\ \tau_{rz} &= \left[2\mu i\xi f' - \mu g_r'' - \mu \frac{(n+1)}{r} g_r' + \mu\left(\frac{n+1}{r^2} - \xi^2 \right) g_r + \mu i\xi \frac{n}{r} g_z \right] \cos n\theta . e^{i(\omega t + \xi z)} \end{aligned} \tag{4.19}$$

and similar expressions can be found for the other three stress components.

The functions *f*, g_r and g_z are defined in terms of Bessel functions by (4.14), while the displacements and stresses are functions of *f*, g_r and g_z and their derivatives. Thus to determine

final expressions for the displacements and stresses, derivatives of Bessel functions must be determined first. The identities $I'_\nu(z) = (\nu/z)I_\nu(z) + I_{\nu+1}(z)$, $K'_\nu(z) = (\nu/z)K_\nu(z) - K_{\nu+1}(z)$, $I'_\nu(z) = I_{\nu-1}(z) - (\nu/z)I_\nu(z)$ and $K'_\nu(z) = -K_{\nu-1}(z) - (\nu/z)K_\nu(z)$ [185] can be used to calculate the required derivatives and thence to find the displacement and stress components of (4.18) and (4.19) in terms of modified Bessel functions of order *n* and $(n+1)$. The harmonic solutions can then be written in matrix form as

$$\mathbf{u} = \begin{Bmatrix} u_r \\ u_\theta \\ u_z \end{Bmatrix} = [\mathbf{S}]\cdot[\mathbf{U}]\cdot\mathbf{C}e^{i(\omega t+\xi z)}$$

$$\boldsymbol{\tau} = \begin{Bmatrix} \tau_{rr} \\ \tau_{r\theta} \\ \tau_{rz} \\ \tau_{\theta\theta} \\ \tau_{\theta z} \\ \tau_{zz} \end{Bmatrix} = \begin{bmatrix} \mathbf{S} & \mathbf{0} \\ \mathbf{0} & \mathbf{S} \end{bmatrix}\cdot[\mathbf{T}]\cdot\mathbf{C}e^{i(\omega t+\xi z)} \qquad (4.20)$$

$$\text{with } [\mathbf{S}] = \begin{bmatrix} \cos n\theta & 0 & 0 \\ 0 & \sin n\theta & 0 \\ 0 & 0 & \cos n\theta \end{bmatrix}$$

The stress vector has been arranged so that the first three elements are the surface stresses τ_{rr}, $\tau_{r\theta}$ and τ_{rz}. $\mathbf{C} = \{A \quad B \quad A_r \quad B_r \quad A_z \quad B_z\}^{\mathrm{T}}$ is the vector of coefficients, determined from boundary conditions. The 3×6 matrix [**U**] defining displacements, and the 6×6 matrix [**T**] defining stresses, are given in full in Appendix B. The elements of both matrices are in terms of modified Bessel functions with arguments of αr and βr, and thus are functions of wavenumber ξ, frequency ω and circumferential mode number *n*, as well as radius *r* and the material properties.

By comparing (4.20) to the solutions (4.4) and (4.5) for the cylindrical shell, the elastic continuum's displacements and stresses can be written in the wavenumber-frequency domain in a way similar to the shell result (4.6). The displacement and surface stress components are

$$\begin{Bmatrix} \tilde{U}_{rn} \\ \tilde{U}_{\theta n} \\ \tilde{U}_{zn} \end{Bmatrix} = [\mathbf{U}]\cdot\mathbf{C} \quad \text{and} \quad \begin{Bmatrix} \tilde{T}_{rrn} \\ \tilde{T}_{r\theta n} \\ \tilde{T}_{rzn} \end{Bmatrix} = [\mathbf{T}_r]\cdot\mathbf{C} \qquad (4.21)$$

where the 3×6 matrix $[\mathbf{T}_r]$ is the top half of the 6×6 matrix [**T**] in (4.20).

4.3 Solution and Results for Particular Boundary Conditions

Before the displacements of either the cylindrical shell for the tunnel or the elastic continuum for the soil can be determined, the boundary conditions must be specified. For modelling the tunnel surrounded by soil, the boundary conditions include the applied loads, compatibility of displacements and equilibrium of stresses at the tunnel-soil interface, and a radiation condition for the infinite soil. The equations can of course be used to model the dynamic behaviour of other problems with cylindrical geometry if the appropriate boundary conditions are used, and this provides a means to check the equations before they are used to model the full tunnel-in-soil case. In general the external loading applied to the tunnel will not be harmonic in *space,* even if, as here, steady-state harmonic variation in *time* is of interest. Each general applied stress will instead be a linear combination of the spatially harmonic components given in (4.4) for the shell or (4.21) for the continuum. The total displacement response can be obtained by adding the individual harmonic displacement components which result from each of the harmonic load terms which make up the total load, calculating the components from (4.6) or (4.21) in combination with the other boundary conditions which apply to a given problem.

4.3.1 Resolution of a Point Load

The most useful result for the tunnel model is its response to a unit point load, as the response to a more complicated loading condition can easily be determined by a superposition of point-load cases with suitable translations and rotations. The greatest effect on the tunnel from interaction with a track supported by it is assumed to be via normal reaction forces; the longitudinal and tangential applied forces are therefore set to zero. The spatial variation of such a point load is shown in Figure 4.4(a). The response to this load is equivalent to the Green's function of the tunnel for a time-harmonic point load in space, although the Green's function is more generally the same as the impulse response function, that is, the response to an input impulsive in both time and space.

The problem here is to cast the load into a form which can be utilised with the previously developed results. The cylindrical shell notation will be used for the following argument, but it holds equally for the elastic continuum as well. The loads p_x, p_y and p_z applied to the inside

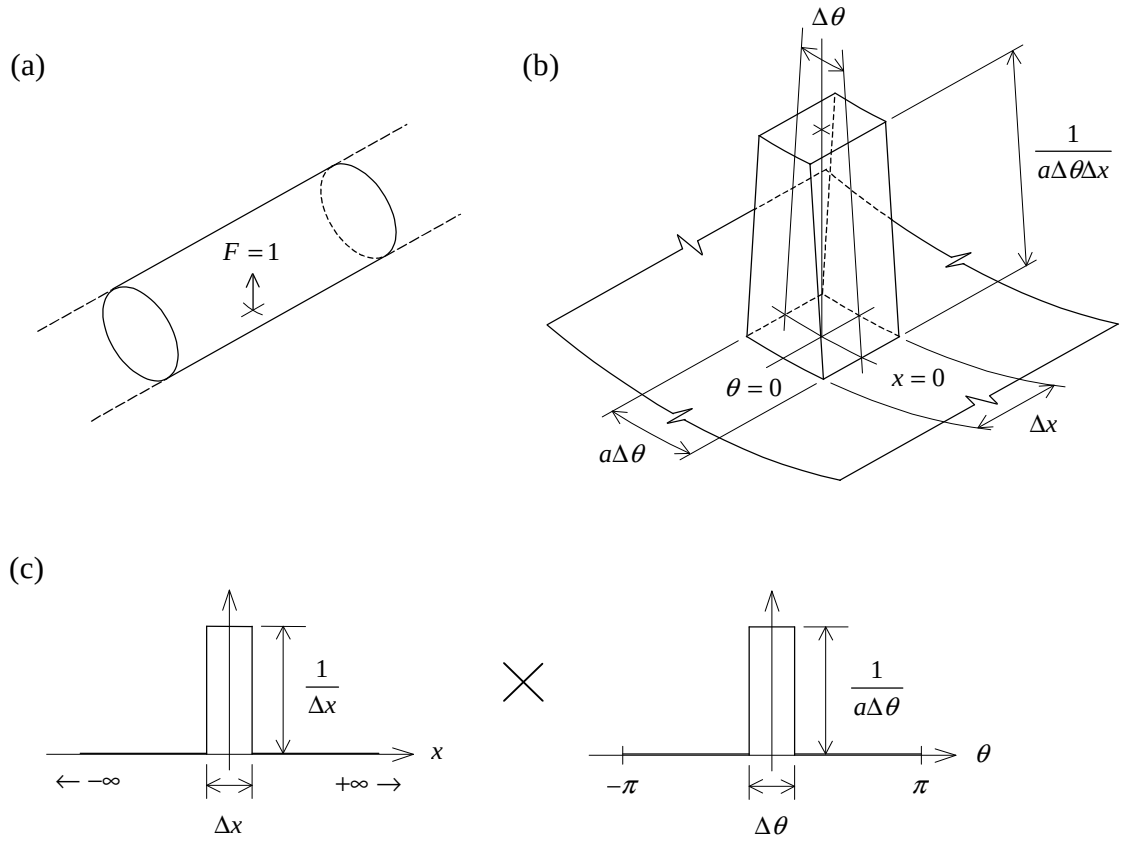

Figure 4.4: (a) A unit normal point force acting on the invert of an infinitely long tunnel can be construed as (b) an appropriately scaled uniform normal stress acting over a small rectangular area centred on $x = 0$ and $\theta = 0$. This normal stress distribution can be decomposed into (c) the product of two rectangular pulse functions, one in *x* and one in θ.

of the shell (which correspond to q_x, q_y and q_z in (4.4) if there are no loads applied to the outside of the shell) are *stresses*, while the proposed normal point load is a *force*. To ensure that the normal stress is scaled correctly to be equivalent to a unit force, the spatial variation of the normal loading can be visualised as a three-dimensional rectangular pulse centred on the position $x = 0$ and $\theta = 0$, of (small) base side-lengths Δx and $a\Delta\theta$, and of height $1/a\Delta\theta\Delta x$ (the stress magnitude), as depicted in Figure 4.4(b). This pulse can be considered as the product of two separate rectangular pulses in *x* and θ, given in Figure 4.4(c). The point load is achieved in the limit as Δx and $\Delta\theta$ tend to zero. Thus the state of applied stress for a unit point load is

$$\begin{aligned} p_x &= p_y = 0 \\ p_z &= \begin{cases} \dfrac{1}{a\Delta\theta\Delta x}\cdot e^{i\omega t} & \text{for } \frac{-\Delta x}{2} \le x \le \frac{\Delta x}{2} \text{ and } \frac{-\Delta\theta}{2} \le \theta \le \frac{\Delta\theta}{2} \\ 0 & \text{otherwise} \end{cases} \\ &\to \frac{\delta(x)\delta(\theta)}{a}\cdot e^{i\omega t} \quad \text{as } \Delta x, \Delta\theta \to 0 \end{aligned} \tag{4.22}$$

where $\delta(x)$ and $\delta(\theta)$ are Dirac delta functions.

The solutions for the cylindrical shell (4.6) and elastic continuum (4.21) are expressed in the wavenumber-frequency domain for a particular circumferential mode number *n*. While the desired final displacement results will be FRFs – that is, will remain in the frequency domain – they will, in general, be linear combinations of the space-harmonic components calculated by (4.6) or (4.21), due to the fact that the applied loading is in general expressed as linear combinations of the space-harmonic stress components, as discussed above. Thus the point load (4.22) must be decomposed into its space-harmonic components before the displacements can be found.

Around the circumference, the space-harmonic variation is represented by the discrete ring modes of order *n*, while the variation of the load is represented by the term $\delta(\theta)/a$. This part of the load can be written as a linear combination of the ring modes by means of the Fourier Series (see Kreyszig [112])

$$\begin{aligned} \frac{\delta(\theta)}{a} &= a_0 + \sum_{n=1}^{\infty}\left(a_n \cos n\theta + b_n \sin n\theta\right) \\ \text{with} \quad a_0 &= \frac{1}{2\pi}\int_{-\pi}^{\pi}\frac{\delta(\theta)}{a}.d\theta = \frac{1}{2\pi a} \\ a_n &= \frac{1}{\pi}\int_{-\pi}^{\pi}\frac{\delta(\theta)}{a}\cos n\theta.d\theta = \frac{1}{\pi a} \\ b_n &= \frac{1}{\pi}\int_{-\pi}^{\pi}\frac{\delta(\theta)}{a}\sin n\theta.d\theta = 0 \end{aligned} \tag{4.23}$$

on the interval $-\pi < \theta \le \pi$. The series has reduced to a Fourier cosine series ($b_n = 0$) because the Dirac delta $\delta(\theta)$ is an even function.

The longitudinal variation of the load is described by the term $\delta(x)$. Since the tunnel is infinitely long, the space-harmonic decomposition of this term is not described by discrete modes, but rather by a continuous function of ξ. The harmonic components are found by taking the Fourier transform of the term $\delta(x)$. Conversely, the total longitudinal variation of the load is described by the inverse Fourier transform of the resulting function $\tilde{\delta}(\xi)$; that is, the sum of the contributions from the harmonics at each increment of ξ. Thus,

$$\begin{aligned} \tilde{\delta}(\xi) &= \int_{-\infty}^{\infty} \delta(x).e^{-i\xi x}.dx = 1 \quad \text{for all } \xi \\ \text{and} \quad \delta(x) &= \frac{1}{2\pi}\int_{-\infty}^{\infty} \tilde{\delta}(\xi).e^{i\xi x}.d\xi = \frac{1}{2\pi}\int_{-\infty}^{\infty} 1.e^{i\xi x}.d\xi \end{aligned} \tag{4.24}$$

where the Fourier transform pair used has the factor of $1/2\pi$ in the inverse transform[†]. This definition will prove the most convenient for transformations from the space to wavenumber domain and vice-versa.

Substituting the results for $\delta(\theta)/a$ and $\delta(x)$ from (4.23) and (4.24) into (4.22) yields

$$\begin{aligned} p_x &= p_y = 0 \\ p_z &= \frac{1}{2\pi}\int_{-\infty}^{\infty}\left(\frac{1}{2\pi a} + \frac{1}{\pi a}\sum_{n=1}^{\infty}\cos n\theta\right).e^{i\xi x}d\xi \; .e^{i\omega t} \end{aligned} \tag{4.25}$$

for the state of applied stress. Recalling that (4.25) is a transform of a sum of modal space-harmonic stress components and comparing it with those components in (4.4) allows the harmonic stresses for a particular circumferential mode number *n* to be deduced as

$$\begin{aligned} \tilde{P}_{xn} &= 0 \\ \tilde{P}_{yn} &= 0 \\ \tilde{P}_{zn} &= \begin{cases} 1/2\pi a, & n = 0 \\ 1/\pi a, & n \geq 1 \end{cases} \end{aligned} \tag{4.26}$$

for all ξ. The harmonic displacements $\{\tilde{U}_n \quad \tilde{V}_n \quad \tilde{W}_n\}^{\mathrm{T}}$ are calculated for each value of *n* from (4.6) by applying the harmonic stresses (4.26). The total displacements resulting from a time-harmonic unit point load are given by the linear combination of these spatially harmonic components. In the same way as the load, the linear combination is achieved by the inverse Fourier transform of a sum of the modal components, but this time there are no scaling factors explicitly apparent, since the modal displacements are derived from the correctly scaled modal stresses. Thus the total displacements are given by

[†] This is the definition of Fourier transform usually used (though for functions of time) in electrical engineering and digital signal processing (see Maloney et al [127], Stearns [168]). However, the position of the factor of $1/2\pi$ can vary. The convention used in the field of random vibration has the $1/2\pi$ in the forward transform (see Newland [144]), while a definition with a $1/\sqrt{2\pi}$ in each of the forward and inverse transforms is often used in mathematics and physics (see Kreyszig [112]).

$$\begin{Bmatrix} u \\ v \\ w \end{Bmatrix} = \begin{Bmatrix} U \\ V \\ W \end{Bmatrix} e^{i\omega t} = \frac{1}{2\pi}\int_{-\infty}^{\infty} \left(\begin{Bmatrix} \tilde{U}_0 \\ 0 \\ \tilde{W}_0 \end{Bmatrix} + \sum_{n=1}^{\infty} \begin{Bmatrix} \tilde{U}_n \cos n\theta \\ \tilde{V}_n \sin n\theta \\ \tilde{W}_n \cos n\theta \end{Bmatrix} \right) . e^{i\xi x} d\xi \; . e^{i\omega t} \qquad (4.27)$$

where the term which would correspond to $\tilde{V}_0$ is zero because it is properly multiplied by $\sin n\theta\big|_{n=0} = 0$, while the other two elements of the same vector are properly multiplied by $\cos n\theta\big|_{n=0} = 1$. In other words, the total wavenumber-domain displacements $\tilde{U}$ and $\tilde{W}$ are Fourier cosine series (which start from $n = 0$), while the displacement $\tilde{V}$ is a Fourier sine series (which starts from $n = 1$). In practice it is not possible to calculate an infinite number of circumferential modes for the summation, so only as many as required to reach satisfactory convergence are used.

Thus the time-harmonic displacement response is, in general, the inverse Fourier transform (from the wavenumber to space domain) of a sum of the circumferential modes in the wavenumber domain; or, alternatively, a sum of the circumferential modes in the space domain, obtained by the inverse Fourier transform of the modes in the wavenumber domain. The result (4.27) holds for any type of time-harmonic loading condition; the modal displacements $\{\tilde{U}_n \quad \tilde{V}_n \quad \tilde{W}_n\}^{\mathrm{T}}$ just have to be calculated for the correct modal stress components, in place of those given by (4.26) for the normal point load. More general loads that are *not* harmonic in time could be treated by introducing a second inverse Fourier transform from the frequency to time domain.

4.3.2 Modelling a Thin-Walled Cylinder with the Elastic Continuum Theory

A useful check on the solutions (4.6) for the cylindrical shell and (4.21) for the elastic continuum, and for the validity of using thin-shell theory for the tunnel, is to make use of the continuum theory to model a thin-walled cylinder.

For an infinitely long, free cylindrical shell loaded on the inside surface only, the modal loading components $\tilde{\mathbf{Q}}_n$ of (4.4) will simply be the applied loading $\tilde{\mathbf{P}}_n$. Thus the modal displacement components can be calculated from (4.6) as

$$\begin{Bmatrix} \tilde{U}_n \\ \tilde{V}_n \\ \tilde{W}_n \end{Bmatrix} = \frac{-a(1-\nu^2)}{Eh}[\mathbf{A}]^{-1}\begin{Bmatrix} \tilde{P}_{xn} \\ \tilde{P}_{yn} \\ \tilde{P}_{zn} \end{Bmatrix} \tag{4.28}$$

To obtain an equivalent solution using continuum theory is more complicated. To begin with, the conventional notations used in shell theory and continuum theory do not correspond exactly to one another. The relationships between the displacements and stresses in the two different coordinate systems can be found by comparing Figures 4.1 and 4.3. They are

$$\begin{aligned} u &\equiv u_z & \tau_{zx} &\equiv -\tau_{rz} \\ v &\equiv u_\theta & \tau_{zy} &\equiv -\tau_{r\theta} \\ w &\equiv -u_r & \tau_{zz} &\equiv \tau_{rr} \end{aligned} \tag{4.29}$$

where the shell quantities have been given first. The shell coordinate system is more convenient here, because in this system stresses applied to an inside cylindrical surface (such as a tunnel invert) are positive in the same direction as the resulting displacements.

The thin-walled cylinder equivalent to the shell will have an inside radius of the mean shell radius *minus* half the shell thickness, and an outside one of the mean radius *plus* half the thickness. The applied stresses on the inside are the same as before, taking note of the differences in directions given by (4.29), and the outside ones are again zero. Using (4.21), these stress boundary conditions can be written

$$[\mathbf{T}_r]_{r=a-h/2}\cdot\mathbf{C} = \begin{Bmatrix} \tilde{P}_{zn} \\ -\tilde{P}_{yn} \\ -\tilde{P}_{xn} \end{Bmatrix} \quad \text{and} \quad [\mathbf{T}_r]_{r=a+h/2}\cdot\mathbf{C} = \begin{Bmatrix} 0 \\ 0 \\ 0 \end{Bmatrix} \tag{4.30}$$

and are sufficient to solve for the 6x1 vector of coefficients **C**, which can then be substituted into the displacement expression of (4.21). For direct comparison to the thin-shell result (4.28), the displacements should be calculated for the mean radius of the cylinder wall. Thus the modal displacement components are given by

$$\begin{Bmatrix} \tilde{U}_{rn} \\ \tilde{U}_{\theta n} \\ \tilde{U}_{zn} \end{Bmatrix} = [\mathbf{U}]_{r=a}\cdot\begin{bmatrix} [\mathbf{T}_r]_{r=a-h/2} \\ [\mathbf{T}_r]_{r=a+h/2} \end{bmatrix}^{-1}\cdot\begin{Bmatrix} \tilde{P}_{zn} \\ -\tilde{P}_{yn} \\ -\tilde{P}_{xn} \\ 0 \\ 0 \\ 0 \end{Bmatrix} \tag{4.31}$$

Either of the solutions (4.28) or (4.31) can be used to determine the total displacement due to a particular set of load stresses by a modal summation then inverse Fourier transform, as given by equation (4.27). If the cylinder is excited by a normal point load, then the stress components (4.26) are used in (4.28) or (4.31).

4.3.3 Results for the Thin-Walled Cylinder

The numerical results for the thin-walled cylinder were calculated using the unit point load described by (4.26) to determine the wavenumber-domain modal displacement components from (4.28) for the shell theory, or (4.31) for the continuum theory, for a range of modenumber *n*. These components were then summed and inverse Fourier transformed as in (4.27) to give total displacements in the space domain. All these operations were accomplished numerically in Matlab, and are described in this section.

The geometry and material parameters were chosen for comparison to match those used by Tuchinda [179], who uses the finite-element (FE) method to model a free, infinitely long cylindrical shell. An 88m-long cylindrical unit of 704 8-node thick-shell elements (16 circumferentially by 44 longitudinally) was analysed through the ABAQUS FE package to compute its dynamic-stiffness matrix (DSM). The repeating-unit method (see Chapter 3) was applied to this DSM to join the cylindrical units at 8 nodes at each end, giving the DSM of a semi-infinite cylindrical shell, two of which make an infinite shell.

The numerical values of the parameters used are given in Table 4.1. Those for the shell theory come directly from values given in [179], while those for the continuum theory are derived from them. The material parameters are for concrete and the radius and thickness are typical for an underground railway tunnel, so the infinite cylinder with these properties represents a very long, free tunnel with no surrounding soil.

The material damping used for the FE model was Rayleigh (or proportional) damping, governed by the two parameters α_{R} and β_{R} in Table 4.1. This form of damping is such that the FE model is represented by

$$\begin{gathered}[\mathbf{M}]\ddot{\mathbf{x}} + [\mathbf{C}]\dot{\mathbf{x}} + [\mathbf{K}]\mathbf{x} = \mathbf{f} \\ \text{with } [\mathbf{C}] = \alpha_{\mathbf{R}}[\mathbf{M}] + \beta_{\mathrm{R}}[\mathbf{K}]\end{gathered} \tag{4.32}$$

Cylindrical Shell	Elastic Continuum
$E = 50\times10^9$ Pa	$\lambda = 28.85\times10^9$ Pa
$\nu = 0.3$	$\mu = 19.23\times10^9$ Pa
$\rho = 2500\,\mathrm{kg/m^3}$	$\rho = 2500\,\mathrm{kg/m^3}$
$\alpha_\mathrm{R} = 10\,\mathrm{s^{-1}}$	$c_1 = 5189\,\mathrm{m/s}$
$\beta_\mathrm{R} = 40\times10^{-6}\,\mathrm{s}$	$c_2 = 2774\,\mathrm{m/s}$
$a = 3.125\,\mathrm{m}$	$\alpha_\mathrm{R} = 10\,\mathrm{s^{-1}}$
$h = 0.25\,\mathrm{m}$	$\beta_\mathrm{R} = 40\times10^{-6}\,\mathrm{s}$
	r from a and h

Table 4.1: Parameter values used to model a thin-walled cylinder.

where [**M**] is the mass matrix, [**C**] the damping matrix, [**K**] the stiffness matrix, **x** the vector of nodal displacements and **f** the vector of forces applied to nodes. In the frequency domain with $\mathbf{x} = \mathbf{X}e^{i\omega t}$, this is equivalent to using complex mass and stiffness matrices of the form $[\mathbf{M}]^* = (1+\alpha_\mathrm{R}/i\omega)[\mathbf{M}]$ and $[\mathbf{K}]^* = (1+i\omega\beta_\mathrm{R})[\mathbf{K}]$ without a separate damping matrix [**C**]. The Rayleigh damping can thus similarly be accounted for in the continuous shell model (4.28) by including the mass-proportional damping in a complex density $\rho^* = \rho(1+\alpha_\mathrm{R}/i\omega)$ and the stiffness-proportional damping in a complex Young's modulus $E^* = E(1+i\omega\beta_\mathrm{R})$. The same complex density can be used in the corresponding elastic-continuum result (4.31), while Lamé's constants λ and μ are proportional to E and so can be replaced by the complex values $\lambda^* = \lambda(1+i\omega\beta_\mathrm{R})$ and $\mu^* = \mu(1+i\omega\beta_\mathrm{R})$. Rayleigh damping is only used here to allow comparison to the FE results. Loss-factor damping as used later is perfectly adequate for most purposes.

Once the modal wavenumber-domain displacements are calculated from (4.28) or (4.31), the total solution is obtained by substituting them into (4.27). This involves two operations: a sum of circumferential modes and an inverse Fourier transform from the ξ- to x-domain. The ξ-domain displacements are calculated numerically by matrix operations on the analytical solutions, so the transform must also be done numerically, using the inverse discrete Fourier transform (DFT) described in standard texts such as Newland [143, 144] or Stearns [168]. The DFT pair which corresponds to the definition of Fourier transform used to resolve the load in (4.24) and to obtain the solution (4.27) is

$$\begin{aligned} \text{DFT:} \quad \hat{Y}_k &= \sum_{m=0}^{N-1} Y_m e^{-i(2\pi km/N)}, \qquad k = 0,1,2,\ldots,(N-1) \\ \text{IDFT:} \quad Y_m &= \frac{1}{N}\sum_{k=0}^{N-1} \hat{Y}_k e^{i(2\pi km/N)}, \quad m = 0,1,2,\ldots,(N-1) \\ \xi_k &= \frac{2\pi k}{N\Delta x} \end{aligned} \tag{4.33}$$

where N is the number of discrete points at a spacing of Δx in the sample Y_m of $Y(x)$ and hence in the sample $\hat{Y}_k$ of $\hat{Y}(\xi)$ at wavenumbers ξ_k. The exponential $e^{i(2\pi km/N)}$ corresponds to the $e^{i\xi x}$ in the continuous Fourier transform. The DFT $\hat{Y}(\xi)$ is related to the continuous Fourier transform $\tilde{Y}(\xi)$ by [168]

$$\hat{Y}(\xi) = \frac{1}{\Delta x}\sum_{k=-\infty}^{\infty} \tilde{Y}\left(\xi - \frac{2\pi k}{\Delta x}\right) \tag{4.34}$$

that is, the DFT is a superposition of an infinite number of shifted Fourier transforms. While the Fourier transform is not periodic, (4.34) shows that the DFT is, so that (4.33) represents just one period of the DFT. For this DFT period to be a close approximation of the Fourier transform, Δx must be small enough to give sufficient separation between the Fourier transforms in the sum of (4.34), otherwise they will overlap and add at ξ where they contain significant energy. This condition can be met by satisfying the Nyquist criterion (or sampling theorem): the sampling frequency $2\pi/\Delta x$ in the *x*-domain must be at least *twice* the largest ξ-component of the signal to correctly capture all ξ-components. If it is not satisfied, aliasing will occur, where high-wavenumber components will be falsely mapped to lower wavenumbers, that is, overlap will occur in (4.34). It follows from this that the highest ξ-component extracted by a DFT is half the sampling wavenumber, known as the Nyquist wavenumber. Similar considerations apply to the inverse DFT. In practice, therefore, the DFT can be considered equivalent to the Fourier transform if both the sample and its transform decay to zero at their respective extremities.

The inverse DFT was carried out by the inverse fast Fourier transform (FFT) algorithm provided in Matlab. This FFT computes the transform (4.33), which represents a DFT period from zero to $2\xi_{\text{Nyquist}}$ rather than one centred on $\xi = 0$. The analytical displacement expressions (4.28) or (4.31) give an exact Fourier transform which is centred on $\xi = 0$ by definition. Thus a sample set calculated using (4.28) or (4.31) must be scaled by $1/\Delta x$ from (4.34) and rearranged

by transposing the negative-ξ data to come *after* the positive-ξ data, so that the discrete sample resembles the correct DFT period and the inverse DFT of (4.33) can be applied.

The inverse DFT of (4.33) can be used to transform individual modal displacement components into the space domain to check that the Nyquist criterion is satisfied and to examine modal behaviour. Figure 4.5 shows the radial modal displacement for $n = 3$ in both the wavenumber and space domains, calculated from the shell theory. The DFT parameters used were $\Delta x = 0.5\text{m}$ and $N = 2048$. Figure 4.5(a) shows this displacement at a frequency of 30Hz. The displacement is a sharp localised pulse at $x = 0$ and this follows from the broad wavenumber content shown in the ξ-domain. Thus at this frequency, the small Δx is required to give a maximum wavenumber (2π here) large enough to capture all the broad wavenumber information and ensure the Nyquist criterion is met. Figure 4.5(b) shows the displacement at a

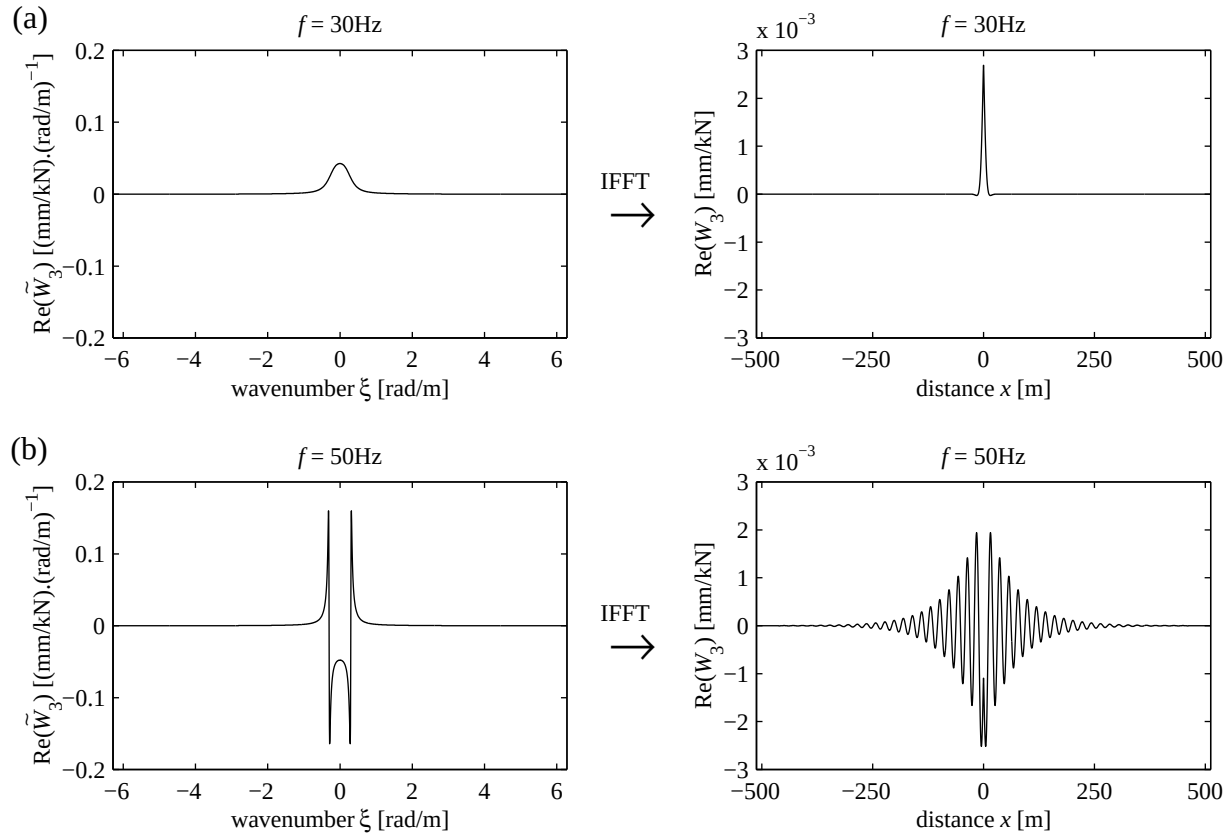

Figure 4.5: The real part of the radial modal displacement components $\tilde{W}_n(\xi)$ and $W_n(x)$, for $n = 3$, for an infinitely long, thin cylindrical shell with properties as given in Table 4.1 and loaded by a unit point force at $x = 0$, at a frequency (a) below the natural frequency for the ring mode and (b) above the natural frequency. The real part in the *x*-domain represents a "snapshot" for time $t = 0$. The imaginary parts are of similar form. The inverse FFT is done with $\Delta x = 0.5\text{m}$ and $N = 2048$ and is performed on the complete complex displacement components $\tilde{W}_n(\xi)$, not just the real parts illustrated. Loading of $\tilde{P}_{xn} = \tilde{P}_{yn} = 0$ and $\tilde{P}_{zn} = 1$.

frequency of 50Hz. In the *x*-domain there is now a propagating wave rather than a localised displacement pulse. In the ξ-domain the displacement is concentrated around a single value of wavenumber of about $0.3\,\mathrm{rad/m}$, corresponding to the 21m wavelength of the travelling wave. This time the large *N* is needed to capture all of the displacement response in the *x*-domain. It can be seen that the chosen values of *N* and Δx result in all the functions shown in Figure 4.5 decaying to zero at the ends of their sample sets, so the inverse DFTs to the *x*-domain can be trusted as good representations of the actual inverse Fourier transforms.

The transition from localised to propagating modal displacement seen in Figure 4.5 occurs at the natural frequency of the $n=3$ circumferential ring mode. The radial displacement *w* is associated with in-plane flexural modes of the circular cross-section, Figure 4.2(a). The natural frequency f_n of the n^{th} in-plane flexural ring mode for a slender ring is (see Den Hartog [45] or Blevins [17])

$$f_n = \frac{1}{2\pi a^2}\frac{n(n^2-1)}{(n^2+1)^{1/2}}\sqrt{\frac{EI_x}{m}} = \frac{1}{2\pi a^2}\frac{n(n^2-1)}{(n^2+1)^{1/2}}\sqrt{\frac{Eh^2}{12\rho}}, \quad n=1,2,3,\ldots \tag{4.35}$$

where I_x is the second moment of area and *m* the mass per unit length of the beam forming the circular ring. The right-hand side of (4.35) can be applied to the infinitely long thin-walled cylinder. The first in-plane mode associated with *w* is, however, the expansion mode with $n=0$. This is really a type of in-plane extensional ring mode, the higher orders of which correspond to tangential displacement *v*. The natural frequency f_n of the n^{th} in-plane extensional ring mode for a slender ring is [17]

$$f_n = \frac{(1+n^2)^{1/2}}{2\pi a}\sqrt{\frac{E}{\rho}}, \quad n=0,1,2,\ldots \tag{4.36}$$

The values of the natural frequencies for the radial in-plane ring modes of the thin-walled cylinder can be calculated from (4.35) and (4.36) and are given in Table 4.2 for the first eleven values of *n*. For the $n=3$ mode $f_n = 39.9\mathrm{Hz}$, which accords with the localised displacement at 30Hz and propagating displacement at 50Hz apparent in Figure 4.5.

n	f_n [Hz]	n	f_n [Hz]
0	227.8	6	181.6
1	0	7	249.9
2	14.1	8	328.8
3	39.9	9	418.2
4	76.5	10	518.2
5	123.8		

Table 4.2: Natural frequencies for in-plane ring modes associated with radial displacement of the thin-walled cylinder with properties given in Table 4.1.

Having established the spacing and the number of points required for the inverse DFT, there remains the question of how many modal displacement terms have to be included in the Fourier series sum of the solution (4.27) to give satisfactory convergence. Each modal displacement behaves like the $n = 3$ one discussed above, with a localised displacement below the ring-mode natural frequency, and a propagating displacement above. At a given driving frequency, the response at a point some distance from the driving point will only depend on modal displacements which have begun to propagate, that is, have natural frequencies below the driving frequency. From Table 4.2 it can be deduced that only the modes up to $n = 4$ would have to be included to achieve convergence at a remote point along the cylinder for driving frequencies up to 100Hz. However, the total driving point response at $x = 0$ has significant contributions from both propagating and localised modal displacements. Nevertheless, the localised modal displacements decrease in maximum magnitude with increasing modenumber *n*, that is, the further their natural frequencies lie above the driving frequency. It was found that convergence at $x = 0$, both longitudinally and circumferentially, was reached with a sum of the modes up to $n = 10$ for frequencies up to 100Hz. Thus all calculations were done using the first eleven modes.

The general procedure adopted to calculate numerical values of the total displacements can be summarised as follows:

1. Calculate an array of modal displacement values from (4.28) or (4.31) for a grid of 2048 ξ-points by 100 ω-points, for each *n* from 0 to 10;
2. Multiply each array by the appropriate $\cos n\theta$ or $\sin n\theta$ term and add them together to effect the Fourier-series part of (4.27), giving total displacements in the ξ-domain;

3. Apply the inverse FFT over the columns of the summed array to effect the Fourier-transform part of (4.27), giving total displacements in the *x*-domain.

The frequency range started at 1Hz because zero frequency causes the matrices of coefficients to become singular. Each row of the final array corresponds to the FRF at a particular value of *x*.

Figure 4.6 gives the driving point response of the thin-walled cylinder calculated from the shell theory, the continuum theory and from Tuchinda's FE plus repeating-unit method. These three results are also compared to a free bending beam of infinite length, which models the translation of the cross-section ($n=1$ ring mode) only. Starting from the equation of motion (3.1) for an Euler beam it is easy to show that the displacement frequency response $Y(x,\omega)$ of such a beam excited by a unit point harmonic force at $x=0$ is given by

$$Y(x,\omega) \;=\; \frac{1}{4\alpha^3 EI}\left(e^{\alpha|x|} + ie^{i\alpha|x|}\right), \quad \text{with } \alpha^4 = \frac{m\omega^2}{EI} \tag{4.37}$$

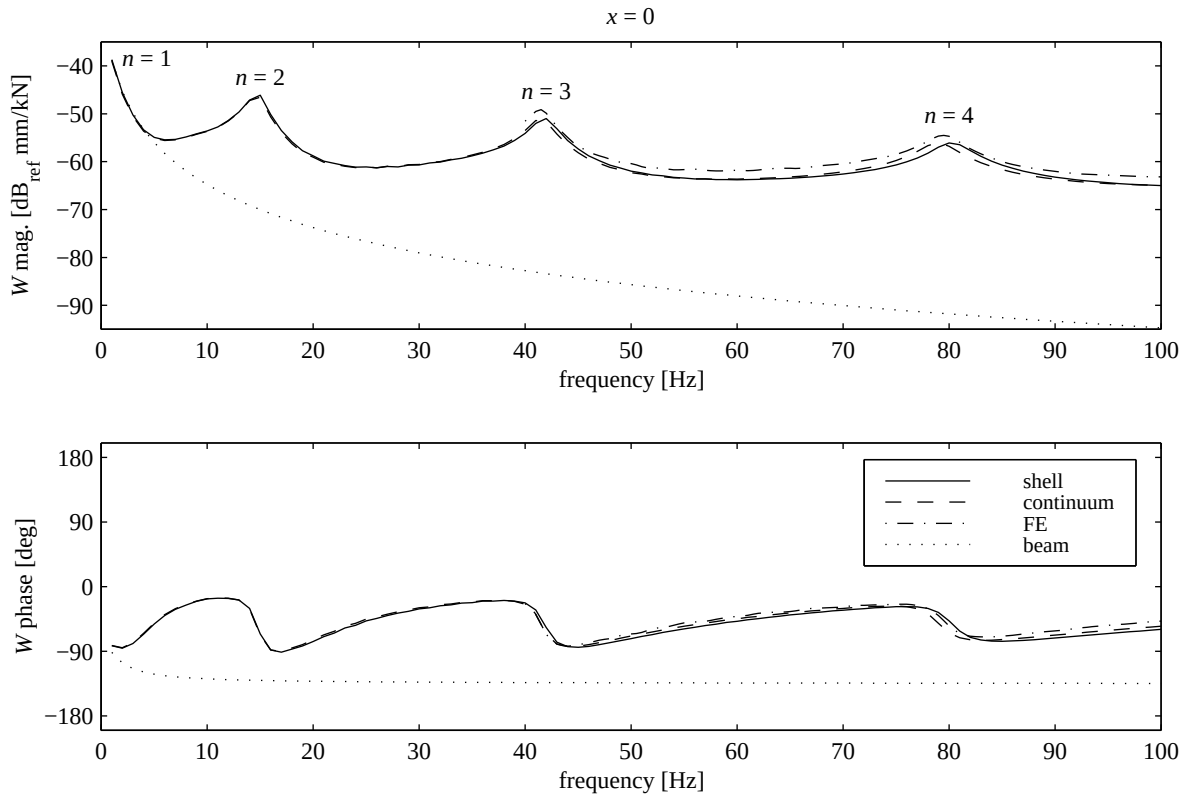

Figure 4.6: The radial driving point response (at $x=0$, $\theta=0$) for an infinitely long, free thin-walled cylinder with properties as given in Table 4.1, showing results calculated from the shell theory, continuum theory and Tuchinda's [179] FE plus repeating-unit approach, compared to the driving point response of an infinitely long, free Euler beam with equivalent material and cross-sectional properties. The resonant peaks are marked with their corresponding modenumber *n*; their frequencies can be compared to those given in Table 4.2.

where m is the mass per unit length of the beam and EI its bending stiffness. The root α used is the second-quadrant one, so that both α and $i\alpha$ have negative real parts and the two exponentials in (4.37) decay as $|x| \to \infty$. The beam parameters equivalent to the thin-walled cylinder defined by Table 4.1 are $m = 12.27 \times 10^3$ kg/m and $EI = 1.200 \times 10^{12}$ Pa.m^4.

Figure 4.6 shows that the infinite free beam gives a good approximation of the driving-point response until the $n = 2$ ring mode of the cylinder starts to resonate. The resonances correspond well with the calculated ring-mode natural frequencies given in Table 4.2, but are a little higher because the different types of modes are coupled in the cylinder but not in a ring. Figure 4.7 gives the response at 88m along the infinite cylinder. This time the bending beam gives a good approximation all the way up to 15Hz, above which frequency the $n = 2$ ring mode begins propagating from $x = 0$ and reaches $x = 88$m. Both the driving-point and remote responses show very good agreement between the shell, continuum and FE results. This consistency means firstly that the shell and continuum equations are working correctly and secondly that the use of the shell equations is justified to model the thin-walled cylinder of the tunnel. The tunnel could

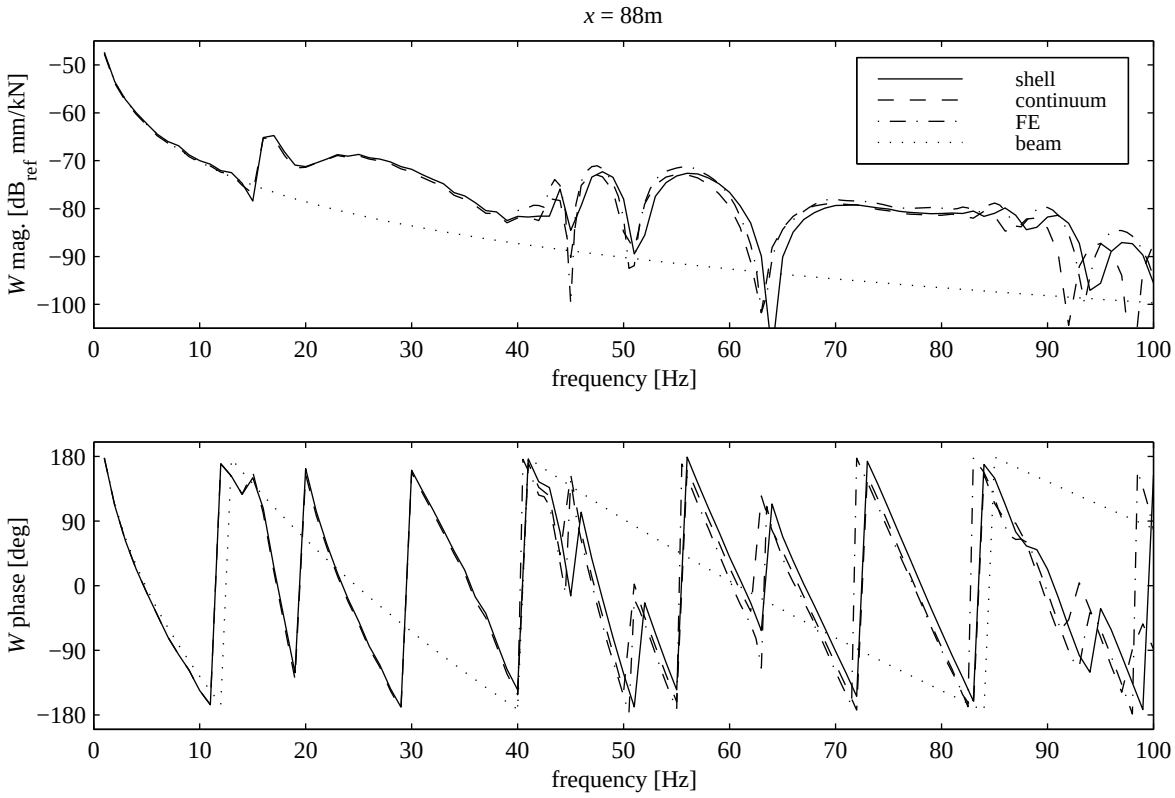

Figure 4.7: The radial response of an infinitely long, free cylindrical shell at a point remote ($x = 88$m, $\theta = 0$) from the normal point load (at $x = 0$, $\theta = 0$), calculated by the same methods and for the same shell properties (Table 4.1) as Figure 4.6.

just as well be modelled by the continuum method, but the shell solution (4.28) involves one 3×3 matrix instead of the three 3×6 matrices of the continuum solution (4.31), so saving computation time. There are also great advantages over the FE method. To calculate the response of one unit at 61 frequency points (40Hz to 100Hz), the ABAQUS FE model required a total of 18 hours run time and 7320MB disk space [179]. In contrast, the Matlab shell model required 6 hours of run-time on the same computer system to calculate the eleven 2048×100 arrays (1Hz to 100Hz) of radial modal displacement, using a total of 35MB disk space. This run time could be considerably reduced by use of compiled program code instead of Matlab's interpreted-code environment. The shell theory therefore gives significant savings in computation time and storage requirements over FE methods.

4.3.4 Modelling a Tunnel in Soil

For the complete tunnel-in-soil system, the tunnel is modelled by a cylindrical shell and the soil by an elastic continuum of infinite extent surrounding the tunnel. Three sets of boundary conditions are needed to solve this system completely:

1. The stresses on the inside of the tunnel shell are equal to the applied loading;
2. The displacements must be compatible and the stresses in equilibrium at the interface of the tunnel shell and the soil continuum;
3. The displacements of the soil continuum must decay to zero as the radius from the centre of the tunnel increases towards infinity (the radiation condition).

This time the stresses on the outside of the shell are not zero, so that the first condition can be used with the shell results (4.6) to write

$$[\mathbf{A}_E]\cdot\tilde{\mathbf{U}}_n = \frac{-Eh}{a(1-\nu^2)}[\mathbf{A}]\begin{Bmatrix}\tilde{U}_n\\ \tilde{V}_n\\ \tilde{W}_n\end{Bmatrix} = \begin{Bmatrix}\tilde{Q}_{xn}\\ \tilde{Q}_{yn}\\ \tilde{Q}_{zn}\end{Bmatrix} = \begin{Bmatrix}\tilde{P}_{xn}\\ \tilde{P}_{yn}\\ \tilde{P}_{zn}\end{Bmatrix} - \begin{Bmatrix}\tilde{T}_{zxn}\\ \tilde{T}_{zyn}\\ \tilde{T}_{zzn}\end{Bmatrix}_{\text{outside}} \tag{4.38}$$

The third condition can be used to reduce the dimensions of the equations describing the response of the continuum. It will be recalled that the displacements **u** and stresses **τ** for the continuum are expressed in (4.20) as linear combinations of modified Bessel functions $I_n(\alpha r)$, $K_n(\alpha r)$, $I_n(\beta r)$, $K_n(\beta r)$, $I_{n+1}(\beta r)$ and $K_{n+1}(\beta r)$, originally found as solutions for the functions

f, g_r, g_z of (4.17) which specify the radial variation of the potentials describing the displacements. Only the modified Bessel functions of the second kind K decay for all arguments as r increases. Thus the coefficients of the modified Bessel functions of the first kind I in (4.20) must be set to zero for the radiation condition to be satisfied, so that

$$\begin{aligned} A = A_r = A_z = 0 \\ \Rightarrow \quad \mathbf{C} = \{0 \quad B \quad 0 \quad B_r \quad 0 \quad B_z\}^{\mathrm{T}} \end{aligned} \tag{4.39}$$

Correspondingly, this means that the terms containing Bessel functions I in the matrices [**U**] and [**T**] (that is, the first, third and fifth elements of each row) drop out of the equation. Hence the radiation condition reduces the size of the problem for the continuum by half.

The condition of compatibility can be used with the radiation condition expressed by (4.39), remembering the differences in the shell and continuum coordinate systems given by (4.29), to write the displacements at the tunnel-soil interface as

$$\begin{Bmatrix} \tilde{U}_n \\ \tilde{V}_n \\ \tilde{W}_n \end{Bmatrix} = \begin{Bmatrix} \tilde{U}_{zn} \\ \tilde{U}_{\theta n} \\ -\tilde{U}_{rn} \end{Bmatrix}_{r=a} = \begin{bmatrix} u_{32} & u_{34} & u_{36} \\ u_{22} & u_{24} & u_{26} \\ -u_{12} & -u_{14} & -u_{16} \end{bmatrix}_{r=a} \begin{Bmatrix} B \\ B_r \\ B_z \end{Bmatrix} = [\mathbf{U}_\infty]_{r=a} \cdot \mathbf{B} \tag{4.40}$$

while equilibrium means that the stresses at the interface are given by

$$\begin{Bmatrix} \tilde{T}_{zxn} \\ \tilde{T}_{zyn} \\ \tilde{T}_{zzn} \end{Bmatrix}_{\text{outside}} = \begin{Bmatrix} -\tilde{T}_{rzn} \\ -\tilde{T}_{r\theta n} \\ \tilde{T}_{rrn} \end{Bmatrix}_{r=a} = \begin{bmatrix} -t_{32} & -t_{34} & -t_{36} \\ -t_{22} & -t_{24} & -t_{26} \\ t_{12} & t_{14} & t_{16} \end{bmatrix}_{r=a} \begin{Bmatrix} B \\ B_r \\ B_z \end{Bmatrix} = [\mathbf{T}_\infty]_{r=a} \cdot \mathbf{B} \tag{4.41}$$

where the u_{jk} and t_{jk} are the remaining elements of [**U**] and [$\mathbf{T}_r$] of (4.21). By substituting (4.41) into (4.38) to eliminate the stresses acting on the outside of the shell tunnel and using (4.40), the unknown displacements and coefficients can be found, after some rearrangement, from

$$\begin{Bmatrix} \tilde{\mathbf{U}}_n \\ \mathbf{B} \end{Bmatrix} = \begin{bmatrix} [\mathbf{A}_E] & [\mathbf{T}_\infty]_{r=a} \\ [\mathbf{I}] & -[\mathbf{U}_\infty]_{r=a} \end{bmatrix}^{-1} \begin{Bmatrix} \tilde{\mathbf{P}} \\ \mathbf{0} \end{Bmatrix} \tag{4.42}$$

where [**I**] is a 3×3 identity matrix. The displacements $\tilde{\mathbf{U}}_n = \{\tilde{U}_n \quad \tilde{V}_n \quad \tilde{W}_n\}^{\mathrm{T}}$ at the interface result directly from (4.42), but the displacements at some radius R elsewhere in the soil have to be calculated using the coefficients **B** from

$$\tilde{\mathbf{U}}_n \Big|_{r=R} = [\mathbf{U}_\infty]_{r=R} \cdot \mathbf{B} \tag{4.43}$$

Of course, the foregoing argument determines the modal displacement components in the wavenumber domain. Once a sufficient number of these have been obtained, equation (4.27) can be used to obtain the total displacements in the space domain.

4.3.5 Results for the Tunnel in Soil

Table 4.3 gives the parameter values used to model the tunnel surrounded by soil. Parameters not used directly in each particular theory (shell or continuum) are nevertheless given to allow direct comparison between the properties of the tunnel and those of the soil. Frequencies up to 200Hz are of interest for ground-vibration propagation here.

Tunnel (Cylindrical Shell)	Soil (Elastic Continuum)
$E = 50 \times 10^9$ Pa	$E = 550 \times 10^6$ Pa
$\nu = 0.3$	$\nu = 0.44$
$\rho = 2500\,\mathrm{kg/m^3}$	$\rho = 2000\,\mathrm{kg/m^3}$
$c_1 = 5189\,\mathrm{m/s}$	$\lambda = 1.400 \times 10^9$ Pa
$c_2 = 2774\,\mathrm{m/s}$	$\mu = G = 191 \times 10^6$ Pa
$a = 3.0\,\mathrm{m}$	$K = 1.528 \times 10^9$ Pa
$h = 0.25\,\mathrm{m}$	$c_1 = 944\,\mathrm{m/s}$
zero damping	$c_2 = 309\,\mathrm{m/s}$
	$\eta_G = 0.06$
	$\eta_K = 0$

Table 4.3: Parameter values used to model a tunnel surrounded by soil.

The tunnel parameters are for concrete. The material damping of the concrete is assumed to be negligible compared to that of the soil, so is taken as zero. The tunnel is the same as the thin-walled cylinder described by Table 4.1, except for a slightly smaller radius and zero damping. The soil parameters are based on the averages of the values given by Hunt [89] for Oxford Clay and Middle Chalk. As in [89], all energy dissipation due to material damping in the soil is assumed to occur through shear motion, characterised by the shear modulus *G*, with no losses in volumetric expansion, characterised by the bulk modulus $K = E/3(1-2\nu)$. The constant hysteretic loss factor η_G is derived from the frequency-dependent viscous damping factor in [89] at 100Hz. The soil damping is included in the model by using the complex material parameters

$G^* = G(1+i\eta_G)$ and $K^* = K(1+i\eta_K) = K$ in the frequency domain. The other damped Lamé constant λ^* required can most simply be obtained via the elastic relations (which still hold due to the correspondence principle, see Bland [15]) and a complex Poisson's ratio ν^*. Although the normal practice is to take ν as the purely real parameter, there is no good reason why this has to be so. A complex Poisson's ratio merely implies a phase difference between the transverse and axial strains in a piece of the material subjected to uniaxial harmonic loading. Thus $\nu^* = \frac{1}{2}(3K^* - 2G^*)/(3K^* - G^*)$, $\mu^* = G^*$ and $\lambda^* = 2G^*\nu^*/(1-2\nu^*)$.

Calculation of the total tunnel and soil displacements was done with a sum of modal displacement components and an inverse DFT in the same way described in Section 4.3.3 for the thin-walled cylinder. However, the modal displacements now depend on (4.42), the tunnel ones directly and the soil ones via the coefficients **B** and (4.43). The inverse matrix in (4.42) comprises four submatrices of vastly different orders of magnitude: the elements of $[\mathbf{A}_{\mathrm{E}}]$ are typically of order 10^{11}, those of $[\mathbf{T}_\infty]_{r=a}$ 10^1, those of $[\mathbf{I}]$ 10^0 and those of $[\mathbf{U}_\infty]_{r=a}$ 10^{-7}, for the parameters of Table 4.3 and for frequencies of up to 200Hz. This span of 18 orders of magnitude means the assembled matrix is so badly scaled that a numerical solution to (4.42) is inaccurate or even impossible. Row and column normalisation was therefore used to reduce the elements of the assembled matrix to magnitudes between zero and unity, before numerical solution. This process is described in more detail in Appendix C.

As for the thin-walled cylinder, the inverse DFT was calculated by FFT, using $N = 2048$ and $\Delta x = 0.5\mathrm{m}$. The individual modal displacements can be examined as done before. Figure 4.8 shows the tunnel's $n = 3$ modal displacements in all three directions, at a frequency of 50Hz so that the radial displacement of the tunnel surrounded by soil, Figure 4.8(c), can be compared to the radial displacement of the free tunnel at the same frequency, Figure 4.5(b). The free tunnel, even with significant material damping, has relatively high radial displacement away from the load, due to the propagating waves above the ring-mode resonance; but the tunnel in soil has a rapidly decaying response, despite the tunnel's zero damping. The tunnel in soil is still exhibiting propagating waves at 50Hz, as can be seen by the peaks in the wavenumber domain at

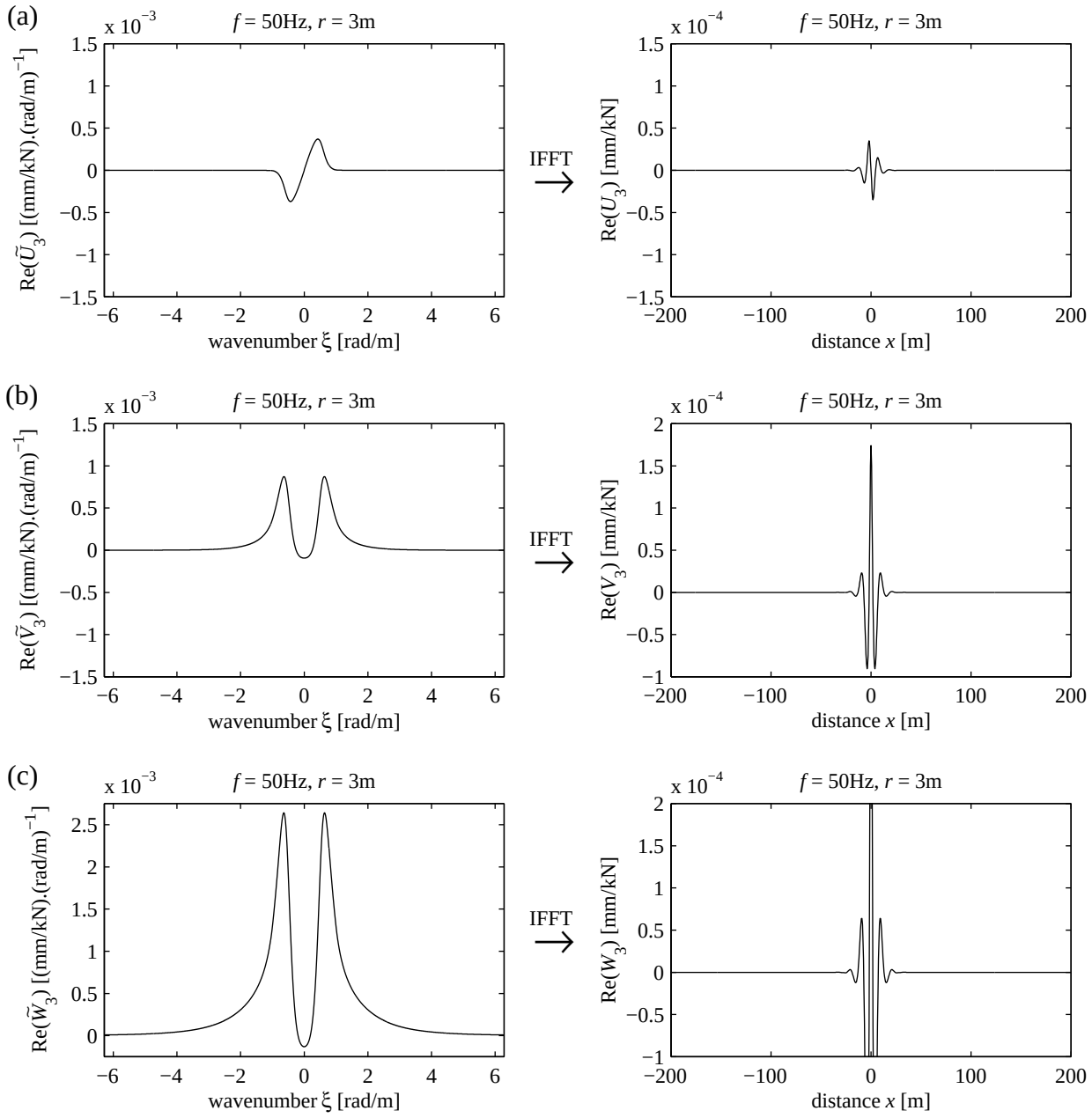

Figure 4.8: The real part of the tunnel's ($r = 3\text{m}$) modal displacement components, for $n = 3$, for a tunnel-in-soil model with properties as given in Table 4.3, showing (a) longitudinal, (b) tangential and (c) radial components in both ξ- and x-domains. Inverse FFT as for Figure 4.5, with $\Delta x = 0.5\text{m}$ and $N = 2048$. Loading of $\tilde{P}_{xn} = \tilde{P}_{yn} = 0$ and $\tilde{P}_{zn} = 1$. Note that the full range of x from –512m to 512m is not shown, and that the full vertical range of $W_n(x)$ in (c) is -2.5×10^{-4} to 7.0×10^{-4} kN/mm.

about $0.7\,\text{rad/m}$. Indeed, the net effect of adding soil of about the same density as the tunnel but about 100 times less stiff should be to lower the frequency at which longitudinal propagation begins for each circumferential mode. However, apart from a change in propagation frequencies, the soil greatly modifies the tunnel response by allowing energy to propagate away from the tunnel radially. Because the soil is infinite in extent, this energy cannot come back: the effect is

"radiation damping" and the much reduced responses of Figure 4.8. The radiation damping is much more important here than the relatively low material damping of the soil. All three modal displacement components for the tunnel show similar behaviour.

Figure 4.9 shows the three corresponding modal displacement components in the soil at a radius of 20m. The behaviour is somewhat different from that seen at the tunnel, but still shows maximum activity near $x = 0$ with rapidly decaying response on either side. Figures 4.8 and 4.9 both exhibit sufficient decay of the displacements at the extremes of the signals in both wavenumber and space domains, indicating that the requirements for using the DFT have been met. It could be argued that although the small Δx is near optimal to capture all the wavenumber (small-wavelength) information, the number of points N could be substantially reduced since the current resolution in the wavenumber domain is not required (or equivalently, the responses in the space domain decay to zero long before the limits of the x-range are reached). However, the addition of a track mounted on slab bearings (see Chapter 5) between the applied load and the tunnel invert gives rise to larger displacements away from $x = 0$ because energy can travel along the track before being transmitted to the tunnel and soil. For this $N = 2048$ is required.

Figures 4.8 and 4.9 also show the symmetry of the displacements. Because the two halves of the tunnel either side of $x = 0$ are identical, a radial load applied at $x = 0$ as here should produce displacements which are mirrored in the $x = 0$ plane, which is the case. Component U is parallel to the x-axis, so is an *odd* function of x, while V and W are orthogonal to the x-axis, so are *even* functions of x. The same is true of the displacement components in the wavenumber domain. This symmetry is useful in the computation of the individual modal displacements, since only values for positive ξ need to be calculated, as the values for negative ξ can be generated by the correct reflection when needed at the inverse DFT stage. Calculating only half the values halves the computation time and disk storage space required, and reduces the amount of memory needed to hold modal components during the summation stage to obtain total displacements.

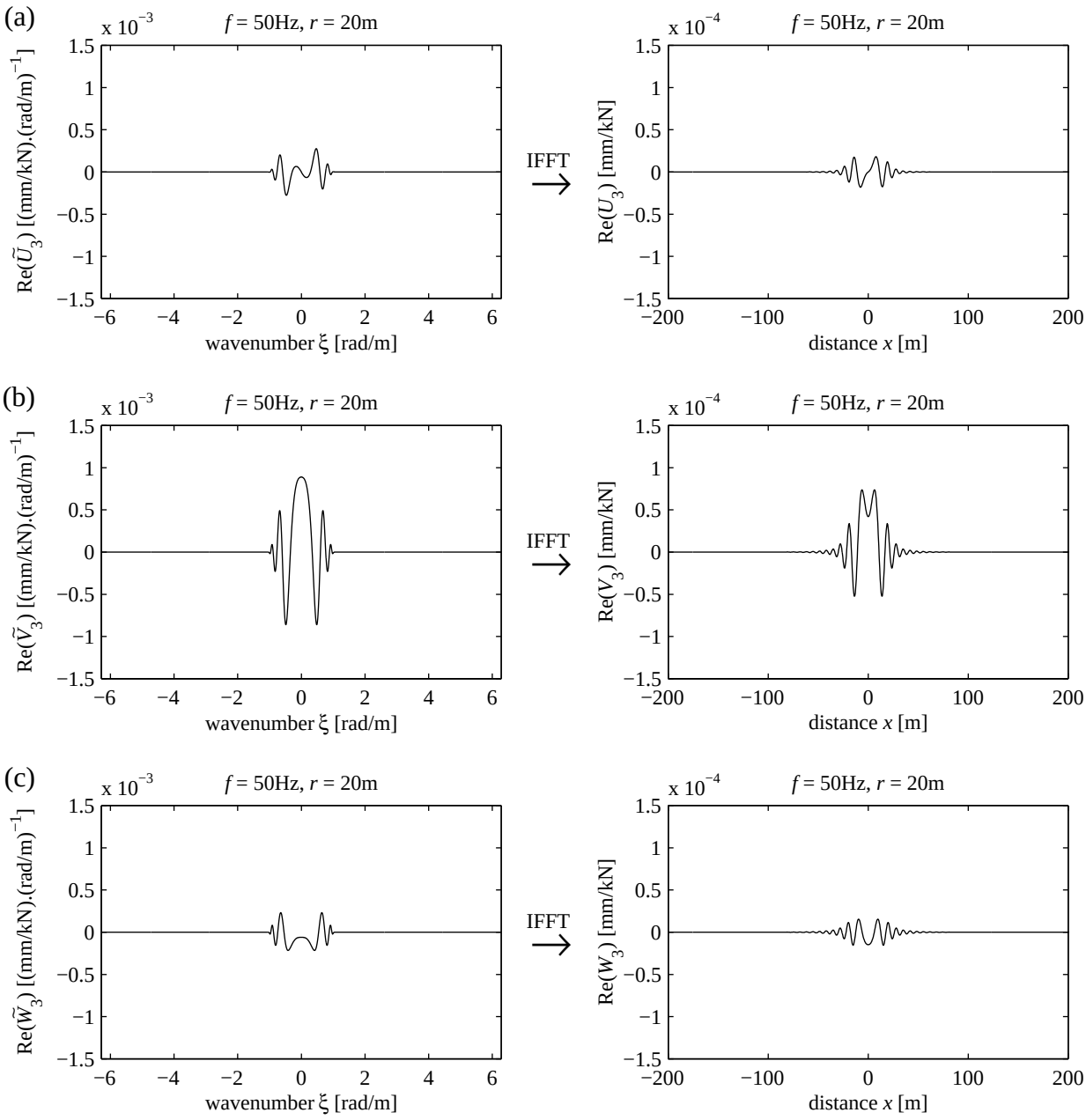

Figure 4.9: The real part of the soil's modal displacement components at $r = 20\text{m}$, for $n = 3$, for a tunnel-in-soil model with properties as given in Table 4.3, showing (a) longitudinal, (b) tangential and (c) radial components in both ξ- and x-domains. Inverse FFT as for Figure 4.5, with $\Delta x = 0.5\text{m}$ and $N = 2048$. Loading of $\tilde{P}_{xn} = \tilde{P}_{yn} = 0$ and $\tilde{P}_{zn} = 1$. Note that the full range of x from –512m to 512m is not shown.

The same procedure as before was used, summing the modal displacement components – this time calculated from (4.42) and (4.43) – then using the inverse DFT to give the total displacements of the tunnel or the soil by (4.27). As for the free tunnel, modal displacements from $n = 0$ to $n = 10$ were found to give sufficient convergence for frequencies from 1Hz to 200Hz with the model parameters of Table 4.3. Figure 4.10 illustrates the types of responses

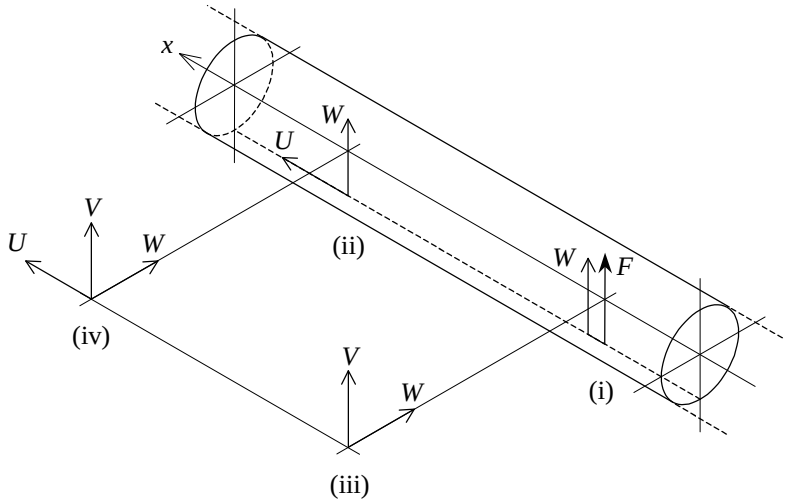

Figure 4.10: The non-zero displacement components of the tunnel-in-soil model (i) at the driving point ($x = 0$, $r = 3\text{m}$, $\theta = 0$) on the tunnel invert, (ii) at a point on the tunnel invert ($x = 20\text{m}$, $r = 3\text{m}$, $\theta = 0$) away from the load, (iii) at a point a distance horizontally ($x = 0$, $r = 20\text{m}$, $\theta = 90^\circ$) out into the soil, opposite the load, and (iv) at a distance horizontally out into the soil and a distance longitudinally parallel to the tunnel ($x = 20\text{m}$, $r = 20\text{m}$, $\theta = 90^\circ$).

which can be calculated. It is convenient to look at responses at $\theta = 0$ in the tunnel (corresponding to the tunnel invert upon which a track rests), and responses at $\theta = 90^\circ$ in the soil (corresponding to the horizontal plane likely to contain building foundations), as in both cases the cylindrical coordinate system then coincides with the absolute horizontal, vertical and longitudinal directions. Because of the symmetry about $x = 0$ and $\theta = 0$, some displacements are zero at some of the positions shown. However, all non-zero displacements include the effects of several modal contributions. The tunnel-invert displacements *U* and *W* at (ii) are simple sums of all their modal contributions, because $\cos n\theta = 1$ for all n when $\theta = 0$; while at (iv) with $\theta = 90^\circ$, the soil displacements *U* and *W* include only the even-numbered modal contributions as $\cos(2k+1)\theta = 0$ for odd $n = 2k+1$, and *V* includes only the odd-numbered modal contributions as $\sin 2k\theta = 0$ for even $n = 2k$.

Figure 4.11 shows the driving-point response of the tunnel invert. Only the vertical displacement *W* is non-zero. This does not show any ring-mode resonances like the free thin-walled cylinder's driving-point response in Figure 4.6, but is instead smooth and decreases slightly in magnitude as frequency increases. The loss of noticeable resonances is due to the radiation damping of the infinite soil now surrounding the tunnel.

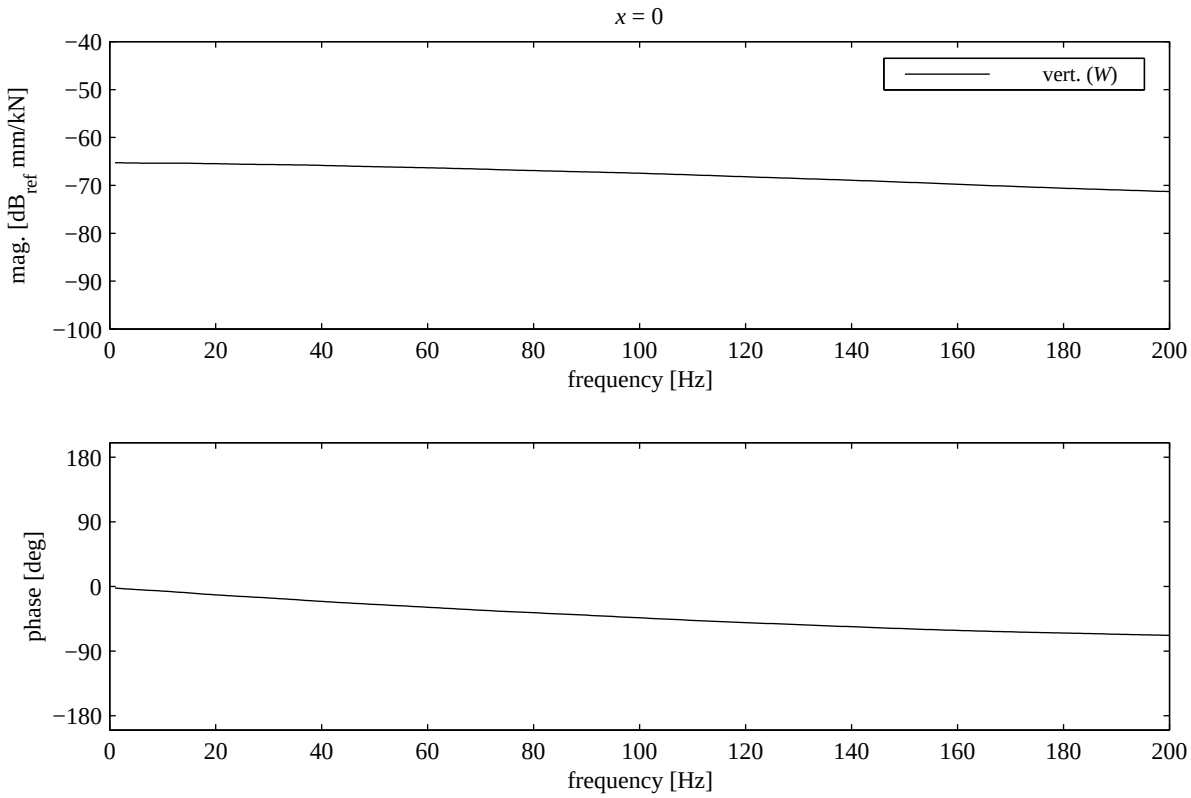

Figure 4.11: The driving point response of the tunnel in the tunnel-in-soil model with parameters given in Table 4.3, under a normal unit point force, corresponding to position (i) in Figure 4.10. The longitudinal component U is zero because $x = 0$, while the horizontal (tangential) component V is zero because $\theta = 0$.

Figure 4.12 shows the response of the tunnel invert at a distance of 20m from the load. The vertical response W has troughs at about 51Hz, 119Hz and 184Hz. The spacing between these is 68Hz and 65Hz respectively. If a standing wave is set up between a source at one point and a node at a second, then their separation L must correspond to an odd multiple of quarter wavelength. Thus the possible wavelengths are $4L/(2k-1)$ with $k = 1, 2, 3, \ldots$ and with a wavespeed c, the corresponding frequencies are $c(2k-1)/4L$. In other words, each successive standing wave represents an increase in frequency of $c/2L$. Standing waves with an antinode at each end have frequencies that fall between these but which are characterised by the same frequency step. Although the infinitely long tunnel has no suitable boundaries to set up standing waves longitudinally, the shape of W in Figure 4.12 suggests some kind of correspondence of wavelength with the distance from the load to observation point. For a distance of 20m, the speed of shear (transverse) waves in the tunnel concrete of $c_2 = 2774\,\text{m/s}$ gives a standing-wave frequency step of 69Hz, which matches the observed spacing between the troughs in the vertical

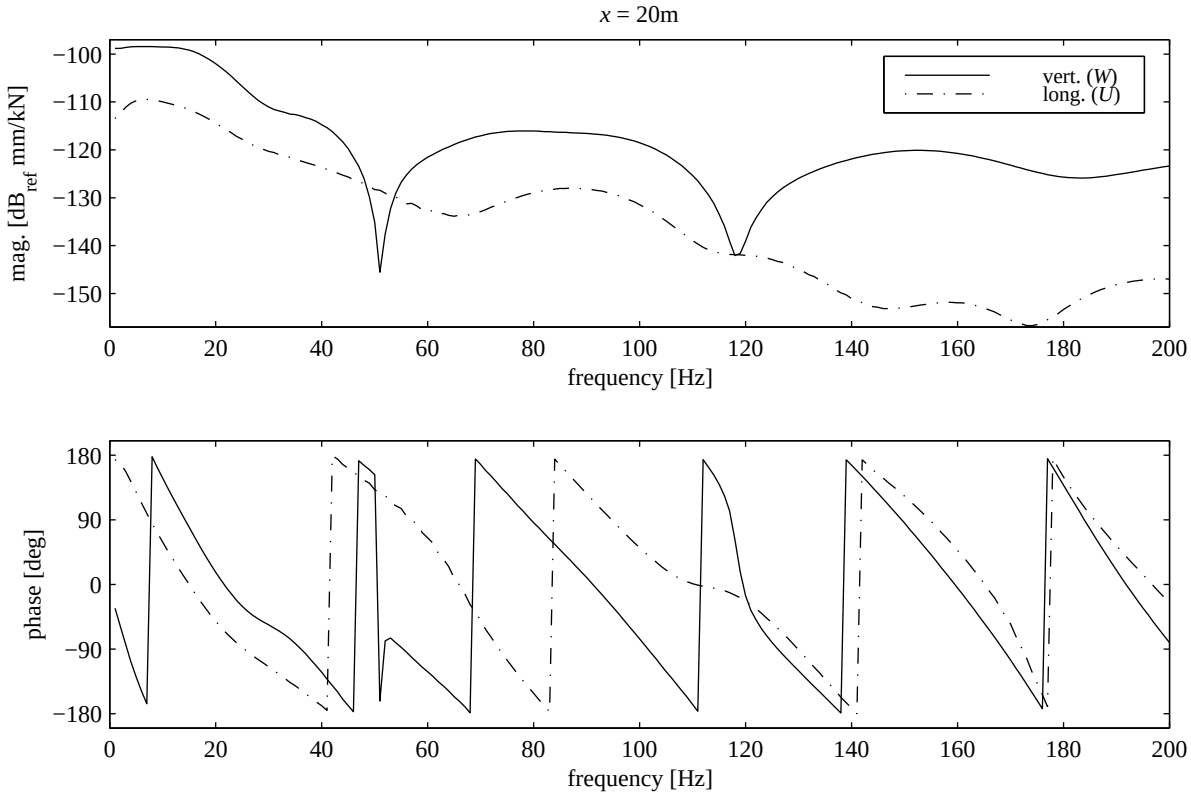

Figure 4.12: The response of the tunnel invert at a distance $x = 20\text{m}$ from the load, corresponding to position (ii) in Figure 4.10, for tunnel-in-soil parameters given in Table 4.3. The horizontal (tangential) component *V* is zero because $\theta = 0$.

(transverse) displacement *W*. The longitudinal displacement *U* exhibits less pronounced variation, with changing frequency intervals between troughs, none of which seem to correspond to the shear- or pressure-wave speeds in either the tunnel concrete or the soil. The variation is probably due to the behaviour of the interface between the tunnel and the soil.

Figure 4.13 shows the soil response 20m horizontally opposite the position of the load applied to the tunnel. The horizontal displacement *W* shows clear undulations with a step of about 20Hz between troughs (or peaks), while the vertical displacement *V* shows similar, but very slight, undulation. This is probably due to interference effects, with points along the tunnel acting as sources transmitting energy propagated from the load. At each "source", some energy radiates into the soil and the remainder continues along the tunnel. The exact distribution of "sources" will depend on which parts of the tunnel show maximum activity at a given frequency. However, the load at $x = 0$ will always act as one of the sources. The distance between any source and an observation point has to be a multiple of half the wavelength (to give antinodes at each end) for an interference node or antinode to be observed. Thus the distance between the

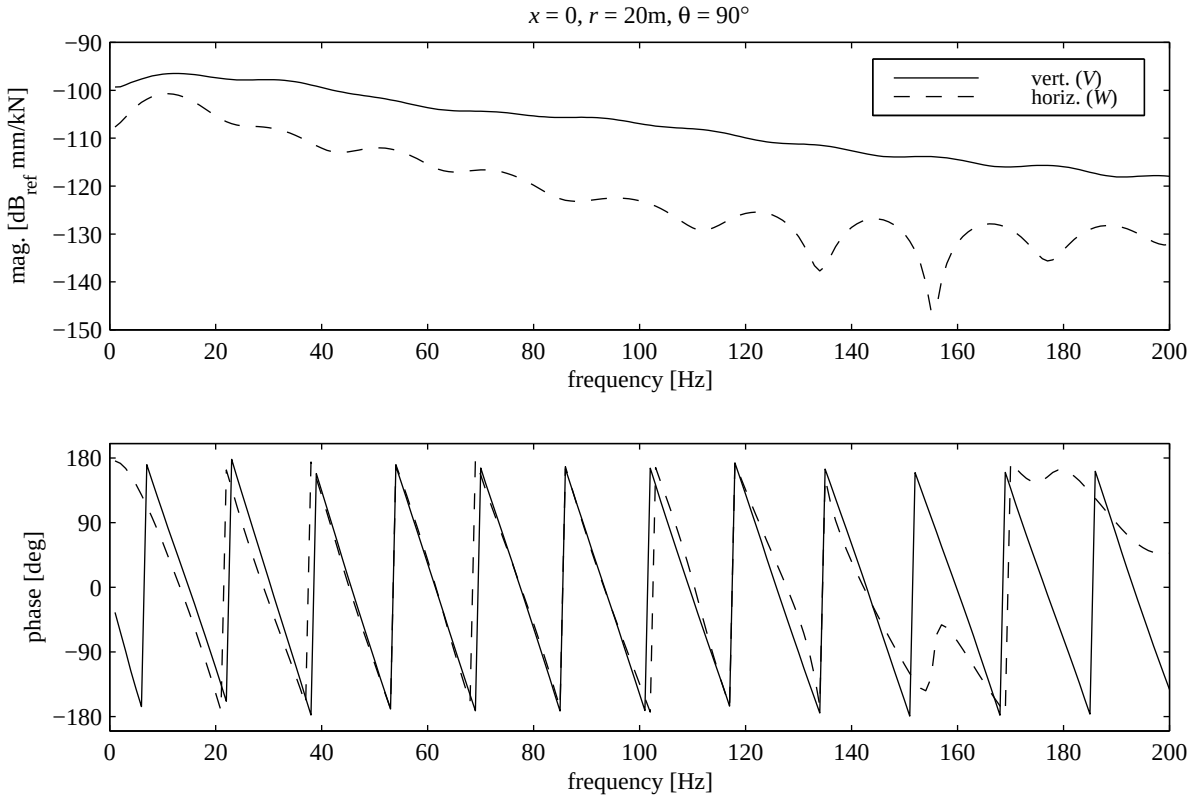

Figure 4.13: The response in the soil at $x = 0$, $r = 20\text{m}$, $\theta = 90^\circ$, horizontally opposite the point load acting on the tunnel invert, corresponding to position (iii) in Figure 4.10, for tunnel-in-soil parameters given in Table 4.3. The longitudinal component U is zero because $x = 0$.

load and the observation point can be used to estimate the frequency step between the peaks or the troughs in Figure 4.13. As for standing waves, the frequency step between successive interference patterns is $c/2L$. The direct distance from the bottom of the tunnel (of radius 3m), where the load is applied, to the point 20m horizontally out into the soil, is 20.2m, although this line cuts through the tunnel cross-section. For a distance L of 20.2m, soil pressure waves of speed $c_1 = 944\,\text{m/s}$ give a frequency step of 23.3Hz, while shear waves of speed $c_2 = 309\,\text{m/s}$ give a step of 7.6Hz. Thus the undulating response of Figure 4.13 appears to be due to the interference of pressure waves propagating through the soil from different points along the tunnel. Hence the greatest influence is on W, which lies nearly along the line of propagation which is also the direction of oscillation of the pressure (longitudinal) waves; there is little influence on V, which lies nearly perpendicular to the line of propagation.

The dominance of pressure-wave effects in the soil raises the question of the influence of shear waves. The answer lies in the material damping. Reduction in magnitude due to material damping depends on the number of cycles of vibration the material has gone through, the more

cycles, the more reduction. Since the speed of pressure waves in the soil is about three times the speed of shear waves, a propagating shear wave will go through three times as many cycles as a propagating pressure wave over the same distance, for any given frequency. If the reduction per cycle due to material damping were the same for all types of motion, then it would be expected that shear-wave magnitudes would be reduced by the cube of the factor that pressure-wave magnitudes are. However, the original assumption was that all material damping losses in the soil are due to shear motion. Therefore material damping has a much bigger effect on the decay of shear waves than of pressure waves, even without considering number of cycles, and after some distance of propagation, pressure waves are predominant.

Figure 4.14 shows the response of the soil at a radius of 20m horizontally from the centre of the tunnel and 20m longitudinally from the load on the invert. This means the observation point is a direct distance of 28.4m from the load. This distance gives a frequency step of 16.6Hz for pressure waves involved in interference. Undulations of about this spacing can be clearly seen in the horizontal and longitudinal displacements *W* and *U* (each with a significant component in the direction of the line of propagation) above 60Hz, and in the vertical displacement *V* (which is nearer orthogonal to the line of propagation) above 120Hz. On a larger scale, dips in *V* can be observed at 43Hz and 123Hz. These correspond quite closely to the vertical displacement of the tunnel invert at 20m from the load (Figure 4.12), the part of the tunnel closest to the soil observation point here. In the case of *V*, the adjacent vertical tunnel displacement is transmitted by shear waves. Above 120Hz, the shear waves complete eight or more cycles over 20m, so have decayed sufficiently that the pressure-wave effects appear clearly in *V*. Thus it appears that at lower frequencies the local displacement of the tunnel has the biggest effect on the soil displacement, while at higher frequencies interference effects dominate.

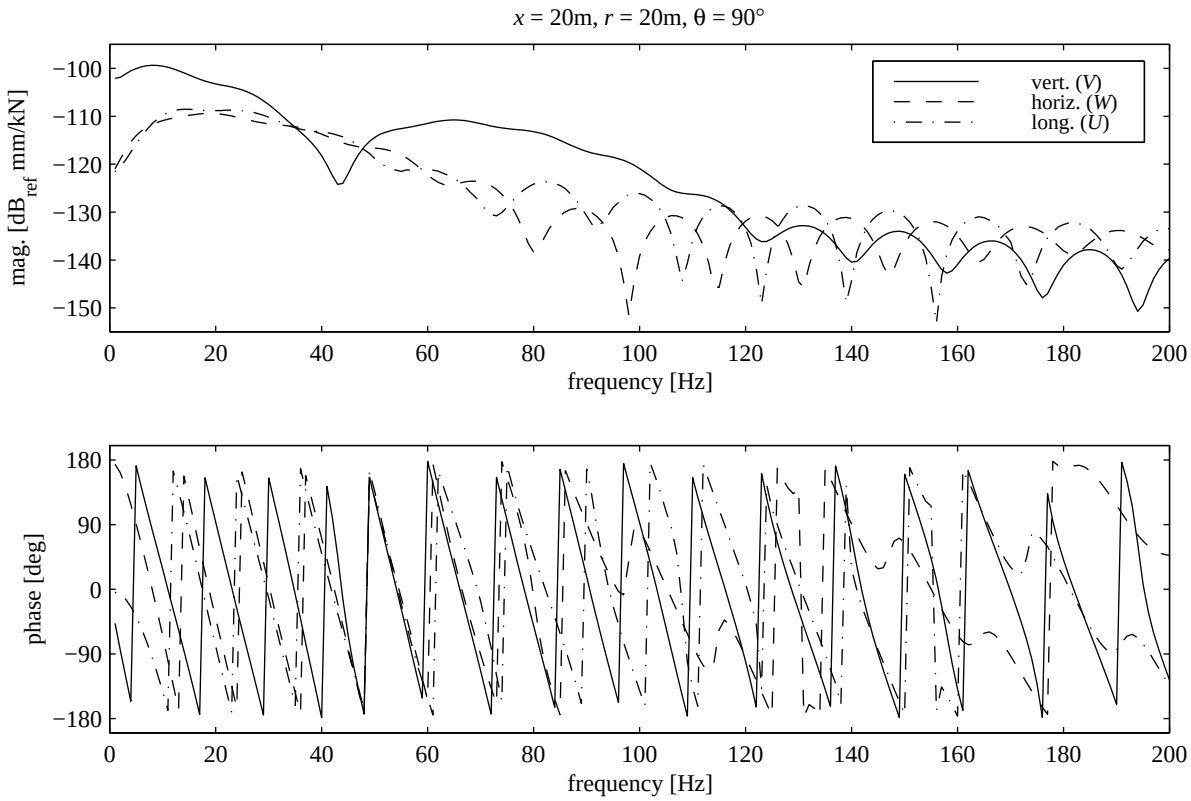

Figure 4.14: The response in the soil at $x = 20\text{m}$, $r = 20\text{m}$, $\theta = 90^\circ$, horizontally out from the load then parallel to the tunnel, corresponding to position (iv) in Figure 4.10, for tunnel-in-soil parameters given in Table 4.3.

4.4 Conclusions

A tunnel surrounded by soil can be modelled by considering the tunnel as an infinitely long, thin cylindrical shell and the soil as an infinite homogeneous isotropic continuum. An analytical solution for the time-harmonic displacements of the tunnel and soil can be found in the form of the spatial inverse Fourier transform of an infinite sum of components, representing ring modes of the tunnel cross-section, which are harmonic in both space and time. The modal harmonic displacement components are calculated from the modal harmonic components of the total load applied to the tunnel. Numerical computation of results from this analytical solution is straightforward for typical values of tunnel and soil parameters. The infinite sum converges with the first eleven terms, and the inverse Fourier transform is satisfactorily represented by an inverse DFT of 2048 sample points, of which symmetry requires only 1025 to be calculated. The

computation time and disk storage space required for the analytical solution are much more modest than those for an FE model of the same system.

Numerical results for the case of a normal unit point load applied to the tunnel invert reveal several aspects of the system's behaviour. A tunnel surrounded by soil does not show the ring-mode resonances apparent in the driving-point response of a free tunnel, due to the radiation-damping effect of the infinite soil. The response of the tunnel away from the load is influenced by the propagation of shear waves in the tunnel material and interaction with the soil interface. The soil response seems to be influenced in large measure by the response of the closest part of the tunnel, with strong interference patterns based on soil pressure waves propagating from different parts of the tunnel appearing particularly in the higher part of the frequency range, where shear-wave effects are reduced by soil damping. The tunnel-in-soil model can be used as a realistic track foundation so that the true effectiveness of floating-slab track can be evaluated by looking at soil responses directly.

Chapter 5

MODELLING TRACKS IN TUNNELS

The results obtained for the tunnel-in-soil model of Chapter 4 and the general ideas from Chapter 3 regarding the modelling of floating-slab track with infinite beams on elastic foundations can be combined to produce a complete model of an underground railway. Much better assessments of the vibration-isolation effectiveness of a given track structure can be obtained from this combined model than if a rigid foundation is used for the track as was done in Chapter 3. In particular, vibration levels in the surrounding soil due to a train running on the track can be calculated, providing a direct measure of the track's effectiveness.

5.1 A Simple Track Slab

The simplest track model that can be combined with the tunnel is an infinitely long, continuous slab beam, as shown in Figure 5.1. The approach used is similar to that employed by Ng [146] to join an infinite beam directly to an elastic halfspace to model a surface railway. The slab beam and tunnel are joined along a single continuous line running longitudinally along the bottom of the tunnel invert. The coupling is achieved through the interaction force $G(x)$ which acts on the tunnel and its equal and opposite counterpart $-G(x)$ which acts on the beam.

5.1.1 Coupling Equations for the Simple Slab Beam and Tunnel

Figure 5.2 shows a general continuous distribution of time-harmonic force per unit length $Q(x)$ acting along a line such as the joining line on the slab beam or tunnel invert. The distributed

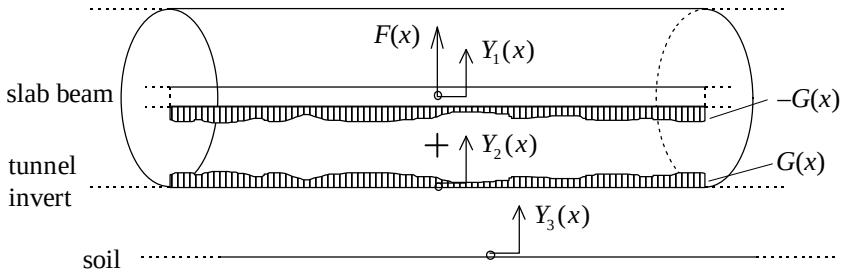

Figure 5.1: Joining a simple slab beam of infinite length to the tunnel, showing the equal and opposite interaction forces acting on the beam and the tunnel.

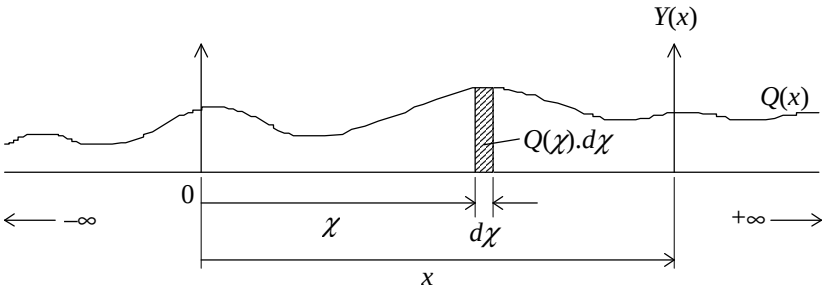

Figure 5.2: General force distribution per unit length $Q(x)$ acting along a single line of joining. The displacement response $Y(x)$ is obtained by the convolution in space of the force increments $Q(\chi).d\chi$ with the frequency-response function to a point load.

force can be considered as a train of point loads represented by pulses of infinitesimal width $d\chi$ and magnitude $Q(\chi)$, so that the increment of the time-harmonic displacement response $Y(x)$ to one of these point loads is $dY(x) = H(x-\chi)Q(\chi)d\chi$, where $H(x)$ is the frequency-response function (FRF) for $Y(x)$ to a point load acting at $x = 0$. Thus the total displacement response is the sum of these increments over the whole length of the infinite joining line, giving the integral

$$Y(x) = \int_{-\infty}^{\infty} H(x-\chi)Q(\chi)d\chi \tag{5.1}$$

which is a convolution (or Duhamel) integral (see Newland [144]) in space, rather than in time as familiar from signal-processing applications. This is equivalent to a Green's function formulation for the response, where $H(x-\chi)$ is the Green's function. If the Fourier transform of both sides of (5.1) is taken using the first integral of the transform pair

$$\begin{aligned} \tilde{Y}(\xi) &= \int_{-\infty}^{\infty} Y(x)e^{-i\xi x}dx \\ Y(x) &= \frac{1}{2\pi}\int_{-\infty}^{\infty} \tilde{Y}(\xi)e^{i\xi x}d\xi \end{aligned} \tag{5.2}$$

where ξ is angular wavenumber, then (5.1) becomes

$$\tilde{Y}(\xi) = \tilde{H}(\xi)\tilde{Q}(\xi) \tag{5.3}$$

so that the convolution in space has been reduced to a simple multiplication in the wavenumber domain. Applying (5.3) to the coupled slab beam and tunnel invert in turn yields

$$\begin{aligned} \tilde{\tilde{Y}}_1 &= \tilde{\tilde{H}}_{11}(-\tilde{\tilde{G}}+1) \\ \tilde{\tilde{Y}}_2 &= \tilde{\tilde{H}}_{22}\tilde{\tilde{G}} \end{aligned} \tag{5.4}$$

for the displacements $\tilde{\tilde{Y}}_1$ along the beam and $\tilde{\tilde{Y}}_2$ along the invert, when a unit point load acts on the slab at $x = 0$. The applied point load, additional to the interaction force, is equivalent to a force per unit length of $F = \delta(x)$, which gives $\tilde{\tilde{F}} = 1$ when transformed; hence the total ξ-domain force $(-\tilde{\tilde{G}} + 1)$ acting on the slab beam. The functions $\tilde{\tilde{H}}_{11}$ and $\tilde{\tilde{H}}_{22}$ are the FRFs H_{11} (for the response of the free beam to a point load at $x = 0$) and H_{22} (for the response of the uncoupled tunnel invert to a point load at $x = 0$) in the wavenumber domain.

The slab beam can either be joined directly to the tunnel invert, or be supported on the invert via resilient slab bearings. For direct joining, the displacements of the slab and invert must be equal, so that in the wavenumber domain

$$\tilde{\tilde{Y}}_1 = \tilde{\tilde{Y}}_2 \tag{5.5}$$

Using (5.5) with equations (5.4) to eliminate $\tilde{\tilde{G}}$ gives

$$\tilde{\tilde{Y}}_1 = \tilde{\tilde{Y}}_2 = \frac{\tilde{\tilde{H}}_{11}\tilde{\tilde{H}}_{22}}{\tilde{\tilde{H}}_{11} + \tilde{\tilde{H}}_{22}} \tag{5.6}$$

for the displacements in the direct-joining case.

When the slab is joined to the invert via resilient slab bearings, the interaction force is determined by the extension of the bearings and their stiffness. If the bearings are modelled as a continuous resilient layer of stiffness *k* per unit length (like a Winkler foundation but without the rigid base), then the joining condition becomes

$$\tilde{\tilde{G}} = k(\tilde{\tilde{Y}}_1 - \tilde{\tilde{Y}}_2) \tag{5.7}$$

Using this new condition (5.7) with (5.4) yields

$$\begin{aligned} \tilde{\tilde{Y}}_1 &= \frac{\tilde{\tilde{H}}_{11}(1 + k\tilde{\tilde{H}}_{22})}{1 + k\tilde{\tilde{H}}_{11} + k\tilde{\tilde{H}}_{22}} \\ \tilde{\tilde{Y}}_2 &= \frac{k\tilde{\tilde{H}}_{11}\tilde{\tilde{H}}_{22}}{1 + k\tilde{\tilde{H}}_{11} + k\tilde{\tilde{H}}_{22}} \end{aligned} \tag{5.8}$$

for the displacements when the slab is joined to the tunnel via an elastic layer. Damping can be included by using a complex stiffness *k* to model a visco-elastic layer.

The response along a line in the soil parallel to the joining line (see Figure 5.1) can be determined, once the displacement $\tilde{Y}_2$ is known, by using the second of equations (5.4) to find the interaction force $\tilde{G}$ which acts on the tunnel invert. The soil displacement is then

$$\tilde{Y}_3 = \tilde{H}_{32}\tilde{G} = \tilde{H}_{32}\frac{\tilde{Y}_2}{\tilde{H}_{22}} \tag{5.9}$$

for either joining method, where H_{32} is the FRF of a particular soil-displacement component Y_3 to a point force acting on the uncoupled tunnel invert at $x = 0$.

Any of the displacements found from (5.6), (5.8) or (5.9) can be inverse Fourier-transformed from the wavenumber to the space domain by means of the second transform of the pair (5.2). With the unit point-load condition assumed, the physical displacements in the space domain represent the FRFs of the combined system for a point load acting at $x = 0$ on the slab beam.

It is worth noting that if the alternative definition of the Fourier transform pair is adopted, with the factor of $1/2\pi$ in the forward transform rather than the inverse one as in (5.2), then a factor of 2π appears on the right-hand side of the ξ-domain multiplication (5.3). This is then also true for equations (5.4), with the end result that every term containing a *k* in equations (5.8) is also multiplied by 2π. This extra complication is avoided by using the definition (5.2).

5.1.2 Calculation of FRFs for Simple Coupling

The only quantities left to determine are the FRFs in the wavenumber domain for the tunnel-in-soil model and the slab beam before joining. The soil displacements $\tilde{\mathbf{U}} = \{\tilde{U} \quad \tilde{V} \quad \tilde{W}\}^{\mathrm{T}}$ at a particular radius *r* and angular position θ which result from a spatial unit point load acting on the invert are the sum

$$\begin{Bmatrix} \tilde{U} \\ \tilde{V} \\ \tilde{W} \end{Bmatrix}_r = \begin{Bmatrix} \tilde{U}_0 \\ 0 \\ \tilde{W}_0 \end{Bmatrix}_r + \sum_{n=1}^{\infty} \begin{Bmatrix} \tilde{U}_n \cos n\theta \\ \tilde{V}_n \sin n\theta \\ \tilde{W}_n \cos n\theta \end{Bmatrix}_r \tag{5.10}$$

of the modal displacement components calculated from (4.42) and (4.43) using the modal stress components for a unit load given by (4.26) . The sum is of the same form as (4.27) but without

the integral for the inverse Fourier transform from wavenumber to space domain. The tunnel invert FRF $\tilde{H}_{22}$ is thus $\tilde{W}$ for $r = a$ and $\theta = 0$, while the soil FRF $\tilde{H}_{32}$ can be whichever displacement component is of interest for any line in the soil defined by constant $r = R$ and $\theta = \beta$. These can be expressed as

$$\begin{aligned} \tilde{H}_{22} &= \tilde{W}\big|_{\substack{r=a \\ \theta=0}} \\ \tilde{H}_{32} &= \tilde{U},\ \tilde{V} \text{ or } \tilde{W}\big|_{\substack{r=R \\ \theta=\beta}} \end{aligned} \tag{5.11}$$

Note that the Fourier transform used in (4.24) to transform the unit point load acting on the tunnel into the ξ-domain must be the same as the Fourier transform defined by (5.2) if the ξ-domain FRFs of (5.11) are to be compatible with the coupling equations (5.3) to (5.9). This is because the transformation used for the input force also determines the transformation for the FRFs, since the input force is the only quantity affected by the Fourier-transform definition during the solution for tunnel and soil displacements. Thus the Fourier transforms in (4.24) were chosen to match those defined by (5.2), which give the simplest coupling equations.

The FRF for the free beam can be determined from the equation of motion for its vertical displacement $y(x,t)$. This is (see Meirovitch [136])

$$m\frac{\partial^2 y}{\partial t^2} + EI\frac{\partial^4 y}{\partial x^4} = f(x,t) \tag{5.12}$$

where m is mass per unit length, EI is bending stiffness (E Young's modulus and I the second moment of area), and $f(x,t)$ is applied force per unit length. Substituting a harmonic solution $y = \tilde{Y}e^{i(\omega t+\xi x)}$ with a force $f = \tilde{F}e^{i(\omega t+\xi x)}$ of the same form yields

$$\tilde{H}_{YF} = \tilde{Y}\big|_{\tilde{F}=1} = \frac{1}{EI\xi^4 - m\omega^2} \tag{5.13}$$

Using harmonic solutions in this way is equivalent to taking the Fourier transform of (5.12) twice, once for time to frequency domain, and once for space to wavenumber domain. The force $\tilde{F} = 1$ represents a unit spatial point load acting at $x = 0$ as discussed above. Thus the free-beam FRF $\tilde{H}_{11}$ is simply

$$\tilde{H}_{11} = \tilde{H}_{YF} \tag{5.14}$$

5.1.3 Results for the Tunnel with a Simple Slab Beam

As mentioned earlier, the slab beam can be joined either directly to the tunnel invert or via slab bearings, represented by springs. Either case can be compared to the Winkler beam model often used for track design, as shown in Figure 5.3. To allow comparison of results, the Winkler frequency response $Y(x,\omega)$ must be determined. This is easily obtained by applying (5.12) to a beam on an elastic foundation, giving

$$Y(x,\omega) = \frac{1}{4\alpha^3 EI}\left(e^{\alpha|x|} + ie^{i\alpha|x|}\right), \quad \text{with } \alpha^4 = \frac{m\omega^2 - k_W}{EI} \tag{5.15}$$

where k_W is the stiffness per unit length of the elastic foundation. The root α used is the second-quadrant one, so that both α and $i\alpha$ have negative real parts and the two exponentials in (5.15) decay as $|x| \to \infty$. To make the Winkler beam "equivalent" to the slab beam on the tunnel, its static displacement at $x = 0$ is equated to the numerical value for the static displacement of the directly joined slab beam, resulting in k_W being the effective Winkler stiffness k_{eff} of the tunnel invert, as depicted in Figures 5.3(a) and (b). If the slab is then supported on bearings of stiffness *k* per unit length, Figure 5.3(c), the equivalent Winkler beam has the additional stiffness added in series, Figure 5.3(d), giving $k_W = 1/(1/k_{eff} + 1/k)$. The Winkler beam has a resonance at $\omega_n = \sqrt{k_W/m}$ as can be seen from (5.15), so *k* can be selected to give specific Winkler "natural frequencies". Classic vibration-isolation theory using a mass on a spring predicts that isolation should be achieved at frequencies greater than $\sqrt{2}\omega_n$; this assumption can now be tested.

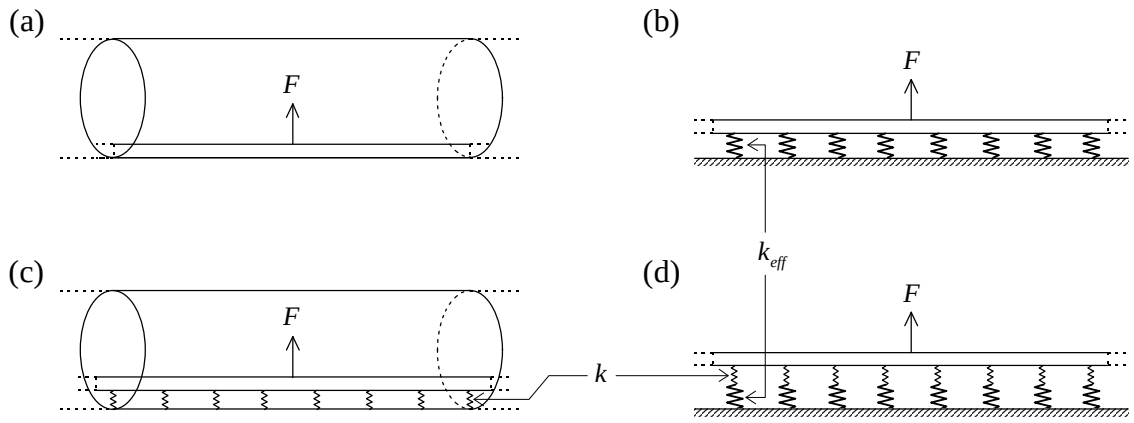

Figure 5.3: A simple slab beam joined (a) directly to the tunnel invert and compared to (b) an "equivalent" Winkler beam on the effective stiffness of the tunnel invert. The slab beam (c) with resilient bearings between it and the tunnel can then be compared to (d) the "equivalent" Winkler beam with the extra foundation stiffness of the bearings added in series.

The displacements (5.6), (5.8) or (5.9) of the tunnel-plus-slab model were calculated using Matlab. The inverse Fourier transforms were carried out with Matlab's inverse FFT function. The values of the parameters for the slab beam and its support stiffness are given in Table 5.1, the slab beam having the same properties as that used in the track models of Chapter 3 (see Table 3.1). The tunnel FRFs were calculated as described in Chapter 4, using the parameters in Table 4.3. In conjunction with the slab properties, these determine the effective stiffness k_{eff} of the tunnel invert for use with the equivalent Winkler beam. Once the effective stiffness is calculated, the slab-support stiffnesses can be determined for various Winkler natural frequencies. Three stiffnesses are given in Table 5.1 for increasingly softer support, with the 30Hz frequency representative of actual floating-slab tracks.

Damping in the springs is hysteretic, described by a constant loss factor such that complex stiffnesses $k(1+i\eta)$ are substituted for real stiffnesses *k*. The calculated loss factor η_{eff} is very close to the shear loss factor given in Table 4.3 for the soil. The loss factor of $\eta_k = 0.5$ for the slab-support stiffness is relatively high but not unreasonable for rubber with high damping (see data in Nashif et al [142] for instance). Its value is also influenced by the numerical considerations arising from the Nyquist criterion for the inverse FFT, which are discussed in Section 4.3.3. For frequencies up to 200Hz, a spacing of $\Delta x = 0.5\text{m}$, as used for the tunnel model, was found sufficient to capture all the wavenumber information of the slab-plus-tunnel model, and with $N = 2048$ points and the given loss factor, the response of the slab beam decayed sufficiently at the sample ends in both ξ- and *x*-domains for the FFT to be considered an accurate representation of the Fourier transform. The symmetry of the responses in both domains means that all ξ-domain calculations could be done for the 1025 points of the sample with $\xi \geq 0$, and the portion for $\xi < 0$ created by a suitable reflection just prior to the inverse FFT.

Simple Slab Beam
$EI = 1430 \times 10^6$ Pa.m^4
$m = 3500$ kg/m
$k_{eff} = 821.2 \times 10^6$ N/m^2
$\eta_{eff} = 0.0643$
$k = 1262 \times 10^6$ N/m^2 when $f_n = 60$ Hz
$k = 424.4 \times 10^6$ N/m^2 when $f_n = 45$ Hz
$k = 146.6 \times 10^6$ N/m^2 when $f_n = 30$ Hz
$\eta_k = 0.5$

Table 5.1: The simple slab beam's properties, the effective stiffness of the tunnel invert described by the parameters of Table 4.3, and three resulting slab-support stiffnesses.

Figure 5.4 shows the driving-point response of the slab beam for the various slab-support stiffnesses, compared to that of an "equivalent" Winkler beam in each case. The directly joined slab shows a flat response very like the uncoupled tunnel's driving-point response shown in Figure 4.11, while the corresponding Winkler response shows a clear resonance just below 80Hz. The energy of the slab beam is radiated into the soil quite effectively when the slab is closely coupled to the tunnel, whereas this radiation damping effect is not accounted for in the loss factors of the elastic foundation of the Winkler beam. As the slab-support stiffness is reduced, the slab response gets closer to the Winkler response, until the two almost coincide for $f_n = 30$Hz. With lower values of *k*, the slab beam is less strongly coupled to the tunnel, or in other words, the tunnel becomes more like a rigid foundation (compare the values of *k* with the value of k_{eff} in Table 5.1). At this point it might be assumed that for realistic, soft bearings, the Winkler theory adequately describes the behaviour of a floating slab. However, a glance at Figure 5.5, which gives responses at 20m from the load, shows that this is not the case. The slab beam supported by the tunnel has significant response (about –100dB) at low frequencies no matter what value *k* has, while the equivalent Winkler beams do not show much response below the Winkler natural frequencies, at which travelling waves occur and propagate energy along the beam. This illustrates how the tunnel can transmit energy to the coupled slab beam even when there are no travelling waves in the slab itself.

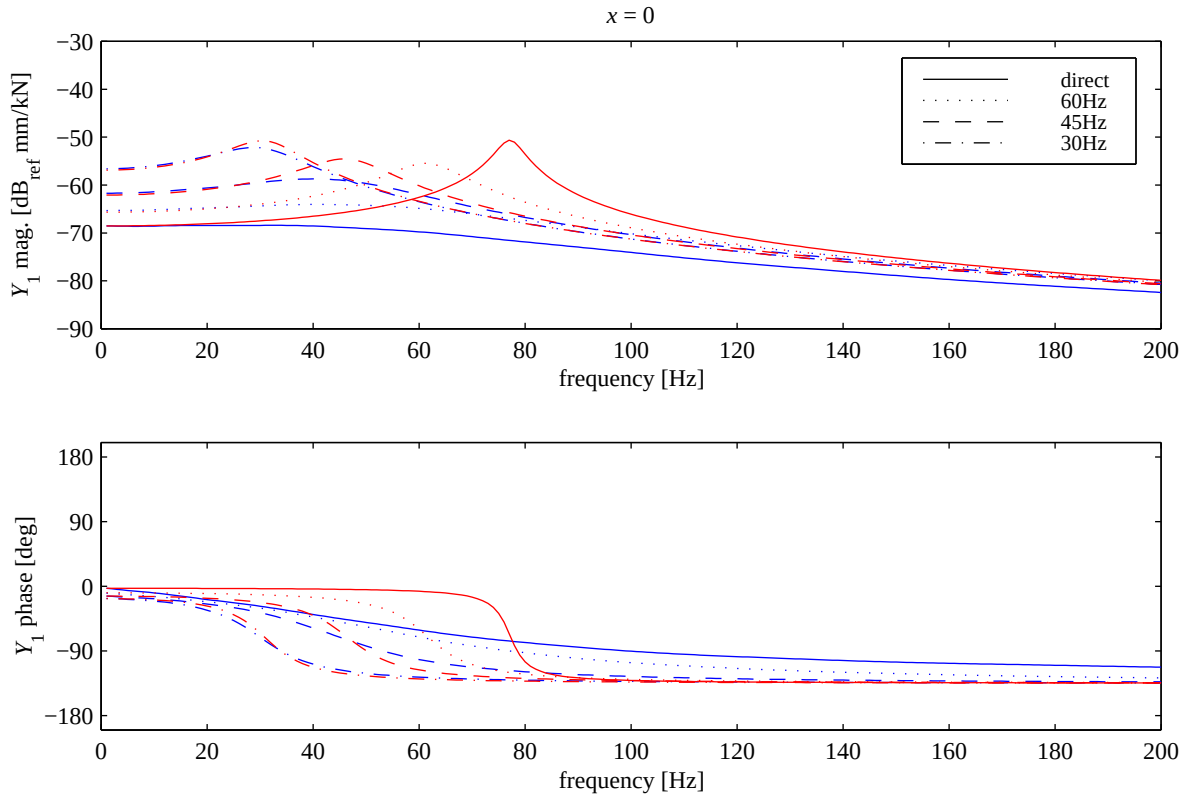

Figure 5.4: Vertical driving-point displacement response of a simple slab beam on the tunnel (blue) compared to the "equivalent" Winkler beam (red) for direct joining and various support stiffnesses for different Winkler "natural frequencies".

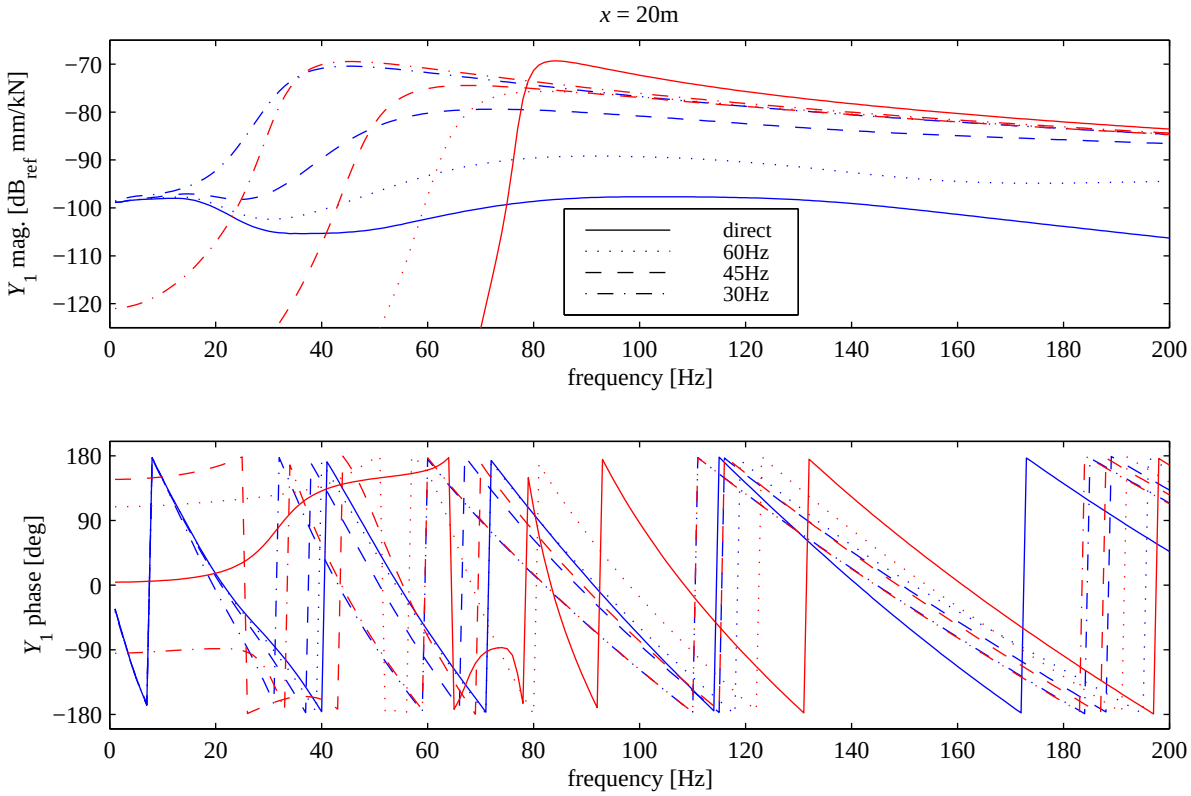

Figure 5.5: Vertical displacement response of the simple slab beam 20m from the load (blue), compared to the "equivalent" Winkler beam (red) with various slab support stiffnesses.

Even if the Winkler theory were adequate for describing the slab beam, it cannot predict the response of the tunnel invert and the soil surrounding the tunnel. Figure 5.6 shows the vertical response of the invert directly beneath the load applied to the slab at $x = 0$. Small circles mark the $\sqrt{2}\, f_n$ frequencies above which, according to simple theory, vibration isolation is supposed to occur. It can be seen in this case that the responses for a slab on bearings drop below the response of the directly joined slab well before these cut-off points, so simple vibration-isolation theory holds so far. However, the response 20m along the tunnel invert, shown in Figure 5.7, is actually made *higher* by the insertion of rubber between the slab and the invert, with only the softest bearings ($f_n = 30\,\text{Hz}$) eventually giving a lower response at about 145Hz. The higher responses are to be expected since the bearings decouple the slab from the tunnel and hence allow energy to propagate further along the beam before being transmitted to the invert. This is not necessarily a problem: it could indeed be beneficial if it means that vibrational energy is confined to the slab beam and the tunnel and is not radiated into the soil.

The most important measure of the isolation effectiveness of a track is the vibration level in the soil. As for the results in Chapter 4, soil responses here are given for the horizontal plane

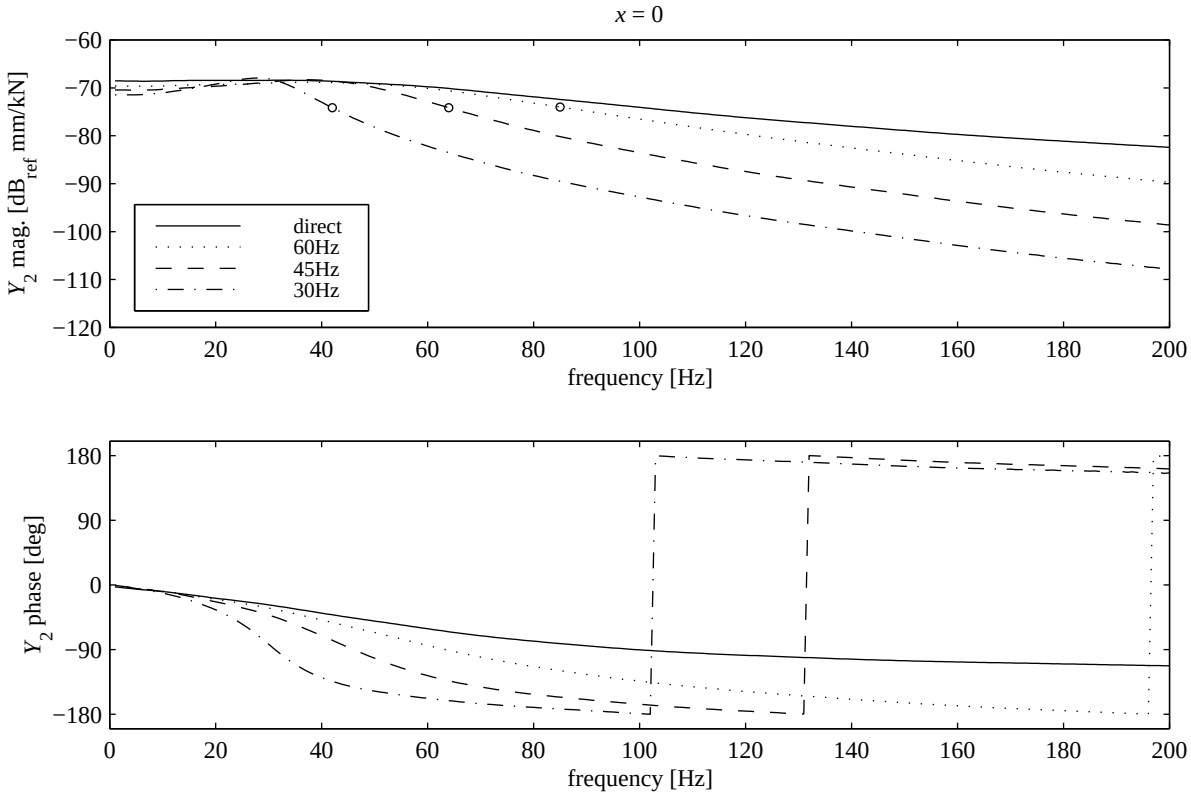

Figure 5.6: Vertical displacement response of the tunnel invert directly under the load on the slab beam for various slab-support stiffnesses, with circles marking the $\sqrt{2}\, f_n$ points.

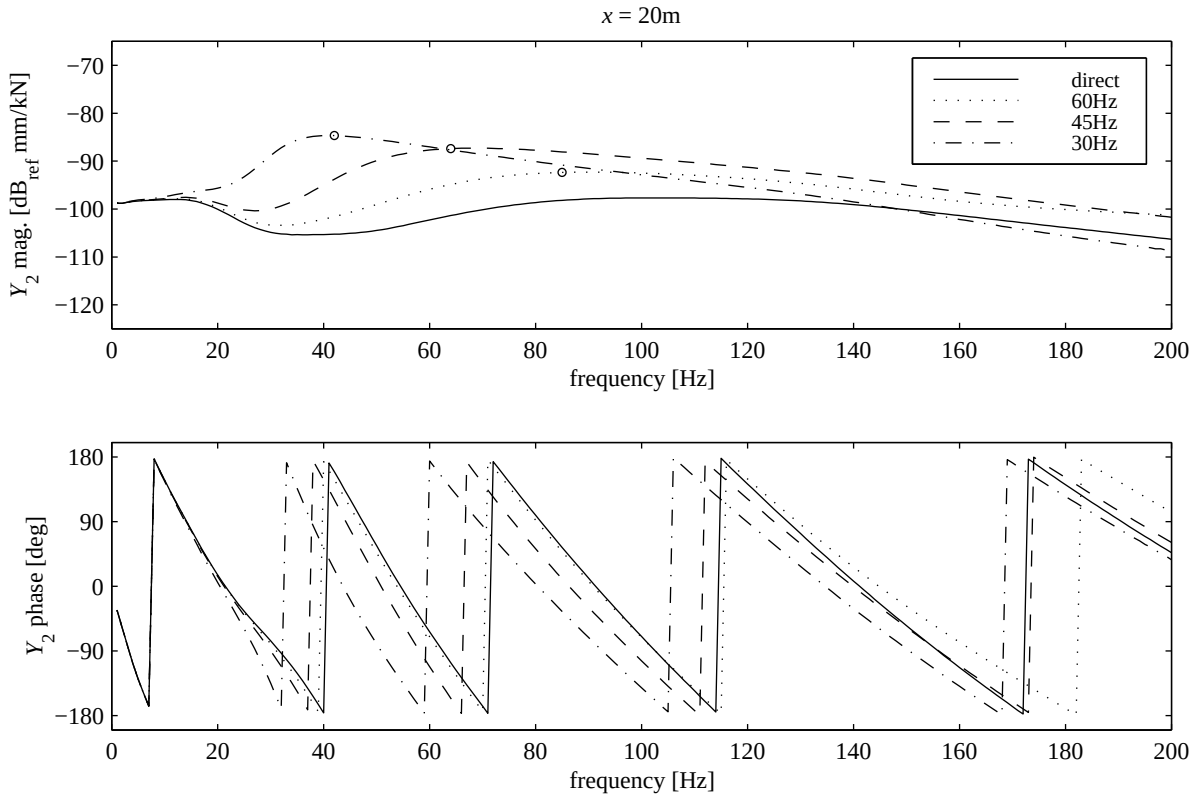

Figure 5.7: Vertical displacement response of the tunnel invert 20m along the tunnel from the load applied to the slab beam, for various slab-support stiffnesses, with circles marking the $\sqrt{2}\, f_n$ points.

$\theta = 90^\circ$, so that the displacement components *W* and *V* coincide with the horizontal and vertical directions (see Figure 4.10). Figure 5.8 shows the horizontal soil displacement at a radius of 20m horizontally out into the soil, opposite the load on the slab. The responses exhibit the peaks and troughs of the pressure-wave interference pattern observed and discussed in Chapter 4 for the uncoupled tunnel. At this position in the soil, increasingly softer slab support results in reduction starting at frequencies near the $\sqrt{2}\, f_n$ points, again marked with circles, obeying simple vibration-isolation theory just as the tunnel invert did directly under the slab load . Figure 5.9 shows similar behaviour for the horizontal response at $x = 20\text{m}$, although now isolation is delayed somewhat (the "isolated" responses cross the directly joined response at higher frequencies than before), because at frequencies near the resonance the slab on bearings is propagating energy further along the tunnel before it enters the soil.

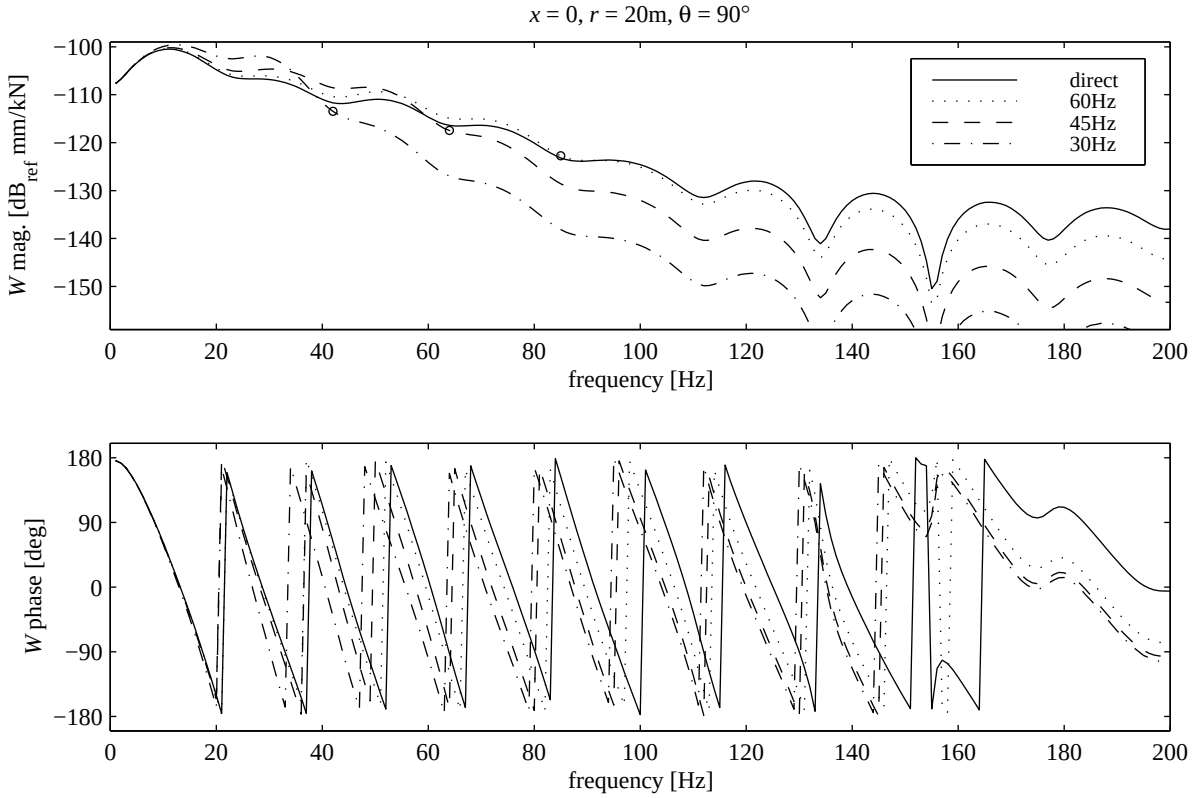

Figure 5.8: Horizontal soil displacement response 20m horizontally out into the soil opposite the load on the slab for various slab-support stiffnesses, with circles marking the $\sqrt{2}\, f_n$ points.

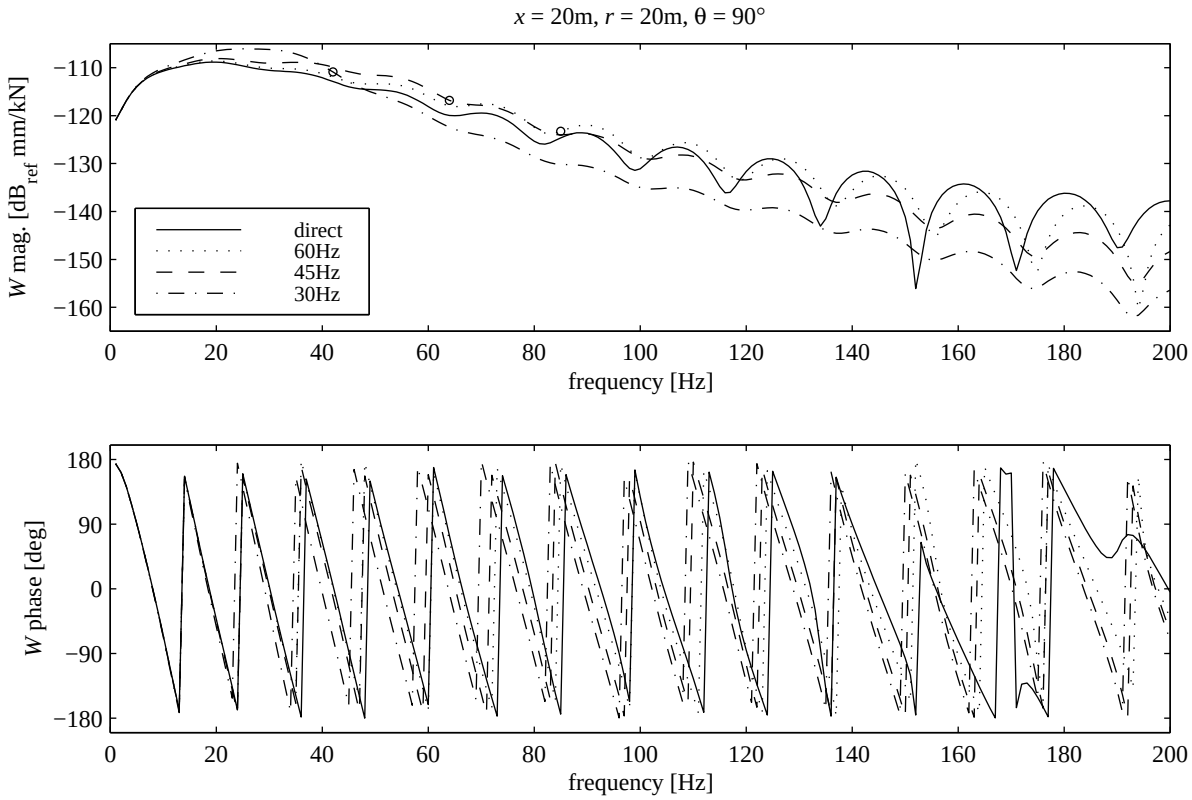

Figure 5.9: Horizontal soil displacement response 20m horizontally out into the soil and 20m longitudinally parallel to the tunnel from the slab load, for various slab-support stiffnesses, with circles marking the $\sqrt{2}\, f_n$ points.

The vertical soil response at 20m radius opposite the load, Figure 5.10, also shows classic vibration isolation, this time very clearly because the pressure-wave effects are subdued. But as the observation point is shifted longitudinally, this behaviour changes. Figure 5.11 shows that, at $x = 20\text{m}$, the insertion of the stiffer rubber bearings ($f_n = 60\text{Hz}$ and $f_n = 45\text{Hz}$) has almost no effect on the vertical soil displacement, while for the softest bearings ($f_n = 30\text{Hz}$) only a modest, roughly constant reduction of 5-10dB is achieved, rather than an ever-increasing reduction with frequency as exhibited in Figure 5.10 (and expected from simple isolation theory). At $x = 40\text{m}$, Figure 5.12, adding any slab bearings at all increases the vertical displacement for all frequencies between 40Hz and 200Hz. This can again be explained by the transmission of energy along the slab on bearings, giving higher response at the portion of the tunnel nearest the observation point. The longitudinal soil response at $x = 20\text{m}$, given in Figure 5.13, is very similar to the horizontal response given in Figure 5.9, showing the same type of delayed isolation, for the same reason (the longitudinal displacement at $x = 0$ is zero because it is an asymmetric function).

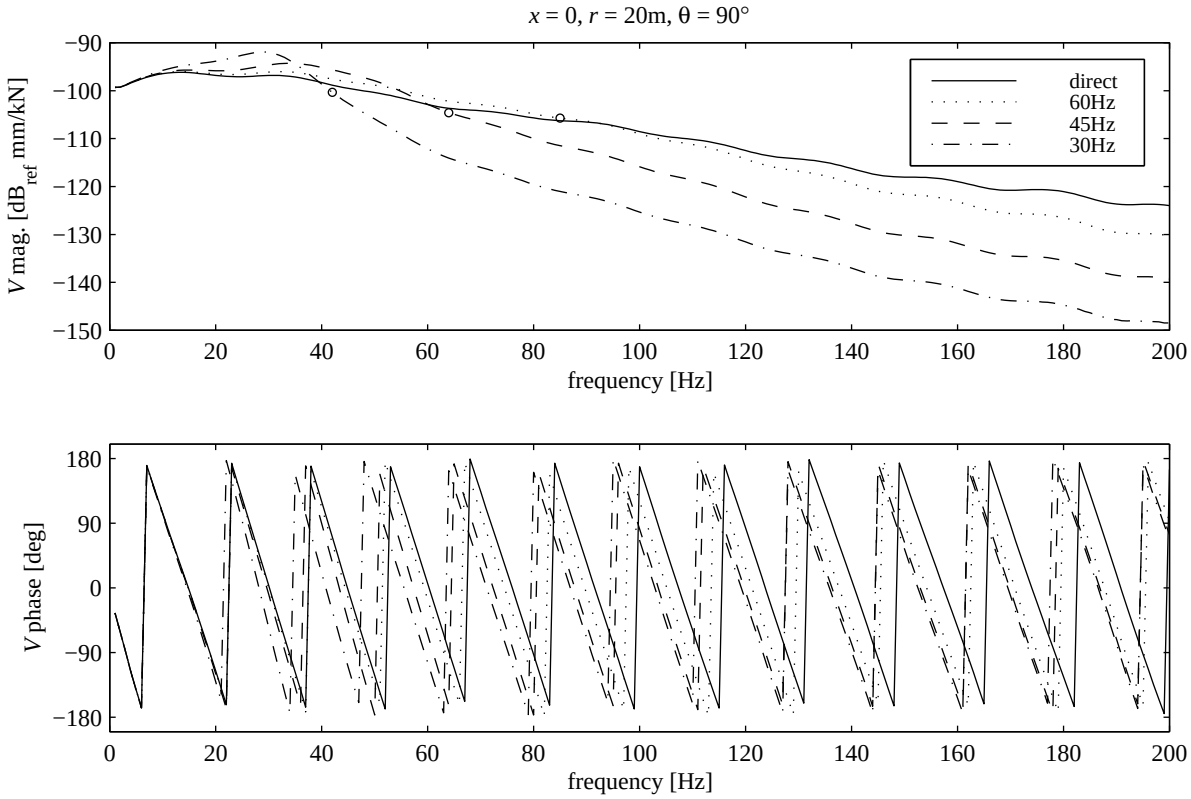

Figure 5.10: Vertical soil displacement response 20m horizontally out into the soil from the load, for various slab-support stiffnesses, with circles marking the $\sqrt{2}\ f_n$ points.

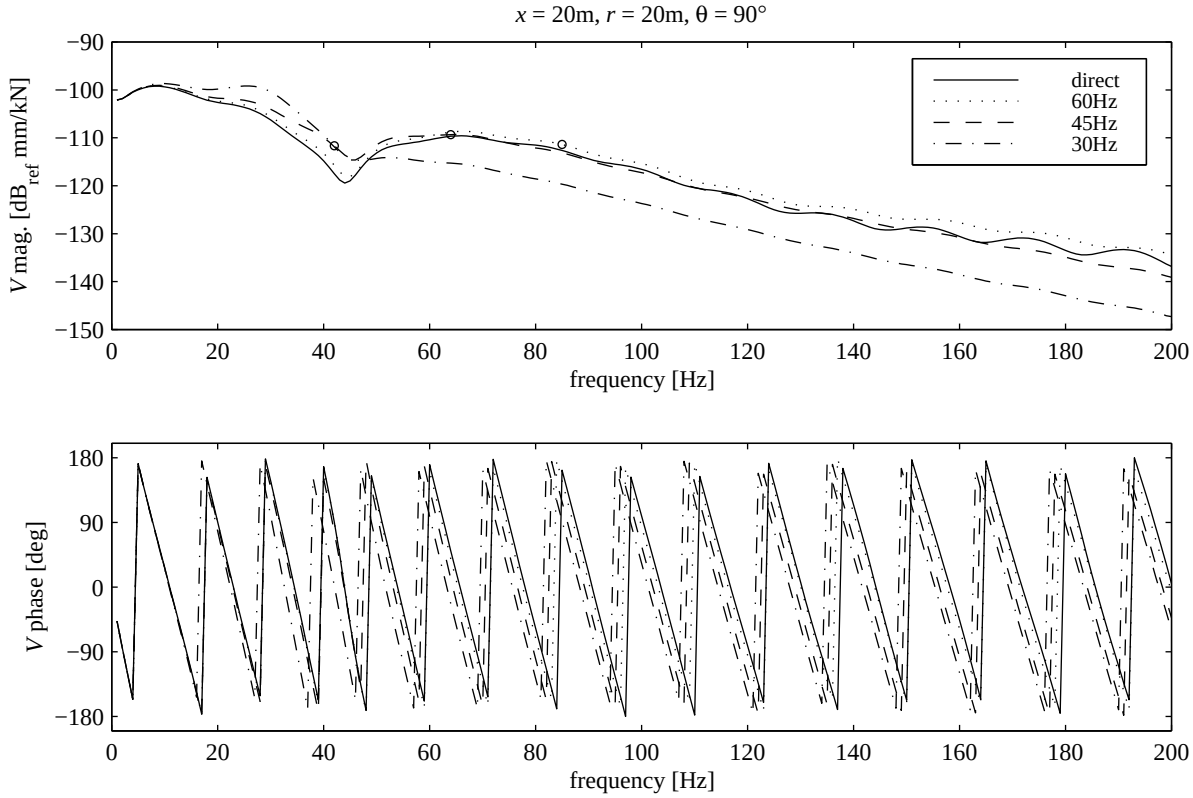

Figure 5.11: Vertical soil displacement response 20m horizontally out into the soil and 20m longitudinally parallel to the tunnel from the slab load, for various slab-support stiffnesses, with circles marking the $\sqrt{2}\, f_n$ points.

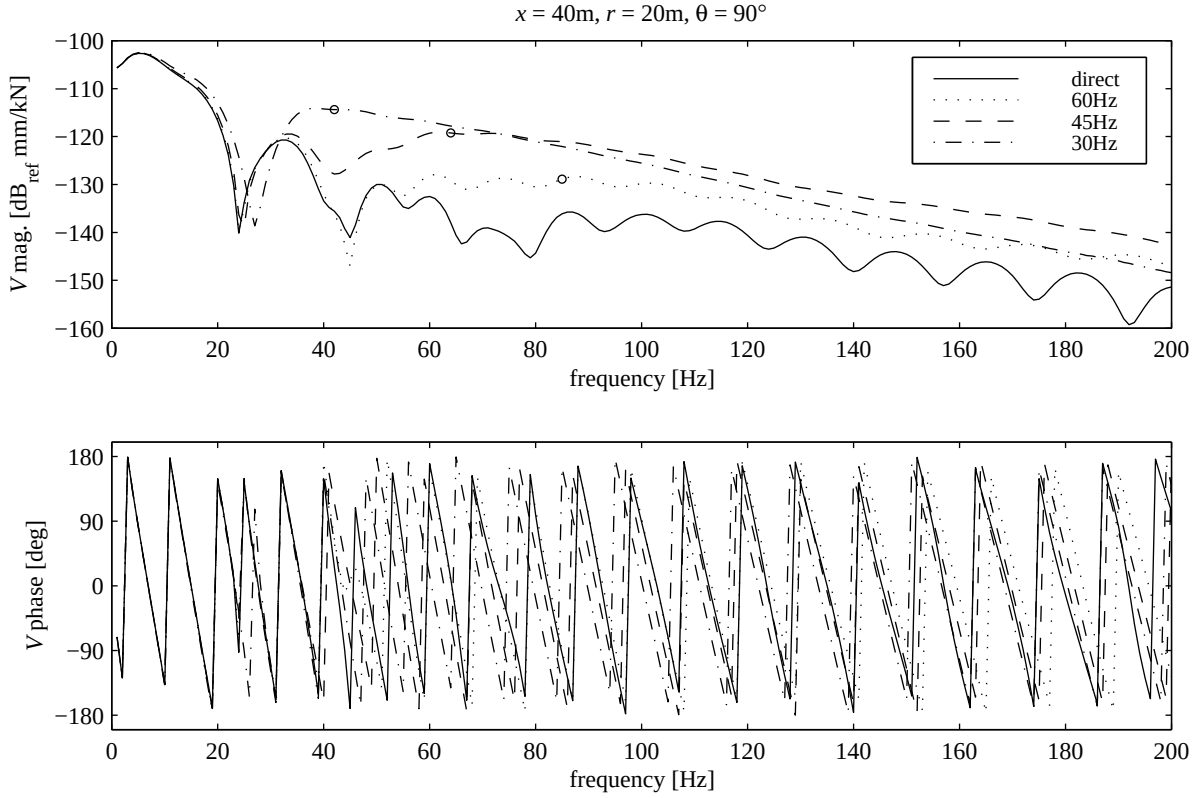

Figure 5.12: Vertical soil displacement response 20m horizontally out into the soil and 40m longitudinally parallel to the tunnel from the slab load, for various slab-support stiffnesses, with circles marking the $\sqrt{2}\, f_n$ points.

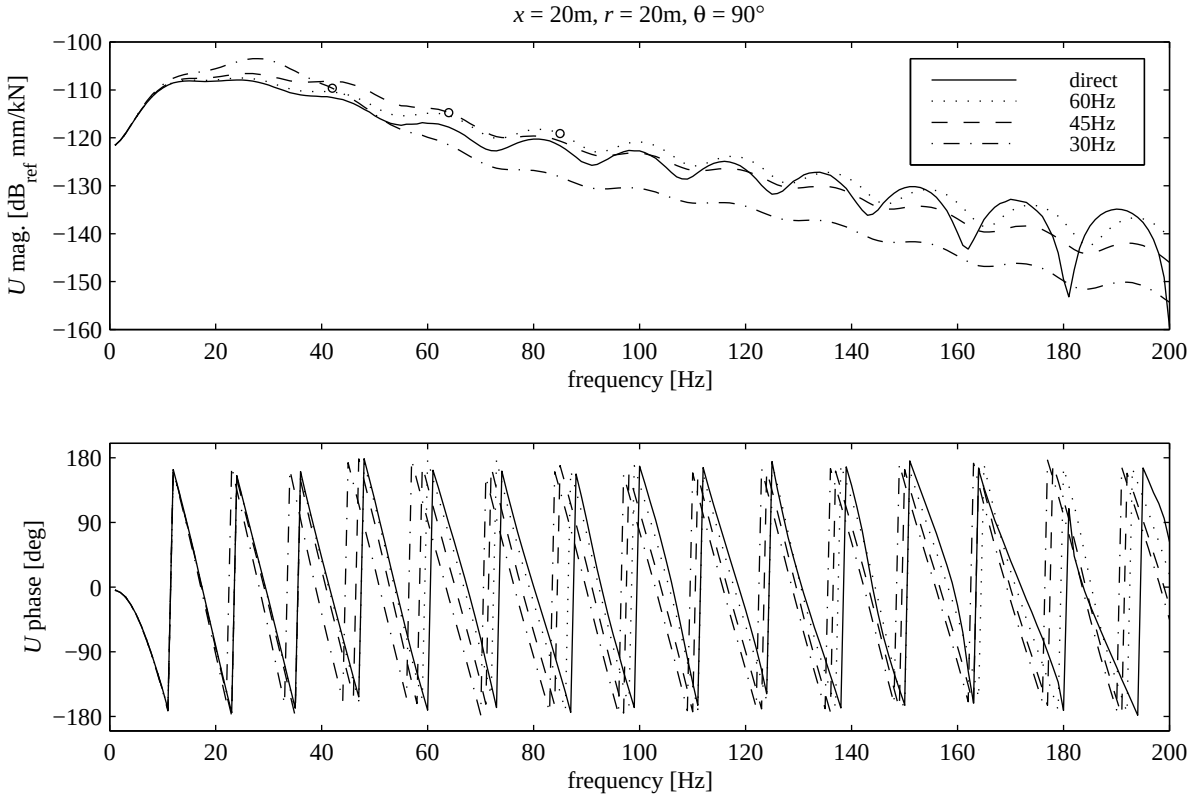

Figure 5.13: Longitudinal soil displacement 20m horizontally out into the soil and 40m longitudinally parallel to the tunnel from the slab load, for various slab-support stiffnesses, with circles marking the $\sqrt{2}\, f_n$ points.

The results discussed above have considered the responses to a single load acting on the slab beam. In reality a train provides a series of simultaneous inputs to the track. This means that the total response at an observation point in the soil will be some kind of sum of the responses for the various loads applied at different points along the track. Taking the vertical displacement component as an example, this would be the sum of the responses (among others) represented by Figures 5.10 to 5.12. The magnitudes of these separate responses are all of the same order (near –120dB), but with slab bearings sometimes reducing response and sometimes increasing it. Whether floating the slab gives a beneficial reduction in soil vibration depends on how these various responses add up.

5.2 A Track Slab with Bending and Torsion

A real track has two rails, whose inputs will not necessarily be correlated, so it is reasonable to assume that the motion of the slab will not be pure, laterally symmetric bending, but that there will be some torsional motion as well. Such a three-dimensional slab beam can be joined to the

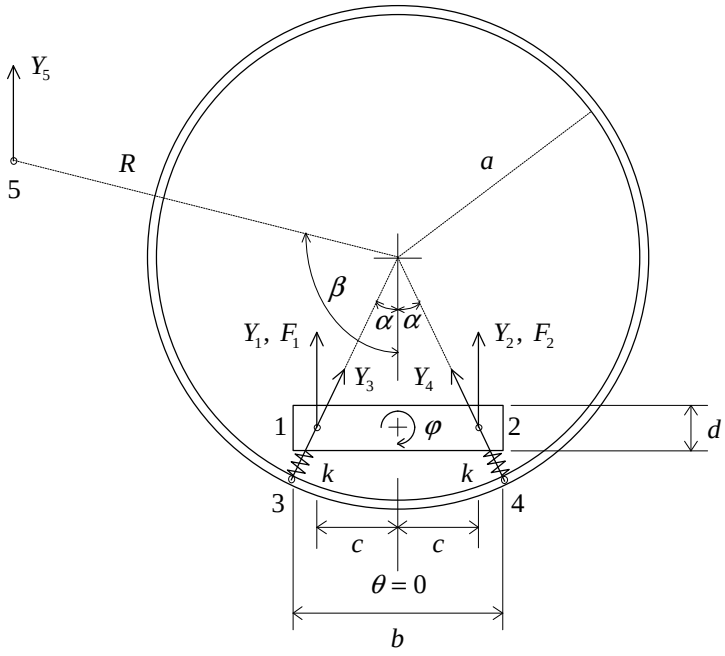

Figure 5.14: Tunnel cross-section showing how a torsional slab beam is joined to the tunnel invert along two longitudinal lines between the beam at 1 and 2 and the invert at 3 and 4.

tunnel along two lines of support as shown in cross-section in Figure 5.14, instead of just one line as for the simple slab beam.

5.2.1 Coupling Equations for the Torsional Slab Beam and Tunnel

Figure 5.15 shows the general case of a body loaded by two parallel lines of distributed force. Because there are now two lines of load $Q_1(x)$ and $Q_2(x)$, the equations describing the time-harmonic displacement responses $Y_1(x)$ and $Y_2(x)$ are coupled. However, the idea of convolution in space can still be used, to give

$$\begin{aligned} Y_1(x) &= \int_{-\infty}^{\infty} H_{11}(x-\chi)Q_1(\chi)d\chi + \int_{-\infty}^{\infty} H_{12}(x-\chi)Q_2(\chi)d\chi \\ Y_2(x) &= \int_{-\infty}^{\infty} H_{21}(x-\chi)Q_1(\chi)d\chi + \int_{-\infty}^{\infty} H_{22}(x-\chi)Q_2(\chi)d\chi \end{aligned} \tag{5.16}$$

where the FRFs $H_{11}(x)$, $H_{12}(x)$, $H_{21}(x)$ and $H_{22}(x)$ are for point-load inputs at $x = 0$, with, for example, $H_{12}(x)$ denoting the FRF along line 1 to an input on line 2. Fourier transformation of both equations of (5.16) into the wavenumber domain allows the coupled system to be written in the matrix form

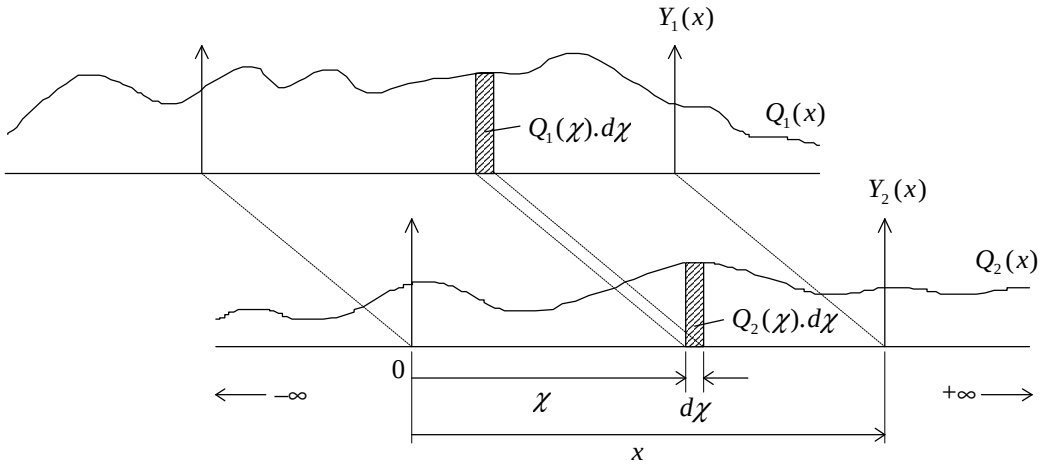

Figure 5.15: General force distributions acting along two lines of joining. The displacement responses along the lines are obtained by coupled convolutions in space.

$$\begin{Bmatrix} \tilde{Y}_1 \\ \tilde{Y}_2 \end{Bmatrix} = \begin{bmatrix} \tilde{H}_{11} & \tilde{H}_{12} \\ \tilde{H}_{21} & \tilde{H}_{22} \end{bmatrix} \begin{Bmatrix} \tilde{Q}_1 \\ \tilde{Q}_2 \end{Bmatrix} \tag{5.17}$$

The joining of the torsional slab beam to the tunnel is complicated by the fact that the lines of motion of the tunnel and those of the slab are not coincident, as can be seen from Figure 5.14. It will be assumed that interaction forces can only be transmitted along lines normal to the tunnel, and that the absolute displacements also lie in these directions. Thus the vertical slab-beam displacements Y_1 and Y_2 at the small angle α to the tunnel normals are really just the vertical components of the motion of the slab's edges; the lateral dynamics of the slab beam are neglected as having only a small effect on total response. Applying (5.17) to both the slab and the tunnel therefore gives

$$\begin{Bmatrix} \tilde{Y}_1 \\ \tilde{Y}_2 \end{Bmatrix} = \begin{bmatrix} \tilde{H}_{11} & \tilde{H}_{12} \\ \tilde{H}_{21} & \tilde{H}_{22} \end{bmatrix} \left(-\begin{Bmatrix} \tilde{G}_1 \\ \tilde{G}_2 \end{Bmatrix} \cos\alpha + \begin{Bmatrix} \tilde{F}_1 \\ \tilde{F}_2 \end{Bmatrix} \right)$$

$$\text{and} \quad \begin{Bmatrix} \tilde{Y}_3 \\ \tilde{Y}_4 \end{Bmatrix} = \begin{bmatrix} \tilde{H}_{33} & \tilde{H}_{34} \\ \tilde{H}_{43} & \tilde{H}_{44} \end{bmatrix} \begin{Bmatrix} \tilde{G}_1 \\ \tilde{G}_2 \end{Bmatrix} \tag{5.18}$$

where $\tilde{G}_1$ and $\tilde{G}_2$ are the normal interaction forces impinging on the tunnel invert at the contact lines 3 and 4 (i.e. coincident with Y_3 and Y_4), and $\tilde{F}_1$ and $\tilde{F}_2$ are the external forces acting vertically on the slab at lines 1 and 2 (see Figure 5.14).

As for the simple slab beam, the torsional slab can either be joined directly or be supported on springs. For the directly joined case, the absolute displacements of the slab and the tunnel must be the same, that is

$$\frac{1}{\cos\alpha}\begin{Bmatrix}\tilde{\tilde{Y}}_1\\ \tilde{\tilde{Y}}_2\end{Bmatrix} = \begin{Bmatrix}\tilde{\tilde{Y}}_3\\ \tilde{\tilde{Y}}_4\end{Bmatrix} \tag{5.19}$$

Using the joining condition (5.19) with (5.18) allows the displacements to be found as

$$\begin{aligned}\tilde{\tilde{\mathbf{Y}}}_{12} &= \left([\mathbf{I}]+[\tilde{\tilde{\mathbf{H}}}_{12}][\tilde{\tilde{\mathbf{H}}}_{34}]^{-1}\right)^{-1}[\tilde{\tilde{\mathbf{H}}}_{12}]\tilde{\tilde{\mathbf{F}}}\\ \tilde{\tilde{\mathbf{Y}}}_{34} &= \frac{1}{\cos\alpha}\tilde{\tilde{\mathbf{Y}}}_{12}\end{aligned} \tag{5.20}$$

where $\tilde{\tilde{\mathbf{Y}}}_{12}=\{\tilde{\tilde{Y}}_1 \quad \tilde{\tilde{Y}}_2\}^{\mathrm{T}}$, $\tilde{\tilde{\mathbf{Y}}}_{34}=\{\tilde{\tilde{Y}}_3 \quad \tilde{\tilde{Y}}_4\}^{\mathrm{T}}$, $\tilde{\tilde{\mathbf{F}}}=\{\tilde{\tilde{F}}_1 \quad \tilde{\tilde{F}}_2\}^{\mathrm{T}}$, and the FRF matrices $[\tilde{\tilde{\mathbf{H}}}_{12}]$ and $[\tilde{\tilde{\mathbf{H}}}_{34}]$ are those in respectively the first and second equations of (5.18).

For the case of support by springs, the interaction forces are dependent on the differences in the absolute displacements of the slab and tunnel, and the stiffness of the springs. Assuming equal slab-support stiffness of *k* per unit length acting normally to the tunnel for both lines of joining, the coupling condition becomes

$$\begin{Bmatrix}\tilde{\tilde{G}}_1\\ \tilde{\tilde{G}}_2\end{Bmatrix} = k\left(\frac{1}{\cos\alpha}\begin{Bmatrix}\tilde{\tilde{Y}}_1\\ \tilde{\tilde{Y}}_2\end{Bmatrix} - \begin{Bmatrix}\tilde{\tilde{Y}}_3\\ \tilde{\tilde{Y}}_4\end{Bmatrix}\right) \tag{5.21}$$

Substituting (5.21) into (5.18) results in expressions for the displacements of

$$\begin{aligned}\tilde{\tilde{\mathbf{Y}}}_{12} &= \left[[\mathbf{I}] + k[\tilde{\tilde{\mathbf{H}}}_{12}] - k^2[\tilde{\tilde{\mathbf{H}}}_{12}]\left([\mathbf{I}]+k[\tilde{\tilde{\mathbf{H}}}_{34}]\right)^{-1}[\tilde{\tilde{\mathbf{H}}}_{34}]\right]^{-1}[\tilde{\tilde{\mathbf{H}}}_{12}]\tilde{\tilde{\mathbf{F}}}\\ \tilde{\tilde{\mathbf{Y}}}_{34} &= \frac{k}{\cos\alpha}\left([\mathbf{I}]+k[\tilde{\tilde{\mathbf{H}}}_{34}]\right)^{-1}[\tilde{\tilde{\mathbf{H}}}_{34}]\tilde{\tilde{\mathbf{Y}}}_{12}\end{aligned} \tag{5.22}$$

Once the tunnel displacements $\tilde{\tilde{\mathbf{Y}}}_{34}$ are calculated from (5.20) or (5.22), the interaction forces can be calculated from the second of equations (5.18) and thus the response $\tilde{\tilde{Y}}_5$ along a line in the soil at some constant radius $r = R$ and angle $\theta = \beta$ (see Figure 5.14) is

$$\tilde{\tilde{Y}}_5 = \{\tilde{\tilde{H}}_{53} \quad \tilde{\tilde{H}}_{54}\}\begin{Bmatrix}\tilde{\tilde{G}}_1\\ \tilde{\tilde{G}}_2\end{Bmatrix} = \{\tilde{\tilde{H}}_{53} \quad \tilde{\tilde{H}}_{54}\}[\tilde{\tilde{\mathbf{H}}}_{34}]^{-1}\tilde{\tilde{\mathbf{Y}}}_{34} \tag{5.23}$$

where $\tilde{\tilde{H}}_{53}$ and $\tilde{\tilde{H}}_{54}$ are the FRFs for the response at line 5 to inputs at lines 3 and 4 respectively on the uncoupled tunnel invert. As before, the responses in the space domain are obtained by the inverse Fourier transforms of the ξ-domain responses calculated above.

5.2.2 Calculation of FRFs for Torsional Coupling

The various FRFs for the uncoupled tunnel and slab have to be calculated before any of the foregoing results can be utilised. The tunnel FRFs can be determined from (5.10) as they were for the simple slab case. Referring to Figure 5.14 and using symmetry (noting that $\tilde{U}$ and $\tilde{W}$ are even functions of θ while $\tilde{V}$ is an odd function of θ), they are given by

$$\begin{aligned}
\tilde{H}_{33} &= \tilde{H}_{44} = \tilde{W}\big|_{\substack{r=a\\ \theta=0}} \\
\tilde{H}_{34} &= \tilde{H}_{43} = \tilde{W}\big|_{\substack{r=a\\ \theta=2\alpha}} \\
\tilde{H}_{53} &= \tilde{U},\ \tilde{V} \text{ or } \tilde{W}\big|_{\substack{r=R\\ \theta=\beta-\alpha}} \\
\tilde{H}_{54} &= \tilde{U},\ \tilde{V} \text{ or } \tilde{W}\big|_{\substack{r=R\\ \theta=\beta+\alpha}}
\end{aligned} \tag{5.24}$$

The bending response $\tilde{Y}$ of the slab beam is governed by the FRF $\tilde{H}_{YF}$ of (5.13). The torsional response is determined from the equation of motion for the angle of twist $\varphi(x,t)$ of a shaft in torsion, which is (see Meirovitch [136])

$$J\frac{\partial^2\varphi}{\partial t^2} - GK\frac{\partial^2\varphi}{\partial x^2} = \tau(x,t) \tag{5.25}$$

where J is the polar moment of inertia per unit length, GK is the torsional rigidity (G the shear modulus, K the torsional constant of the cross-section), and $\tau(x,t)$ the applied torque per unit length. To put (5.25) into the wavenumber domain, harmonic solutions of the form $\varphi = \tilde{\Phi}e^{i(\omega t+\xi x)}$ and $\tau = \tilde{\mathrm{T}}e^{i(\omega t+\xi x)}$ are substituted to give

$$\tilde{H}_{\Phi\mathrm{T}} = \tilde{\Phi}\big|_{\tilde{\mathrm{T}}=1} = \frac{1}{GK\xi^2 - J\omega^2} \tag{5.26}$$

where $\tilde{\mathrm{T}}=1$ represents the unit spatial torque (acting at $x=0$) given by a torque per unit length of $\mathrm{T}=\delta(x)$ in the space domain. With only the two lines of force $\tilde{F}_1$ and $\tilde{F}_2$ acting on the slab beam, the torque per unit length is $\tilde{T} = \tilde{F}_1.c - \tilde{F}_2.c$ in the wavenumber domain, where c is the distance of the edge loading lines from the centreline of the slab, as indicated in Figure 5.14. Thus the vertical displacements of the two edges of the slab under combined bending and torsion are given by

$$\begin{aligned}
\tilde{Y}_1 &= \tilde{Y} + c\tilde{\Phi} = \tilde{H}_{YF}(\tilde{F}_1 + \tilde{F}_2) + c\tilde{H}_{\Phi\mathrm{T}}(\tilde{F}_1.c - \tilde{F}_2.c) \\
\tilde{Y}_2 &= \tilde{Y} - c\tilde{\Phi} = \tilde{H}_{YF}(\tilde{F}_1 + \tilde{F}_2) - c\tilde{H}_{\Phi\mathrm{T}}(\tilde{F}_1.c - \tilde{F}_2.c)
\end{aligned} \tag{5.27}$$

By applying a unit spatial point load to each edge in turn, that is, forces per unit length of $\tilde{\tilde{F}}_1 = 1$ and $\tilde{\tilde{F}}_2 = 0$, then $\tilde{\tilde{F}}_1 = 0$ and $\tilde{\tilde{F}}_2 = 1$, the free-beam FRFs can be deduced from (5.27) as

$$\begin{aligned} \tilde{\tilde{H}}_{11} &= \tilde{\tilde{H}}_{22} = \tilde{\tilde{H}}_{YF} + c^2 \tilde{\tilde{H}}_{\Phi T} \\ \tilde{\tilde{H}}_{12} &= \tilde{\tilde{H}}_{21} = \tilde{\tilde{H}}_{YF} - c^2 \tilde{\tilde{H}}_{\Phi T} \end{aligned} \tag{5.28}$$

5.2.3 Results for the Tunnel with a Torsional Slab Beam

As for the simple-slab model, the tunnel and soil FRFs were calculated as described in Chapter 4 for the parameters of Table 4.3. Table 5.2 gives the other parameters required. The bending stiffness *EI* and the mass per unit length *m* of the torsional slab are taken to be the same as for the simple slab, but this still leaves the torsional rigidity *GK* and the moment of inertia per unit length *J* to be determined. If the cross-section of the slab is rectangular, then the torsional constant *K* is given to an accuracy of 4% by (see Young [202])

$$K = bd^3 \left[\frac{1}{3} - 0.21 \frac{d}{b} \left(1 - \frac{d^4}{12 b^4} \right) \right] \tag{5.29}$$

for the slab of width *b* and height *d* depicted in Figure 5.14. Taking the slab to be 2000mm wide and 700mm deep, (5.29) together with the bending properties (assuming a Poisson's ratio for the slab concrete of 0.2) results in the values of *GK* and *J* given in Table 5.2.

Torsional Slab Beam
$EI = 1430 \times 10^6$ Pa.m^4
$m = 3500$ kg/m
$b = 2000$ mm $\quad c = 750$ mm
$d = 700$ mm $\quad \alpha = 14.7^\circ$
$GK = 1.857 \times 10^9$ Pa.m^4
$J = 1310$ kg.m^2/m
$k = 630.8 \times 10^6$ N/m^2 when $f_n = 60$ Hz
$k = 212.2 \times 10^6$ N/m^2 when $f_n = 45$ Hz
$k = 73.3 \times 10^6$ N/m^2 when $f_n = 30$ Hz
$\eta_k = 0.5$

Table 5.2: The torsional slab beam's properties. The slab-support stiffnesses are half those of used for the simple slab (see Table 5.1), since there are now two lines of support.

The joining geometry shown in Table 5.2 is determined by the gauge of the rails, taken as 1500mm. Half the gauge gives the distance *c* (see Figure 5.14). The angle α of the normals to the tunnel invert at the joining lines 3 and 4 is calculated by assuming a clearance between the slab and invert of 50mm along the normals – enough space to insert a ballast mat – and recalling that the tunnel radius *a* is 3m. Although this 50mm clearance would result in interference between the ends of the assumed rectangular slab and the tunnel wall, a real slab would be shaped to fit the wall's curve and would only be approximately rectangular in cross-section. To allow direct comparison with the simple-slab model, the three different values of slab-support stiffness *k* shown in Table 5.2 were chosen to give a bending response equivalent to the simple slab. Since there are now two lines of joining, they are *half* the values given in Table 5.1; a spring has the same apparent vertical stiffness for any inclination which remains constant, as was assumed in formulating the torsional-slab equations.

The ξ-domain displacements were calculated from (5.20), (5.22) and (5.23) using Matlab, and then the physical *x*-domain displacements were obtained by an inverse FFT with $N = 2048$ points and a sampling interval of $\Delta x = 0.5\text{m}$, as done for the simple-slab model. To examine bending effects only, the applied forces per unit length are set at $\tilde{F}_1 = 0.5$ and $\tilde{F}_2 = 0.5$ (which gives a net unit vertical force applied at $x = 0$ in the space domain); to examine torsional effects only, the forces are set at $\tilde{F}_1 = 0.5$ and $\tilde{F}_2 = -0.5$ (which gives a net unit torque applied at $x = 0$). The response to a single off-centre unit force is given by the sum of these two cases, that is, with $\tilde{F}_1 = 1$ and $\tilde{F}_2 = 0$.

Figure 5.16 shows the vertical driving-point response of the torsional slab beam, which can be compared to Figure 5.4 for the simple slab. Figure 5.16(a) shows the response of the slab beam in pure bending, where the two edges of the slab are moving in-phase with the same magnitude. While the response for the directly joined slab is quite flat as before, the peaks of the responses with slab bearings inserted have shifted upwards in frequency compared to the simple slab, most apparent in the $f_n = 45\text{Hz}$ case where the peak actually occurs at 53Hz rather than 45Hz as in Figure 5.4, despite choosing support stiffnesses *k* to make the two slab models apparently equivalent. This indicates that the tunnel as a foundation is effectively stiffer when it supports the slab beam along two lines instead of one: two lines of force would tend to deform the

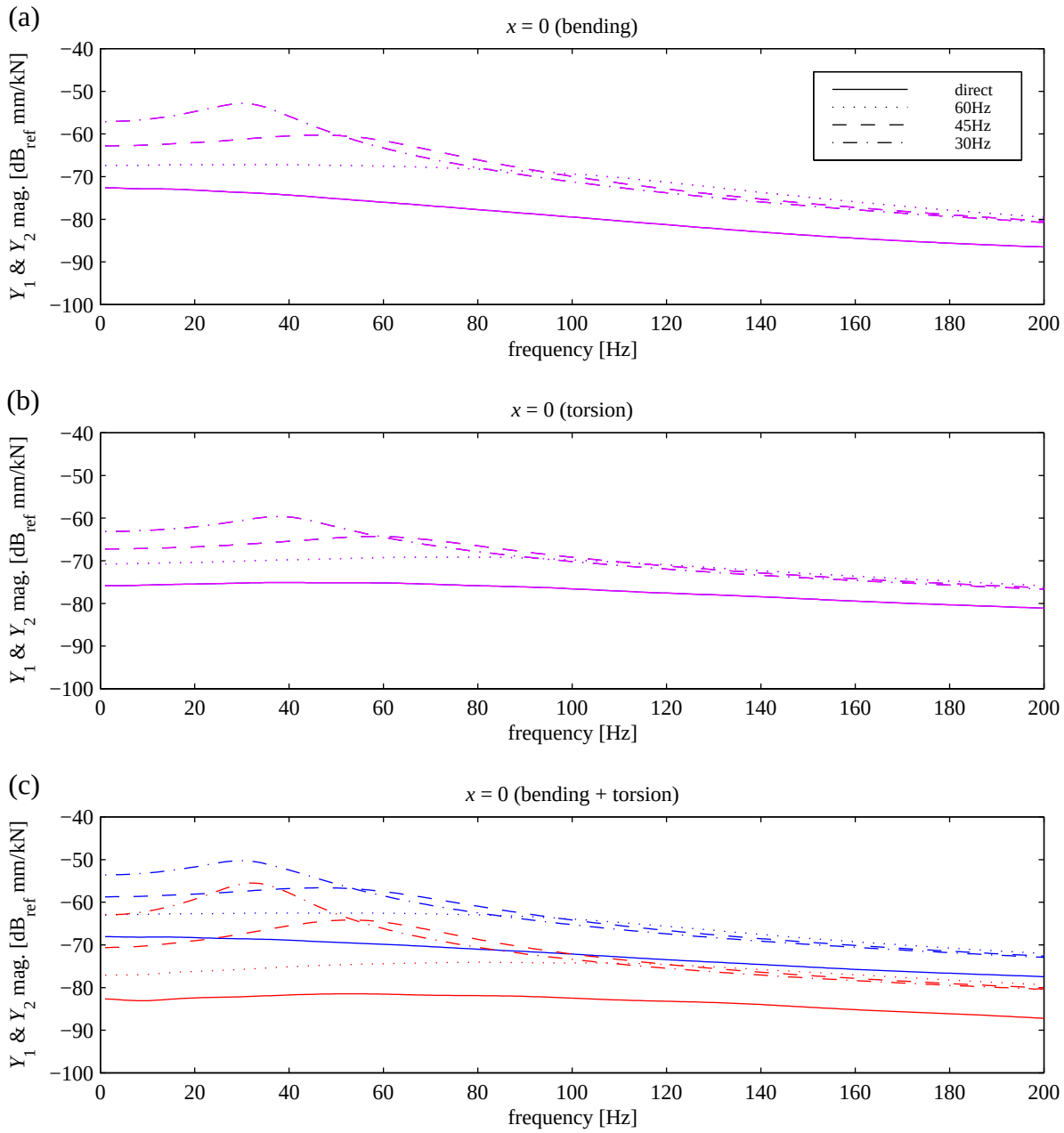

Figure 5.16: Vertical responses Y_1 (blue) and Y_2 (red) of a torsional slab beam supported on a tunnel, at the applied loads of (a) $F_1 = 0.5$, $F_2 = 0.5$ (b) $F_1 = 0.5, F_2 = -0.5$ and (c) $F_1 = 1$, $F_2 = 0$. Slab-support stiffnesses giving various natural frequencies as indicated. (Magenta indicates overlap of the blue and red curves).

tunnel cross-section in ways which involve greater contributions from the more complicated (and hence "stiffer") circumferential modeshapes than those for a single line of force. How the floating slab is supported on the tunnel is therefore an important factor. Figure 5.16(b) shows the motion of the slab beam in pure torsion, where the two edges are moving exactly out of phase with the same magnitude. The resonance peaks are higher than for pure bending, indicating that, for the parameters used here, torsional waves start propagating along the slab at higher

frequencies than bending waves. This means that even if a simple isolation theory were valid for floating-slab track, a Winkler-beam model – which only considers bending – would under-predict the natural frequencies and hence would predict vibration isolation at frequencies lower than would actually be the case. Figure 5.16(c) illustrates the effect of combined bending and torsion, as might be expected from a pair of unbalanced train-wheel loads. There is a difference of about 10dB between the motion of the two edges, so the greater motion of Y_1 will have more influence on the forces transmitted to the tunnel invert and then the soil.

The normal response of the tunnel invert directly under the applied loads is given in Figure 5.17. The displacements of the two joining lines under pure bending of the slab, Figure 5.17(a), are in phase and of the same magnitude, with behaviour very similar to Figure 5.6, the tunnel response for a simple-slab model. Slab bearings of any stiffness reduce the response because the decoupling effect allows energy to propagate further along the slab beam and thus away from this part of the tunnel invert. The performance is apparently better than what classic theory would predict, as the reduced response occurs below the $\sqrt{2}\, f_n$ points, despite the two-line joining arrangement being "stiffer" than the single-line one upon which the natural frequencies are based. The purely torsional response (with Y_3 and Y_4 out of phase), Figure 5.17(b), suggests that mounting the slab on springs allows torsional energy to propagate more effectively down the slab than bending energy, since the responses with bearings are all significantly lower than that for the directly joined slab, for *all* frequencies. The combination of bending and torsion due to an off-centre load, Figure 5.17(c), shows two different behaviours for the two adjacent lines along the bottom of the tunnel. Insertion of rubber bearings reduces Y_3 for all frequencies, whereas for the smaller displacement Y_4, it results in a more familiar response with reduction in vibration delayed to frequencies slightly above the $\sqrt{2}\, f_n$ points.

Examination of the responses 20m along the tunnel from the applied loads confirms that torsional motion of the slab on bearings transmits proportionally more energy down the tunnel. Figure 5.18(a) shows that the tunnel response to pure bending of the slab is very similar to Figure 5.7 for the simple slab, with slab bearings giving higher response than if the slab is directly joined, for most of the frequency range. However, Figure 5.18(b) shows that pure torsion of the slab results in much higher response with slab bearings than without. Nevertheless, the

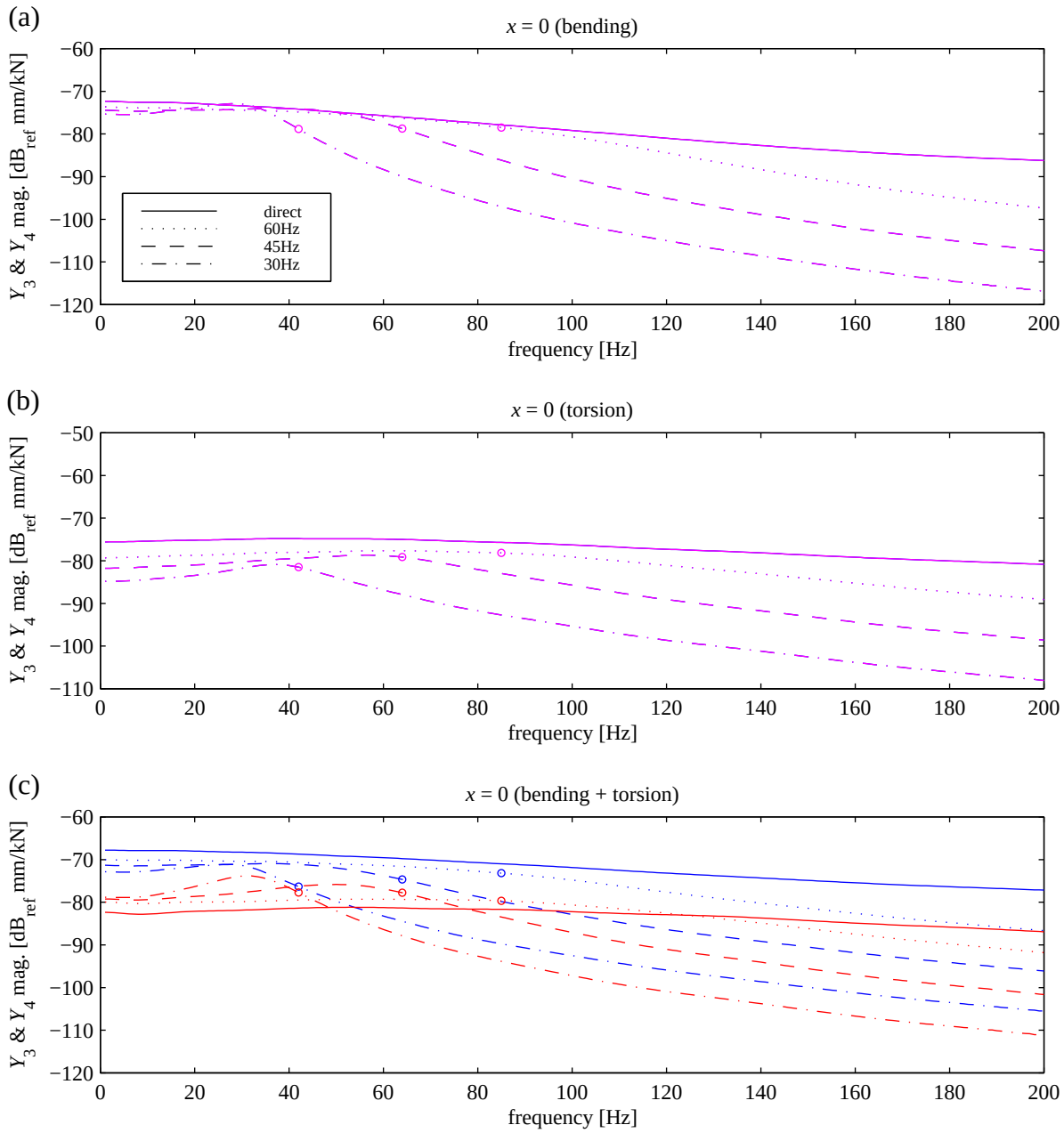

Figure 5.17: Normal responses Y_3 (blue) and Y_4 (red) of the tunnel invert under a torsional slab beam directly under applied loads of (a) $F_1 = 0.5$, $F_2 = 0.5$ (b) $F_1 = 0.5, F_2 = -0.5$ and (c) $F_1 = 1$, $F_2 = 0$. Slab-support stiffnesses giving various natural frequencies as indicated. Circles mark the $\sqrt{2}\, f_n$ points. (Magenta indicates overlap of the blue and red curves).

combined response, Figure 5.18(c), is dominated by the higher-magnitude bending component, although the introduction of torsion does dramatically reduce the levels of two of the Y_3 responses at 105Hz and 160Hz respectively.

To allow comparison with soil displacements previously discussed, soil responses were calculated for the line given by $r = 20$m and $\theta = 90^\circ$ (which correspond to R and β in equations (5.24) and Figure 5.14), resulting in W and V coinciding with horizontal and vertical

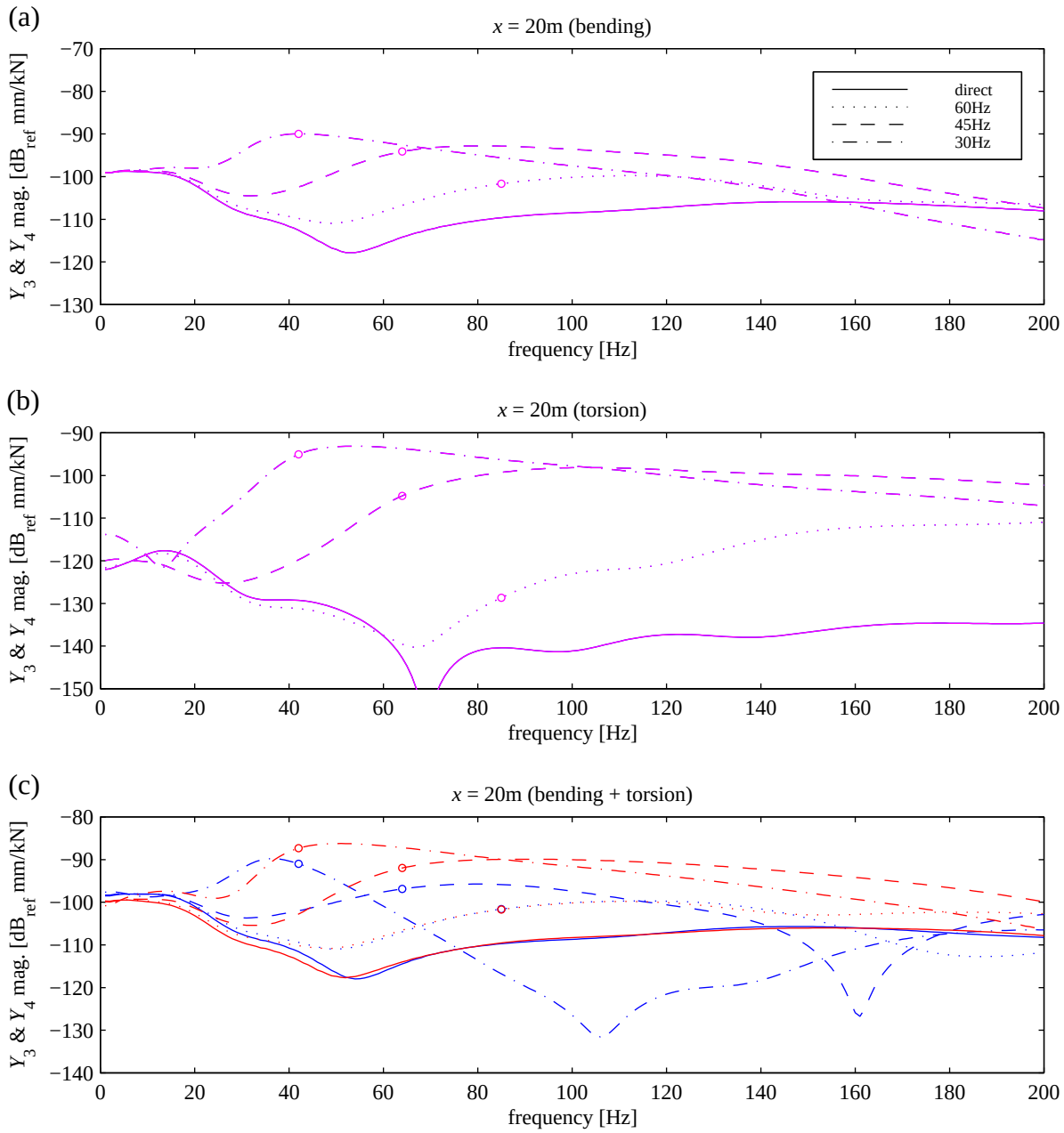

Figure 5.18: Normal responses Y_3 (blue) and Y_4 (red) of the tunnel invert under a torsional slab beam 20m along the tunnel from applied loads of (a) $F_1 = 0.5$, $F_2 = 0.5$ (b) $F_1 = 0.5$, $F_2 = -0.5$ and (c) $F_1 = 1$, $F_2 = 0$. Slab-support stiffnesses giving various natural frequencies as indicated. Circles mark the $\sqrt{2}\, f_n$ points. (Magenta indicates overlap of the blue and red curves).

displacement components. Figure 5.19 gives the horizontal soil response directly opposite the loads on the slab. The response to pure slab bending, Figure 5.19(a), is very like that in Figure 5.8, although "isolation" is delayed to higher frequencies than for the simple slab, because of the stiffer mounting of the torsional slab, and the undulations due to pressure-wave effects are more pronounced. The response to pure torsion, Figure 5.19(b), is not particularly different from that to pure bending, giving a combined response in Figure 5.19(c) that shows the same type of

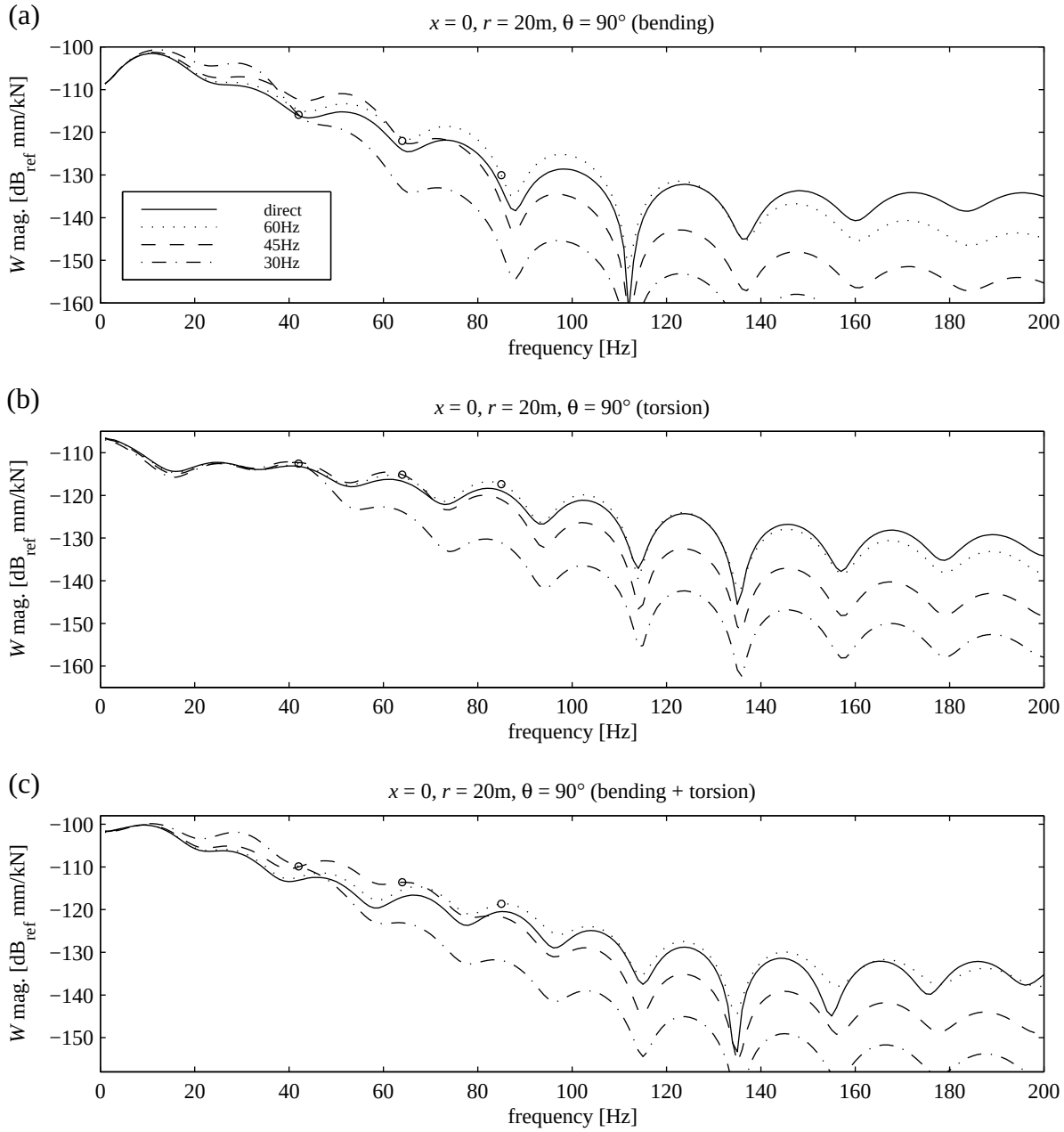

Figure 5.19: Horizontal soil displacement response with a torsional slab beam, 20m horizontally out into the soil opposite applied loads of (a) $F_1 = 0.5$, $F_2 = 0.5$ (b) $F_1 = 0.5, F_2 = -0.5$ and (c) $F_1 = 1$, $F_2 = 0$. Slab-support stiffnesses giving various natural frequencies as indicated. Circles mark the $\sqrt{2}\, f_n$ points.

classic isolation as the simple slab, albeit slightly delayed. The horizontal displacement at 20m away longitudinally, Figure 5.20, shows a bending response like that in Figure 5.9 and a torsional response different in shape but generally of lower magnitude, so that again the combined response is most like the bending-only response. Only the softest bearings with $f_n = 30\text{Hz}$ give significant vibration reduction at this point.

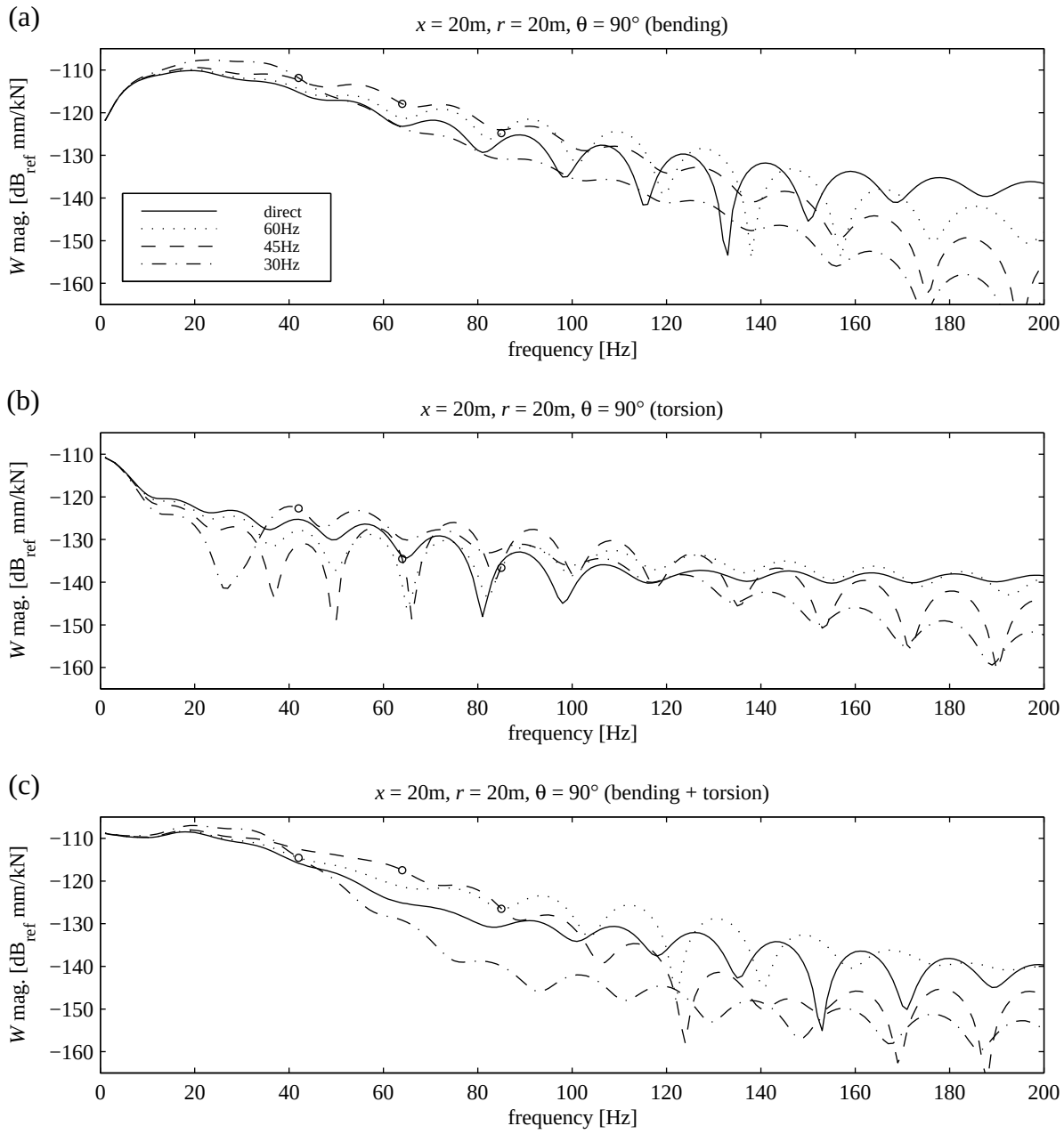

Figure 5.20: Horizontal soil displacement response with a torsional slab beam, 20m horizontally out into the soil and 20m longitudinally parallel to the tunnel from applied loads of (a) $F_1 = 0.5$, $F_2 = 0.5$ (b) $F_1 = 0.5, F_2 = -0.5$ and (c) $F_1 = 1$, $F_2 = 0$. Slab-support stiffnesses giving various natural frequencies as indicated. Circles mark the $\sqrt{2}\, f_n$ points.

Slab torsion has a greater effect on the vertical vibration of the soil. Figure 5.21 shows this displacement component directly opposite the slab loads. Like the horizontal response to bending in Figure 5.19(a), the bending response in Figure 5.21(a) is like that for the simple slab, Figure 5.10, conforming to classic isolation theory more or less (but with isolation at higher frequencies than predicted because of the stiffer foundation) and with more pronounced undulations from pressure-wave effects. At frequencies below about 40Hz, the torsion-only

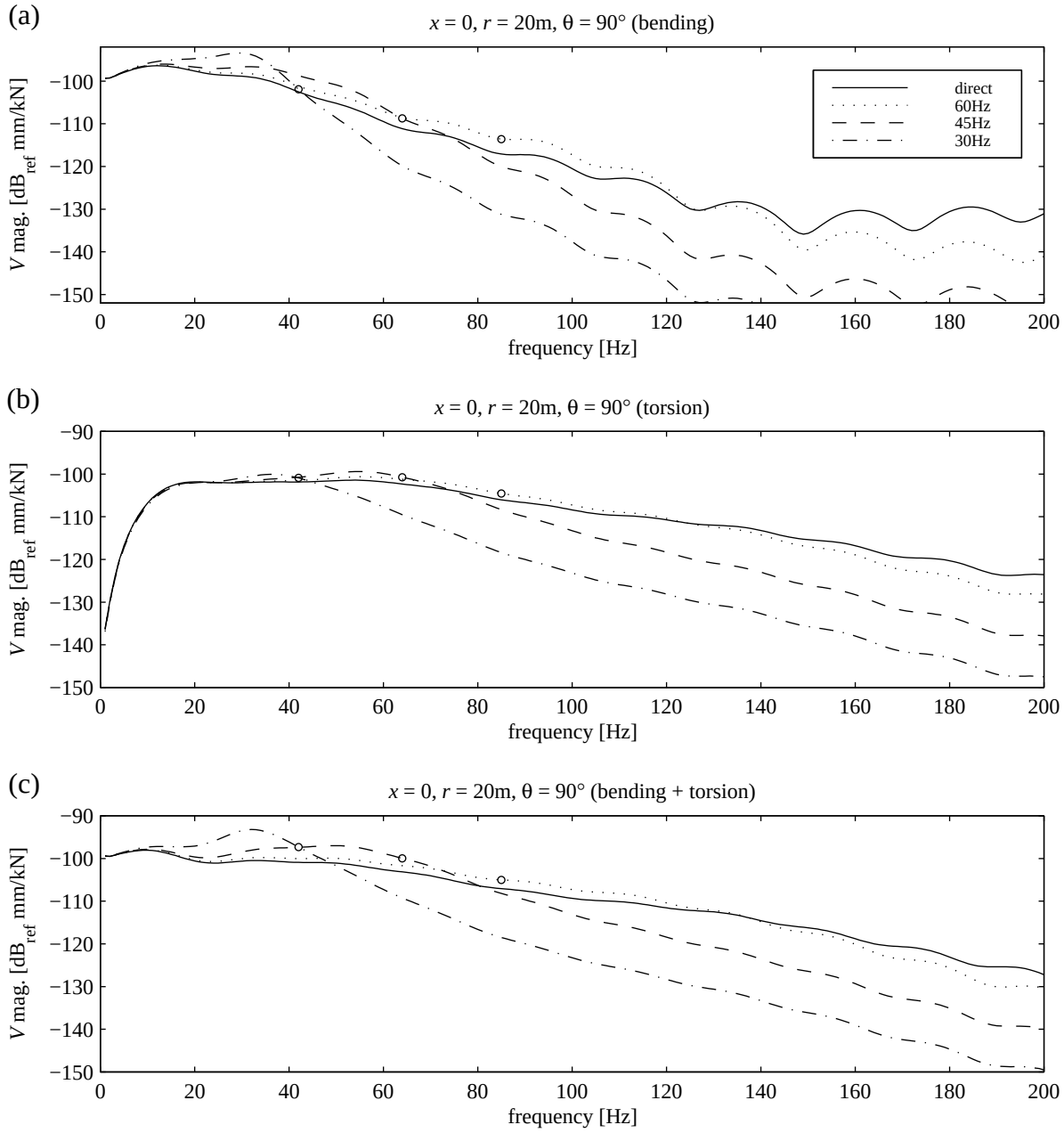

Figure 5.21: Vertical soil displacement response with a torsional slab beam, 20m horizontally out into the soil opposite applied loads of (a) $F_1 = 0.5$, $F_2 = 0.5$ (b) $F_1 = 0.5, F_2 = -0.5$ and (c) $F_1 = 1$, $F_2 = 0$. Slab-support stiffnesses giving various natural frequencies as indicated. Circles mark the $\sqrt{2}\, f_n$ points.

response of Figure 5.21(b) is less than the bending-only one, but above 40Hz its magnitude becomes comparable or greater than the bending-only magnitude, so that the torsion effects predominate above 40Hz in the combined response of Figure 5.21(c). The very low level of the torsional response below 10Hz can be attributed to cancellation of the two lines of input 3 and 4 on the tunnel invert. The *V* component of soil displacement at $r = 20$m and $\theta = 90^\circ$ is largely dependent on the propagation of shear waves, while the two lines 3 and 4 are producing out-of-

phase vertical shear motion when the slab is in pure torsion. At low frequencies the separation of these two lines is small compared to the shear wavelength, and so can be construed as a single source; but they are out of phase, so the "single source" is effectively motionless. At higher frequencies the separation is great enough that cancellation does not occur at source. It is interesting to observe that the torsional response shows little influence from pressure-wave interference, so that the combined response of Figure 5.21(c) is much less undulating than the bending response, and hence actually more like Figure 5.10 for the simple slab than Figure 5.21(a) is. This raises the question of whether it is necessary to include torsional effects at all, beyond the effects that different slab-mounting arrangements have on support stiffness.

Figure 5.22 gives the vertical displacement at a longitudinal position of $x = 20\text{m}$. This time the torsional response, Figure 5.22(b), is again of significant magnitude, but of very different shape to the bending-only response in Figure 5.22(a), with addition of rubber bearings *increasing* the response above the $\sqrt{2}\, f_n$ points and *reducing* it below. The bending-only response is very like that for the simple slab in Figure 5.11 (although there is some more undulation at the high-frequency end and the trough at 45Hz is deeper), with slab bearings making little difference except for the $f_n = 30\text{Hz}$ case, which gives a modest reduction. However, the combined response, Figure 5.22(c), is not very like Figure 5.11 at all, the torsional component resulting in slab bearings giving generally larger vertical soil displacements. This demonstrates that the effects of slab torsion *are* significant for some observation points in the soil.

The longitudinal soil displacement at $x = 20\text{m}$ is given in Figure 5.23 (as explained for the simple-slab case, longitudinal displacement at $x = 0$ is zero because *U* is an odd function of *x*). All three types of motion are very similar to the horizontal motion for the same position (see Figure 5.20), because both longitudinal and horizontal motion here are largely due to the propagation of pressure waves from the tunnel. The bending-only response, Figure 5.20(a), resembles the simple-slab case of Figure 5.9, with slab bearings having little effect below 100Hz. The effect of slab torsion is not very great – the combined response of Figure 5.20(c) is quite similar to the bending-only one, with an adverse effect over the whole frequency range with the $f_n = 60\text{Hz}$ bearings. This illustrates the recurring theme that a beneficial effect is only achieved with the softest slab bearings, if it is possible at all.

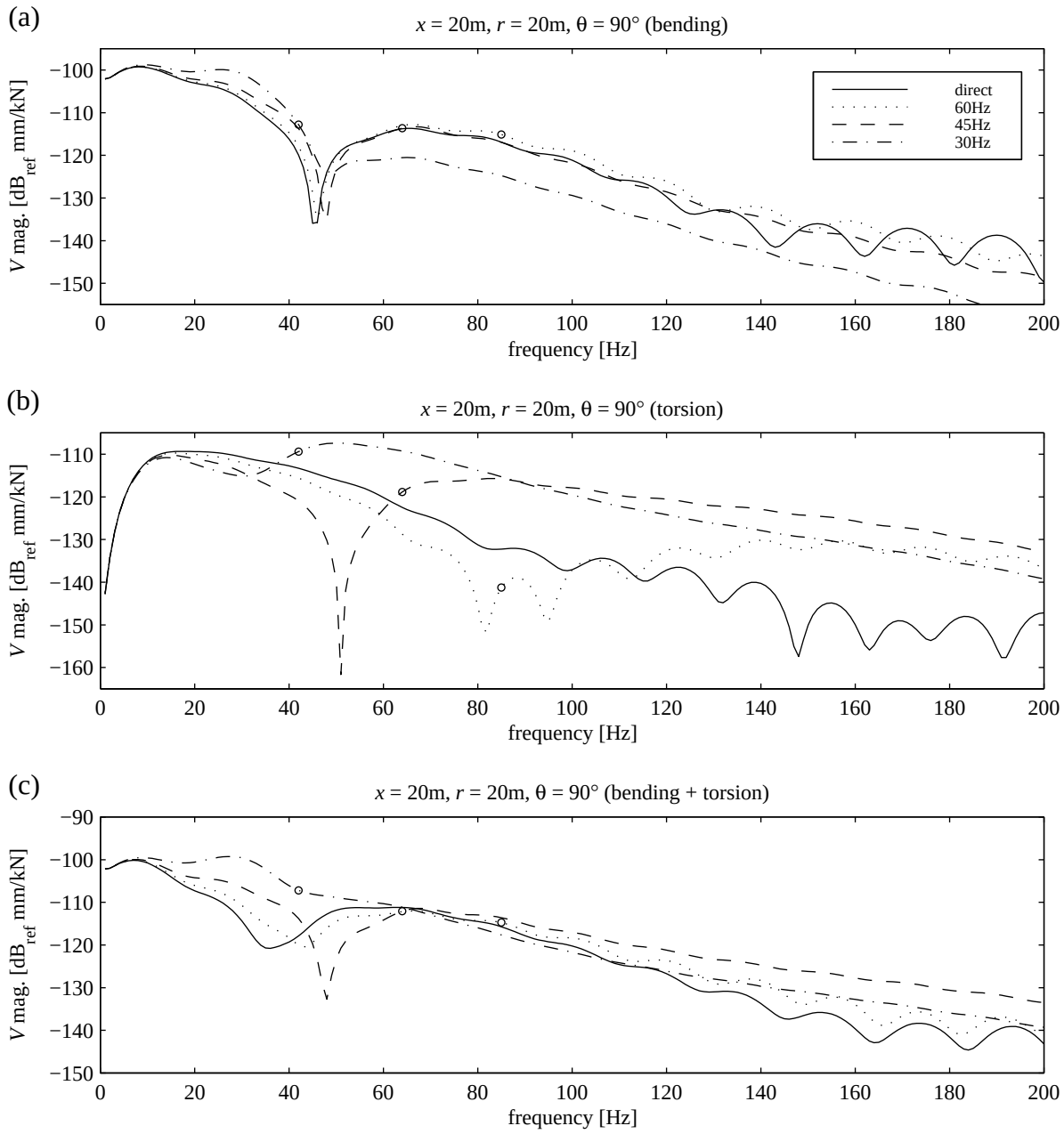

Figure 5.22: Vertical soil displacement response with a torsional slab beam, 20m horizontally out into the soil and 20m longitudinally parallel to the tunnel from applied loads of (a) $F_1 = 0.5$, $F_2 = 0.5$ (b) $F_1 = 0.5, F_2 = -0.5$ and (c) $F_1 = 1$, $F_2 = 0$. Slab-support stiffnesses giving various natural frequencies as indicated. Circles mark the $\sqrt{2}\, f_n$ points.

All the responses discussed above are for one pair of loads applied to the track slab. As for the simple slab, the responses at different longitudinal positions are of comparable magnitude, so it is difficult to estimate the exact effect of adding up these responses to give the response to a train which provides many simultaneous inputs. It is not simple to predict the effect of torsional motion of the slab on the vibration levels in the soil: sometimes it is not very significant, so that the response to combined bending and torsion is approximately the same as to bending alone;

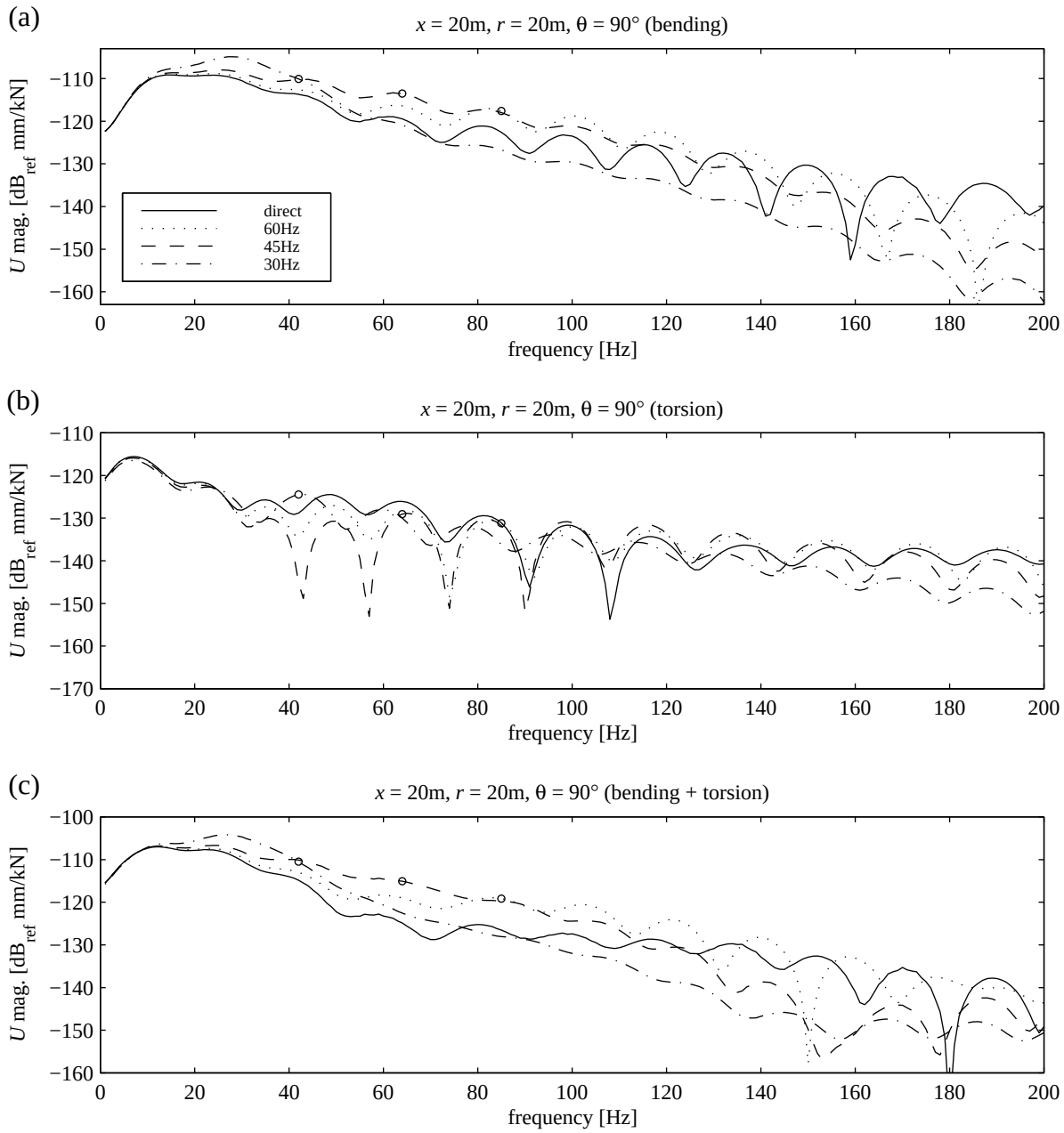

Figure 5.23: Longitudinal soil displacement response with a torsional slab beam, 20m horizontally out into the soil and 20m longitudinally parallel to the tunnel from applied loads of (a) $F_1 = 0.5$, $F_2 = 0.5$ (b) $F_1 = 0.5, F_2 = -0.5$ and (c) $F_1 = 1$, $F_2 = 0$. Slab-support stiffnesses giving various natural frequencies as indicated. Circles mark the $\sqrt{2}\, f_n$ points.

sometimes it affects the combined response very significantly, to the extent that it makes the insertion of slab bearings unfavourable, when soft bearings would seem to have some benefit if only slab bending was considered.

5.3 A Full Track with Axle Masses

As well as the effects of the track slab, a track model should take the dynamics of the rail and the train interacting with it into account. An improved track model is depicted in Figure 5.24. It consists of a simple slab beam supporting a rail beam (representing the two rails together) with masses placed at intervals to represent the axle-wheel assemblies of a train. The slab and rail beams are infinitely long. The form is similar to the track models described in Chapter 3, with resilient layers to model the slab bearings and rail pads, but now the foundation of the track is a tunnel instead of a rigid base. The axle masses are a first-approximation train model which only considers the unsprung mass of the train, assuming that the primary suspension isolates the rest of each vehicle in the train. Real train vehicles have pairs of axles attached to bogies, which also contribute to the low-frequency interaction with the rail (below and around the primary suspension's natural frequency, that is, below about 20Hz). However, the important frequencies for ground-borne vibration from underground railways are well above this region (for example, Cryer [38] gives acceleration spectra of a pile cap due to the passage of London Underground trains, showing most activity between 40Hz and 100Hz). Therefore the bogie dynamics are not significant for the current problem. Also neglected is a Hertzian contact spring between each wheel and the rail, because this only plays a role at frequencies higher than those of interest (for

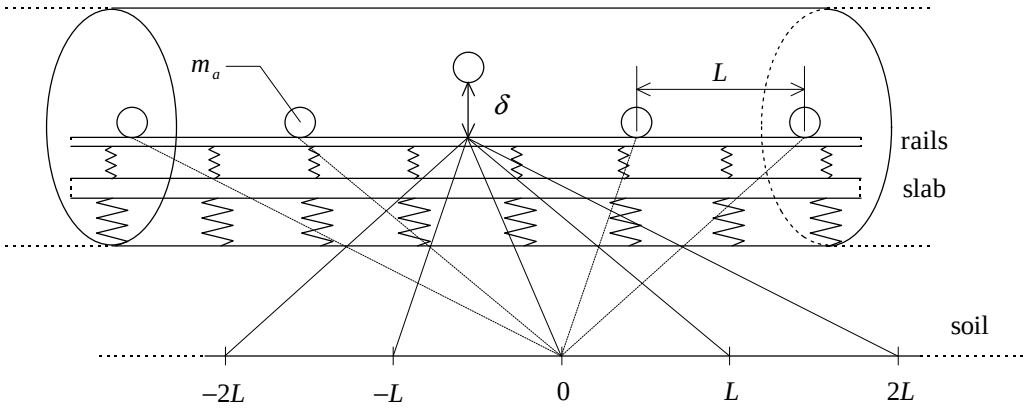

Figure 5.24: Full track model supported on the tunnel invert, with masses added to represent axles of a train. The centre mass is excited by a roughness displacement input δ. The tunnel's infinite length means the responses at one point in the soil to each axle input (paths with dashed lines) are equivalent to the line of separate responses to the single input shown (paths with solid lines) for an infinite number of masses at regular spacing.

example, Clark et al [35] conclude that the Hertzian contact does not have a significant effect on rail response below 750Hz).

The aim is to find the response at a single representative point in the soil when there is a series of input loads along the rails due to a train running on the track. For just one input load, the infinite length of the tunnel means that the load and the observation point can be *shifted* longitudinally while maintaining their separation, and the response at the observation point will not change. In other words, the response in the soil at $x = 0$ to a load on the rail at $x = L$ is always identical to the response at $x = -L$ to the same load at $x = 0$. (For tangential and radial soil-response components, which are even functions of *x*, it is also identical to the response at $x = L$ to the load at $x = 0$, so that only the magnitude of the separation matters.) Hence, the problem of finding the set of FRFs for the soil response at $x = 0$ to a set of loads at various positions on the rail can be recast into the problem of finding the FRFs for the soil at those various longitudinal positions to a single load at $x = 0$. The shifting principle for a tunnel and track model with axle masses is depicted in Figure 5.24. Note that in this case it only works for an infinite number of axle masses at regular spacing, so that the overall model remains infinite and the longitudinal symmetry is maintained with any amount of shifting. Nevertheless, when the shifting principle is invoked so that only an input at the middle axle ($x = 0$) is used, a finite number of axles is sufficient if there are enough of them that the responses of the model do not change with more axles added at the ends, that is, a convergence has been reached.

The total soil response due to all the axle loads acting simultaneously can be calculated by adding up all the FRFs for an input at $x = 0$, after scaling and phasing each one appropriately. If the train is infinitely long and the inputs random, the sum represents the response anywhere along the soil line and thus condenses the three-dimensional problem represented by the individual FRFs to a two-dimensional problem of the vibration level at a particular point in the cross-section of the tunnel and soil.

5.3.1 Joining a Rail Beam to the Slab-Plus-Tunnel Model

The easiest way to construct the basic track model is to add a rail beam to the combined slab-plus-tunnel model of Section 5.1, using the principle of convolution in space. Although the

repeating-unit method of Chapter 3 could be used to construct a track model complete with axle masses (but minus slab bearings), there is the difficulty of obtaining the displacement function for the whole structure between unit junctions. In addition, the displacement function would have to be transformed into the wavenumber domain in order to join the track to the tunnel via the slab-supporting stiffness. Since this function would not be a simple analytical expression, the transformation would have to be done numerically by FFT with its attendant condition of sufficient decay of the function (see Section 4.3.3), which is unlikely to be met for a free double-beam track model without excessive internal material damping.

To join the rail beam to the model, therefore, the coupling equations (5.8) are applied to the rail beam and slab-plus-tunnel as the two entities being joined. To avoid confusion with the numerals already used in Section 5.1 to denote the lines along the slab (1), the tunnel invert (2) and the soil (3), the line along the rail beam will be denoted by 0 (zero). Thus the vertical rail and slab responses $\tilde{\tilde{Y}}_{0a}$ and $\tilde{\tilde{Y}}_{1a}$ of the new combined system to a vertical unit spatial point load acting on the rail beam at $x = 0$ are

$$\begin{aligned} \tilde{\tilde{Y}}_{0a} &= \frac{\tilde{H}_{00a}(1 + k_r \tilde{H}_{11a})}{1 + k_r \tilde{H}_{00a} + k_r \tilde{H}_{11a}} \\ \tilde{\tilde{Y}}_{1a} &= \frac{k_r \tilde{H}_{00a} \tilde{H}_{11a}}{1 + k_r \tilde{H}_{00a} + k_r \tilde{H}_{11a}} \end{aligned} \tag{5.30}$$

where $\tilde{H}_{00a}$ is the ξ-domain FRF for the unjoined rail beam, $\tilde{H}_{11a}$ is the ξ-domain FRF of the slab beam to a load on the slab before the rail is added, and k_r is the stiffness per unit length of the resilient layer between the rail and slab beams. In the same way as (5.9), responses along lines not involved in the joining can be determined by means of the coupling interaction force. In this case the interaction force acts on the slab beam and is given by the slab's response in the new combined model divided by it's pre-rail-beam FRF, that is, $\tilde{\tilde{Y}}_{1a} / \tilde{H}_{11a}$. Hence the responses $\tilde{\tilde{Y}}_{2a}$ along the tunnel invert and $\tilde{\tilde{Y}}_{3a}$ in the soil are

$$\begin{aligned} \tilde{\tilde{Y}}_{2a} &= \tilde{H}_{21a} \frac{\tilde{\tilde{Y}}_{1a}}{\tilde{H}_{11a}} \\ \tilde{\tilde{Y}}_{3a} &= \tilde{H}_{31a} \frac{\tilde{\tilde{Y}}_{1a}}{\tilde{H}_{11a}} \end{aligned} \tag{5.31}$$

where $\tilde{H}_{21a}$ and $\tilde{H}_{31a}$ are the ξ-domain FRFs of the tunnel invert and the soil to a load on the pre-rail-beam slab. The physical displacement functions in the *x*-domain can be obtained by the inverse Fourier transform of the results (5.30) and (5.31) according to (5.2).

The FRFs of the slab, tunnel and soil displacements which appear in equations (5.30) and (5.31) are just the displacements determined by (5.8) and (5.9) for the slab-plus-tunnel model. The FRF for the rail beam is that given by (5.13) for a free beam, but now with the properties of the two rails instead of the slab. Thus

$$\begin{aligned} \tilde{H}_{00a} &= \tilde{H}_{YF} \\ \tilde{H}_{11a} &= \tilde{Y}_1 \\ \tilde{H}_{21a} &= \tilde{Y}_2 \\ \tilde{H}_{31a} &= \tilde{Y}_3 \end{aligned} \tag{5.32}$$

5.3.2 Adding Axle Masses to the Rail Beam

Adding axle masses to the model constructed so far is most simply done in the space domain. Since the axles interact with the rail, the coupled rail's *x*-domain FRF $H_0(x)$ is required. This can be obtained by the inverse Fourier transform of the ξ-domain result from (5.30), that is,

$$H_0(x) = \frac{1}{2\pi}\int_{-\infty}^{\infty} \tilde{Y}_{0a}(\xi) e^{i\xi x} d\xi \tag{5.33}$$

which represents the FRF of the rail to a point load acting at $x = 0$ on the rail, at a particular frequency ω. To find the final response in the soil, the soil's *x*-domain FRF $H_3(x)$ to the same load on the rail is required. This latter FRF is obtained in the same way as $H_0(x)$, but from the result (5.31), so that

$$H_3(x) = \frac{1}{2\pi}\int_{-\infty}^{\infty} \tilde{Y}_{3a}(\xi) e^{i\xi x} d\xi \tag{5.34}$$

where $\tilde{Y}_{3a}(\xi)$ can be the *u*, *v*, or *w* component of soil displacement.

As the first step in the addition of axle masses, the rail responses at the positions where the masses are to be added must be formed into an FRF matrix $[\mathbf{H}_0]$ which satisfies

$$\mathbf{Y}_0 = [\mathbf{H}_0]\mathbf{F}_0 \tag{5.35}$$

where $\mathbf{Y}_0$ is the vector of rail displacements at the stations where masses will be added, and $\mathbf{F}_0$ is the vector of forces acting at those positions on the rail (once masses are added, these will be

the interaction forces between the masses and the rail). Keeping this in mind, it is interesting to note that (5.35) is exactly analogous to the convolutions in space presented earlier. While convolution was used to find the *function* of responses along a line to a *continuous* interaction force acting along that line, the matrix multiplication here is used to find the *vector* of responses along a line to a set of *discrete* interaction forces acting on the line. The elements of the matrix $[\mathbf{H}_0]$ are determined by the rail-displacement FRF $H_0(x)$ of (5.33) as described below.

The case of adding only five masses will be considered here as an example of the general approach. It can easily be extended to more added masses to give the convergence necessary to model an infinitely long train. The infinite length and the symmetry of the track and tunnel mean that a given rail FRF is only dependent on the magnitude of the separation between the displacement and load involved, as discussed above in the context of soil displacements. Thus the rail FRF matrix is

$$[\mathbf{H}_0] = \begin{bmatrix} H_0(0) & H_0(L_1) & H_0(L_1+L_2) & H_0(L_1+L_2+L_3) & H_0(L_1+L_2+L_3+L_4) \\ H_0(L_1) & H_0(0) & H_0(L_2) & H_0(L_2+L_3) & H_0(L_2+L_3+L_4) \\ H_0(L_1+L_2) & H_0(L_2) & H_0(0) & H_0(L_3) & H_0(L_3+L_4) \\ H_0(L_1+L_2+L_3) & H_0(L_2+L_3) & H_0(L_3) & H_0(0) & H_0(L_4) \\ H_0(L_1+L_2+L_3+L_4) & H_0(L_2+L_3+L_4) & H_0(L_3+L_4) & H_0(L_4) & H_0(0) \end{bmatrix} \tag{5.36}$$

where L_1, L_2, L_3 and L_4 are the consecutive spacings between the five points where axles will be added. If the spacing is regular so that $L_1 = L_2 = L_3 = L_4 = L$, (5.36) can be simplified to

$$[\mathbf{H}_0] = \begin{bmatrix} H_0(0) & H_0(L) & H_0(2L) & H_0(3L) & H_0(4L) \\ H_0(L) & H_0(0) & H_0(L) & H_0(2L) & H_0(3L) \\ H_0(2L) & H_0(L) & H_0(0) & H_0(L) & H_0(2L) \\ H_0(3L) & H_0(2L) & H_0(L) & H_0(0) & H_0(L) \\ H_0(4L) & H_0(3L) & H_0(2L) & H_0(L) & H_0(0) \end{bmatrix} \tag{5.37}$$

To facilitate the process of adding axles, the FRF matrix $[\mathbf{H}_0]$ of (5.36) or (5.37) should be inverted, allowing the dynamic-stiffness matrix (DSM) expression

$$\mathbf{F}_0 = [\mathbf{H}_0]^{-1}\mathbf{Y}_0 = [\mathbf{K}_0]\mathbf{Y}_0 \tag{5.38}$$

to be written. Axles are then added to the model as concentrated masses m_a by adding inertia terms of the form $-m_a\omega^2 Y$, where Y is the displacement at the axle's station, to the appropriate diagonal elements of the DSM $[\mathbf{K}_0]$, leaving the centre station free. In the same way as in Section 3.3.2, an axle mass is added to this centre station via a roughness displacement $\delta = \Delta e^{i\omega t}$, as shown in Figure 5.24. The overall matrix equation then becomes

$$\begin{bmatrix} k_{11}-m_a\omega^2 & k_{12} & k_{13} & k_{14} & k_{15} & 0 \\ k_{21} & k_{22}-m_a\omega^2 & k_{23} & k_{24} & k_{25} & 0 \\ k_{31} & k_{32} & k_{33} & k_{34} & k_{35} & -m_a\omega^2 \\ k_{41} & k_{42} & k_{43} & k_{44}-m_a\omega^2 & k_{45} & 0 \\ k_{51} & k_{52} & k_{53} & k_{54} & k_{55}-m_a\omega^2 & 0 \\ 0 & 0 & -1 & 0 & 0 & 1 \end{bmatrix} \begin{Bmatrix} Y_1 \\ Y_2 \\ Y_3 \\ Y_4 \\ Y_5 \\ Y_a \end{Bmatrix} = \begin{Bmatrix} 0 \\ 0 \\ 0 \\ 0 \\ 0 \\ \Delta \end{Bmatrix} \tag{5.39}$$

where the k_{ij} are the elements of $[\mathbf{K}_0]$. Equation (5.39) is of order one greater than the original DSM because of the extra displacement component Y_a introduced by the independent axle mass at the centre. As mentioned earlier, if a model with an input at the middle, such as (5.39), is to be used in conjunction with the shifting principle to calculate the responses to several different inputs, the axle spacing must be regular.

After the displacements of the rail at the axle masses have been calculated from (5.39), the corresponding interaction forces $\mathbf{F}_0$ acting on the rail at the mass stations can be determined by substituting the vector of displacements $\mathbf{Y}_0 = \{Y_1 \quad Y_2 \quad Y_3 \quad Y_4 \quad Y_5\}^{\mathrm{T}}$ (that is, omitting Y_a) back into (5.38). Knowing the interaction forces which act on the rail, the soil displacements $\mathbf{Y}_3$ can be found from the FRF function $H_3(x)$ given by (5.34). In matrix form this can be expressed as

$$\mathbf{Y}_3 = [\mathbf{H}_3]\mathbf{F}_0 \tag{5.40}$$

where $[\mathbf{H}_3]$ is the FRF matrix for the soil line to input forces acting on the rail (with no axle masses added). For the tangential and radial components of soil displacement, *V* and *W*, $[\mathbf{H}_3]$ is of the same form as $[\mathbf{H}_0]$ given by (5.36) or, for constant axle spacing, (5.37), but with $H_3(x)$ replacing $H_0(x)$. This is because these components are *even* functions of *x* for a vertical load applied at $x = 0$, just like the vertical displacements of the rail. However, the longitudinal component *U* is an *odd* function of *x* for such a load, so that the sign of the longitudinal separation between a given load and displacement is important. The soil FRF matrix is then

$$[\mathbf{H}_3{}^{u}] = \begin{bmatrix} H_3{}^{u}(0) & -H_3{}^{u}(L_1) & -H_3{}^{u}(L_1+L_2) & -H_3{}^{u}(L_1+L_2+L_3) & -H_3{}^{u}(L_1+L_2+L_3+L_4) \\ H_3{}^{u}(L_1) & H_3{}^{u}(0) & -H_3{}^{u}(L_2) & -H_3{}^{u}(L_2+L_3) & -H_3{}^{u}(L_2+L_3+L_4) \\ H_3{}^{u}(L_1+L_2) & H_3{}^{u}(L_2) & H_3{}^{u}(0) & -H_3{}^{u}(L_3) & -H_3{}^{u}(L_3+L_4) \\ H_3{}^{u}(L_1+L_2+L_3) & H_3{}^{u}(L_2+L_3) & H_3{}^{u}(L_3) & H_3{}^{u}(0) & -H_3{}^{u}(L_4) \\ H_3{}^{u}(L_1+L_2+L_3+L_4) & H_3{}^{u}(L_2+L_3+L_4) & H_3{}^{u}(L_3+L_4) & H_3{}^{u}(L_4) & H_3{}^{u}(0) \end{bmatrix} \tag{5.41}$$

where similar simplifications of the kind exhibited in going from (5.36) to (5.37) can be made if the spacing between axles is a constant value *L*.

5.3.3 Random Process Theory Applied to the Full-Track Model

The roughness and other irregularities of real rail and wheel surface profiles will be randomly distributed, so the roughness-displacement inputs at the wheels of a train travelling on the track will be random processes. The calculation of the resultant soil responses therefore requires the use of the theory of random vibration, which is dealt with by Newland [144], whose approach will be used here.

A random process is stationary if its mean, mean square and standard deviation are independent of time. Consider a system with *N* stationary random inputs x_j (such as the axle inputs provided by a train) and one (stationary random) output *y* (such as the displacement response of a particular point in the soil). The power-spectral density (PSD), or spectrum, $S_y(\omega)$ of the output process *y* is then given by

$$S_y(\omega) = \sum_{p=1}^{N}\sum_{q=1}^{N} H_p{}^*(\omega)H_r(\omega)S_{x_p x_q}(\omega) \tag{5.42}$$

where $H_p(\omega)$ and $H_q(\omega)$ are the FRFs of *y* to the inputs x_p and x_q respectively (with star denoting the complex conjugate), and $S_{x_p x_q}(\omega)$ is the cross-spectral density, or cross-spectrum, between the two inputs. If two input processes have the same statistical properties, that is, have the same spectrum $S_0(\omega)$, but one lags the other such that $x_2(t) = x_1(t-T)$, then the cross-spectra are given by

$$\begin{aligned} S_{x_1 x_2}(\omega) &= S_0(\omega)e^{-i\omega T} \\ S_{x_2 x_1}(\omega) &= S_0(\omega)e^{i\omega T} \end{aligned} \tag{5.43}$$

which also satisfies the general relationship that $S_{x_2 x_1}(\omega)$ is always the complex conjugate of $S_{x_1 x_2}(\omega)$. Equation (5.43) can readily be shown to be true by considering the cross-correlation $R_{x_1 x_2}(\tau) = \int_{-\infty}^{\infty} x_1(t)x_2(t-\tau)dt$, the Fourier transform of which (including a factor of $1/2\pi$) gives the cross-spectrum $S_{x_1 x_2}(\omega)$.

If the train's wheels are assumed to be perfectly smooth, so that all irregularities are contained in the rail surface, the axle inputs can be assumed to differ by a time delay only, giving cross-spectra between inputs of the type in (5.43). The time delay between two adjacent axles is $T = L/v$, where *L* is the axle spacing (assumed to be constant) and *v* is the train's speed. If the axles are not adjacent, this time delay is multiplied by the integer difference $(q-p)$ between the

indices of the two axles concerned. Thus the general formula (5.42) for the output spectrum can be written

$$S_y(\omega) = \sum_{p=1}^{N}\sum_{q=1}^{N} H_p^{\,*}(\omega)H_q(\omega).S_0(\omega).e^{-i\omega(q-p)L/v} \tag{5.44}$$

assuming that an axle with a higher index is further to the back of the train.

The FRFs $H_p(\omega)$ and $H_q(\omega)$ in (5.44) can be obtained from the appropriate elements of the soil-response vector $\mathbf{Y}_3$ in (5.40) – which is for an input at the centre axle mass only – by means of the shifting principle. The model should, of course, then include *N* axle masses instead of just five, and *N* should be sufficiently large for convergence of the soil responses so that the shifting principle is valid. Strictly, because of the way the FRFs are derived and because the time delays between axles are taken as all the same, the result (5.44) gives the statistical response of a point which moves longitudinally through the soil at the train speed and so stays opposite the axle mass placed at $x = 0$; but it is the vibration level at a stationary observation point next to the tunnel which is of interest. The response of a stationary point will be influenced by Doppler effects, because the wheels at the front of the train and ahead of the point will be moving away from it, while those at the rear of the train and behind the point will be moving towards it, altering the effective time delays. However, Doppler effects are not very significant in this case, because the train speeds (below $30\,\mathrm{m/s}$) are much less than the speeds of pressure and shear waves in the soil ($944\,\mathrm{m/s}$ and $309\,\mathrm{m/s}$ respectively for the soil parameters given in Table 4.3), so can be ignored. A further consideration despite this is whether the total response varies much with the actual longitudinal position of the observation point, next to an axle or somewhere between two axles. In the soil around an actual underground railway system, a hypothetical observer close to the tunnel will "hear" individual axles as they pass, whereas an observer further away will only detect a continuous "rumble" as the train goes by. Thus if the observation point is at a distance from the tunnel larger than the axle spacing, the point's relative longitudinal position should not have much bearing on the total vibration response perceived. Given these two considerations, the result (5.44) provides a reasonable estimate of the vibration spectrum at a *stationary* observation point in the soil.

The actual input between wheel and rail is a roughness displacement δ which varies along the rail. The spectrum for this would normally be given as a function of wavenumber γ (with units of radians per unit length). The roughness spectrum as a function of frequency depends on the speed v of a vehicle traversing the rough surface, and is given by

$$S_\delta(\omega) = \frac{1}{v} S_\delta\left(\gamma = \frac{\omega}{v}\right) \tag{5.45}$$

An important property of the spectrum of a random process $y(t)$ is that integrating it over all frequencies ω gives the expected value of y^2, or mean-square (MS) value of the process, that is

$$\text{MS} = \text{E}[y^2] = \int_{-\infty}^{\infty} S_y(\omega) d\omega \tag{5.46}$$

The widely used root-mean-square (RMS) value of the process is obtained by taking the square root of the MS value (5.46).

The spectra discussed above are all even (symmetric) functions of angular frequency (or wavenumber), defined for frequencies from $-\infty$ to $+\infty$. However, practical spectra are usually single-sided functions defined for positive frequencies only, with the frequencies themselves in cycles (rather than radians) per unit time (or per unit length). If such single-sided spectra are used, they must still give the MS value when integrated over all frequencies for which they are defined, that is, over 0 to $+\infty$ with a frequency f instead of the angular frequency ω in (5.46). Thus a factor of 2 arises from their being single-sided and a factor of 2π from the change to cyclical frequency, giving the single-sided spectrum $S_y(f)$ as

$$S_y(f) = 4\pi S_y(\omega = 2\pi) \tag{5.47}$$

and similarly for a single-sided spectrum $S_\delta(1/\lambda)$ of roughness

$$S_\delta\left(\frac{1}{\lambda}\right) = 4\pi S_\delta\left(\gamma = \frac{2\pi}{\lambda}\right) \tag{5.48}$$

where λ is wavelength. All the relationships given for double-sided spectra still hold if *all* of them are replaced by the equivalent single-sided spectra.

Note also that the units of a spectrum are $(\text{units of } y)^2/(\text{units of frequency})$, so it is often more convenient to plot graphs of root spectrum with units of $(\text{units of } y)/\sqrt{\text{units of frequency}}$, to reduce the range of values of the spectrum. The results from the full-track model will be plotted as root spectra.

5.3.4 Results for the Tunnel with a Full Track Model

As for the two previous track models, the tunnel and soil FRFs were calculated as described in Chapter 4, using the parameters in Table 4.3. The parameter values for the full track are given in Table 5.3. The slab properties used are the same as those for the simple-slab model given in Table 5.1, including the three different slab-support stiffnesses and loss factor. The beam representing the two rails has the same sectional properties as those given in Table 3.1, but the railpad stiffness has a higher, more realistic value giving a resonance of the rail on the rail pads of 318Hz (instead of 100Hz as in Chapter 3), which is above the 200Hz maximum frequency considered here. Results were calculated in Matlab, with the inverse Fourier transforms computed by inverse FFT using 2048 points with a sampling interval of $\Delta x = 0.5\text{m}$, as for previous results. This gives a maximum x-value of 512m, so the maximum longitudinal separation which can be used with the shifting principle to create the FRF matrices such as (5.37) is also 512m; all the axle masses must therefore fit within this distance. With a regular spacing of $L = 20\text{m}$, the maximum odd number of axles (odd to retain symmetry about $x = 0$) which can be added is thus $N = 25$. This number of axles gave converged soil responses for a roughness input at the $x = 0$ axle mass.

Slab Beam	Rail Beam	Axle Masses
$EI = 1430 \times 10^6\ \text{Pa.m}^4$ $m = 3500\,\text{kg/m}$ $k = 1262 \times 10^6\ \text{N/m}^2$ (60 Hz) $k = 424.4 \times 10^6\ \text{N/m}^2$ (45 Hz) $k = 146.6 \times 10^6\ \text{N/m}^2$ (30 Hz) $\eta_k = 0.5$	$EI_r = 10 \times 10^6\ \text{Pa.m}^4$ $m_r = 100\,\text{kg/m}$ $k_r = 400 \times 10^6\ \text{N/m}^2$ $\eta_{k_r} = 0.3$	$m_a = 500\,\text{kg}$ $N = 25$ $L = 20\,\text{m}$

Table 5.3: Parameter values for the various parts of the full track. The three different slab-support stiffnesses are the same as those given in Table 5.1 for the simple slab.

Due to the cylindrical geometry of the tunnel-in-soil model, the displacement is expressed as longitudinal, tangential and radial components *U*, *V* and *W* (see Figure 4.1). However, horizontal and vertical components are more meaningful when considering inputs to building foundations, so an absolute coordinate system *XYZ* needs to be defined. The longitudinal direction *X*

coincides with the longitudinal *x*-axis of the tunnel, the horizontal direction *Y* with the $\theta = 90^\circ$ radius, and the vertical direction *Z* with the $\theta = 180^\circ$ radius. Thus the relationships of the new longitudinal, horizontal and vertical displacement components U_X, U_Y and U_Z to the original components *U*, *V* and *W* are

$$\begin{aligned} U_X &= U \\ U_Y &= V\cos\theta - W\sin\theta \\ U_Z &= V\sin\theta + W\cos\theta \end{aligned} \tag{5.49}$$

The FRFs can be calculated for the *U*, *V* and *W* components of soil displacement, then resolved according to (5.49) before being used in the PSD equation (5.44).

A useful way to evaluate the effect of floating the track slab is to take the ratio of the soil responses with and without resilient bearings inserted between the slab and tunnel invert. A common measure of this ratio is the "Insertion Loss" in dB, which gives the amount of *reduction* in vibration provided by the bearings, so Insertion Losses greater than zero indicate vibration isolation. However, this notion is opposite to all the results presented so far, where a higher (absolute) response is worse. To maintain consistency, the concept of "Insertion Gain" in dB, indicating the *increase* in vibration levels caused by the bearings (hence the negative of Insertion Loss), will be used here; it is increasingly being used in industry (see Greer and Manning [77] for example). The definition of Insertion Gain for the current results is

$$\text{Insertion Gain [dB]} \;=\; 20\log_{10}\sqrt{\frac{S_j\big|_{f_n}}{S_j\big|_{direct}}}, \qquad j = X, Y \text{ or } Z \tag{5.50}$$

that is, the ratio of the soil-displacement root spectrum for a slab "natural frequency" of f_n to the root spectrum for a model with a directly joined slab. Insertion Gains less than zero indicate vibration isolation.

The computation procedure for calculating the PSDs of soil displacement for the full-track model can be summarised as follows:

1. Join the slab beam to the tunnel by (5.6) or (5.8) for each slab-support stiffness *k*, join the rail beam to the slab by (5.30), and obtain the rail FRF (5.33) by inverse FFT;
2. Obtain the rail DSM via the FRF matrix (5.37), add axle masses according to (5.39), and use the resulting displacement vector to calculate the rail interaction forces from (5.38);

3. For each radius *r* and angular position θ in the soil,
   (i) Calculate the soil FRFs for the uncoupled tunnel by summing the appropriate modes for *n* from 1 to 10 according to (5.10);
   (ii) Add the effect of the slab beam by (5.9) and that of the rail beam by (5.31), then obtain the soil FRF (5.34) for a tunnel with a floating-slab track by inverse FFT;
   (iii) Form the soil FRF matrix and obtain the soil displacement vector from (5.40) and the interaction forces calculated above;
   (iv) Calculate the soil PSDs for this position from (5.44) for each train speed *v* required.

The PSDs for different slab-support stiffnesses can then be used to calculate Insertion Gains from (5.50) or RMS levels via the MS (5.46).

Computation time can be reduced by the use of symmetry. The longitudinal symmetry means that ξ-domain displacements need only be calculated at the 1025 points with $\xi \geq 0$, with the rest of the sample being created by a suitable reflection just prior to the inverse FFT; and symmetry about the vertical centreline of the tunnel cross-section means that only soil positions within the range $0 \leq \theta \leq 180^\circ$ need to be considered. Computation speed in the Matlab environment can be increased by maximising the use of matrix or array operations (vectorised code) in place of looping procedures where possible. Even so, program execution can be severely slowed by large memory requirements. Each ξ-domain tunnel or soil mode was represented as an array of 1025 space points by 200 frequency points for a given radius *r* and modenumber *n*, filling 3.1MB (16 bytes per double-precision complex number); thus the eleven modes for *one* displacement component at *one* radius fill 34.4MB. All 132 soil modes, required in step 3(i) at various stages to calculate the PSDs for all three displacement components at four radii, therefore did not physically fit within the 256MB of memory of the Unix workstation used, even leaving aside the memory needed by the operating system and Matlab for itself and intermediate calculations. This necessitated heavy use of time-consuming swapping between memory and the hard disk. Leaving this swapping largely to Matlab and the operating system resulted in a program still running after three days. Thus the program was rewritten to explicitly load only one set of eleven modes from the hard disk at a time, which still involved the same set being loaded and unloaded many times, but gave a full set of PSDs after 18 hours of computation.

Spectra were computed for a "white" (uniform) input roughness spectrum of $S_0 = 1\,\text{mm}^2/\text{Hz}$ in (5.44). This gives equal weighting to all frequencies. Although a uniform roughness spectrum is unrealistic, it does show the fundamental transmission behaviour of the track-tunnel-soil system. It is clear from (5.44) that the output PSD for a non-uniform input is obtained simply by multiplying the uniform result by the actual input $S_0(\omega)$, which is independent of the summation. This also means that the Insertion Gain (5.50) is independent of the details of input, as $S_0(\omega)$ will cancel in the ratio of the two output spectra.

Figures 5.25, 5.26 and 5.27 give contour plots of the longitudinal, horizontal and vertical PSDs respectively, at a radius of 20m and a train speed of $40\,\text{km/h}$, on axes of frequency versus angular position. Graph (a) in each figure shows the soil displacement spectrum for a white input when the slab is joined directly to the tunnel invert, while graphs (b) to (d) show the Insertion Gains for the three slab-support stiffnesses given in Table 5.3. Thus the absolute displacement spectrum for a given stiffness is the sum (because a dB scale is used) of graph (b), (c) or (d) with graph (a). The contour intervals are 10dB, with red or "hot" colours indicating higher levels than blue or "cold" colours. Instead of one 10dB band for the 0dB level in the Insertion Gains, there are two 5dB bands: $> 0\text{dB}$ (up to 5dB) and $< 0\text{dB}$ (down to –5dB). This is to clearly show the cross-over between worsened performance and reduced vibration. Thus the yellow $< 0\text{dB}$ areas denote marginal improvement over a directly joined slab. Such marginal reduction may not be worth the cost of floating the track slab.

The three spectra (a) in Figures (5.25) to (5.27) for a directly joined slab beam have some common features. The soil vibration levels for frequencies below 10Hz are all very small compared to the rest of the frequency range, and because the Insertion Gains (b) to (d) in each figure are all near 0dB below 10Hz, this can also be said for the slabs supported on varying stiffness. Since all input frequencies have equal weighting, this shows that very low frequencies are highly attenuated by the track-tunnel-soil system; therefore the assumption that these frequencies are relatively insignificant is justified. Maximum activity occurs between 100Hz and 160Hz, but longitudinal levels seem to be lower than horizontal and vertical ones. The highest levels occur mainly for angular positions less than 100°, underneath and to the sides of the tunnel, resulting in a "vibration shadow" in the soil above the tunnel. The vibration shadow is

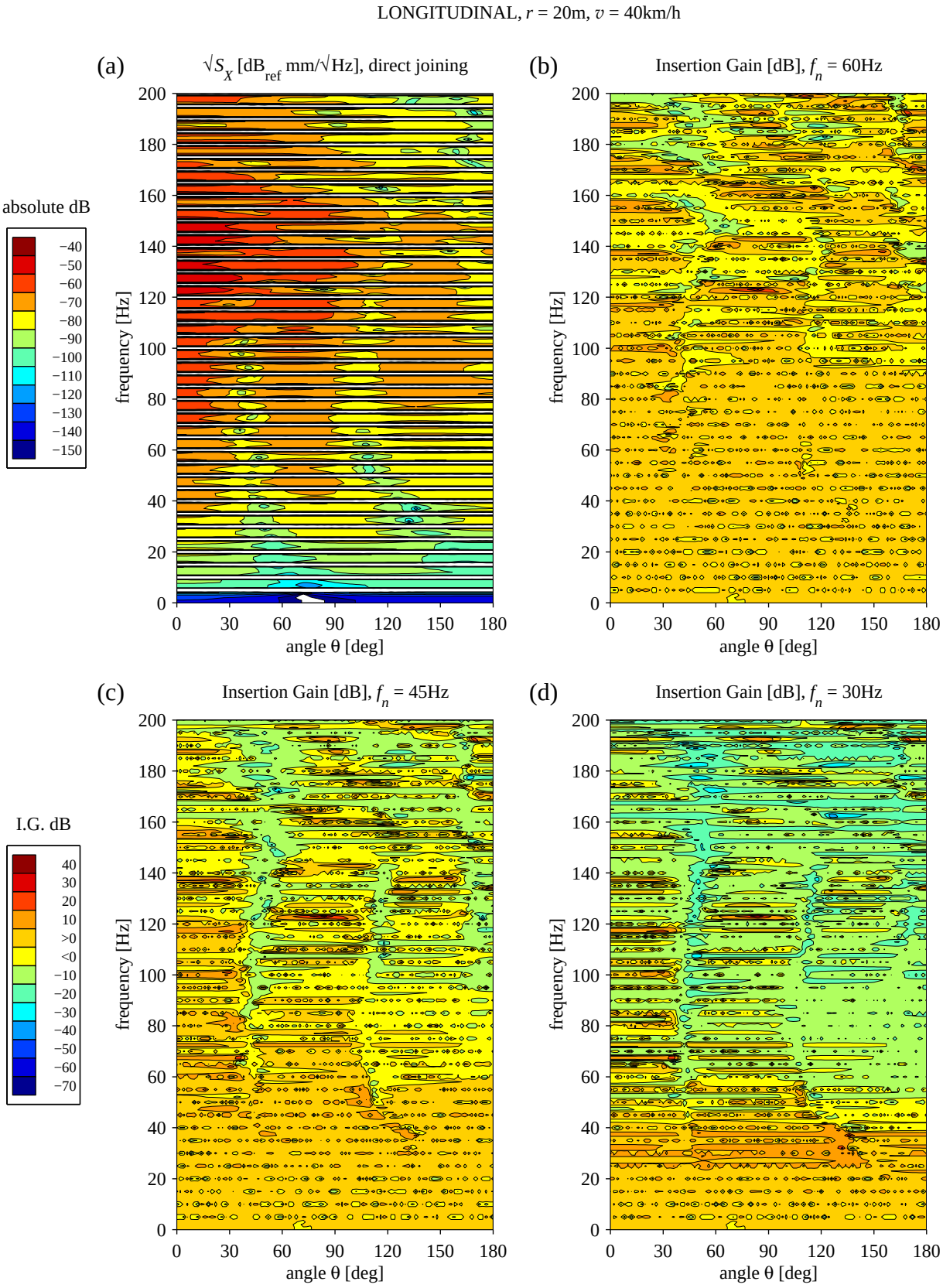

Figure 5.25: (a) Longitudinal soil displacement spectrum for a full track model joined directly to the tunnel invert and (b)-(d) Insertion Gains relative to (a) with increasingly softer slab-support stiffnesses, at a radius of 20m with a train speed of $40\,\mathrm{km/h}$. $\theta = 0$ is directly underneath the tunnel invert and $\theta = 180^\circ$ is directly above the tunnel. White (uniform) input roughness spectrum of $1\mathrm{mm}/\sqrt{\mathrm{Hz}}$ between rail and wheel. The contour intervals are 10dB, centred on the values given in the legends, except for the <0dB and >0dB bands which represent –5dB to 0dB and 0dB to 5dB respectively.

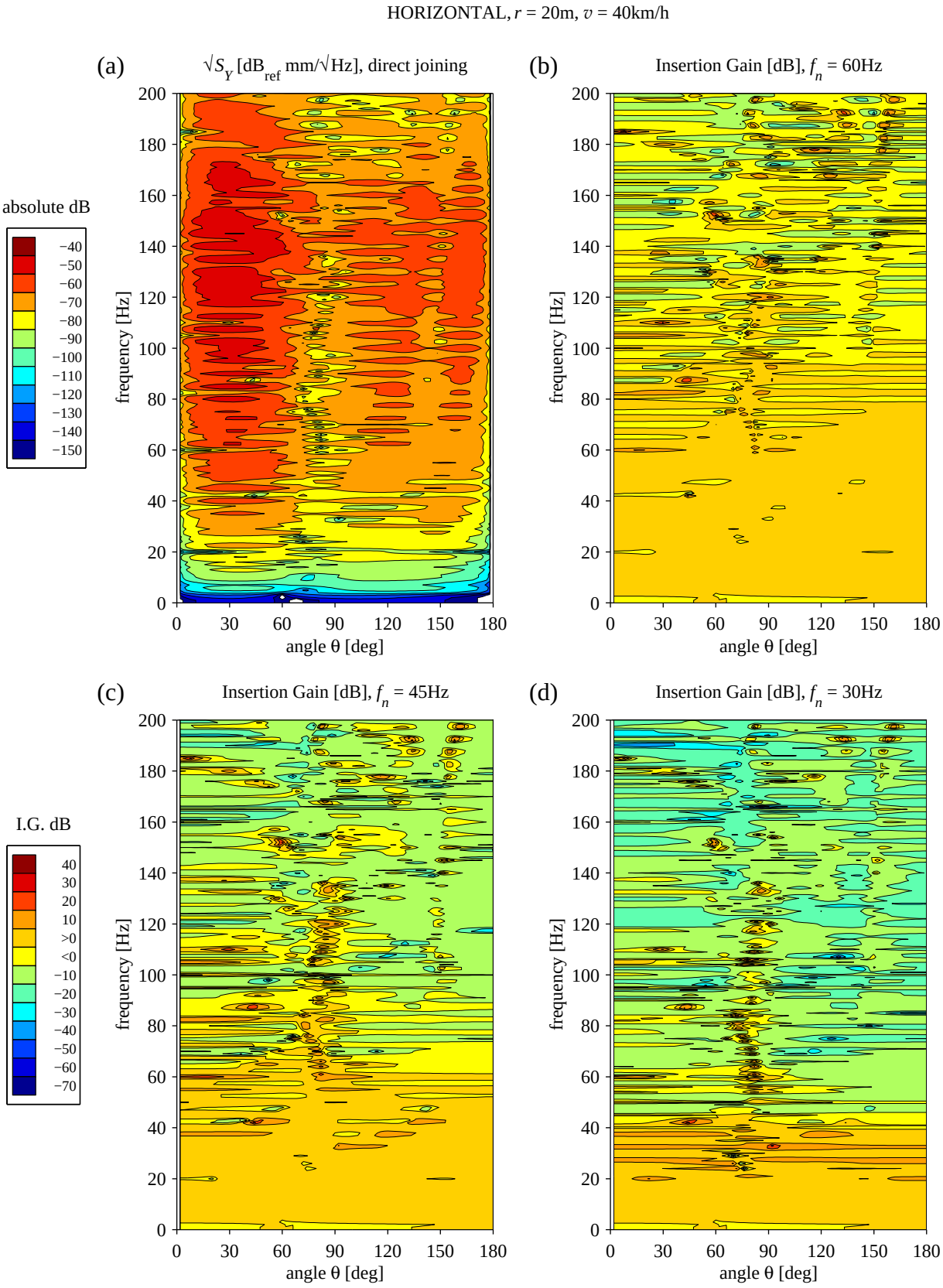

Figure 5.26: (a) Horizontal soil displacement spectrum for a full track model joined directly to the tunnel invert and (b)-(d) Insertion Gains relative to (a) with increasingly softer slab-support stiffnesses, at a radius of 20m with a train speed of 40 km/h. Otherwise as for Figure 5.25.

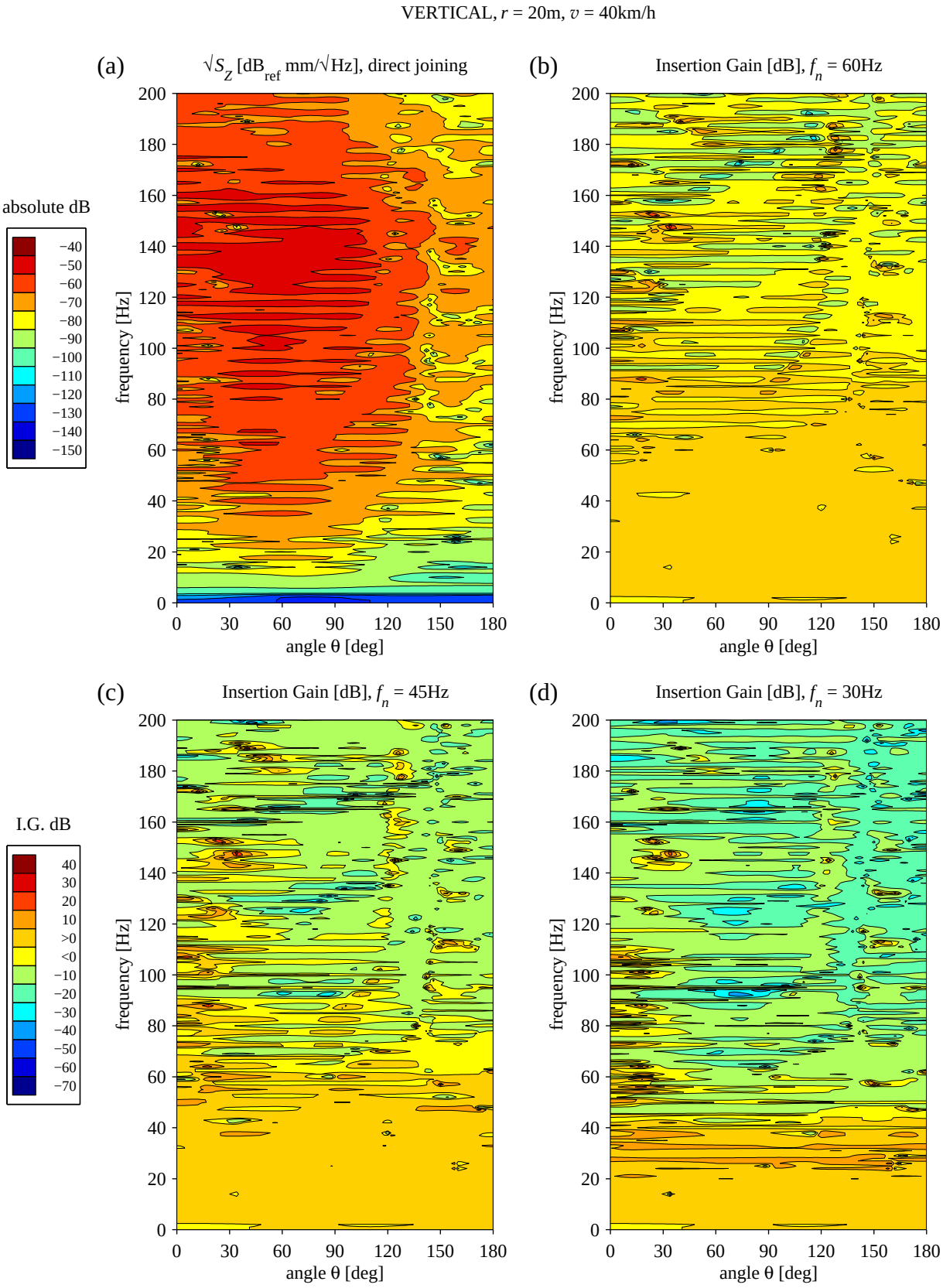

Figure 5.27: (a) Vertical soil displacement spectrum for a full track model joined directly to the tunnel invert and (b)-(d) Insertion Gains relative to (a) with increasingly softer slab-support stiffnesses, at a radius of 20m with a train speed of 40 km/h. Otherwise as for Figure 5.25.

probably beneficial, if a high proportion of energy propagated downwards means propagation away from nearby building foundations. The Insertion Gain plots (b), (c) and (d) are for increasingly softer resilient bearings with designed natural frequencies of 60Hz, 45Hz and 30Hz. This gives $\sqrt{2}\,f_n$ frequencies, above which isolation is supposed to occur, of 84.9Hz, 63.6Hz and 42.4Hz respectively. Insertion Gains are generally positive until the $\sqrt{2}\,f_n$ frequencies, but do not become uniformly negative above these – there are many pockets of increased response at higher frequencies. Clearly, simple vibration-isolation theory is not applicable in the current situation.

Each displacement component has some individual characteristics. Figure 5.25(a) for the longitudinal PSD has a series of white horizontal strips at 5Hz intervals. White areas mean that the level is below the minimum of the scale, so these strips represent troughs of very low magnitude in the PSD surface plotted. It is not clear how these deep antiresonances arise. The antisymmetric nature of the FRF for longitudinal displacement does not fundamentally alter the way the terms in the PSD summation (5.44) add up compared to the symmetric FRFs for the horizontal and vertical displacement components. The antiresonances cannot be due to standard wheelbase filtering, because they were found to appear at the same 5Hz intervals regardless of train speed. Further investigation is required to determine the mechanism responsible for this regular attenuation. The many small, round contours in Figures 5.25(b)-(d) giving a "dotted" appearance are most probably due to numerical fluctuation in the Insertion Gain ratio of the very small magnitudes at the trough frequencies, so should be ignored. Nevertheless, Figures 5.25(b) and (c) show that insertion of only a small amount of resilience gives only marginal vibration reduction over the whole frequency range, with some positions showing quite large increases right up to 200Hz when the slab is floated. The softest mounting, Figure 5.25(d), gives worthwhile reductions (green and blue areas) for many soil positions above 70Hz, but this is much higher than the corresponding $\sqrt{2}\,f_n$ value of 42.4Hz and there are still significant areas of increased response.

The spectrum of horizontal displacement, Figure 5.26(a), has a vertical white line at $\theta = 0$ and at $\theta = 180^\circ$, since the horizontal displacement at these two positions, as given by (5.49), is wholly made up of the tangential component *V*, which is zero directly above and below the

tunnel. There are high levels of vibration (red areas) for a wider frequency range than the longitudinal displacement. Clearly discernible are horizontal fingers of colour, indicating undulation in the surface represented by the contour plot. The most obvious frequency spacing from crest to crest is about 5Hz, though closer inspection reveals smaller spacing on some parts of the surface. This undulation arises from wheelbase filtering, due to coincidence of roughness wavelength with the axle spacing on the track: crests occur when all the axle masses move up and down in phase, troughs when they move out of phase, as explained at the end of Chapter 3. For the train speed of $40\,\text{km/h}$ $(11.1\,\text{m/s})$ and axle spacing of 20m, the expected frequency interval between peaks of in-phase force transmitted to the tunnel invert is 0.556Hz. This is not discernible in Figure 5.26(a) for two reasons. Firstly, the contour interval of 10dB will not show many surface undulations of smaller magnitude. Secondly, the spectrum results were computed for a frequency step of 1Hz, which is a resolution too coarse to show variation at a period of 0.556Hz. Thus the variation can only be seen at a multiple of the fundamental frequency interval. The Insertion Gains, Figures 5.26(b)-(d), show the same kind of behaviour as Figure 5.25 when the slab bearings become softer, but there are now more positions that have significantly reduced vibration levels. The positions above the $\sqrt{2}\,f_n$ frequencies with increased vibration are concentrated around $\theta = 90^\circ$, the horizontal plane bisecting the tunnel. Once again, largely beneficial results are only achieved with the softest slab bearings, Figure 5.26(d).

The spectrum of vertical displacement, Figure 5.27(a), is similar to the horizontal one in Figure 5.26(a), showing the same surface undulation due to wheelbase filtering. However, the highest levels of vibration extend further around the tunnel, from directly underneath to more than 90°. The Insertion Gains follow a similar pattern too, although Figure 5.27(d) shows that the softest bearings reduce vertical vibration more than the horizontal vibration of Figure 5.26(d). The positions with increased vibration above the $\sqrt{2}\,f_n$ frequencies are now concentrated near $\theta = 0$, underneath the tunnel.

PSDs can be calculated for other soil radii and train speeds to determine the effects these parameters have. The vertical component of displacement will be used for this purpose, so comparisons are to Figure 5.27. The response at a radius of 10m (with the train speed still $40\,\text{km/h}$) is shown in Figure 5.28. The absolute spectrum, Figure 5.28(a), shows higher levels

than at 20m. This is to be expected because the cylindrical surface around the tunnel at 10m is smaller than at 20m, so even if there was no material damping, equal energy passing through each surface would mean that the displacements at 20m have to be less. However, the tunnel model includes shear material damping in the soil, so the resulting energy loss also reduces displacement levels as radius increases. The spectrum for a radius of 30m, Figure 5.29(a), shows lower levels than 10m or 20m, consistent with the larger distance from the tunnel. For both cases, the undulations due to wheelbase filtering are at the same spacing as before. The general characteristics of the Insertion Gains are much the same at the different radii. Nevertheless, at 10m radius, Figures 5.28(b)-(d), marginal reduction (yellow areas) starts at lower frequencies than at 20m, and at 30m radius, Figures 5.29(b)-(d), there is markedly less significant reduction (blue areas) than at 20m.

The effect of halving the train speed to $20\,\mathrm{km/h}$ on the levels at 20m radius is shown in Figure 5.30, while that of doubling the train speed to $80\,\mathrm{km/h}$ is shown in Figure 5.31. The main effect seems to be on the frequency interval of undulations due to wheelbase filtering. Halving the speed halves the apparent frequency of a given roughness wavelength, so the spacing between peaks is halved, as seen in Figure 5.30(a), while doubling the speed similarly doubles the spacing, as seen in Figure 5.31(a). Apart from this, the levels of each graph correspond with the $40\,\mathrm{km/h}$ levels in Figures 5.27(a)-(d) in their overall disposition with respect to frequency and angular position. Halving the speed just splits the different areas into more fingers, while doubling it causes separate fingers to coalesce into wider ones.

Although it is informative to plot the response of the full-track model to a white roughness input spectrum, ultimately the soil vibration levels induced by actual wheel-rail roughness need to be known. Frederich [62] gives a formula for rail irregularity PSDs based on many measurements of the track geometry of different surface railways. The spatial PSD of track irregularity is given by the single-sided spectrum

$$S_\delta\left(\frac{1}{\lambda}\right) = \frac{a}{(b + 1/\lambda)^3} \tag{5.51}$$

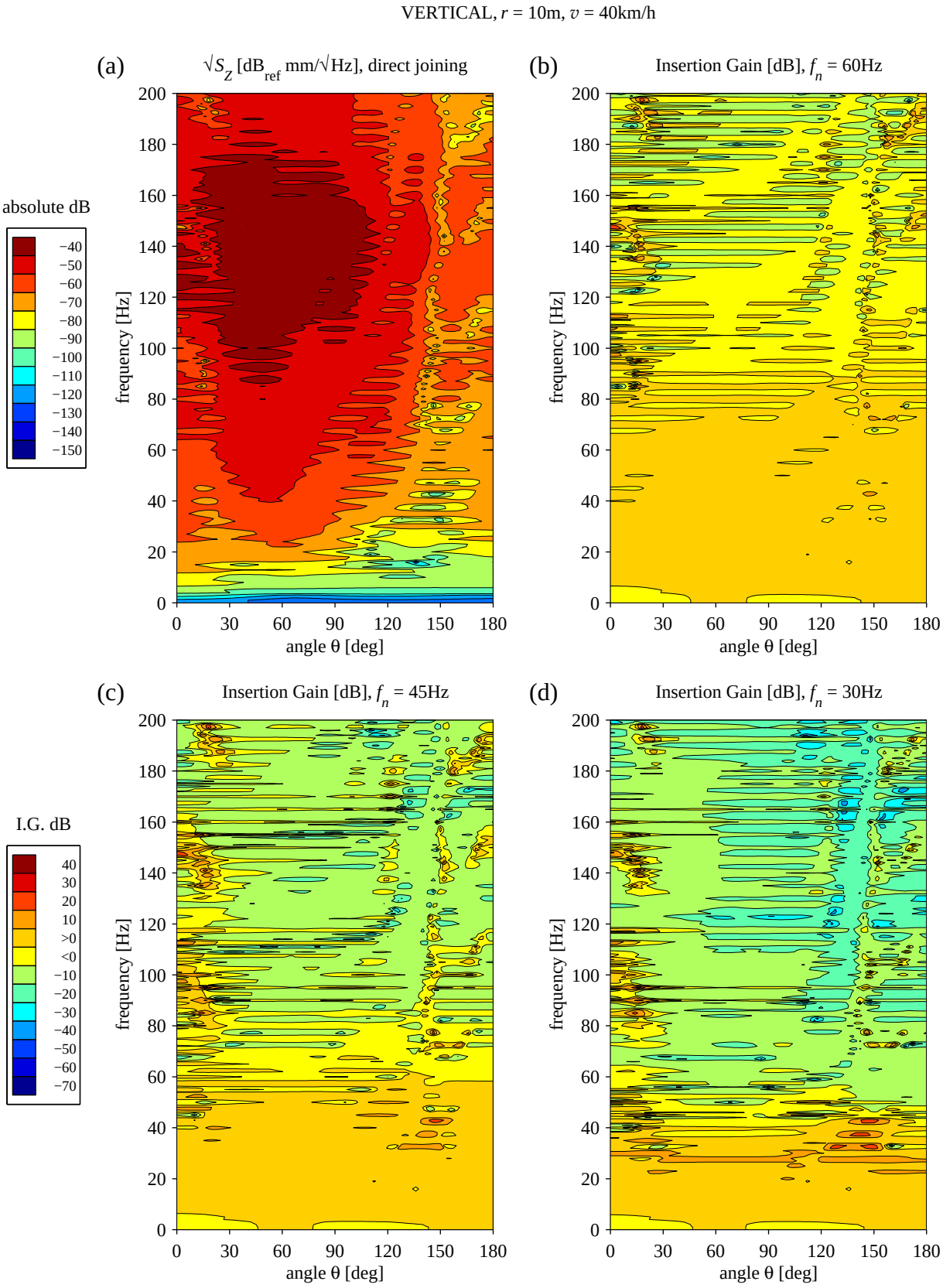

Figure 5.28: (a) Vertical soil displacement spectrum for a full track model joined directly to the tunnel invert and (b)-(d) Insertion Gains relative to (a) with increasingly softer slab-support stiffnesses, at a radius of 10m with a train speed of 40 km/h. Otherwise as for Figure 5.25.

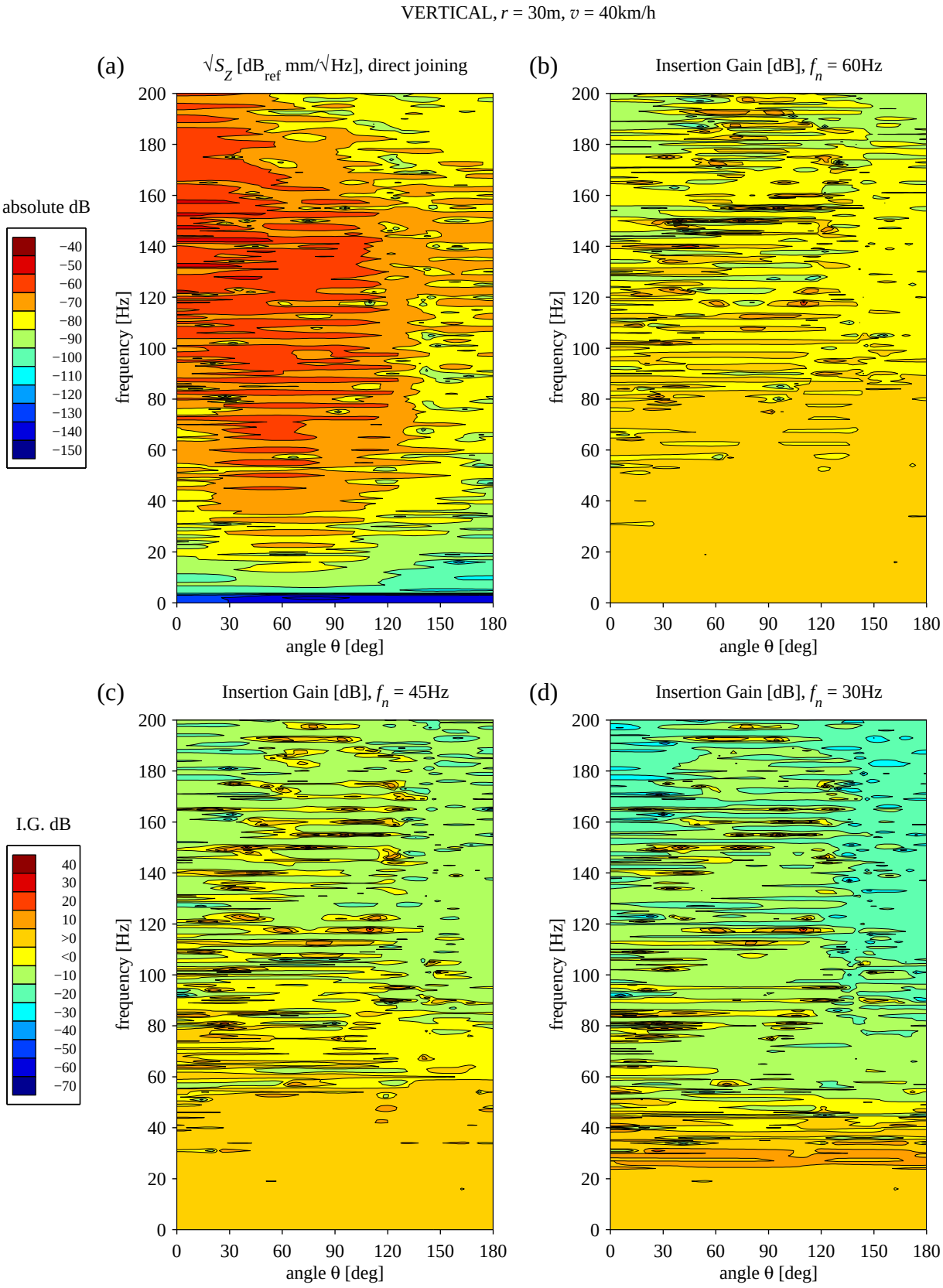

Figure 5.29: (a) Vertical soil displacement spectrum for a full track model joined directly to the tunnel invert and (b)-(d) Insertion Gains relative to (a) with increasingly softer slab-support stiffnesses, at a radius of 30m with a train speed of 40 km/h. Otherwise as for Figure 5.25.

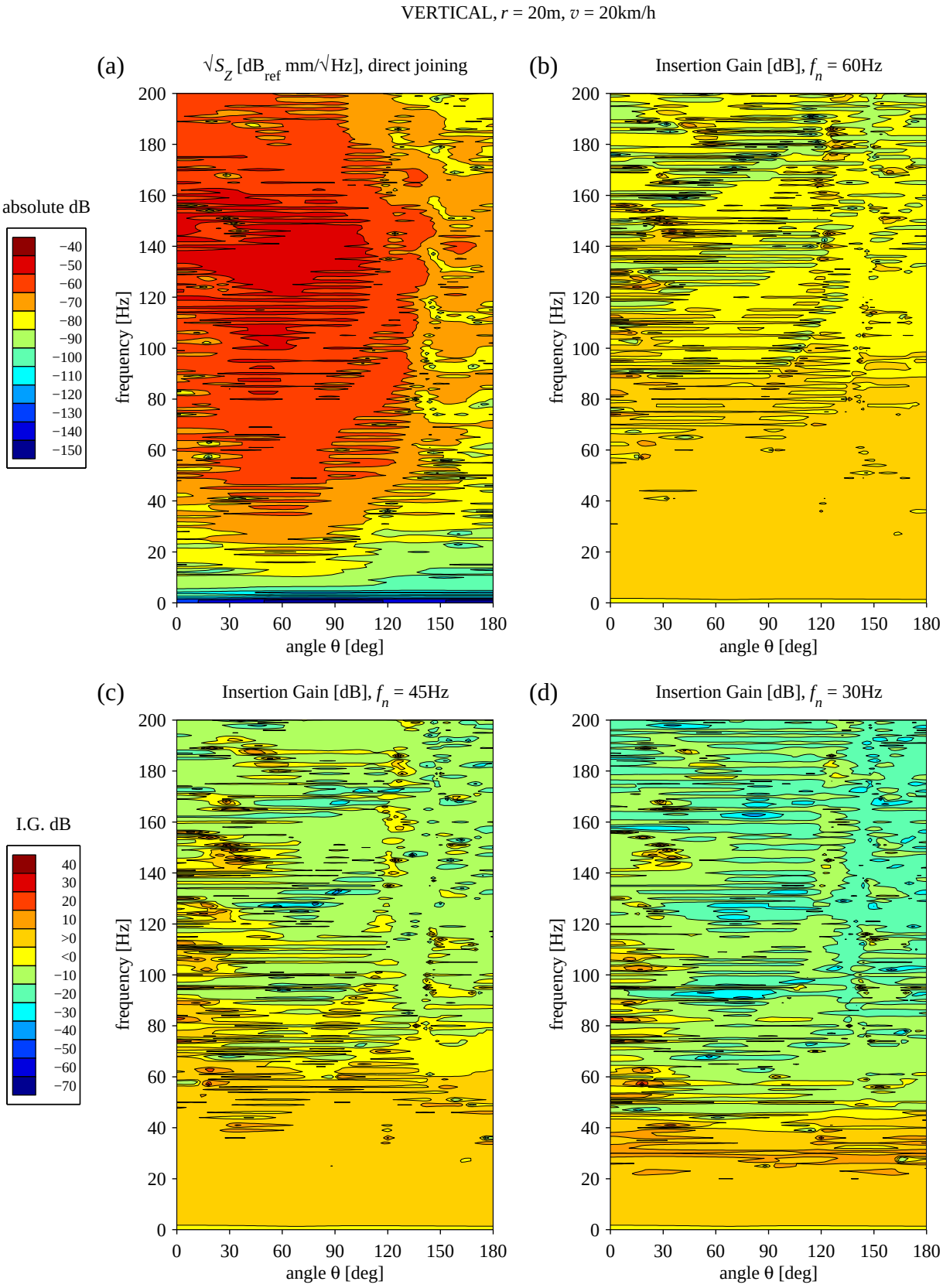

Figure 5.30: (a) Vertical soil displacement spectrum for a full track model joined directly to the tunnel invert and (b)-(d) Insertion Gains relative to (a) with increasingly softer slab-support stiffnesses, at a radius of 20m with a train speed of 40 km/h. Otherwise as for Figure 5.25.

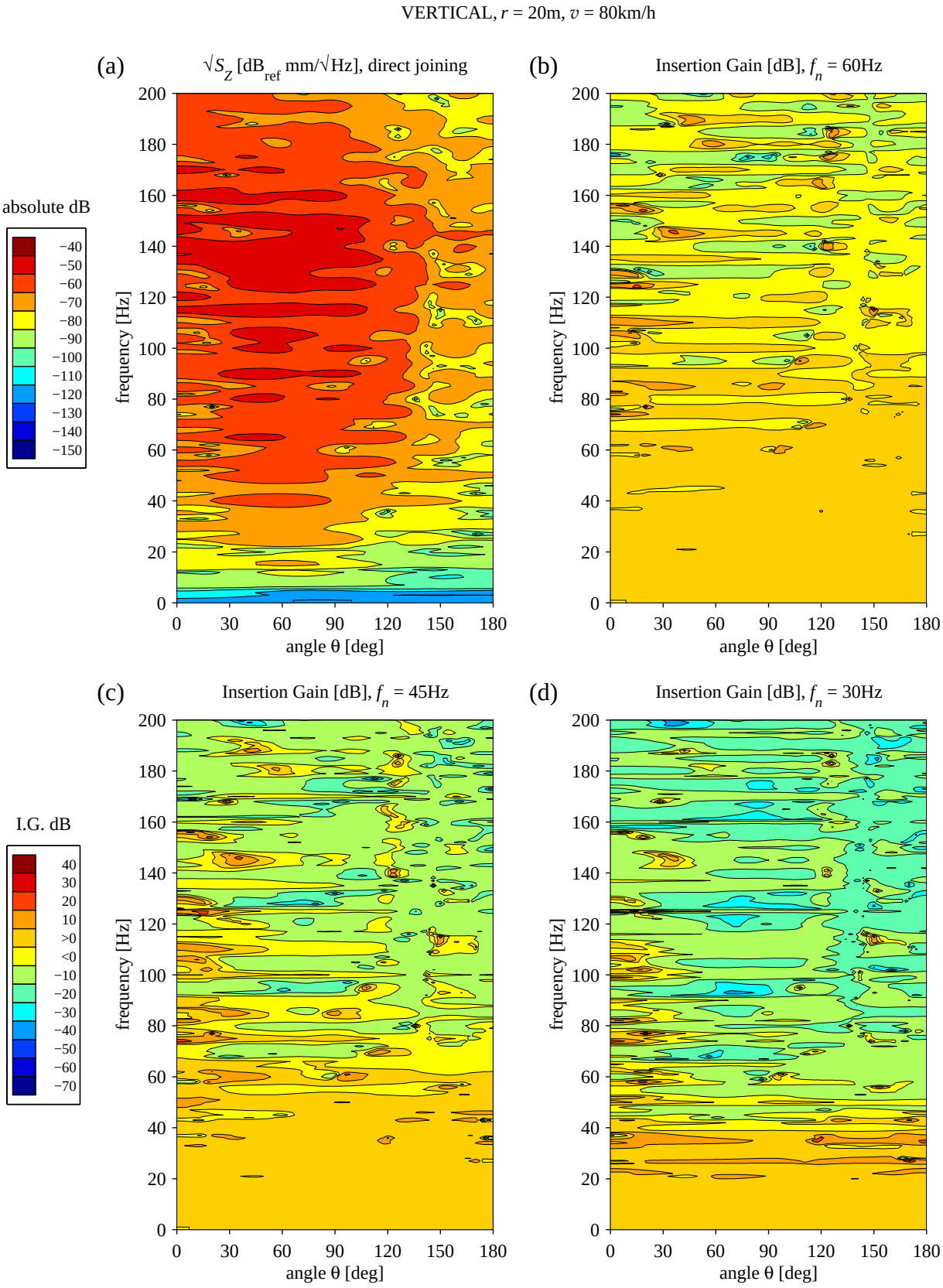

Figure 5.31: (a) Vertical soil displacement spectrum for a full track model joined directly to the tunnel invert and (b)-(d) Insertion Gains relative to (a) with increasingly softer slab-support stiffnesses, at a radius of 20m with a train speed of 40 km/h. Otherwise as for Figure 5.25.

where λ is the irregularity wavelength, a is an "unevenness" parameter and b is a "waviness" parameter. The values of a and b for irregularity in the vertical height of the rails are given in Table 5.4, derived by fitting (5.51) to measured data. The parameters for track in "worst" and "best" condition define the envelope of all measured data. The formula (5.51) is valid for wavelengths λ from 0.1m to 200m; smaller wavelengths are due to rail surface roughness and larger ones to variations in the topography of the ground surface. The function (5.51) is plotted in Figure 5.32 for the three track conditions described by the parameters in Table 5.4.

	a $[\mathrm{mm}^2.(1/\mathrm{m})^2]$	b $[1/\mathrm{m}]$
worst	9.39×10^{-1}	6.89×10^{-2}
average	1.31×10^{-2}	2.94×10^{-2}
best	1.90×10^{-4}	9.71×10^{-3}

Table 5.4: Values of the unevenness a and waviness b of vertical railway track irregularity, for three different track conditions. From Frederich [62].

To convert the PSD (5.51) to a function of frequency f, relation (5.45) is applied, recalling that $1/\lambda = f/v$ where v is the train speed, to give the single-sided roughness spectrum

$$S_\delta(f) = \frac{1}{v}\frac{a}{(b + f/v)^3} \tag{5.52}$$

which can be used as S_0 in (5.44). Function (5.52) is plotted in Figure 5.33 for a track in average condition, for three different train speeds. The frequencies below 20Hz (corresponding to long wavelengths) receive a very high weighting. Note that to cover frequencies up to 200Hz, (5.52) is extrapolated beyond the 0.1m minimum wavelength (frequencies greater than 56Hz at $20\,\mathrm{km/h}$ and 111Hz at $40\,\mathrm{km/h}$) for which the function was originally defined. It is arguable whether rail surface roughness and corrugation has a smaller (as given by the extrapolation in Figure 5.33) or comparable magnitude to small-wavelength irregularity in the track geometry.

The actual spectra of soil vibration are obtained by multiplying the previously calculated spectra for a white input by S_δ of (5.52) according to the PSD formula (5.44). For a radius of 20m and train speed of $40\,\mathrm{km/h}$, this results in the spectra of vertical soil vibration shown in Figure 5.34. Although Figure 5.33 shows a large bias in the input towards low frequencies, these are not over-emphasised in Figures 5.34(a)-(d). The frequencies below 5Hz remain of small

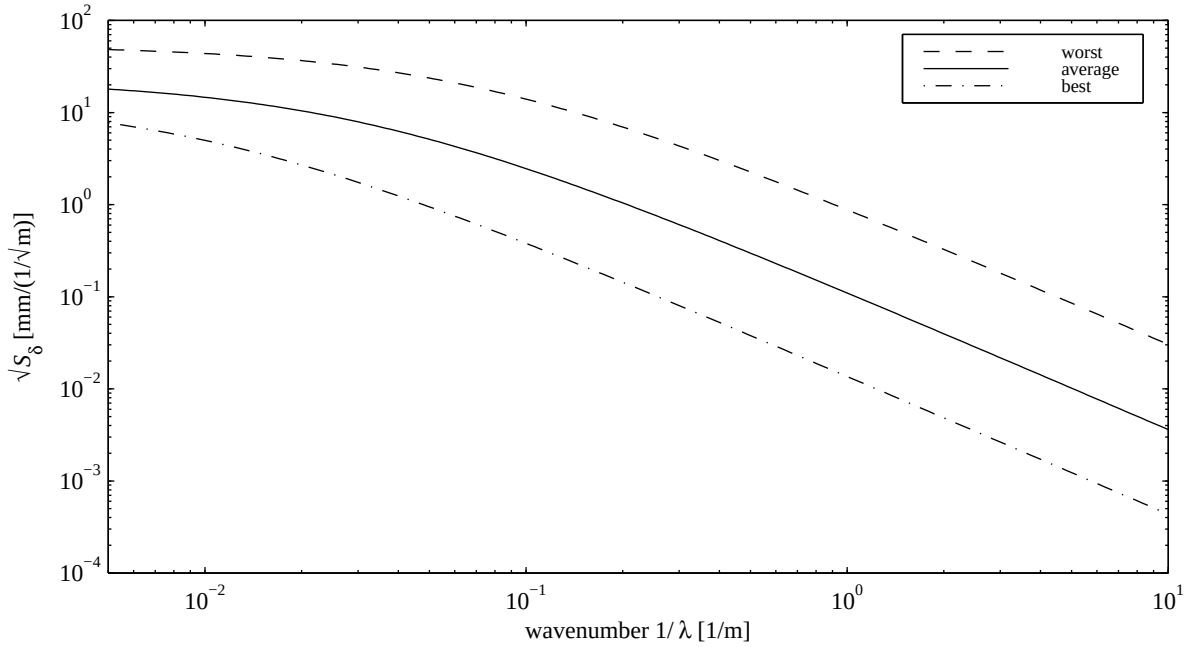

Figure 5.32: Spectrum of vertical rail irregularity versus wavenumber of the irregularity for railways in worst, average and best condition. Plotted from equation (5.51) using the parameters of Table (5.4), based on Frederich [62].

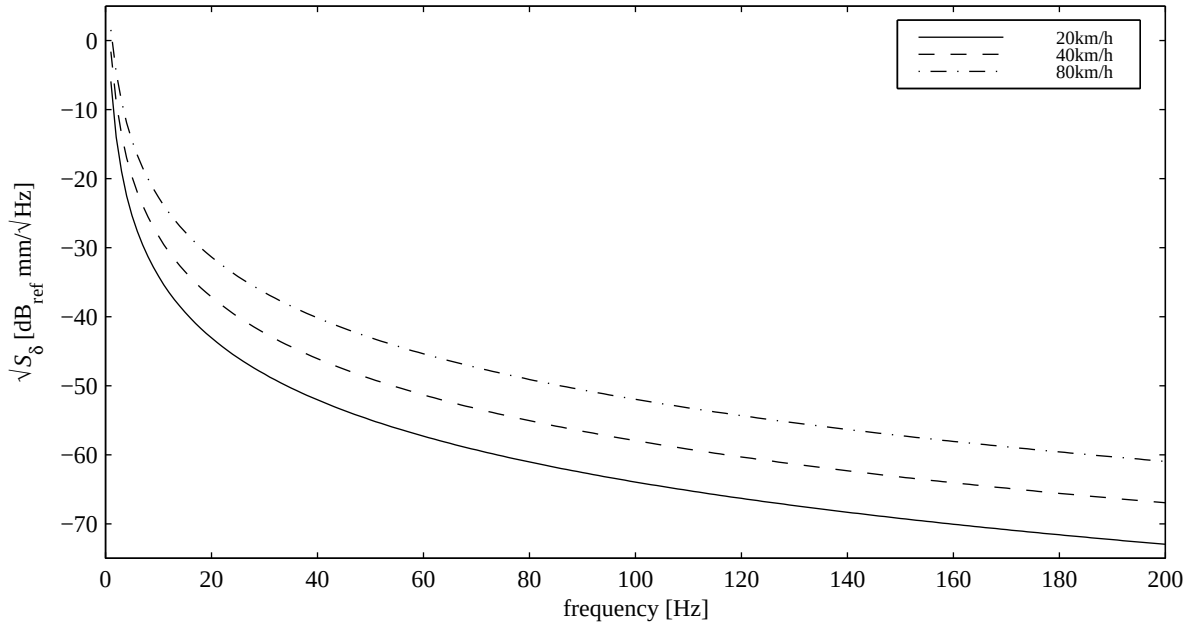

Figure 5.33: Spectrum of vertical rail irregularity versus frequency for railway in average condition, calculated for three different train speeds from equation (5.52) and corresponding to the "average" curve of Figure 5.32. Note that this is an extrapolation on Frederich's [62] data for $f > 56\text{Hz}$ when $v = 20\,\text{km/h}$ and for $f > 111\text{Hz}$ when $v = 40\,\text{km/h}$.

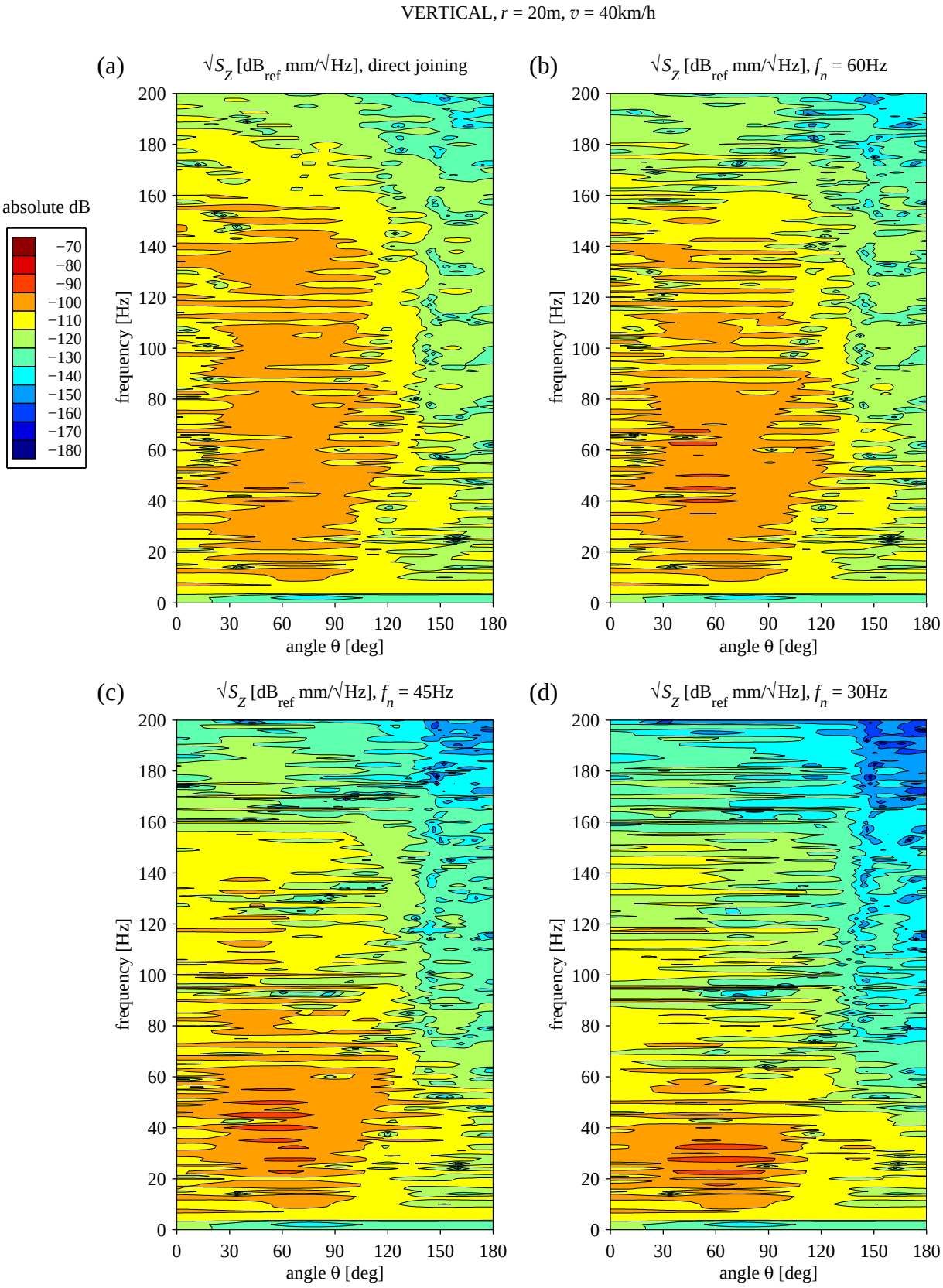

Figure 5.34: Realistic spectra of vertical soil displacement with a full track model, at a radius of 20m with a train speed of 40 km/h, for (a) direct joining and (b)-(d) increasingly softer slab-support stiffnesses. $\theta = 0$ is directly underneath the tunnel invert and $\theta = 180^\circ$ is directly above the tunnel. The input roughness spectrum between rail and wheel is that given in Figure 5.33. When integrated over frequency, (a)-(d) give the four RMS curves on Figure 5.37(b).

magnitude, while there are small maxima near the respective natural frequencies of the slab on its bearings; the overall effect is to flatten out each spectrum over the whole frequency range. Nevertheless, if the extrapolated rail-roughness magnitude above 111Hz is indeed underestimated, then the spectra could be increased by up to 7dB for the highest frequencies shown.

The RMS levels of soil vibration are obtained by integrating the spectra for a realistic input, such as those in Figure 5.34, over frequency, using the MS (5.46). Each spectrum surface is thus condensed to a single curve which is a function of angular position. Figure 5.35 shows the effect of resilient slab bearings on the RMS level of longitudinal soil vibration at various radii for a train speed of $40\,\mathrm{km/h}$. Close to the tunnel at 10m radius, the effect of adding resilience is to increase the RMS level at most positions around the tunnel, with only the softest bearings giving a reduction for angles greater than 120°, above the tunnel. As the radius is increased, the levels for angles less than 90° drop below the directly joined case, but this is all under the tunnel and

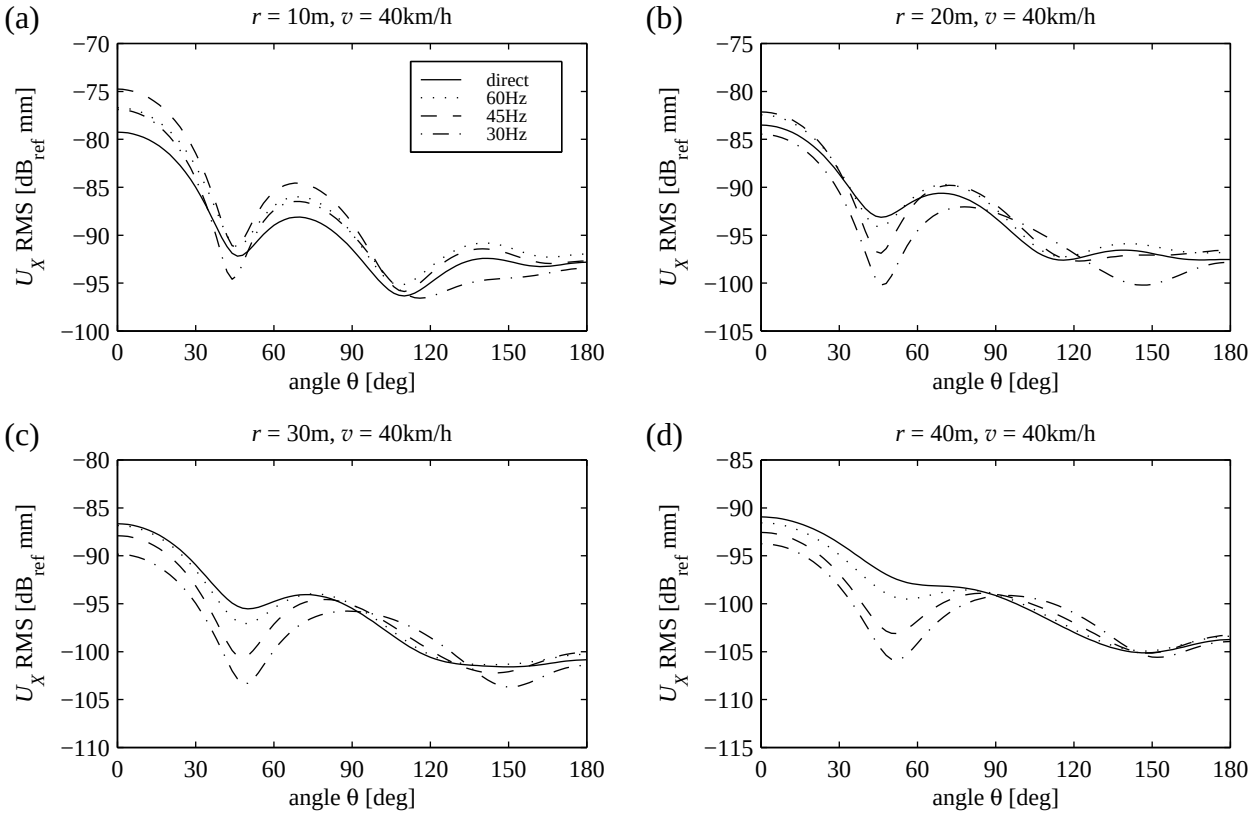

Figure 5.35: Longitudinal soil displacement RMS levels for a train speed of $40\,\mathrm{km/h}$, around the tunnel at radii of (a) 10m (b) 20m (c) 30m and (d) 40m. $\theta = 0$ is directly underneath the tunnel invert and $\theta = 180^\circ$ is directly above the tunnel. Calculated with the realistic roughness input spectrum of Figure 5.33 for varying slab-support stiffnesses giving the natural frequencies indicated.

thus not so important. At angles corresponding to positions above the tunnel, adding resilience generally increases the levels by a few dB, with a marginal improvement provided at some positions again only by the softest bearings. Note that the variation about the levels for the directly joined slab are all within about $\pm 5\text{dB}$, which is not very much compared to the tens of dB reduction predicted using simple mass-spring models.

The RMS levels of horizontal displacement in Figure 5.36 show that at 10m radius, this component behaves in a way opposite to the longitudinal one. Any amount of resilience reduces vibration at most positions, with the softest giving up to 7dB reduction. But this effect is diminished as the radius increases, with all responses collapsing on to that for the directly joined slab at 40m radius, the vibration for angles greater than 90° even being slightly increased. A similar picture emerges from the RMS levels of vertical soil displacement shown in Figure 5.37. As for the original PSDs, the horizontal and vertical RMS levels are generally higher than the longitudinal one. Since the longitudinal levels with resilience start off higher and end up lower than the directly joined case as radius increases, and vice-versa for the horizontal and vertical

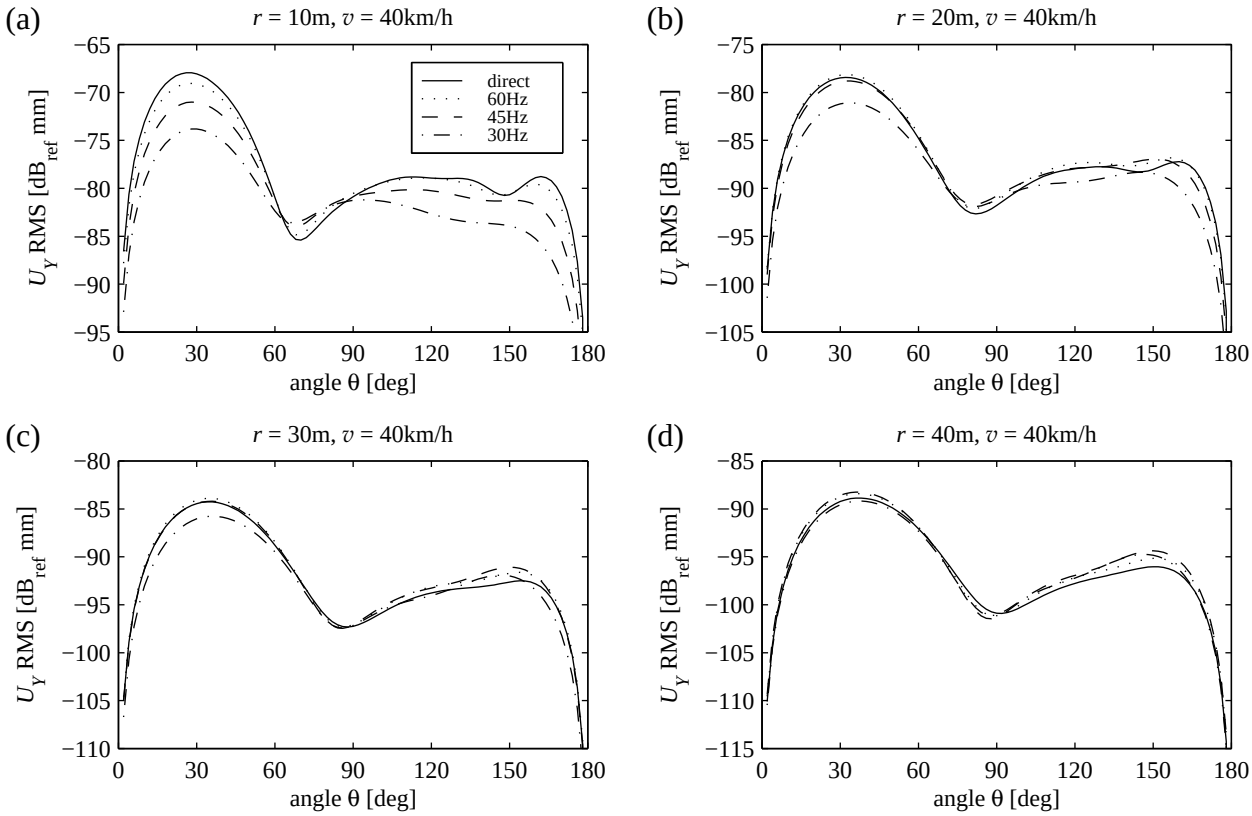

Figure 5.36: Horizontal soil displacement RMS levels for a train speed of $40\,\text{km/h}$, around the tunnel at radii of (a) 10m (b) 20m (c) 30m and (d) 40m. Otherwise as for Figure 5.35.

levels, it would seem that there is some kind of transfer of energy from longitudinal motion to horizontal and vertical motion as waves travel outwards from the tunnel. In addition, shear-wave motion will manifest itself mainly in the horizontal and vertical components of displacement. Because the soil material damping acts in shear, these two components will be attenuated more by damping than the longitudinal one. It is perhaps the case that a closely coupled slab beam induces more shear motion in the soil than one on softer springs, so that the effect of material damping is correspondingly more, eventually reducing responses for all slab-support stiffnesses to similar levels at large radius. The situation is complicated by the fact that the transmission paths from the vicinities of the axles to the observation point at a given angular position are not the same for different radii. The longitudinal position of the observation point relative to the axle stations spaced at 20m could also be significant, especially for smaller radii.

Figure 5.38 shows the effect of doubling the train speed on the RMS levels of vertical displacement. The graphs are almost identical in shape to those in Figure 5.37; they are just increased uniformly by about 5dB. Similarly, halving the speed was found to decrease all levels by about 5dB. This is true for the other two displacement components as well. This follows from the similarity of the curves in Figure 5.33 for the input spectrum at different speeds, and the observation from Figures 5.27, 5.30 and 5.31 that train speed does not change the general distribution of vibration level with respect to frequency and angular position. Thus the maximum achievable reduction in RMS levels is of the order of only 6dB regardless of train speed.

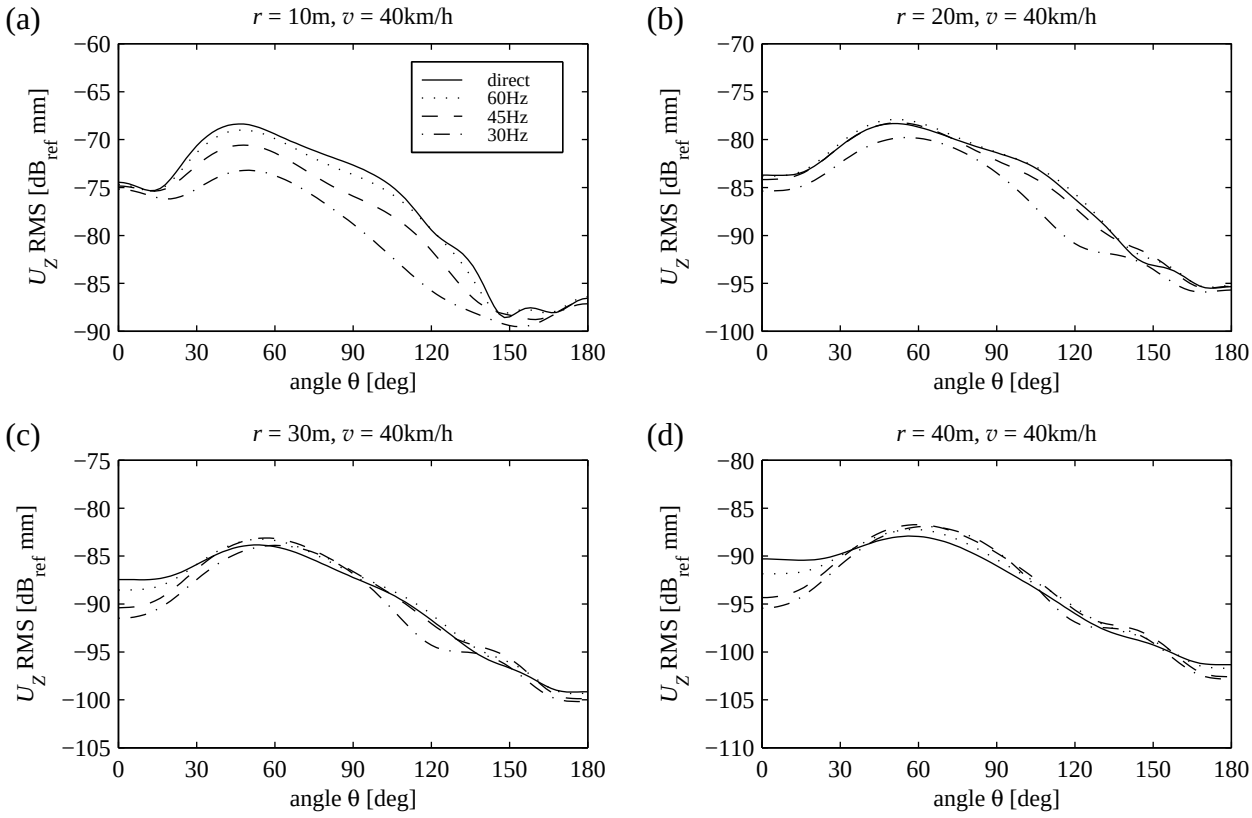

Figure 5.37: Vertical soil displacement RMS levels for a train speed of 40 km/h, around the tunnel at radii of (a) 10m (b) 20m (c) 30m and (d) 40m. Otherwise as for Figure 5.35.

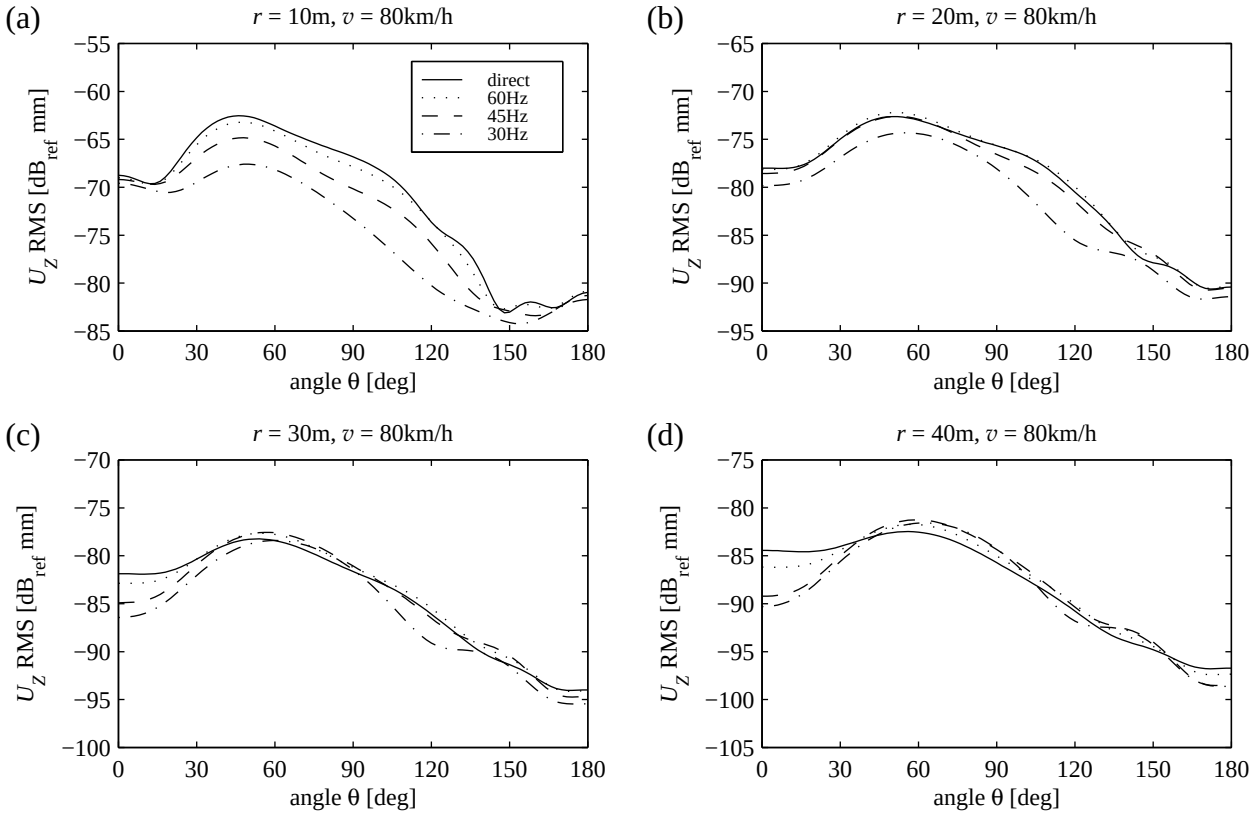

Figure 5.38: Vertical soil displacement RMS levels for a train speed of 80 km/h, around the tunnel at radii of (a) 10m (b) 20m (c) 30m and (d) 40m. Otherwise as for Figure 5.35.

5.4 Conclusions

The track slab can be modelled by a bending beam coupled to the tunnel, either directly or via resilient bearings, using straightforward algebra in the wavenumber domain. This simple model demonstrates that Winkler-beam theory is inadequate for the design of floating-slab track. While the driving-point response of a slab on soft bearings is passably well modelled by a Winkler beam, radiation of energy into the soil heavily attenuates the response of slab beams more closely coupled to the tunnel. The tunnel also transmits energy to the slab beam at points away from the load at low frequencies, whereas a Winkler beam cannot do this below its "natural frequency", which marks the onset of travelling waves. Mounting the track slab on resilient bearings allows energy to propagate down the slab before being transmitted to the tunnel then soil, so that under the slab load, the tunnel invert response is decreased compared to a directly joined slab beam, but is increased at positions further down the tunnel. This is reflected in the soil displacements, for which resilient bearings produce classic vibration isolation for positions next to the slab load, but higher levels at other longitudinal positions.

The coupling equations are made only slightly more complex by the introduction of torsion into the slab beam to model the laterally unbalanced loads expected from the two rails of a real track. The two longitudinal lines of joining for the torsional slab result in similar bending responses to the one line for the simple slab, but appear to make the whole structure "stiffer", despite using equivalent support resilience. This shows that the details of the slab mounting have an important influence on the interaction with the tunnel. Travelling torsional waves in the slab begin at higher frequencies than travelling bending waves, with implications for designing a slab on its bearings to have a given "natural frequency". Addition of slab torsion to slab bending complicates the responses in the soil. For some positions, bending effects are dominant, but for others, torsional effects lead to increased soil response with resilient bearings, when consideration of bending only would have predicted some reduction. However, it does appear that, with resilient bearings, torsional waves propagate along the slab more readily than bending waves, rather than transferring energy to the tunnel in the vicinity of the loads. This effect might be exploited to design a floating-slab track such that input forces induce mainly torsional motion which remains confined to the slab and is eventually dissipated by damping in the slab bearings.

A complete track model can be constructed by adding a rail beam to the simple-slab model using the same original wavenumber-domain coupling equations, then adding axle masses via an FRF matrix for the rail. For a model of infinite length, a shifting principle can be invoked to calculate the soil response due to inputs at every train axle by considering responses to only one input at the middle axle. Contour plots of soil displacement PSDs for uniform random roughness-displacement inputs between the axles and the rail show that the track-tunnel-soil system attenuates frequencies below 10Hz the most and frequencies between 100Hz and 160Hz the least. The highest levels occur under and to the sides of the tunnel, resulting in a vibration shadow above the tunnel. Longitudinal vibration levels are less overall than horizontal and vertical ones. The differences between these three components prompt the question of which ones are the most important in transmitting vibration into building foundations. The PSD surfaces have undulations at regular frequency intervals due to wheelbase filtering by the axles, with train speed changing the interval but not the general distribution of vibration levels with frequency and position. Insertion Gain plots for increasingly softer slab-support stiffnesses confirm that isolation is not achieved at frequencies as low as predicted by simple theory. Any reductions are modest and there are some positions around the tunnel for which resilient slab bearings cause increased response at higher frequencies.

RMS vibration levels can easily be calculated from the PSDs. This was done using a realistic input spectrum giving higher weighting to longer wavelengths of track irregularity. Floating the track slab increases longitudinal RMS levels near the tunnel, but decreases them at greater radii for some positions under the tunnel. Resilient bearings reduce horizontal and vertical RMS levels close to the tunnel, but make little difference at large radii. This suggests some kind of energy transfer between the different components, although this could only be confirmed by a power-flow analysis, requiring calculation of stresses as well as displacements. Doubling the train speed simply increases all RMS levels uniformly by approximately 5dB. Any vibration reduction achieved is modest, no more than 6dB with the softest slab bearings.

Chapter 6

FIELD MEASUREMENTS

Field measurements were undertaken in February 1997 in order to collect some experimental data to compare with the theoretical models described in the previous chapters. The site was an underground section of London's Heathrow Express railway line, then under construction. Since there were no trains yet running, it was relatively straightforward to perform a series of impulse-hammer tests on the track. In the time available (one day of access to the site), it was not feasible to measure vibration responses in the surrounding soil or on the surface, but some useful observations can still be made from the responses of the track and tunnel alone.

6.1 Site Description

The measurement site was near the Heathrow Airport end of the Heathrow Express line. Construction work had progressed to the point where the major structural components such as the tunnel wall and the track itself were complete. Most of the track was fixed directly to the tunnel invert, but a 500m-long section was built with a floating slab to minimise transmission of ground vibration to a nearby airport hotel. This meant that measurements could be performed on isolated and unisolated track under similar conditions.

The cross-section of the tunnel and isolated track is shown in Figure 6.1. The concrete floating slab rests on a 25mm-thick resilient layer of Trackelast FC75, a cork-particle filled rubber material usually used for ballast mats. The space between the sides of the slab and the tunnel floor is filled by 25mm-thick sound-deadening quilt. Longitudinally the slab is effectively

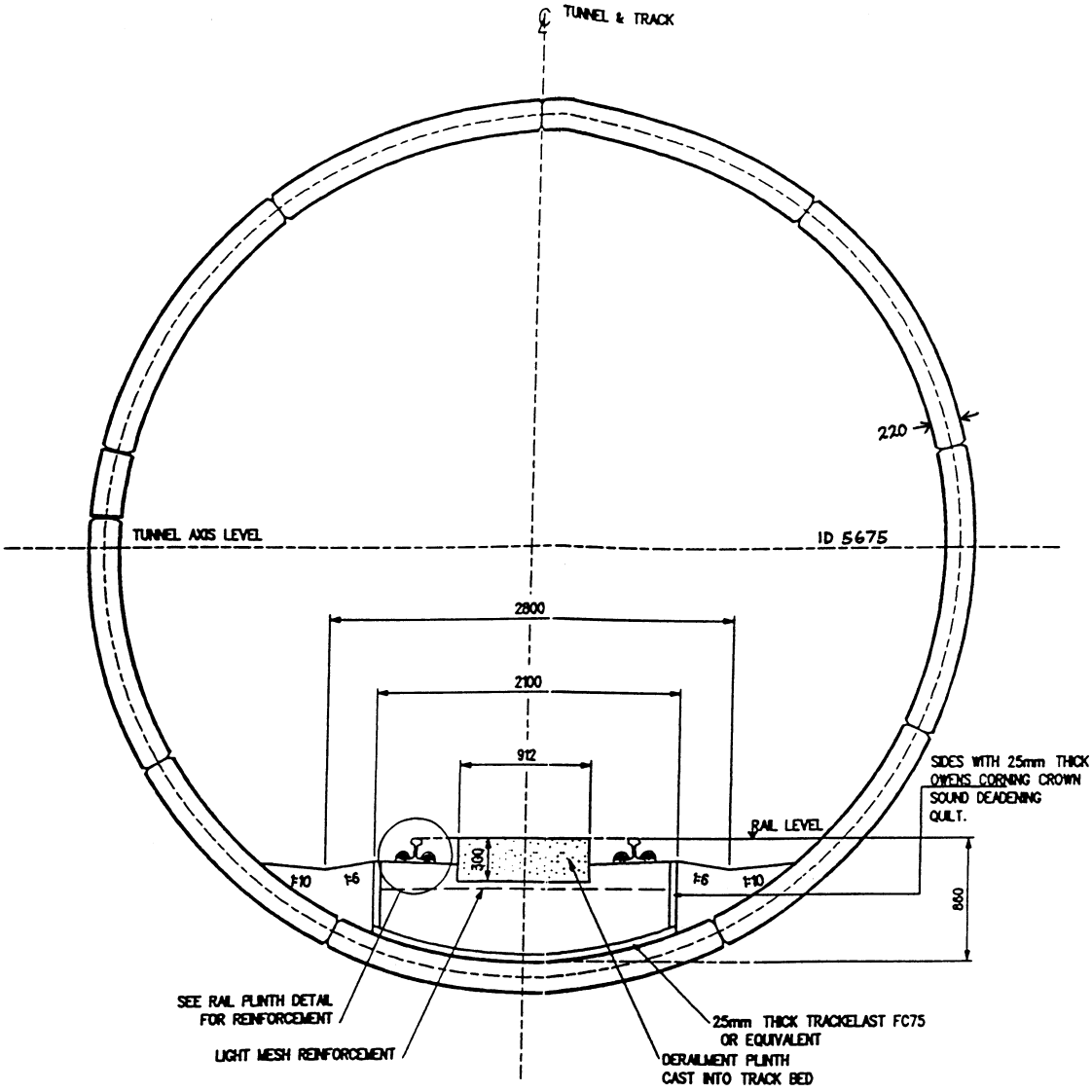

Figure 6.1: Cross-section showing the construction of the floating-slab track at the measurement site. The unisolated track is the same but without the FC75 and quilt layers. A section of tunnel lining consists of nine pieces held in place by a smaller key piece, shown above the horizontal centreline at left. All dimensions mm.

continuous, cast in-situ with expansion joints every 100m or so. The unisolated track is the same but without the rubber and quilt layers, resulting in one solid continuum of concrete across the tunnel floor. In both cases the UIC 54 rails are fastened to the slab every 700mm by Pandrol E2007 clips, with Tiflex FC136 rubber rail pads placed between rail and slab.

The tunnel cross-section is round because it was bored. The complete railway consists of two such tunnels, one for each direction of travel, whose centres are about 18m apart and 22m below the ground surface at the measurement site. The tunnel lining consists of 2m-long cylindrical sections, each comprising nine concrete pieces held in place against the soil by a smaller wedge-

shaped key piece. It is therefore not a continuous concrete shell. About 1.5km from the measurement site in the direction of central London, the two tunnels emerge at the surface via cut-and-cover portions of square cross-section. This distance is large enough for the transition to the surface to have no significant effect on the vibration behaviour of the area of interest.

The geological survey maps for the Heathrow area [22, 23] show the site to be situated in flat and relatively low-lying ground covered by river deposits of the Thames and its tributary the Colne. The surface (drift) layers of 5-10m total depth are variously Alluvium, Brickearth (a stoneless loam), Flood-Plain Gravel and Taplow Gravel. Going downwards, the (solid) layers underlying this surface cover are 80-100m of London Clay (brown weathering grey clays), about 25m of Reading Beds (unfossiliferous red and green mottled clays) and about 150m of Upper-Middle Chalk (white chalk with some beds containing flints). The Heathrow Express tunnels are therefore well into the London Clay layer, which is deep enough for the layers beneath it to have negligible effect on vibration transmission. However, the surface layers are sufficiently close to the tunnels and probably sufficiently different from the London Clay formation to have a significant effect on the wave-propagation behaviour of the ground in the vicinity of the tunnels.

6.2 Equipment Used

The vibration measurements presented in the following sections were all obtained using a transient testing approach with excitation provided by a hand-held impulse hammer. Measurements were recorded by a computerised data-logging system. All equipment was battery powered, making the outfit fully self-contained without the need for a generator. A schematic of the experimental set-up is shown in Figure 6.2 and details of the measuring equipment are given in Table 6.1.

6.2.1 Transducers and Amplifiers

Five piezoelectric accelerometers were used to detect the vibration response to hammer impulses. They were fixed in position on the track and the tunnel invert with small pieces of plasticine. They are convenient because of their small size and wide operating frequency range including low frequencies. Typical accelerometers give a small charge output proportional to acceleration.

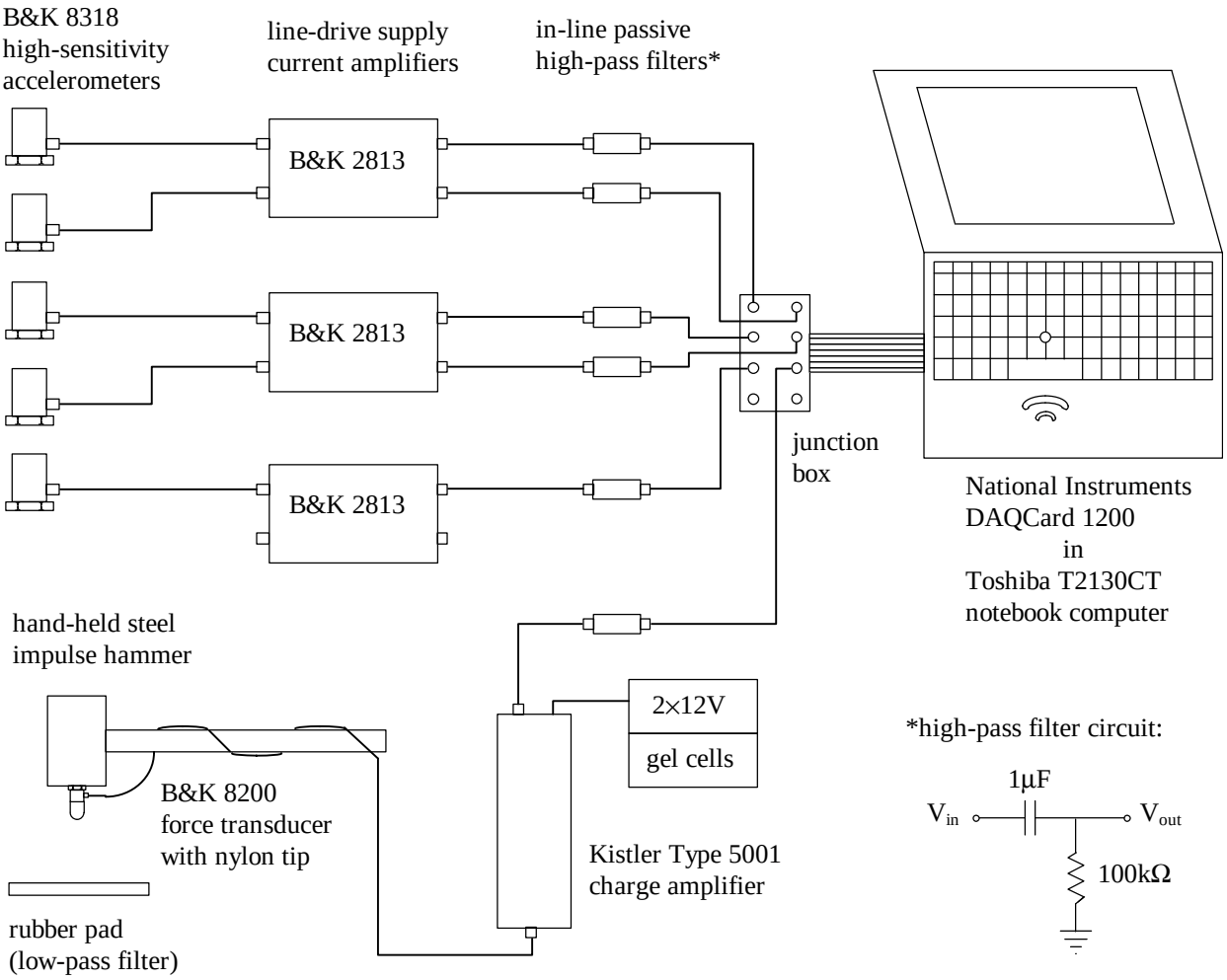

Figure 6.2: Schematic of the experimental set-up for vibration measurement and data logging.

Such accelerometers should be used with short, low-capacitance cables to minimise charge leakage. Their charge amplifiers must then be nearby, which can be inconvenient. However, the B&K 8318 accelerometers used have integral charge amplifiers giving a current output, which allows standard coaxial cables up to 1km long to be used without loss of signal; thus all other equipment can be located together, away from the accelerometers. In addition, they have a high sensitivity suitable for the low level of response expected from the track. The accelerometers were connected to B&K 2813 line-drive supply current amplifiers, each of which has two channels. The resulting voltage signals were passed through passive high-pass filters with a corner frequency of 1.6Hz to remove any DC offset before sampling.

The excitation force was provided by a hand-held impulse hammer. A B&K 8200 force transducer was mounted on the hammer head and the blow was delivered via a hard nylon tip attached to this transducer. Like the accelerometers, the force transducer is a piezoelectric

Item	Specification	Use
Brüel & Kjær 8318 accelerometers	$318\,\mu A/ms^{-2}$	measurement of track and tunnel vibration response
Brüel & Kjær 8200 force transducer	$4\,pC/N$	measurement of force applied by impulse hammer
Brüel & Kjær 2813 line-drive supply current amplifiers	$1\,mV/\mu A$	amplifiers for B&K 8318 accelerometers
Kistler Type 5001 charge amplifier	variable gain, set at $55\times10^{3}\ pC/V = 0.01818\,mV/pC$	amplifier for B&K 8200 force transducer
In-line passive filters	1.6Hz high pass unity gain	removal of any DC offset in transducer signals
Rubber pad	9mm-thick Tiflex FC846 (stiff black rubber with cork particles)	low-pass filtering by increasing duration of hammer impulse
National Instruments DAQCard 1200 data-acquisition PC Card	8-channel 12-bit A/D conversion 1022.5Hz sampling rate and 1024 sample points used gain set to 20	sampling transducer time signals
Toshiba T2130CT notebook computer	75MHz 486 microprocessor 16MB RAM 500MB hard disk	control of DAQCard 1200, data storage and analysis

Table 6.1: Details of the equipment used to determine track and tunnel impulse responses.

device, but its charge output is proportional to force. A Kistler Type 5001 charge amplifier was used to convert this into a voltage signal, which was also passed through a 1.6Hz high-pass filter before sampling. The gain was chosen by trial and error to give a voltage level comparable to that of the greatest accelerometer output. The Kistler amplifier comes as a mains-powered device, but in this case it was converted to run on two rechargeable gel cells set up as a ±12V DC supply.

6.2.2 Anti-Alias Filtering

The measured input force and resulting accelerations were digitally sampled. The Nyquist criterion requires that the sampling frequency be greater than twice the highest frequency contained in the sampled signal in order to avoid aliasing, whereby high-frequency components

appear as lower-frequency ones (see Newland [143, 144] or Stearns [168]). Thus it is standard to apply a low-pass filter to signals before sampling them, so that all components with frequency greater than the Nyquist frequency (half the sampling rate) are removed. The usual way to carry out this low-pass filtering is with some appropriate electronics.

A different approach was used here. Mathematically, an impulse can be idealised as a Dirac delta function of zero width in time and infinite height. However, a real hammer blow has a finite duration, which can be increased by applying the blow via a rubber pad as used here. A longer duration results in reduced higher-frequency content, justified as follows. A smooth impulse of finite duration can be considered as a half sine wave, the force distribution expected from a perfectly elastic impact. Such a pulse $y(t)$ of duration t_0, magnitude *a* and centred on $t = 0$ takes the form

$$y(t) = \begin{cases} \dfrac{a\pi}{2t_0}\cos\left(\dfrac{\pi t}{t_0}\right), & |t| \le \dfrac{t_0}{2} \\ 0, & |t| > \dfrac{t_0}{2} \end{cases} \tag{6.1}$$

The frequency content of the time signal $y(t)$ of (6.1) is described by its Fourier transform $Y(\omega)$, which is given in tables in Maloney et al [127] as

$$\begin{aligned} Y(\omega) &= \int_{-\infty}^{\infty} y(t)e^{-i\omega t}\,dt \\ &= \begin{cases} \dfrac{a\pi}{4}\left[\operatorname{sinc}\left(\dfrac{\omega t_0 - \pi}{2}\right) + \operatorname{sinc}\left(\dfrac{\omega t_0 + \pi}{2}\right)\right], & |\omega| \ne \dfrac{\pi}{t_0} \\ \dfrac{a\pi}{4}, & |\omega| = \dfrac{\pi}{t_0} \end{cases} \end{aligned} \tag{6.2}$$

where $\operatorname{sinc}(x) = \sin(x)/x$. Several rubber pads were tested in the laboratory with the hammer and a digital-storage CRO to assess the smoothness of the force impulse and to measure its duration. The FC846 pad used in the field measurements was chosen because it gave a repeatable smooth impulse like the half sine wave (some specimens gave a "double bounce" effect) with a duration of $t_0 = 4\,\text{ms}$. Figure 6.3(a) shows a representation of this impulse. Its spectrum calculated from (6.2) and given in Figure 6.3(b) shows that the impulse has no significant frequency content above 200Hz. Figure 6.3 also shows that halving the duration doubles the peak force for an impulse of the same magnitude, and increases the frequency

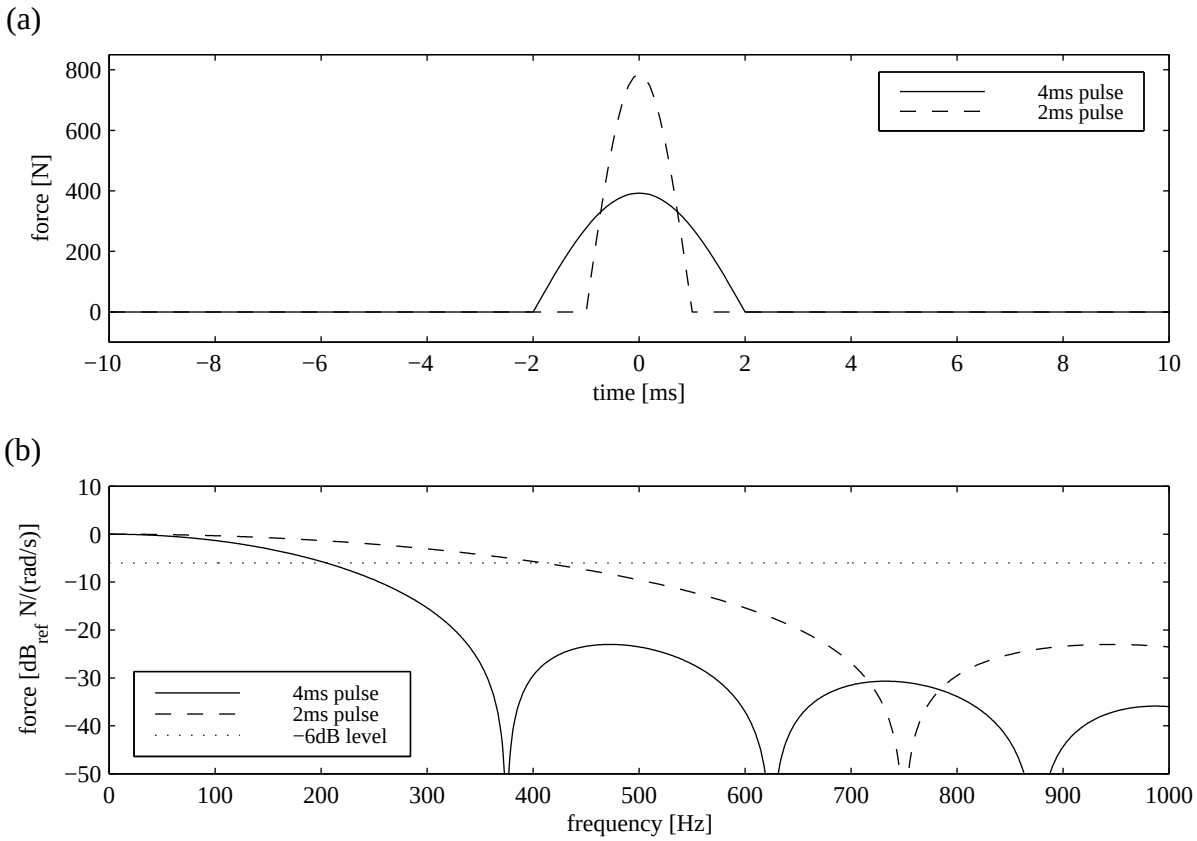

Figure 6.3: Unit impulses of finite duration represented by (a) half sine waves according to equation (6.1) have the frequency-domain spectra (b) calculated from equation (6.2). The longer 4ms pulse approximates the observed shape of the impulse when using the FC846 rubber pad.

content to 400Hz. This technique of manipulating the impulse duration is equivalent to low-pass filtering. The track was only excited by frequencies up to 200Hz, so if it is a linear system – a reasonable assumption for small-magnitude vibration – the responses will contain no significant components of frequency higher than this either. Using the rubber pad in lieu of electronic low-pass filtering meant one less piece of equipment to carry to the measurement area.

6.2.3 Data-Logging System

The data sampling was performed by a National Instruments DAQCard 1200, which fits in a PCMCIA slot in a notebook computer. The DAQCard provides eight channels of 12-bit analogue to digital conversion, of which six were used for the signals from the force transducer and five accelerometers. The maximum sampling rate is 100kHz, more than sufficient for the low frequency range considered. Given the Nyquist criterion and the filtering effect of the rubber pad, a sampling rate of 1kHz was chosen; the DAQCard's nearest setting with six channels in use was 1022.5Hz. Preliminary tests showed that 1s was long enough to capture the transient track

responses, so 1024 samples per channel were taken for each measurement set. The DAQCard provides pre-sampling analogue gain of 1, 2, 5, 10, 20, 50 or 100, the same value applying to all channels. A gain of 20 was found to be the maximum useable without saturating any of the channels. The DAQCard's sampling method is to poll each channel in turn within one sample period. This results in a small artificial phase shift from one channel to the next, which must be corrected at the data analysis stage.

The DAQCard was controlled by a Visual Basic program running on the Toshiba notebook computer. This program was used to make all card settings, start data logging, check for channel saturation and save sampled data to the computer's hard disk. The experimental procedure involved one person operating the computer and providing a countdown to the start of sampling for a second person using the impulse hammer. Some Matlab programs were then used to examine the saved raw data, in particular to check that the impulse was smooth. Responses for any given configuration of accelerometers and impulse input were all measured twice to allow repeatability to be checked.

Figure 6.4 shows the railway tunnel with accelerometers set up along the track slab. The rest of the measuring equipment can be seen in the background. Figure 6.5 shows how the rubber pad was placed on the concrete surface where the impulse was applied, with accelerometers placed across the slab in this case. The rubber pad was steadied with one hand while the hammer was wielded in the other.

6.3 Data Processing

The aim is to calculate frequency-response functions (FRFs) from the time records of input force and acceleration. Since the recorded signals are discrete, they can be transformed into the frequency domain by means of the discrete Fourier transform (DFT) (see Newland [143, 144] or Stearns [168]). DFTs can be calculated using the fast Fourier transform (FFT) algorithm. The FRFs are then given by the ratios of each transformed acceleration to the transformed force, with the appropriate sampling phase correction applied in each case.

Figure 6.4: Photograph of the tunnel, showing at left the supports for the incomplete track-side walkway and above them the wedge-shaped keys in the tunnel lining. The accelerometers are set out along the floating-slab track and the rest of the equipment can be seen in the background.

Figure 6.5: Photograph showing the use of the impulse hammer in conjunction with a rubber pad resting on the structure to be excited. Here the accelerometers are set out across the track.

Figure 6.6 gives typical time records for the sampled force and acceleration signals with accelerometers placed along the track slab. There are some features which were introduced by the measuring equipment and must be removed before FRFs are calculated. Each record has a start-up exponential and decays to a non-zero DC offset long after the transient has finished. In addition, the impulse in Figure 6.6(a) overshoots "zero" after its peak force. The records also contain small-magnitude random noise either side of the transients, particularly significant for the low signal levels from accelerometers far from the impulse, such as those in Figures 6.6(e) and (f). It was found that the noise issuing from accelerometer 2, Figure 6.6(c), was of greater amplitude than the others, so this accelerometer was always used where the response was expected to be large. Some approaches to removing noise in signals from electronic instrumentation are discussed in Wilmhurst [190], on which the following signal-conditioning procedures are partly based.

An interactive Matlab program was written to extract the true impulse and acceleration signals from the recorded ones. This program plotted a given record on screen at each stage of conditioning, allowing graphical selection of points when necessary. The program was used to condition each measurement set of one force record and five acceleration records, and to save the conditioned records in a new data file. The conditioning processes for the impulse and the accelerations are slightly different, so will be described separately.

6.3.1 Conditioning the Impulse Signal

The steps in conditioning a typical impulse record are illustrated in Figure 6.7. The final DC offset in the raw signal is apparent in Figure 6.7(a). A point well after the impulse, marked by a cross, is manually selected and the mean of all points from this to the end of the sample is calculated. This end mean is subtracted to give the signal in Figure 6.7(b).

Two points defining the ends of the start-up exponential, marked by crosses in Figure 6.7(b), are then manually selected. All sample points between the selected ends are used to determine the coefficients A and b of the function

$$y_1(t) = Ae^{-bt} \tag{6.3}$$

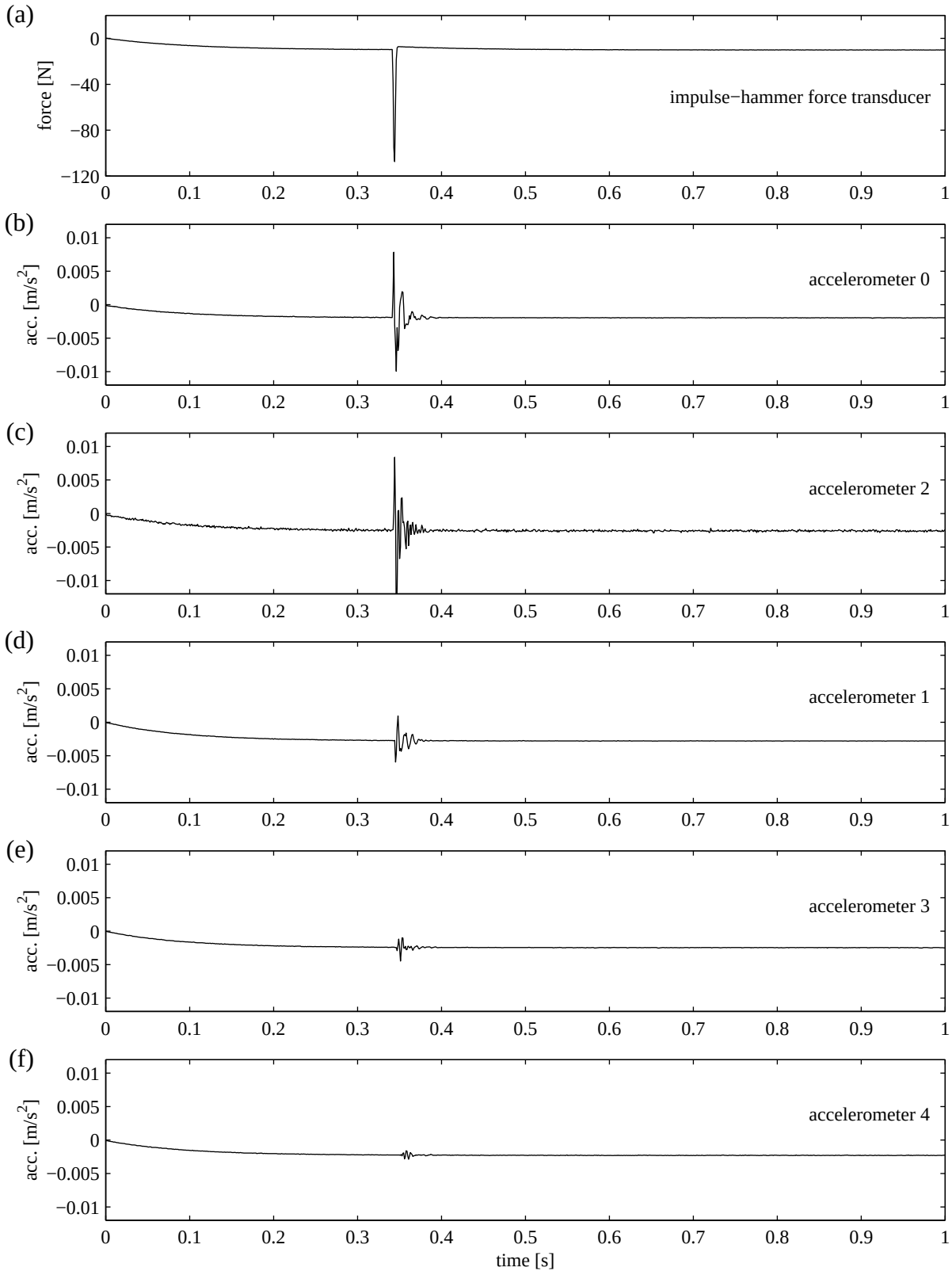

Figure 6.6: Typical raw time records of (a) a force impulse applied midway across the floating slab, (b) slab acceleration at the impulse, (c) rail acceleration next to the impulse, and slab accelerations (d) 5m, (e) 10m and (f) 20m along the slab from the impulse. After signal conditioning and transformation by FFT, records (b)-(f) referenced to record (a) give the FRFs in Figure 6.18.

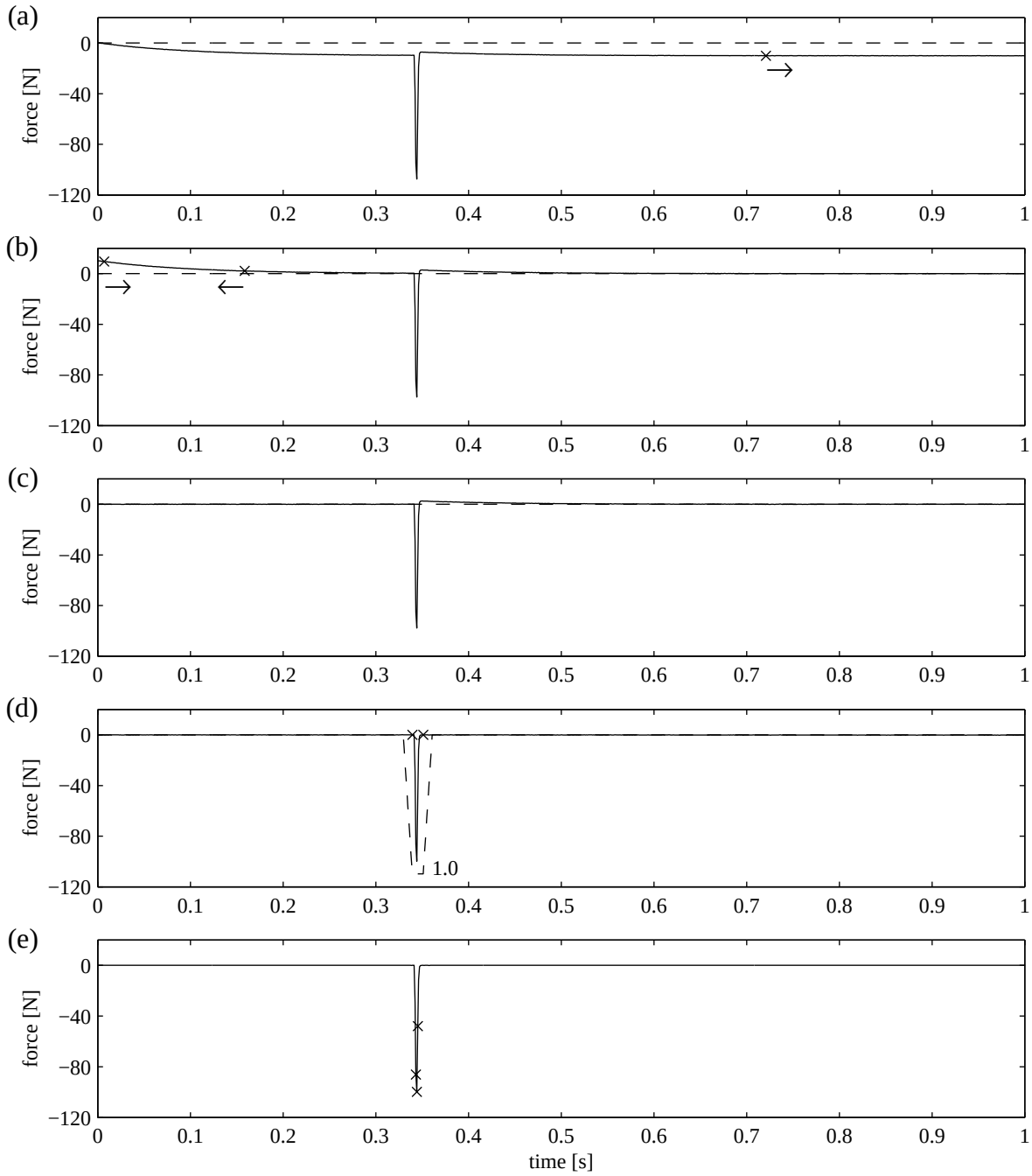

Figure 6.7: The various stages of conditioning an impulse record (using that of Figure 6.6(a) as the example) are (a) subtracting the end mean, (b) subtracting the start-up exponential, (c) eliminating the return overshoot of the impulse caused by the high-pass filter, (d) windowing the non-zero portion of the signal and (e) calculating the position of the impulse's peak for use in conditioning the corresponding acceleration records.

via a linear regression on t and $\log_e y_1$. The start-up exponential (6.3) is then subtracted from the whole signal to give the signal in Figure 6.7(c).

The overshoot just after the peak of the impulse, still present in Figure 6.7(c), is due to the high-pass filter used (see Cryer [38]). Such a filter comprising a first-order resistor-capacitor network with unit gain at high frequencies is described by the differential equation

$$\frac{df}{dt} = \frac{dg}{dt} + \omega_0 g \tag{6.4}$$

where $f(t)$ is the input signal, $g(t)$ is the output signal and ω_0 is the filter's cut-off frequency (1.6Hz in this case). Integrating (6.4) up to time t results in the equation

$$f(t) = g(t) + \omega_0 \int_{-\infty}^{t} g(t)dt \tag{6.5}$$

for the input signal. Applying the integration in (6.5) numerically (by the trapezoidal rule) to the signal in Figure 6.6(c) taken as $g(t)$ results in the impulse signal of Figure 6.6(d) taken as $f(t)$.

The signal in Figure 6.6(d) still contains some random noise before and after the impulse. This noise is not very noticeable here because the impulse is of relatively large peak amplitude, but it still affects the smoothness of FRFs. To eliminate the noise, the non-zero part of the signal is windowed. The start and finish of the impulse are manually selected (marked with crosses), and the signal is multiplied by a window of unit magnitude between these two points and tapered off to zero over 10 samples on either side. The tapering avoids discontinuities which can arise from the use of a rectangular window; such discontinuities introduce spurious frequency content, known as spectral leakage. This is not as great an issue for a transient signal such as this (where windowing is used to remove extraneous noise) as for a periodic signal (where windowing is used to make the signal suitable for transformation by DFT). A Hanning window (see Stearns [168]) might be used in the latter case. The window used here makes the parts of the signal which are expected to be zero actually zero, as shown in Figure 6.7(e).

Conditioning the acceleration records, described in the next section, requires knowledge of the precise position of the peak of the impulse (as opposed to the maximum magnitude recorded). Taking the tip of the impulse as approximately parabolic, the equation

$$y_2 = a_1 t^2 + a_2 t + a_3 \tag{6.6}$$

is fitted by a least-squares method to the signal maximum and the two samples either side of it. These three points are marked with crosses in Figure 6.7(e). The actual peak of the impulse is assumed to occur at the parabola's turning point, given by

$$\frac{dy_2}{dt} = 0 \quad \Rightarrow \quad t = -\frac{a_2}{2a_1} \tag{6.7}$$

This value of *t* usually falls between two samples.

6.3.2 Conditioning the Acceleration Signals

The steps in conditioning a typical acceleration record are illustrated in Figure 6.8. The removal of the DC offset, the start-up exponential and the extraneous noise by windowing, Figures 6.8(a)-(c), are carried out in the same way as described for the same operations on the recorded impulse signal. These three steps may seem to be all that is required, but examination of the velocity reveals otherwise.

The velocity $\dot{y}(t)$ is the integral up to time *t* of the acceleration $\ddot{y}(t)$. This integration can be performed numerically on the discrete acceleration record using the trapezoidal rule. Thus the discrete sampled velocity $\dot{y}_k$ can be written as a summation

$$\dot{y}_k = \sum_{j=1}^{k} \ddot{y}_j \Delta t \tag{6.8}$$

of the discrete sampled acceleration $\ddot{y}_j$, where Δt is the sampling period. Applying (6.8) to the windowed acceleration signal results in the velocity signal of Figure 6.8(d). This shows a non-zero final velocity, indicating a non-zero average of the recorded acceleration. This does not tally with the observed behaviour of the tunnel system where responses obviously decayed to nothing very quickly. The acceleration record needs to be corrected so that the final velocity is zero.

When an impulsive force is applied to a system initially at rest, there is a step in the velocity and hence an impulse like a Dirac delta function in the acceleration. It is postulated that this initial acceleration impulse was not properly captured with the sampling rate used. This situation can be remedied by adding a corrective acceleration impulse at the time of the true peak of the input force, determined in the previous section. The magnitude $\ddot{y}_{\text{init}}$ of this corrective impulse is given by

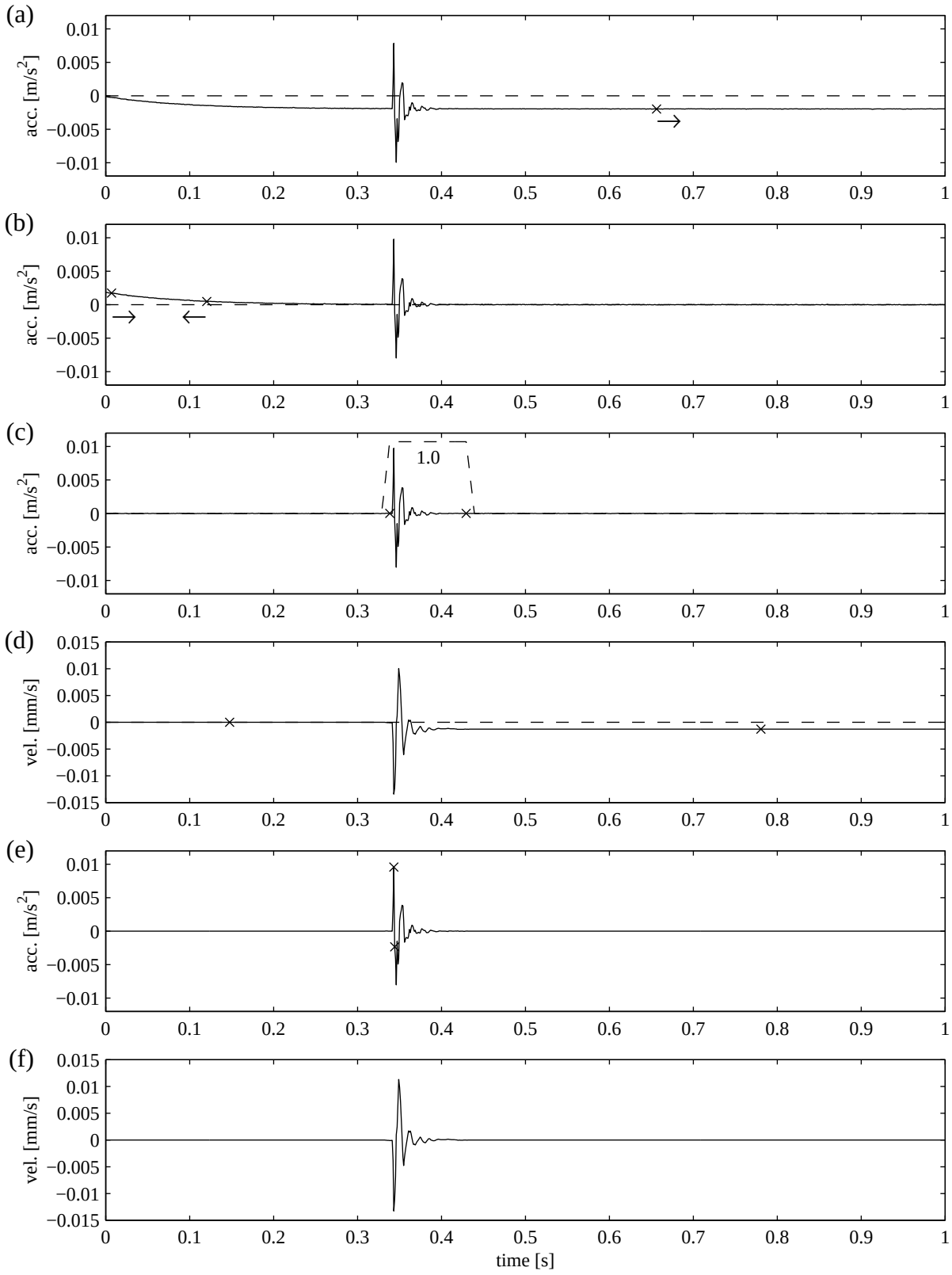

Figure 6.8: The various stages in conditioning an acceleration record (using that of Figure 6.6(b) as the example) are (a) subtracting the end mean, (b) subtracting the start-up exponential, (c) windowing the non-zero portion of the signal, (d) calculating the final velocity step arising when the windowed acceleration is integrated and (e) using this to apply a corrective initial impulse to the acceleration signal to give (f) a final velocity of zero.

$$\ddot{y}_{\text{init}} = -\frac{\Delta\dot{y}}{\Delta t} = -\frac{(\dot{y}_{\text{final}} - \dot{y}_{\text{init}})}{\Delta t} \tag{6.9}$$

that is, the negative of the (falsely non-zero) average acceleration, with the velocity step $\Delta\dot{y}$ calculated as the difference in amplitude between the two samples marked with crosses in Figure 6.8(d). The time interval for determining the average acceleration is Δt because the correction is applied across just one sample; if the mean acceleration were subtracted from the whole signal, the total sample time would be used instead.

The peak force position where the correction should be applied in general falls between two samples, because of both the peak calculation (6.7) and the artificial sampling phase shifts. Thus the acceleration correction (6.9) is implemented as the sum of two separate impulses applied at the two samples either side of the calculated force peak and weighted to have the resultant impulse centre in the correct position. Figure 6.8(e) shows the corrected acceleration with the two altered samples marked with crosses. Integrating the corrected acceleration gives a final velocity of zero, as shown in Figure 6.8(f).

Figure 6.9 shows FRFs calculated from the time records of Figures 6.7 and 6.8 using various combinations of raw and conditioned impulse and acceleration data. The three FRFs based on at least one raw data record all contain periodic variation of 5-10dB magnitude with a frequency interval of 2-3Hz. The small-magnitude random noise apparent on either side of the transients in the time records probably contains frequencies above the Nyquist frequency, since no low-pass filter was used before sampling. These frequencies will have been aliased to lower ones, resulting in the variation in the FRFs. Nevertheless, this variation can be eliminated by windowing the non-zero portions of both the impulse and acceleration records, as shown by the one smooth FRF. Conditioning the acceleration has a very significant effect on the calculated FRF, particularly below 40Hz. This effect is due to the initial acceleration correction applied to give a zero final velocity. Conditioning the impulse and acceleration records as described above results in usable data despite the sampling rate being too low to correctly capture some features of the sampled signals.

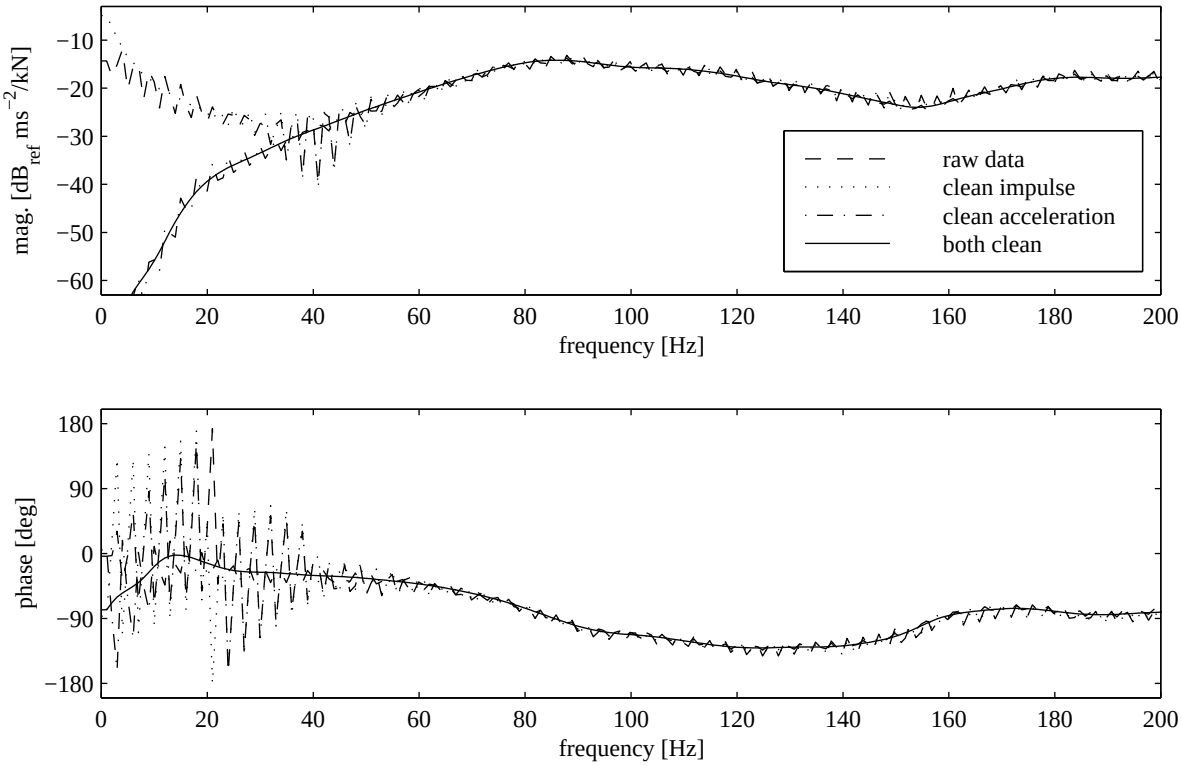

Figure 6.9: FRF calculated as the ratio of the FFT of the acceleration in Figure 6.8 to the FFT of the input force in Figure 6.7, using: the raw unconditioned data in both cases; the fully conditioned impulse and the raw acceleration; the raw impulse and the fully conditioned acceleration; and the fully conditioned data in both cases.

6.4 Results

Some basic modelling can be considered before examining the measured track responses. In Section 5.1.3 it was found that the driving-point response of a continuous simple slab beam on the tunnel is reasonably well approximated by a Winkler beam model (although other responses are not) if the slab bearings are soft compared to the tunnel invert. The experimentally measured driving-point responses of the track can therefore be compared for similarities to the Winkler response $Y(x,\omega)$ given by equation (5.15) with $x = 0$, since the Heathrow Express track has an effectively continuous slab. The slab-beam parameters given in Table 3.1 represent design values which were used for the floating-slab section of the Heathrow Express line: in the notation of (5.15), a mass per unit length of $m = 3500\,\mathrm{kg/m}$, a bending stiffness of $EI = 1430 \times 10^6\ \mathrm{Pa.m^4}$ and a foundation stiffness of $k_W = 50 \times 10^6\ \mathrm{N/m^2}$. Thus the natural frequency that the floating slab was designed for is $f_n = \frac{1}{2\pi}\sqrt{k_W/m} = 19\,\mathrm{Hz}$. These parameters

can be used with (5.15) to calculate the expected driving-point displacement FRF of the track slab. Since the measured responses are accelerations, it is also useful to examine the expected acceleration FRF, which is simply given by $-\omega^2 Y(0,\omega)$.

The driving-point displacement and acceleration FRFs of the Winkler beam model are given in Figure 6.10 for various values of viscous damping factor ζ as used in Chapter 2. This form of damping is frequency dependent such that a complex stiffness per unit length $k_W{}^* = k_W(1+i\omega\zeta)$ is used in equation (5.15). For small values of ζ, the displacement, Figure 6.10(a), shows a distinct resonance at the 19Hz natural frequency, but this peak is flattened and eventually depressed as the damping is increased. Similar behaviour is shown by the acceleration in Figure 6.10(b).

Another way to describe damping is with a constant loss factor η as used in Chapters 4 and 5. In this case, a constant complex stiffness per unit length $k_W{}^* = k_W(1+i\eta)$ is used in equation (5.15). Figure 6.11 shows the driving-point displacement and acceleration FRFs for various

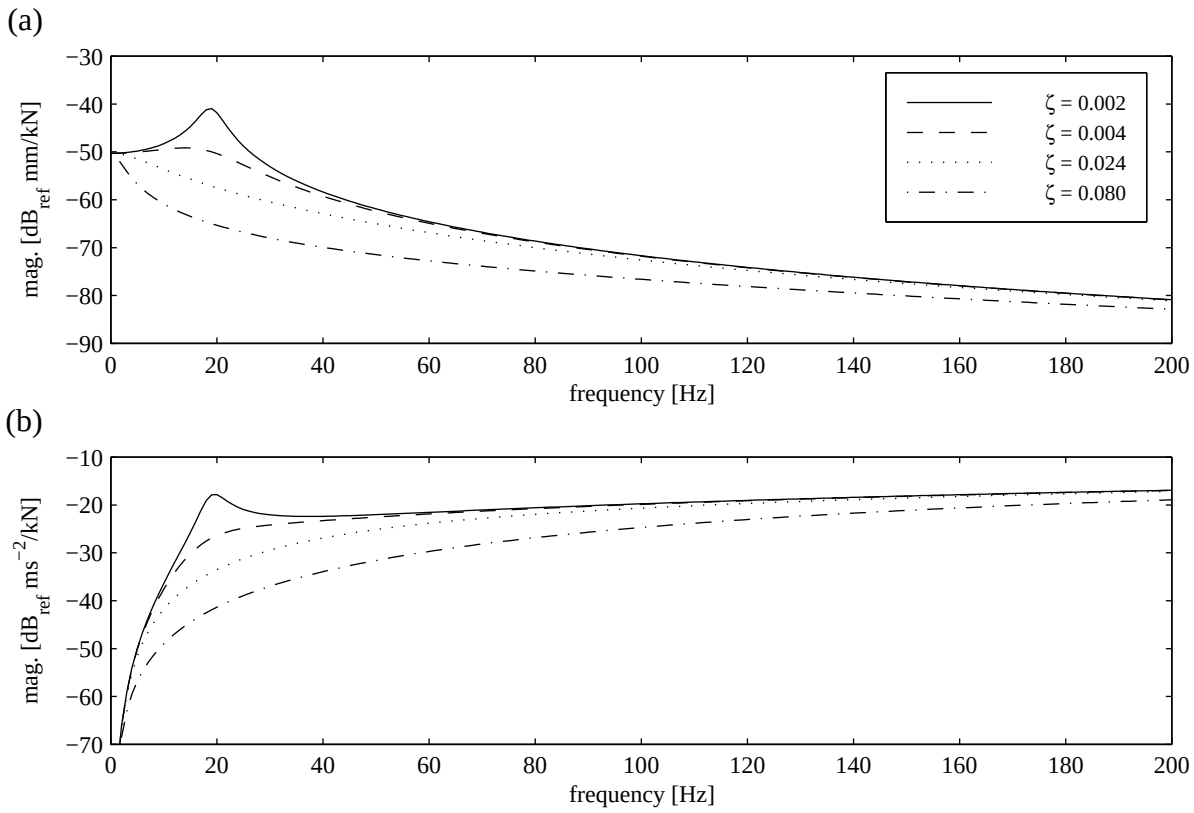

Figure 6.10: The effect of varying viscous slab-bearing damping on the (a) displacement and (b) acceleration driving-point responses of a Winkler-beam model of the floating slab. Slab-beam properties from Table 3.1.

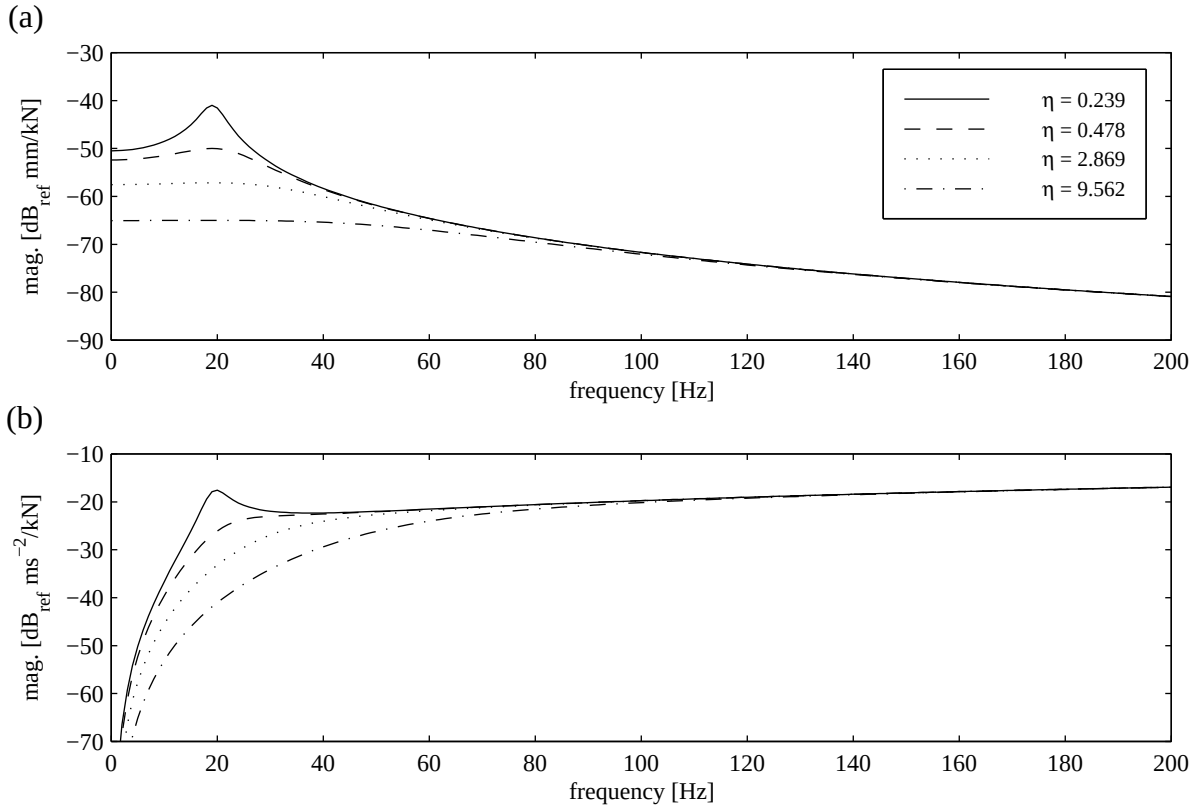

Figure 6.11: The effect of varying loss-factor slab-bearing damping on the (a) displacement and (b) acceleration driving-point responses of a Winkler-beam model of the floating slab. The loss-factors are equivalent to the values of viscous damping in Figure 6.9 at the Winkler beam's natural frequency of 19Hz. Slab-beam properties from Table 3.1.

values of loss-factor damping chosen to be equal to the viscous damping of Figure 6.10 at the 19Hz natural frequency of the slab on its bearings. The acceleration, Figure 6.11(b), looks very similar to that in Figure 6.10(b), with the resonance peak well and truly disappearing with increased damping. However, the displacement response, Figure 6.11(a), is flatter than that in Figure 6.10(a) below about 40Hz for the two higher damping values, although the behaviour for low damping is very similar with a prominent resonance. The most highly damped displacement response with $\eta = 9.562$ is reminiscent of the response of the simple slab beam joined directly to the tunnel invert, shown in Figure 5.4. In Figure 5.4, the Winkler beam model does not agree well with the slab-plus-tunnel model, but the damping in the "effective" Winkler stiffness of the tunnel invert does not take into account the radiation of energy into the surrounding soil in that case. Figure 6.11 shows that the Winkler-beam driving-point response can represent that of a slab beam closely coupled to a tunnel if the Winkler foundation damping is high enough.

The experimentally determined track FRFs can now be considered. They were obtained from a given set of conditioned impulse-response data by taking the ratio of the FFT of each of the five acceleration records to the FFT of the impulse record for that set. Corrections were applied for the calibration factors of the instrumentation and the phase shifts due to the sampling by sequential channel polling. A Matlab program was written to carry out these operations.

6.4.1 FRFs Measured Across the Track Slab

The accelerations measured across the floating slab with a force applied at the middle of the slab are given in Figure 6.12. The driving-point acceleration 2 looks like the acceleration in Figures 6.10(b) or 6.11(b) when the damping is high; the other positions across the slab look similar, with no 19Hz resonance peak apparent. Acceleration 2 is highest being next to the input force, and the off-slab responses 0 and 4 are significantly lower than the on-slab ones. Given the symmetric excitation, the edge accelerations 1 and 3 would be expected to have the same magnitude and be in phase with 2. However, there is a difference of up to 10dB between 1 and 3,

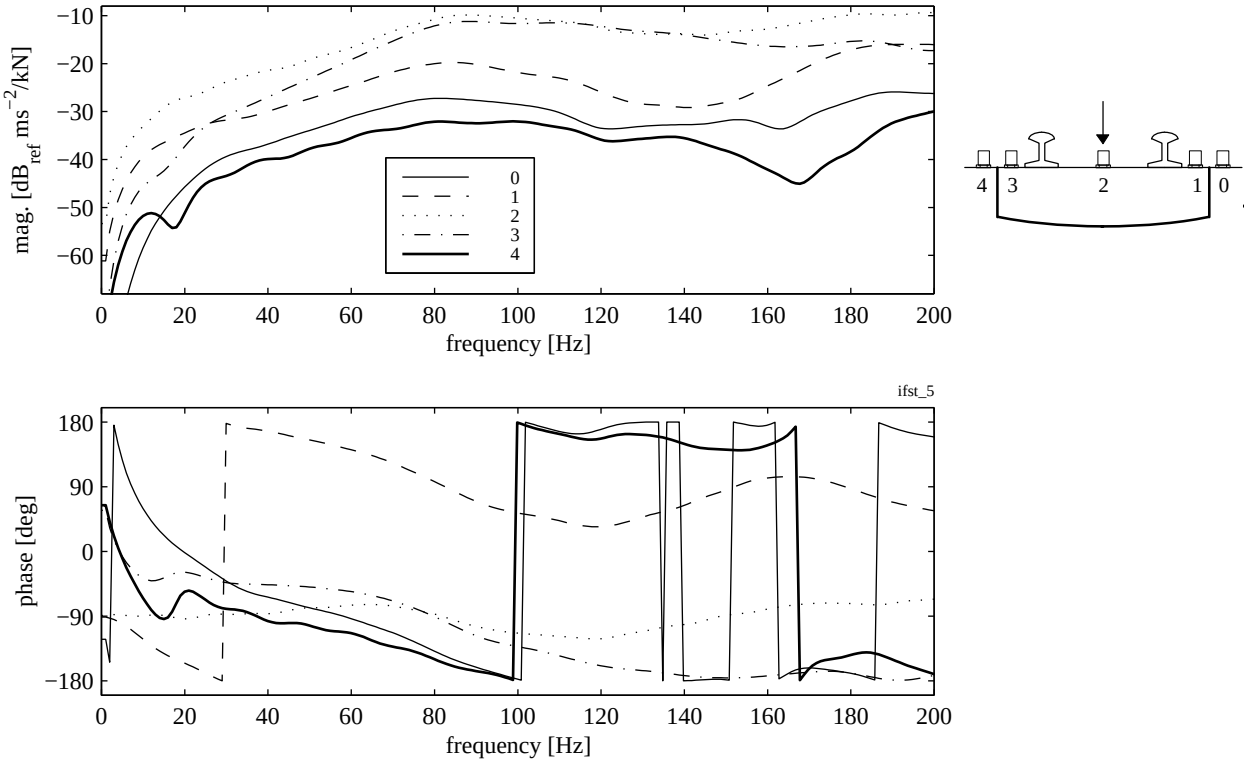

Figure 6.12: Vertical acceleration FRFs across the floating slab with a central vertical input force applied next to accelerometer 2. The cross-section at right shows the accelerometer positions, with the thick line indicating the slab boundary; thus accelerometers 0 and 4 are on the tunnel invert either side of the slab.

and 1 is about 180° out of phase with 2 and 3. Although the cause for the magnitude difference is unclear, it is possible that the recorded 180° phase difference is artificial. The B&K 2813 line-drive supplies have a slider switch for each channel which can be set at either "grounded" (only the AC component of the accelerometer signal is passed) or "floating" (the whole signal is passed). It was found that for the same input, "floating" output is out of phase with "grounded" output. While all these switches were checked to be in the "grounded" position before commencing measurements in one location, they are very easily accidentally knocked into the other position. Therefore the observed phase difference between 1 and 3 could have been caused by accelerometer 1's channel being in the "floating" position.

The displacement $Y(\omega)$ corresponding to a measured acceleration $\ddot{Y}(\omega)$ can be obtained from the relation $Y(\omega) = -\ddot{Y}(\omega)/\omega^2$. Figure 6.13 shows the displacement FRFs corresponding to the acceleration FRFs of Figure 6.12. The same comments can be made about the magnitudes and the phases: the relative phases are now quite clear. There are definitely no resonance peaks at 19Hz. The shape of the driving-point displacement magnitude 2 looks very like the most

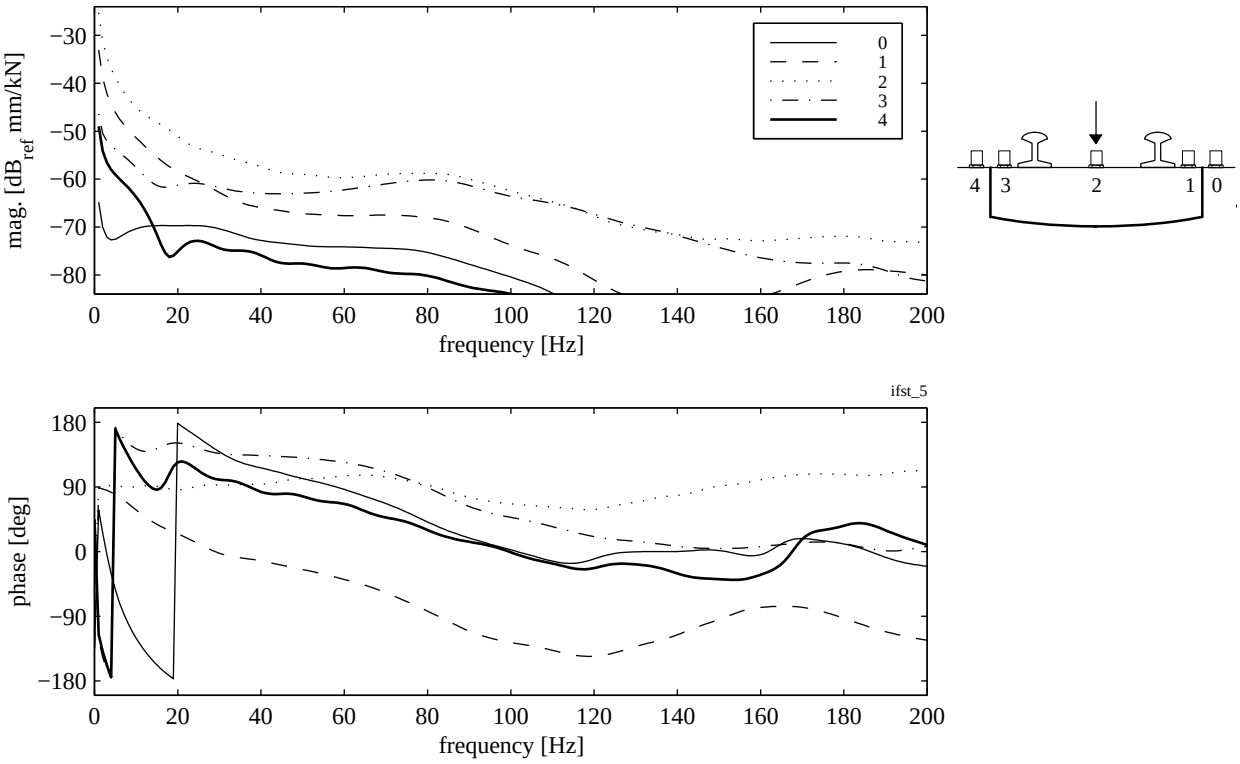

Figure 6.13: Vertical displacement FRFs across the floating slab with a central vertical input force applied next to accelerometer 2. These are derived from the acceleration FRFs shown in Figure 6.12.

highly viscously damped response (the chained line) in Figure 6.10(a), rather than any of the displacements in Figure 6.11(a). This implies that the energy loss due to the combined effect of material damping and radiation into the soil increases with frequency, as does that modelled theoretically by viscous damping. Also, as noted earlier, its loss-factor damped counterpart in Figure 6.11(a) resembles the driving-point response of the slab-plus-tunnel model with a directly joined slab, shown in Figure 5.4. These factors suggest that the Heathrow Express floating slab is more closely coupled to the tunnel than taken into account by the original design calculations, which assumed a rigid tunnel invert.

Figure 6.14 shows the vertical accelerations across the unisolated track with an input force at the middle. Compared to the corresponding floating-slab results in Figure 6.12, they are all of similar magnitude, with accelerations 1, 2 and 3 reduced by about 10dB over the whole frequency range, and accelerations 0 and 4 are the same as before. The phases are all similar and there are no out-of-phase discrepancies as discussed above. The observed reductions in magnitude indicate that energy is being propagated more readily to the tunnel and soil than when

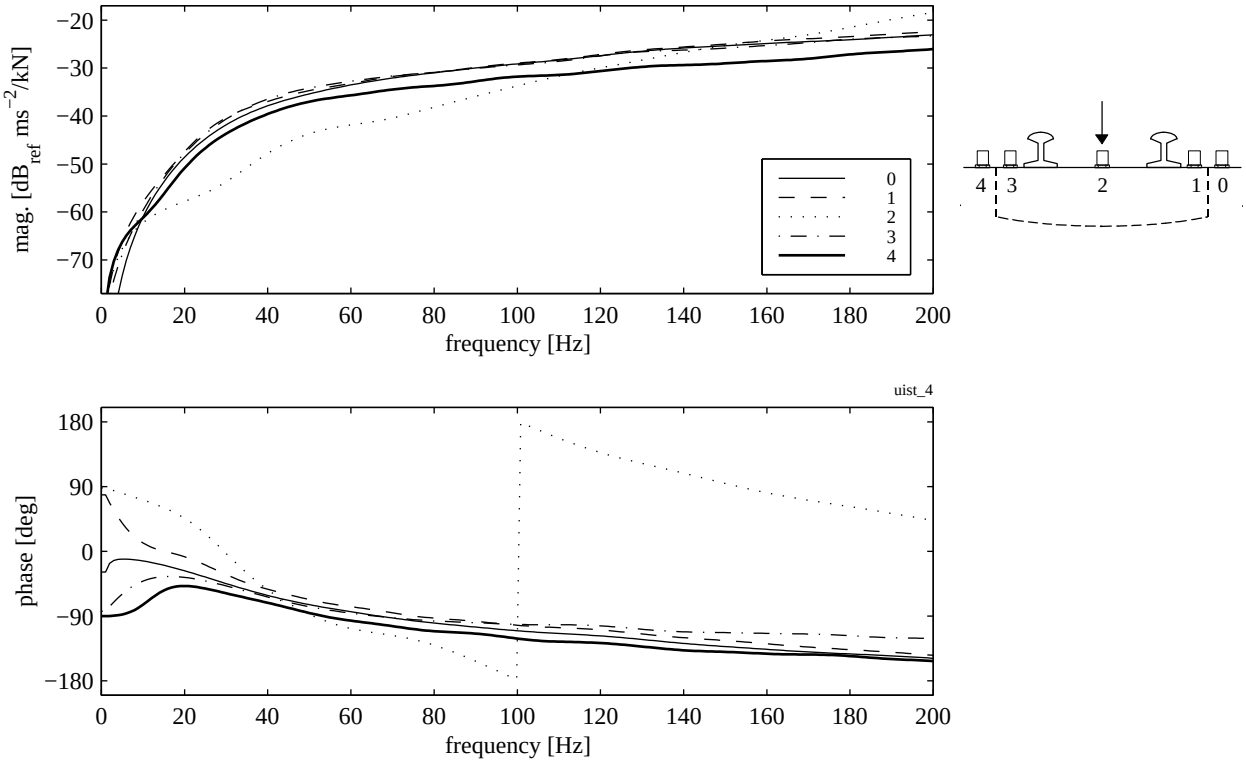

Figure 6.14: Vertical acceleration FRFs across the unisolated track with a central vertical input force applied next to accelerometer 2. The dotted line in the cross-section at right indicates where the slab boundary would be were it a floating slab.

the slab is floated, demonstrating that the FC75 rubber does alter the track dynamics.

The responses to an off-centre force applied to the floating-slab track are shown in Figure 6.15. As for the central load case of Figure 6.12, the off-slab responses 0 and 4 are generally lower than the on-slab ones, but acceleration 0 is higher, being closer to the applied load at 1. Since the accelerations of both slab edges 1 and 3 are of similar magnitude, the higher response at 0 compared to 4 confirms that the slab is closely coupled to the tunnel. Stiff coupling results in direct transfer of energy from the hammer input force at 1 to position 0 rather than an indirect transfer through the induced motion of the slab. The latter would be implied by similar levels at 0 and 4 given the similar levels of the respective adjacent slab edges 1 and 3. Also note that with this off-centre input, the edges 1 and 3 move more than the centre 2. This indicates a rocking motion, that is, torsion of the slab. The phases are not entirely clear on this, but since this measurement set was done at the same time as that shown in Figure 6.11, the same artificial 180° phase difference could be present in acceleration 1. If so, this would mean that the edges 1 and 3 move nearly out-of-phase here, instead of nearly in-phase as recorded. While the combination of bending and torsion expected to be induced by an off-centre input would not result in perfectly

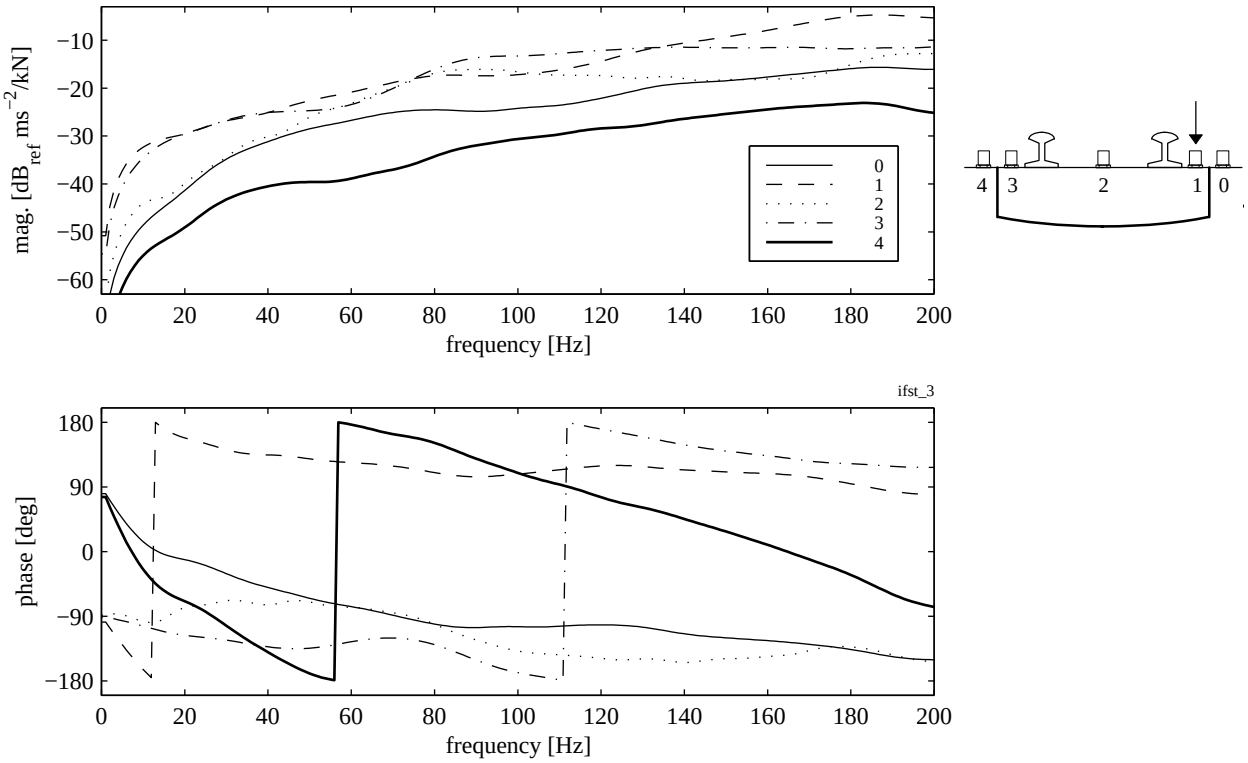

Figure 6.15: Vertical acceleration FRFs across the floating slab with an off-centre vertical input force applied next to accelerometer 1.

out-of-phase edge accelerations, a significant phase difference would confirm the presence of slab torsion. If there is no phase error, then all positions on the slab (1, 2 and 3) move roughly together. This could indicate that the pivot point for the rocking motion is not the centre of the slab, but this would not tally with the observed magnitudes where the centre 2 moves less than the two edges. In either case, the important observation is that the relative phase between the slab edges is *different* from that for a central input as given in Figure 6.11.

The equivalent accelerations for the unisolated track are given in Figure 6.16. Like Figure 6.14, the levels at 1, 2 and 3 are reduced by about 10dB compared to the floating slab. The situation is now one of vibration propagation through the continuous concrete of the track slab and tunnel invert. The magnitudes depend purely on distance from the excitation force, with no rocking motion manifesting itself in the responses. The highest magnitude is at 1, closest to the impulse, and the magnitudes decrease with distance, 3 and 4 being the lowest as they are furthest away. The phases confirm this. The phase of 1 is near zero, since it is the driving point; the phase becomes more negative (taking phase wrap-around into account) the further the measurement point is from the input force, indicating longer time lags. These differences from

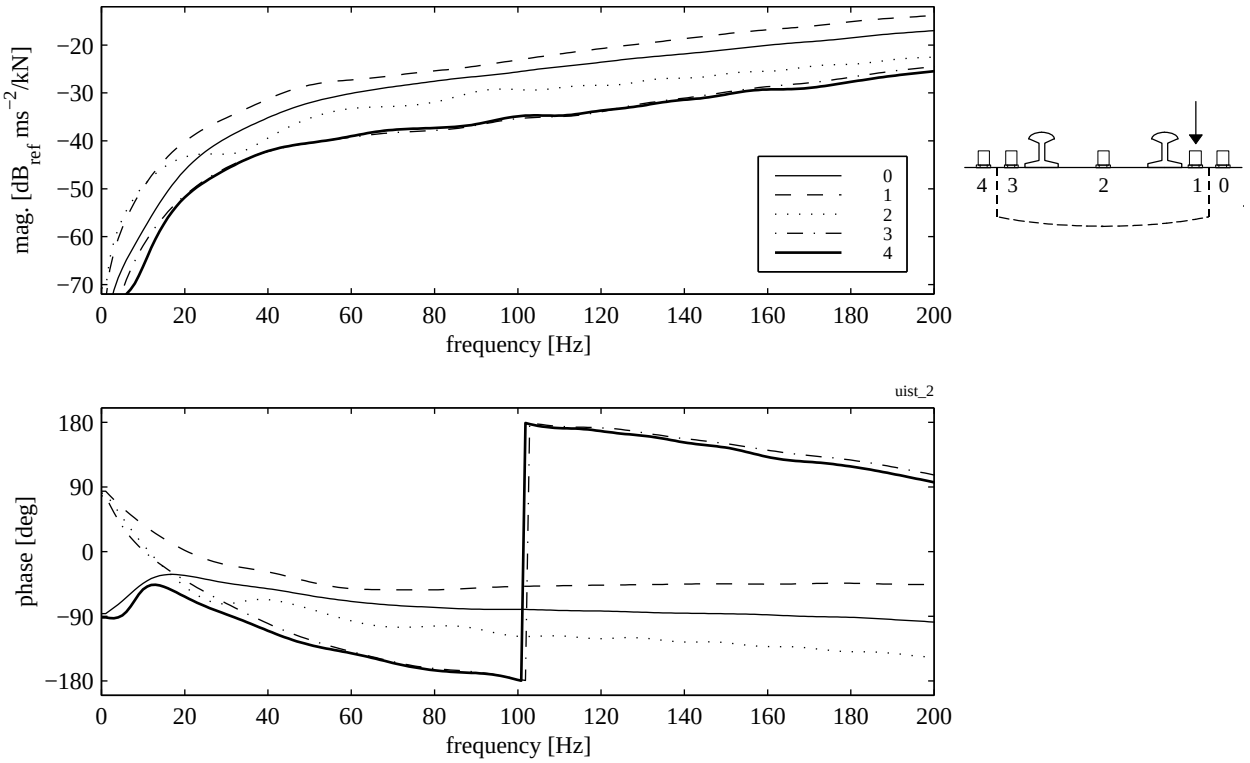

Figure 6.16: Vertical acceleration FRFs across the unisolated track with an off-centre vertical input force applied next to accelerometer 1.

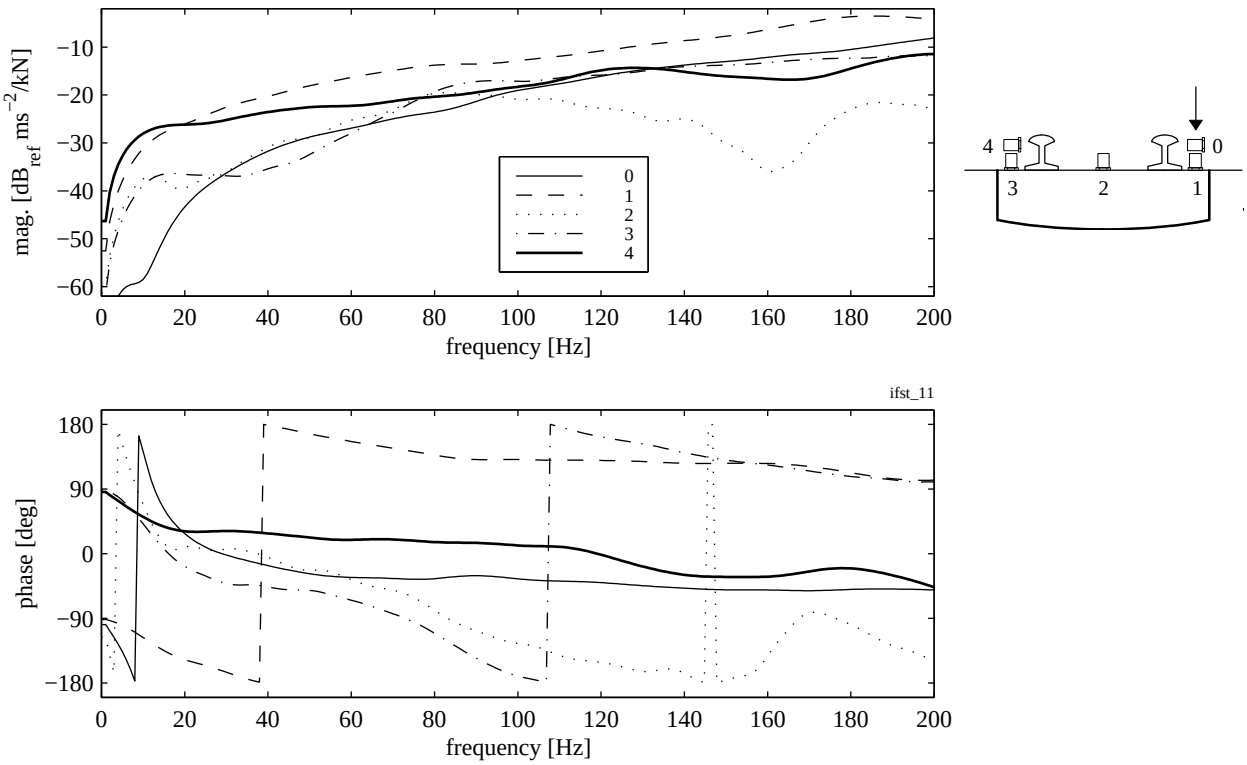

Figure 6.17: Vertical and lateral acceleration FRFs across the floating slab with an off-centre vertical input force applied next to accelerometer 1. Accelerometers 0 and 4 were placed on the slab on their sides, next to accelerometers 1 and 3.

Figure 6.15 again show that the insertion of the FC75 rubber changes the track dynamics.

Lateral slab acceleration is compared to vertical slab acceleration in Figure 6.17. Accelerometers 0 and 4 were fixed to the slab on their sides instead of vertically, placed next to accelerometers 1 and 3. The lateral motion induced by a vertical force input is clearly significant, since the lateral accelerations 0 and 4 are of similar magnitude to the vertical accelerations 1 and 3 at the same positions.

6.4.2 FRFs Measured Along the Track Slab

Figure 6.18 shows the vertical accelerations along the centre of the slab excited by a central force. Like the measurements across the slab, there are no clear resonance peaks, let alone one at 19Hz. The acceleration 2 of the rail next to the input follows that of the driving point 0 very closely. This is because the relatively stiff rail pads give a natural frequency of the rail on the rail pads well above the 200Hz maximum frequency considered here, so that the rail moves with the slab when the slab is excited. Acceleration 0 is also similar in both magnitude and phase to the corresponding slab-centre response 2 given in Figure 6.12, confirming the repeatability of this

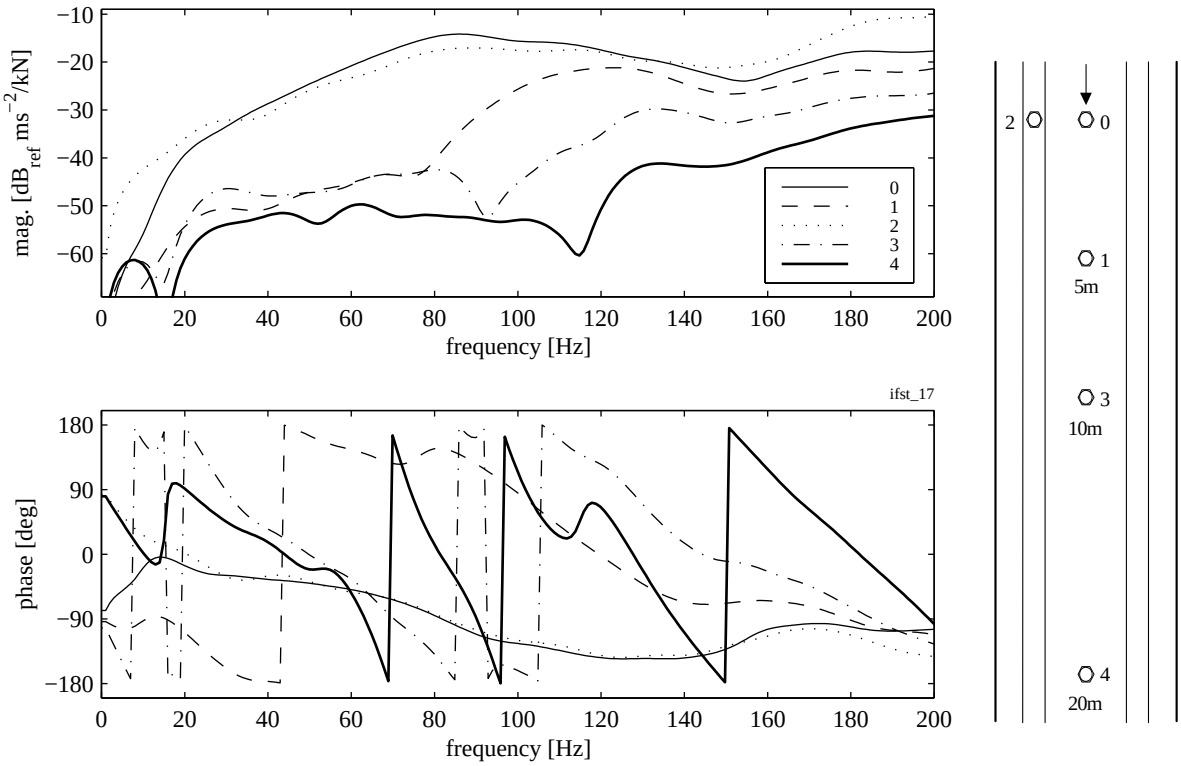

Figure 6.18: Vertical acceleration FRFs along the middle of the floating slab with a central vertical input force applied next to accelerometer 0. The plan view of the track at right shows the positions of the accelerometers, with the thick lines again indicating the edges of the slab; accelerometer 2 is mounted on one of the rails.

driving-point response. The responses 1 at 5m down the slab from the input, 3 at 10m and 4 at 20m show more variation than the driving point 0, but essentially they show that the response decreases with distance from the load. The low levels between 30Hz and 120Hz compared to acceleration 0 indicate that less energy is propagated down the slab in this range than at higher frequencies.

The corresponding responses along the unisolated track are shown in Figure 6.19. The accelerations are smoother than in Figure 6.18. Having the track slab fixed to the tunnel invert has suppressed some of the floating-slab dynamics. The driving-point response 0 is significantly lower for frequencies above 40Hz, and the responses 1, 3 and 4 at increasing distance from the input are between 10dB and 15dB lower than those in Figure 6.18, particularly above 80Hz. This is further confirmation that the FC75 rubber does influence the track response.

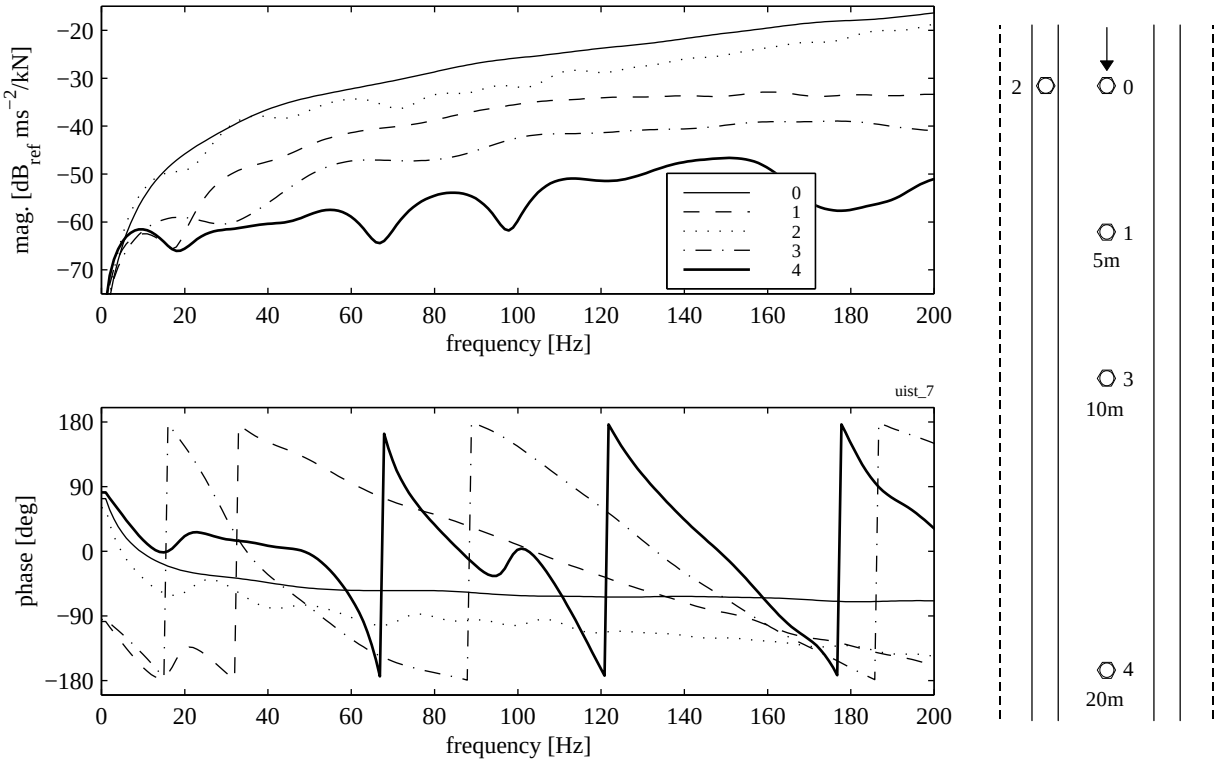

Figure 6.19: Vertical acceleration FRFs along the middle of the unisolated track with a central vertical input force applied next to accelerometer 0. The dotted lines in the plan view at right indicate where the edges of the slab would be were it a floating slab.

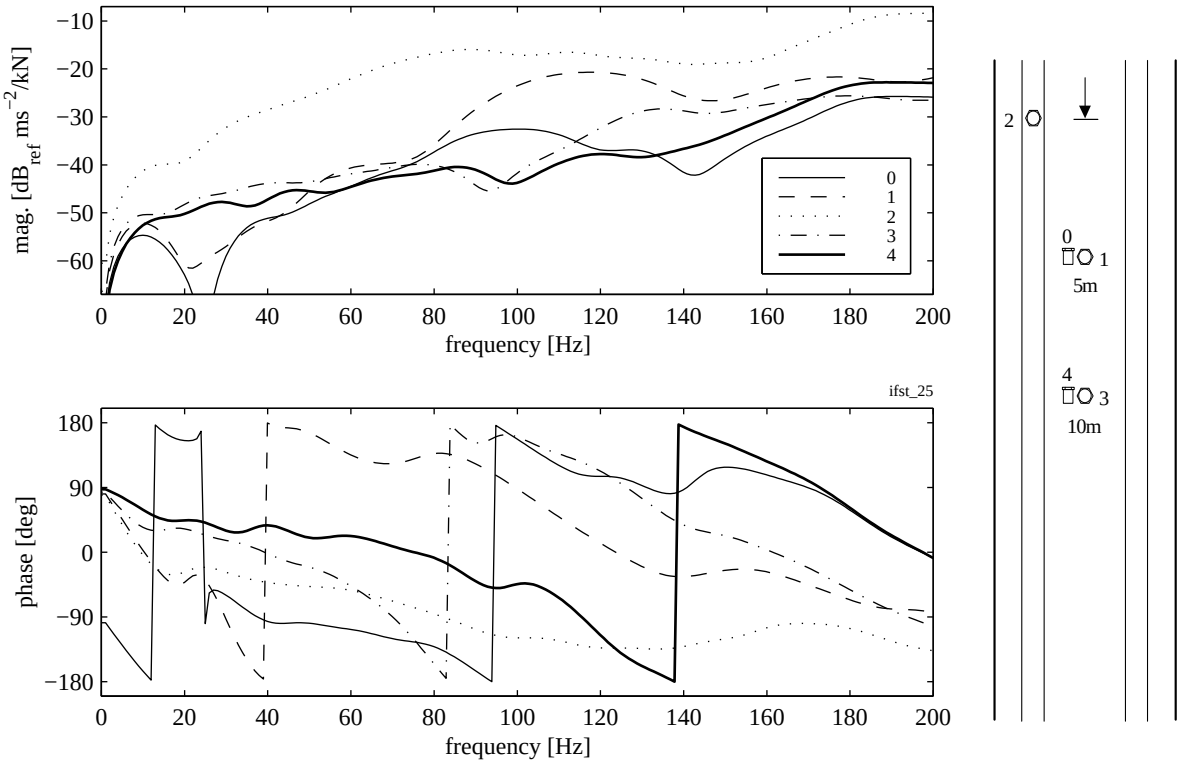

Figure 6.20: Vertical and longitudinal acceleration FRFs along the middle of the floating slab with a central vertical input force applied opposite accelerometer 2. Accelerometers 0 and 4 were placed on their sides next to accelerometers 1 and 3.

Longitudinal accelerations of the floating slab are compared to vertical ones in Figure 6.20. As in obtaining the lateral accelerations given in Figure 6.17, accelerometers 0 and 4 were fixed to the slab on their sides next to accelerometers 1 and 3, but this time aligned along instead of across the slab. The vertical accelerations 2, 1 and 3 show good repeatability compared to the same accelerations in Figure 6.18. The longitudinal accelerations 0 and 4 are of similar magnitude to the vertical accelerations at the same positions. Thus longitudinal motion of the slab is also significant.

Figure 6.21 gives the vertical acceleration of the tunnel invert next to the floating slab at various longitudinal distances from a central slab force. The slab-edge acceleration 0 is very like the rail acceleration 2 from Figure 6.18. This confirms that the rail moves with the slab in the frequency range considered. Since in Figure 6.18 the rail motion 2 and the central slab motion 0 are comparable, Figure 6.21 shows that the edges and centre of the slab have roughly the same motion with the symmetric central loading, which accords with Figure 6.12. The off-slab accelerations 2, 1, 3 and 4 look quite like the central accelerations for the unisolated track, Figure 6.19. The off-slab response decreases with longitudinal distance, although above 150Hz the

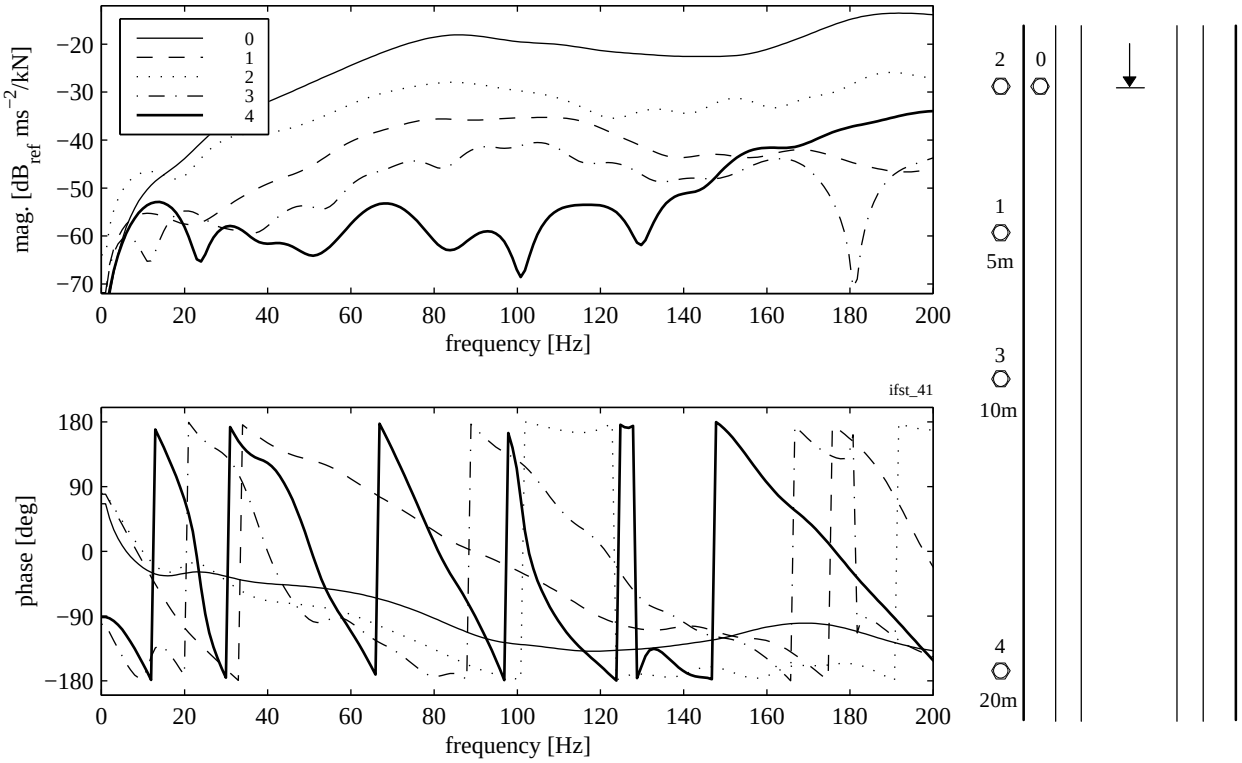

Figure 6.21: Vertical acceleration FRFs along the tunnel invert next to the floating slab with a central vertical input force applied opposite accelerometers 0 and 2.

response 4 at 20m distance is greater than the others. This could be due to numerical errors introduced by the low signal levels recorded at large distances from the input force, as shown in Figure 6.6(f). Generally, the off-slab accelerations are 10-15dB lower than the corresponding on-slab results given in 6.18, particularly above 80Hz.

6.5 Conclusions

The experimental results presented in this chapter illustrate several features of the dynamic behaviour of a real floating-slab railway track. While comparisons to an equivalent unisolated track show that mounting the track slab on a rubber ballast mat does noticeably alter responses, no resonance peak corresponding to the theoretical natural frequency can be observed: all the responses are relatively smooth with no prominent resonances at all in the frequency range considered. The measured driving-point response of the floating slab is similar to that of a Winkler beam with a highly damped foundation, which in turn resembles the response of a simple slab beam joined directly to a tunnel. These factors suggest that the floating-slab track examined is closely coupled to the tunnel, in contrast to the design assumptions. Other significant aspects of the floating-slab dynamics observed in the measured responses include torsion, lateral motion and longitudinal motion. The measured floating-slab FRFs show that off-slab accelerations are lower than on-slab ones for an input force applied to the track. This might be taken as proof of vibration isolation, but as the theoretical results of Chapter 5 have shown, the actual soil response cannot be predicted by track response alone.

Chapter 7

CONCLUSIONS AND FURTHER WORK

This chapter summarises the conclusions reached from the work described in the previous chapters. Based on these conclusions, suggestions for further work are given.

7.1 Conclusions

The results presented in this dissertation demonstrate that the simple mass-spring models commonly used in the design of floating-slab track are inadequate because they ignore the interacting three-dimensional dynamics of the track, tunnel and soil. Such simple models give misleadingly large estimates of vibration reduction. The results for complete track-tunnel-soil models as developed in this dissertation suggest that insertion-loss predictions greater than 6dB are exaggerated, and that floating the track slab may actually increase transmission of vibration unless resilient bearings which are very soft compared to the tunnel and soil are used.

An infinitely long double-beam model of floating-slab track has been implemented by means of a repeating-unit method utilising a dynamic-stiffness approach. A concept of total transmitted force has enabled investigation of the effect of slab length, axle mass and axle spacing on track performance. Multiple track inputs at train axles have also been considered. All these parameters significantly influence track dynamics. However, this approach considers the tunnel invert to be rigid, an assumption which has been shown to have severe limitations.

The objective of creating an analytical model of the three-dimensional track-tunnel-soil system has been realised by combining beam track models with a tunnel-in-soil model consisting

of an infinitely long thin cylindrical shell surrounded by an infinite viscoelastic soil medium. The equations of motion for the tunnel and soil are solved in a modal wavenumber-frequency domain, and the track models are coupled to the tunnel by a spatial convolution method, achieved by wavenumber-domain multiplication. Final results are obtained by a spatial inverse Fourier transform. Three different track models have been considered: a simple slab beam in bending only, a slab beam in bending and torsion, and a full track comprising a rail beam and slab beam in bending. Random process theory has been used to calculate the power spectral density of soil vibration around a tunnel with the full track model; the track inputs due to a train are represented as roughness displacements between axle masses and the rail beam. RMS soil vibration levels can easily be calculated from the spectra. The effect of varying the slab-support stiffness has been investigated, showing as mentioned above that only modest vibration reduction is achievable and that using a "little bit of rubber" to isolate the slab can have adverse results.

Various aspects of the dynamic behaviour of floating-slab track have been observed in frequency-response functions calculated from impulse-response measurements made in a railway tunnel. This data confirms that track response can be highly damped due to radiation of energy into the surrounding soil and that track torsion is important. Significant lateral and longitudinal slab motion has also been observed.

7.2 Recommendations for Further Work

The track-plus-tunnel models presented in this dissertation have only considered variation of slab-support stiffness. A more comprehensive parametric study of the effect of track design, tunnel geometry and soil type (for instance) on transmitted vibration would be useful. In this context the choice of appropriate material properties for the resilient track elements and the soil also deserves attention. A calculation of power flow into the soil would check that all energy is accounted for in the current models and could also form a better basis for quantifying vibration-isolation effectiveness of different track and tunnel designs. There is scope for more extensive experimental investigations than those undertaken, including measurements of soil vibration levels with trains running in a tunnel.

To make the analytical approach presented more attractive for use as a comparative design tool, the programs used could be made more efficient. This would facilitate multiple runs with different parameter values. The programs were run in the interpreted Matlab environment, which is quite efficient for vectorised operations but relatively slow for looping procedures. Despite extensive use of vectorised code, many looping iterations were still required, to solve matrix equations at each frequency and wavenumber step for example. Compiling the programs would significantly increase computation speed. While it is possible to use pre-compiled functions with Matlab, the greatest speed gains would probably be obtained by using a lower-level language such as C for all the program code. This would also have the advantage of more subtle memory management to control the manipulation of large amounts of data such as the tunnel and soil modes.

The track-plus-tunnel models could be extended to consider more complicated situations than covered in this dissertation. Discrete rail pads and discrete resilient bearings in floating-slab track models would introduce parametric excitation like the sleeper-passage effects noted in the literature on ballasted railways. The effect on soil vibration of discrete track slabs could be investigated. The torsional slab model could be extended to a full track model including rails and wheels. Lateral slab motion and the resulting tangential tunnel inputs could also be added to the model. The simple train model of equally spaced axle masses could be extended to bogie pairs of axle masses; a more complete train model could be used to check the assumption that only the unsprung mass has a significant effect on ground vibration.

Other factors which could be considered are a second tunnel nearby, the free surface of the soil and inhomogeneity in the soil. Ultimately, the transmission of vibration from an underground railway into a nearby building could be modelled. While analytical methods can be applied to some special cases, a numerical approach such as FEM-BEM would have to be used for many situations which take these extra factors into account. The track-plus-tunnel models described in this dissertation could be used to validate a simple version of such a numerical model prior to introducing realistic but analytically intractable features into it.

REFERENCES

[1] J.D. Achenbach, *Wave Propagation in Elastic Solids*, North-Holland, Amsterdam, 1973.

[2] J. Ackva and S. Niedermeyer, "Ganzheitliches Ausbreitungsgesetz für Erschütterungen aus dem Schienenverkehr – Ausgangslage und Möglichkeiten der Prognose [Comprehensive propagation law for soil waves resulting from rail traffic – conditions and possibilities of prediction]" in N. Chouw and G. Schmid (eds.), *Wave Propagation and Reduction of Vibrations – Wave'94*, Berg-Verlag, Bochum, Germany, 1994, pp. 79-94.

[3] B. Alabi, "A parametric study on some aspects of ground-borne vibrations due to rail traffic", *Journal of Sound and Vibration*, vol. 153, no. 1, pp. 77-87, 1992.

[4] D. Anderson, "Isolation of buildings from railway vibration: a case study", *Proceedings of ICSV5, December 15-18, 1997, Adelaide, South Australia*, vol. 5, pp. 2897-2904, paper no. 448, International Institute of Acoustics and Vibration, Adelaide, Australia, 1997 (on CD-ROM).

[5] K. Ando, T. Horiike, K. Kubomura, M. Hansaka and T. Nagafuji, "Present status on slab track and environmental countermeasure", *Quarterly Report of the Railway Technical Research Institute (Japan)*, vol. 37, no. 4, pp. 204-209, 1996.

[6] D. Aubry and D. Clouteau, "A regularized boundary element method for stratified media" in G. Cohen, L. Halpern and P. Joly (eds.), *Proceedings of the First International Conference on Mathematical and Numerical Aspects of Wave Propagation Phenomena*, SIAM, 1991, pp. 660-668.

[7] D. Aubry, D. Clouteau and G. Bonnet, "Modelling of wave propagation due to fixed or mobile dynamic sources" in N. Chouw and G. Schmid (eds.), *Wave Propagation and Reduction of Vibrations – Wave'94*, Berg-Verlag, Bochum, Germany, 1994, pp. 109-122.

[8] L. Auersch, "Zur erschütterungsmindernden Wirkung von Schichten im Boden [On the vibration reduction effects of layers in the soil]" in N. Chouw and G. Schmid (eds.), *Wave Propagation and Reduction of Vibrations – Wave'94*, Berg-Verlag, Bochum, Germany, 1994, pp. 189-200.

[9] L. Auersch, "Wave propagation in layered soils: theoretical solution in wavenumber domain and experimental results of hammer and railway traffic excitation", *Journal of Sound and Vibration*, vol. 173, no. 2, pp. 233-264, 1994.

[10] T. Balendra, K.H. Chua, K.W. Lo and S.L. Lee, "Steady-state vibration of subway-soil-building system", *Journal of Engineering Mechanics, ASCE*, vol. 115, no. 1, pp. 145-162, 1989.

[11] T. Balendra, C.G. Koh and Y.C. Ho, "Dynamic response of buildings due to trains in underground tunnels", *Earthquake Engineering and Structural Dynamics*, vol. 20, no. 3, pp. 275-291, 1991.

[12] P.M. Belotserkovskiy, "Forced oscillations of infinite periodic structures. Applications to railway track dynamics", *Vehicle System Dynamics Supplement*, vol. 28, pp. 85-103, 1998.

[13] A. Bhaskar, K.L. Johnson, G.D. Wood and J. Woodhouse, "Wheel-rail dynamics with closely conformal contact, Part 1: dynamic modelling and stability analysis", *Proceedings IMechE, Part F: Journal of Rail and Rapid Transit*, vol. 211, no. 1, pp. 11-26, 1997.

[14] A. Bhaskar, K.L. Johnson and J. Woodhouse, "Wheel-rail dynamics with closely conformal contact, Part 2: forced response, results and conclusions", *Proceedings IMechE, Part F: Journal of Rail and Rapid Transit*, vol. 211, no. 1, pp. 27-40, 1997.

[15] D.R. Bland, *The Theory of Linear Viscoelasticity*, Pergamon Press, Oxford, 1960.

[16] T.E. Blejwas, C.C. Feng and R.S. Ayre, "Dynamic interaction of moving vehicles and structures", *Journal of Sound and Vibration*, vol. 67, no. 4, pp. 513-521, 1979.

[17] R.D. Blevins, *Formulas for Natural Frequency and Mode Shape*, Krieger, Malabar, Florida, USA, 1993.

[18] M. Bocciolone, A. Cigada and M. Falco, "Train-structure interaction: a measurement campaign in the subway of Milan", *Proceedings of the 4th Vehicle-Infrastructure Interaction Conference*, Engineering Foundation, San Diego, USA, 1996.

[19] T. Boudjelal, M. Fafard and A. Gakwaya, "Modelling of damping and its applications to dynamic bridge-vehicle interaction" in Augusti, Borri and Spinelli (eds.), *Structural Dynamics – EURODYN'96*, Balkema, Rotterdam, 1996, pp. 767-774.

[20] E.C. Bovey, "Development of an impact method to determine the vibration transfer characteristics of railway installations", *Journal of Sound and Vibration*, vol. 87, no. 2, pp. 357-370, 1983.

[21] H. Braitsch, "Neues zum 'Kölner Ei' (Oberbau 1403/c) und zur kostensparenden Eindämmung von Körperschall an Nahverkehrsbahnen [Latest information on the 'Cologne Egg' (track 1403/c) and on economic reduction of structure-borne sound in urban railways]", *Vekehr und Technik*, no. 11 & 12, 1981.

[22] British Geological Survey, Geological map of Windsor, Sheet 269, Solid & Drift Edition, 1:50 000 Series, 1981.

[23] British Geological Survey, Geological map of South London, Sheet 270, Solid & Drift Edition, 1:50 000 Series, 1998.

[24] British Standards Institution, "Guide to evaluation of human exposure to vibration in buildings (1Hz-80Hz)", BS 6472: 1992.

[25] Z. Cai and G.P. Raymond, "Use of a generalized beam/spring element to analyze natural vibration of rail track and its application", *International Journal of Mechanical Sciences*, vol. 36, no. 9, pp. 863-876, 1994.

[26] Z. Cai, G.P. Raymond and R.J. Bathurst, "Natural vibration analysis of rail track as a system of elastically coupled beam structures on Winkler foundation", *Computers and Structures*, vol. 53, no. 6, pp. 1427-1436, 1994.

[27] G.F. Capponi, "Vibrations in the Milan underground – types of tracks and train speeds", *Proceedings of the International Conference on Noise Control Engineering (Inter-noise 83), Edinburgh, 13-15 July 1983*, vol. 1, pp. 479-482, Institute of Acoustics, Edinburgh, 1983.

[28] G. Capponi and M.H. Murray, "Reducing vibration in urban rail transport", *Transactions of Mechanical Engineering, IEAust*, vol. ME23, no. 1, pp. 43-45, 1998.

[29] A. Castellani, G. Kajon, P. Panzeri and P. Pezzoli, "Elastomeric materials used for vibration isolation of railway lines", *Journal of Engineering Mechanics, ASCE*, vol. 124, no. 6, pp. 614-621, 1998.

[30] T.-P. Chang, "Deterministic and random vibration of an axially loaded Timoshenko beam resting on an elastic foundation", *Journal of Sound and Vibration*, vol. 178, no. 1, pp. 55-66, 1994.

[31] T.-P. Chang and Y.-N. Liu, "Dynamic finite element analysis of a nonlinear beam subjected to a moving load", *International Journal of Solids and Structures*, vol. 33, no. 12, pp. 1673-1688, 1996.

[32] N. Chouw, "Wave propagation from the source via the subsoil into the building" in N. Chouw and G. Schmid (eds.), *Wave Propagation and Reduction of Vibrations – Wave'94*, Berg-Verlag, Bochum, Germany, 1994, pp. 33-46.

[33] Y.K. Chow and I.M. Smith, "Static and periodic infinite solid elements", *International Journal for Numerical Methods in Engineering*, vol. 17, no. 4, pp. 503-526, 1981.

[34] K.H. Chua, T. Balendra and K.W. Lo, "Groundborne vibrations due to trains in tunnels", *Earthquake Engineering and Structural Dynamics*, vol. 21, no. 5, pp. 445-460, 1992.

[35] R.A. Clark, P.A. Dean, J.A. Elkins and S.G. Newton, "An investigation into the dynamic effects of railway vehicles running on corrugated rails", *Journal of Mechanical Engineering Science, IMechE*, vol. 24, no. 2, pp. 65-76, 1982.

[36] D.E. Commins, C. Leneutre and S. Vanpeperstraete, "Vibration isolation of trains in a French arts complex", *Proceedings of the Institute of Acoustics*, vol. 12, no. 7, pp. 31-38, 1990.

[37] W.M.G. Courage and P.C. van Staalduinen, "Vibration analysis of an elevated railway track" in Augusti, Borri and Spinelli (eds.), *Structural Dynamics – EURODYN'96*, Balkema, Rotterdam, Netherlands, 1996, pp. 791-794.

[38] D.P. Cryer, "Modelling of Vibration in Buildings with Application to Base Isolation", PhD thesis, University of Cambridge, July 1994.

[39] T. Dahlberg, B. Åkesson and S. Westberg, "Modelling the dynamic interaction between train and track", *Railway Gazette International*, vol. 149, no. 6, pp. 407-412, 1993.

[40] M. Dalenbring, "A study of the effect of track parameter changes on vertical rail vibrations", report no. KTH/FKT/FR-95/06-SE, Marcus Wallenberg Laboratory, Royal Institute of Technology, Stockholm, Sweden, 1995.

[41] T.M. Dawn, "Ground vibrations from heavy freight trains", *Journal of Sound and Vibration*, vol. 87, no. 2, pp. 351-356, 1983.

[42] J.D. Deeks and M.F. Randolph, "Axisymmetric time-domain transmitting boundaries", *Journal of Engineering Mechanics, ASCE*, vol. 120, no. 1, pp. 25-42, 1994.

[43] G. Degrande and G. De Roeck, "An absorbing boundary condition for wave propagation in saturated poroelastic media – Part I: Formulation and efficiency evaluation", *Soil Dynamics and Earthquake Engineering*, vol. 12, no. 7, pp. 411-421, 1993.

[44] G. Degrande and G. De Roeck, "An absorbing boundary condition for wave propagation in saturated poroelastic media – Part II: Finite element formulation", *Soil Dynamics and Earthquake Engineering*, vol. 12, no. 7, pp. 423-432, 1993.

[45] J.P. Den Hartog, *Mechanical Vibrations*, 4th ed., Dover Publications, New York, 1985.

[46] D.G. Duffy, "The response of an infinite railroad track to a moving, vibrating mass", *Journal of Applied Mechanics, Transactions ASME*, vol. 57, no. 1, pp. 66-73, 1990.

[47] P. Duval, "Ballastless track – a French approach", *Railway Technology International*, vol. 1989, pp. 248-250, 1989.

[48] G. Eason, J. Fulton and I.N. Sneddon, "The generation of waves in an infinite elastic solid by variable body forces", *Philosophical Transactions of the Royal Society of London, Series A*, vol. 248, pp. 575-607, 1956.

[49] E. Esmailzadeh and M. Ghorashi, "Vibration analysis of beams traversed by uniform partially distributed moving masses", *Journal of Sound and Vibration*, vol. 184, no. 1, pp. 9-17, 1995.

[50] C. Esveld, *Modern Railway Track*, Esveld Consulting Services, Zaltbommel, Netherlands, 1989.

[51] C. Esveld, J. van't Zand, P.N. Scheepmaker and A.S.J. Suiker, "Dynamic behaviour of railway track", *Rail Engineering International Edition*, no. 2, pp. 17-20, 1996.

[52] W.M. Ewing, W.S. Jardetzky and F. Press, *Elastic Waves in Layered Media*, McGraw-Hill, New York, 1957.

[53] Å. Fenander, "Frequency dependent stiffness and damping of railpads", *Proceedings IMechE, Part F: Journal of Rail and Rapid Transit*, vol. 211, no. 1, pp. 51-62, 1997.

[54] Å. Fenander, "A fractional derivative railpad model included in a railway track model", *Journal of Sound and Vibration*, vol. 212, no. 5, pp. 889-903, 1998.

[55] R. Ferrari, "Spatially periodic structures" in T. Itoh, G. Pelosi and P.P. Silvester (eds.), *Finite Element Software for Microwave Engineering*, Wiley, New York, 1996, pp. 25-51.

[56] W. Flügge, *Viscoelasticity*, Blaisdell Publishing Company, Waltham, Massachusetts, USA, 1967.

[57] W. Flügge, *Stresses in Shells*, 2nd ed., Springer-Verlag, Berlin, 1973.

[58] E. Forchap and B. Verbic, "Field tests on wave propagation and reduction of foundation vibrations" in N. Chouw and G. Schmid (eds.), *Wave Propagation and Reduction of Vibrations – Wave'94*, Berg-Verlag, Bochum, Germany, 1994, pp. 165-178.

[59] R.A.J. Ford, "Track and ground vibrations: summary of work to October 1991", report no. 1991/AM/1, School of Mechanical and Industrial Engineering, University of New South Wales, Sydney, Australia, November 1991.

[60] R.A.J. Ford, "Response of a simple model of a vehicle to measured track profiles, Part 1: Proposed CRAMP analysis of track condition", report no. 1993/AM/1, School of Mechanical and Industrial Engineering, University of New South Wales, Sydney, Australia, February 1993.

[61] J.A. Forrest, "Floating slab railway track for isolation of vibration: models of infinite length", *Proceedings of DETC'97, September 14-17, 1997, Sacramento, California*, paper no. VIB-4085, American Society of Mechanical Engineers, New York, 1997 (on CD-ROM).

[62] F. Frederich, "Die Gleislage – aus fahrzeugtechnischer Sicht [Effect of track geometry on vehicle performance]", *Zeitschrift für Eisenbahnwesen und Vekehrstechnik – Glasers Annalen*, vol. 108, no. 12, pp. 355-362, 1984.

[63] R.D. Fröhling, "Measurement, interpretation and classification of South African track geometry", *Vehicle System Dynamics Supplement*, vol. 24, pp. 133-145, 1995.

[64] R.D. Fröhling, "Low frequency dynamic vehicle/track interaction: modelling and simulation", *Vehicle System Dynamics Supplement*, vol. 28, pp. 30-46, 1998.

[65] T. Fujikake, "A prediction method for the propagation of ground vibration from railway trains", *Journal of Sound and Vibration*, vol. 111, no. 2, pp. 357-360, 1986.

[66] T. Fujikake, "A prediction method for the propagation of ground vibration from railway trains on level tracks with welded rails", *Journal of Sound and Vibration*, vol. 128, no. 3, pp. 524-527, 1989.

[67] H. Fujimoto, K. Tanifuji and M. Miyamoto, "Comparision between data from test train running on track irregularities artificially set and results of vehicle dynamics simulation (influence of track gauge variation on rail vehicle dynamics)", *Vehicle System Dynamics Supplement*, vol. 28, pp. 59-72, 1998.

[68] S. Gade and N.J. Wismer, "Improved method for the estimation of complex modulus and damping", *Proceedings of ICSV5, December 15-18, 1997, Adelaide, South Australia*, vol. 3, pp. 1391-1398, paper no. 55, International Institute of Acoustics and Vibration, Adelaide, Australia, 1997 (on CD-ROM).

[69] V.K. Garg and R.V. Dukkipati, *Dynamics of Railway Vehicle Systems*, Academic Press, Toronto, Canada, 1984.

[70] D.C. Gazis, "Three-dimensional investigation of the propagation of waves in hollow circular cylinders. I. Analytical foundation", *Journal of the Acoustical Society of America*, vol. 31, no. 5, pp. 568-573, 1959.

[71] D.C. Gazis, "Three-dimensional investigation of the propagation of waves in hollow circular cylinders. II. Numerical results", *Journal of the Acoustical Society of America*, vol. 31, no. 5, pp. 573-578, 1959.

[72] L. Girardi and P. Recchia, "Use of a computational model for assessing dynamical behaviour of a railway structure", *Vehicle System Dynamics Supplement*, vol. 20, pp. 185-194, 1992.

[73] K.F. Graff, *Wave Motion in Elastic Solids*, Oxford University Press, London, 1975.

[74] S.L. Grassie, "A contribution to dynamic design of railway track", *Vehicle System Dynamics Supplement*, vol. 20, pp. 195-209, 1992.

[75] S.L. Grassie and S.J. Cox, "The dynamic response of railway track with unsupported sleepers", *Proceedings of the Institution of Mechanical Engineers*, vol. 199, no. D2, pp. 123-135, 1985.

[76] S.L. Grassie, R.W. Gregory, D. Harrison and K.L. Johnson, "The dynamic response of railway track to high frequency vertical excitation", *Journal of Mechanical Engineering Science, IMechE*, vol. 24, no. 2, pp. 77-90, 1982.

[77] R.J. Greer and C.J. Manning, "Vibration isolation for railways", *Acoustics Bulletin*, vol. 23, no. 3, pp. 13-17, 1998.

[78] P. Grootenhuis, "Floating track slab isolation for railways", *Journal of Sound and Vibration*, vol. 51, no. 3, pp. 443-448, 1977.

[79] F. Guan and I.D. Moore, "Three-dimensional dynamic response of twin cavities due to travelling loads", *Journal of Engineering Mechanics, ASCE*, vol. 120, no. 3, pp. 637-651, 1994.

[80] T.G. Gutowski and C.L. Dym, "Propagation of ground vibration: a review", *Journal of Sound and Vibration*, vol. 49, no. 2, pp. 179-193, 1976.

[81] H. Hao and T.C. Ang, "Analytical modeling of traffic-induced ground vibrations", *Journal of Engineering Mechanics, ASCE*, vol. 124, no. 8, pp. 921-928, 1998.

[82] M. Heckl, G. Hauck and R. Wettschureck, "Structure-borne sound and vibration from rail traffic", *Journal of Sound and Vibration*, vol. 193, no. 1, pp. 175-184, 1996.

[83] K. Hempelmann, B. Ripke and S. Dietz, "Modelling the dynamic interaction of wheelset and track", *Railway Gazette International*, vol. 148, no. 9, pp. 591-594, 1992.

[84] W.D. Henn, "System comparison: ballasted track – slab track", *Rail Engineering International Edition*, no. 2, pp. 6-9, 1993.

[85] M. Hetényi, *Beams on Elastic Foundation*, University of Michigan Press, Ann Arbor, Michigan, USA, 1946.

[86] R.A. Hood, R.J. Greer, M. Breslin and P.R. Williams, "The calculation and assessment of ground-borne noise and perceptible vibration from trains in tunnels", *Journal of Sound and Vibration*, vol. 193, no. 1, pp. 215-225, 1996.

[87] H.V.C. Howarth and M.J. Griffin, "Human response to simulated intermittent railway-induced building vibration", *Journal of Sound and Vibration*, vol. 120, no. 2, pp. 413-420, 1988.

[88] H.V.C. Howarth and M.J. Griffin, "The annoyance caused by simultaneous noise and vibration from railways", *Journal of Sound and Vibration*, vol. 89, no. 5, pp. 2317-2323, 1991.

[89] H.E.M. Hunt, "Measurement and Modelling of Traffic-induced Ground Vibration", PhD thesis, University of Cambridge, July 1988.

[90] H.E.M. Hunt, "Modelling of road vehicles for calculation of traffic-induced ground vibration as a random process", *Journal of Sound and Vibration*, vol. 144, no. 1, pp. 41-51, 1991.

[91] H.E.M. Hunt, "Stochastic modelling of traffic-induced ground vibration", *Journal of Sound and Vibration*, vol. 144, no. 1, pp. 53-70, 1991.

[92] H.E.M. Hunt, "Prediction of vibration transmission from railways into buildings using models of infinite length", *Vehicle System Dynamics Supplement*, vol. 24, pp. 234-247, 1995.

[93] H.E.M. Hunt, "Modelling of rail vehicles and track for calculation of ground-vibration transmission into buildings", *Journal of Sound and Vibration*, vol. 193, no. 1, pp. 185-194, 1996.

[94] H.E.M. Hunt and J.E. May, "Vibration generated by underground railway trains", *Proceedings of ICSV5, December 15-18, 1997, Adelaide, South Australia*, vol. 5, pp. 2653-2660, paper no. 525, International Institute of Acoustics and Vibration, Adelaide, Australia, 1997 (on CD-ROM).

[95] H. Isaksson, "Ballast-mats for railway bridges: insertion loss for different types", report no. KTH/FKT/EX-97/26-SE, Marcus Wallenberg Laboratory, Royal Institute of Technology, Stockholm, Sweden, 1997.

[96] M. Ishida, S. Miura and A. Kono, "The influence of track stiffness on track dynamic behaviour", *Quarterly Report of the Railway Technical Research Institute (Japan)*, vol. 38, no. 3, pp. 129-134, 1997.

[97] T. Jaquet and D. Heiland, "Erschütterungsprognose mittels Antwortspektrumverfahren [Prediction of vibrations applying the response spectra method]" in N. Chouw and G. Schmid (eds.), *Wave Propagation and Reduction of Vibrations – Wave'94*, Berg-Verlag, Bochum, Germany, 1994, pp. 179-188.

[98] K.L. Johnson, *Contact Mechanics*, Cambridge University Press, Cambridge, 1985.

[99] C.J.C. Jones, "Use of numerical models to determine the effectiveness of anti-vibration systems for railways", *Proceedings of the Institution of Civil Engineers, Transport*, vol. 105, no. 1, pp. 43-51, 1994.

[100] C.J.C. Jones and J.R. Block, "Prediction of ground vibration from freight trains", *Journal of Sound and Vibration*, vol. 193, no. 1, pp. 205-213, 1996.

[101] D.V. Jones and M. Petyt, "Ground vibration in the vicinity of a strip load: a two-dimensional half-space model", *Journal of Sound and Vibration*, vol. 147, no. 1, pp. 155-166, 1991.

[102] D.V. Jones and M. Petyt, "Ground vibration in the vicinity of a strip load: an elastic layer on a rigid foundation", *Journal of Sound and Vibration*, vol. 152, no. 3, pp. 501-515, 1992.

[103] D.V. Jones and M. Petyt, "Ground vibration in the vicinity of a strip load: an elastic layer on an elastic half-space", *Journal of Sound and Vibration*, vol. 161, no. 1, pp. 1-18, 1993.

[104] L.F. Kallivokas, J. Bielak and R.C. MacCamy, "Symmetric local absorbing boundaries in time and space", *Journal of Engineering Mechanics, ASCE*, vol. 117, no. 9, pp. 2027-2048, 1991.

[105] D.L. Karabalis and D.E. Beskos, "Dynamic response of 3-D rigid surface foundations by time domain boundary element method", *Earthquake Engineering and Structural Dynamics*, vol. 12, no. 1, pp. 73-93, 1984.

[106] A.D. Kerr, "On the vertical modulus in the standard railway track analysis", *Rail International*, vol. 18, no. 11, pp. 37-45, 1987.

[107] V. Knall, "Railway noise and vibration: effects and criteria", *Journal of Sound and Vibration*, vol. 193, no. 1, pp. 9-20, 1996.

[108] H.W. Koch, "Propagation of vibrations and structure-borne sound caused by trains running at a maximum speed of 250 km/h", *Journal of Sound and Vibration*, vol. 51, no. 3, pp. 441-442, 1977.

[109] S.A. Kostarev, "An analysis of vibrational field, generated by an underground tunnel in soil", *Journal of Low Frequency Noise and Vibration*, vol. 15, no. 4, pp. 151-156, 1996.

[110] U.G. Köpke, "Transverse vibration of buried pipelines due to internal excitation at a point", *Proceedings IMechE, Part E: Journal of Process Mechanical Engineering*, vol. 207, no. E1, pp. 41-58, 1993.

[111] S. Kraemer, "Noise and Vibration in Buildings from Underground Railway Lines", PhD thesis, University of London, 1984.

[112] E. Kreyszig, *Advanced Engineering Mathematics*, 6th ed., Wiley, New York, 1988.

[113] V.V. Krylov, "Low-frequency ground vibrations from underground trains", *Journal of Low Frequency Noise and Vibration*, vol. 14, no. 1, pp. 55-60, 1995.

[114] V.V. Krylov, "Vibrational impact of high-speed trains. I. Effect of track dynamics", *Journal of the Acoustical Society of America*, vol. 100, no. 5, pp. 3121-3134, 1996.

[115] V.V. Krylov, "Effect of layered ground on ground vibrations generated by high-speed trains", *Conference Papers – Ground Dynamics and Man-made Processes, 20 November 1997, London*, paper no. 5, Institution of Civil Engineers, London, 1997.

[116] V.V. Krylov, "Ground vibration boom from high-speed trains: prediction and reality", *Acoustics Bulletin*, vol. 23, no. 4, pp. 15-22, 1998.

[117] V.V. Krylov and C.C. Ferguson, "Calculation of low-frequency ground vibrations from railway trains", *Applied Acoustics*, vol. 42, no. 3, pp. 199-213, 1994.

[118] H. Lamb, "On the propagation of tremors over the surface of an elastic solid", *Philosophical Transactions of the Royal Society of London, Series A*, vol. 203, pp. 1-42, 1904.

[119] R.S. Langley, "Analysis of power flow in beams and frameworks using the direct-dynamic stiffness method", *Journal of Sound and Vibration*, vol. 136, no. 3, pp. 439-452, 1990.

[120] R.K. Livesley, *Matrix Methods of Structural Analysis*, 2nd ed., Pergamon Press, Oxford, 1975.

[121] K.T. Lo, "Measurement and Modelling of Vibration Transmission through Piled Foundations", PhD thesis, University of Cambridge, October 1994.

[122] J.C. Lucas, "Dynamic loading and response of track components", 1979 (unpublished).

[123] Y. Luo, H. Yin and C. Hua, "The dynamic response of railway ballast to the action of trains moving at different speeds", *Proceedings IMechE, Part F: Journal of Rail and Rapid Transit*, vol. 210, no. 2, pp. 95-101, 1996.

[124] J. Lysmer and R.L. Kuhlemeyer, "Finite dynamic model for infinite media", *Journal of the Engineering Mechanics Division, Proceedings ASCE*, vol. 95, no. EM4, pp. 859-877, 1969.

[125] C. Madhus, B. Bessason and L. Hårvik, "Prediction model for low frequency vibration from high speed railways on soft ground", *Journal of Sound and Vibration*, vol. 193, no. 1, pp. 195-203, 1996.

[126] C. Madhus, A.M. Kaynia, L. Harvik and J.K. Holme, "A numerical ground model for railway-induced vibration", *Conference Papers – Ground Dynamics and Man-made Processes, 20 November 1997, London*, paper no. 3, Institution of Civil Engineers, London, 1997.

[127] C.E. Maloney, N.G. Kingsbury and M.D. Macleod, "Electrical and Information Data Book", Cambridge University Engineering Department, 1995.

[128] C.J. Manning, "Air rights buildings", *Proceedings of the Institute of Acoustics*, vol. 12, no. 7, pp. 23-30, 1990.

[129] K.R. Massarsch, "Massnahmen zur passiven Isolierung von Baugrunderschütterungen [Passive ground vibration isolation measures]" in N. Chouw and G. Schmid (eds.), *Wave Propagation and Reduction of Vibrations – Wave'94*, Berg-Verlag, Bochum, Germany, 1994, pp. 21-32.

[130] D.J. Mead, "A general theory of harmonic wave propagation in linear periodic systems with multiple coupling", *Journal of Sound and Vibration*, vol. 27, no. 2, pp. 235-260, 1973.

[131] D.J. Mead, "Wave propagation and natural modes in periodic systems: I. Mono-coupled systems", *Journal of Sound and Vibration*, vol. 40, no. 1, pp. 1-18, 1975.

[132] D.J. Mead, "Wave propagation and natural modes in periodic systems: II. Multi-coupled systems, with and without damping", *Journal of Sound and Vibration*, vol. 40, no. 1, pp. 19-39, 1975.

[133] D.J. Mead, "Wave propagation in continuous periodic structures: research contributions from Southampton, 1964-1995", *Journal of Sound and Vibration*, vol. 190, no. 3, pp. 495-524, 1996.

[134] D.J. Mead and Y. Yaman, "The response of infinite periodic beams to point harmonic forces: a flexural wave analysis", *Journal of Sound and Vibration*, vol. 144, no. 3, pp. 507-530, 1991.

[135] F. Medina and J. Penzien, "Infinite elements for elastodynamics", *Earthquake Engineering and Structural Dynamics*, vol. 10, no. 5, pp. 699-709, 1982.

[136] L. Meirovitch, *Elements of Vibration Analysis*, 2nd ed., McGraw-Hill, New York, 1986.

[137] J. Melke, "Noise and vibration from underground railway lines: proposals for a prediction procedure", *Journal of Sound and Vibration*, vol. 120, no. 2, pp. 391-406, 1988.

[138] J. Melke and S. Kraemer, "Diagnostic methods in the control of railway noise and vibration", *Journal of Sound and Vibration*, vol. 87, no. 2, pp. 377-386, 1983.

[139] J. Melke and B. Switaiski, "Elastomer rail support systems: problems in dynamic testing", *Journal of Sound and Vibration*, vol. 120, no. 2, pp. 421-429, 1988.

[140] M. Mohammadi and D.L. Karabalis, "Dynamic 3-D soil-railway track interaction by BEM-FEM", *Earthquake Engineering and Structural Dynamics*, vol. 24, no. 9, pp. 1177-1193, 1995.

[141] P. Morse and H. Feshbach, *Methods of Theoretical Physics*, McGraw-Hill, New York, 1953.

[142] A.D. Nashif, D.I.G. Jones and J.P. Henderson, *Vibration Damping*, Wiley, New York, 1985.

[143] D.E. Newland, *Mechanical Vibration Analysis and Computation*, Longman, Harlow, Essex, England, 1989.

[144] D.E. Newland, *An Introduction to Random Vibrations, Spectral & Wavelet Analysis*, 3rd ed., Longman, Harlow, Essex, England, 1993.

[145] D.E. Newland and H.E.M. Hunt, "Isolation of buildings from ground vibration: a review of recent progress", *Proceedings IMechE, Part C: Journal of Mechanical Engineering Science*, vol. 205, no. 1, pp. 39-52, 1991.

[146] S.L.D. Ng, "Transmission of Ground-borne Vibration from Surface Railway Trains", PhD thesis, University of Cambridge, October 1995.

[147] A. Nordborg, "Vertical rail vibrations: pointforce excitation", *Acustica*, vol. 84, no. 2, pp. 280-288, 1998.

[148] A. Nordborg, "Vertical rail vibrations: parametric excitation", *Acustica*, vol. 84, no. 2, pp. 289-300, 1998.

[149] Y. Okumura and K. Kuno, "Statistical analysis of field data of railway noise and vibration collected in an urban area", *Applied Acoustics*, vol. 33, no. 4, pp. 263-280, 1991.

[150] K. Ono and M. Yamada, "Analysis of railway track vibration", *Journal of Sound and Vibration*, vol. 130, no. 2, pp. 269-297, 1989.

[151] ORE D 151 Specialists Committee, "An assessment of vibration counter-measures in current use", report no. 2, *Question D 151: Vibrations transmitted through the ground*, Office for Research & Experiments of the International Union of Railways, Utrecht, Netherlands, April 1982.

[152] ORE D 151 Specialists Committee, "Effect of vibration on buildings and their occupants – Analysis of the literature and commentary", report no. 4, *Question D 151: Vibrations transmitted through the ground*, Office for Research & Experiments of the International Union of Railways, Utrecht, Netherlands, September 1982.

[153] J. Oscarsson and T. Dahlberg, "Dynamic train/track/ballast interaction – computer models and full-scale experiments", *Vehicle System Dynamics Supplement*, vol. 28, pp. 73-84, 1998.

[154] E. Öhrström, "Effects of exposure to railway noise – a comparison between areas with and without vibration", *Journal of Sound and Vibration*, vol. 205, no. 4, pp. 555-560, 1997.

[155] S.P. Patil, "Response of infinite railroad track to vibrating mass", *Journal of Engineering Mechanics, ASCE*, vol. 114, no. 4, pp. 688-703, 1988.

[156] C.L. Pekeris and H. Lifson, "Motion of the surface of a uniform elastic halfspace produced by a buried pulse", *Journal of the Acoustical Society of America*, vol. 29, no. 11, pp. 1233-1238, 1957.

[157] C. Peng and N.M. Toksöz, "An optimal absorbing boundary condition for elastic wave modelling", *Geophysics*, vol. 60, no. 1, pp. 296-301, 1995.

[158] A.T. Peplow, C.J.C. Jones and M. Petyt, "Vibration transmission in a layered ground with a wave impedance block", *Conference Papers – Ground Dynamics and Man-made Processes, 20 November 1997, London*, paper no. 4, Institution of Civil Engineers, London, 1997.

[159] F.E. Richart, J.R. Hall and R.D. Woods, *Vibrations of Soils and Foundations*, Prentice-Hall, Englewood Cliffs, New Jersey, USA, 1970.

[160] J.W. Rudnicki, "Energy radiation from a spherically symmetric homogeneous source", *Bulletin of the Seismological Society of America*, vol. 73, no. 4, pp. 901-908, 1983.

[161] W.F. Rücker and S. Said, "Einwirkung von U-Bahnerschütterungen auf Gebäude; Anregung, Ausbreitung und Abschirmung [Effect of underground tunnel vibrations on buildings; propagation and screening]" in N. Chouw and G. Schmid (eds.), *Wave Propagation and Reduction of Vibrations – Wave'94*, Berg-Verlag, Bochum, Germany, 1994, pp. 59-78.

[162] J. Sadeghi and R. Kohoutek, "Analytical modelling of railway track system", *Journal of the Rail Track Association Australia*, pp. 20-26, 1995.

[163] G. Samavedam and P. Cross, "Dynamic analyses of vibration isolating tracks for tunnels", report no. TN TS 38, Railway Technical Centre, British Rail Research, Derby, England, July 1980.

[164] B.I. Singal, "Design of non-ballasted track for underground mass transit railways", report submitted to Hong Kong Institution of Engineers, Hong Kong, March 1985.

[165] V.P. Singh, P.C. Upadhyay and B. Kishor, "On the dynamic response of buried orthotropic cylindrical shells", *Journal of Sound and Vibration*, vol. 113, no. 1, pp. 101-115, 1987.

[166] V.P. Singh, P.C. Upadhyay and B. Kishor, "A comparison of thick and thin shell theory results for buried orthotropic cylindrical shells", *Journal of Sound and Vibration*, vol. 119, no. 2, pp. 339-345, 1987.

[167] J. Sochacki, "Absorbing boundary conditions for the elastic wave equations", *Applied Mathematics and Computation*, vol. 28, pp. 1-14, 1988.

[168] S.D. Stearns, *Digital Signal Analysis*, Hayden Book Company, Rochelle Park, New Jersey, USA, 1975.

[169] H. Takemiya, "Traffic induced vibrations and wave propagation" in N. Chouw and G. Schmid (eds.), *Wave Propagation and Reduction of Vibrations – Wave'94*, Berg-Verlag, Bochum, Germany, 1994, pp. 151-164.

[170] H. Takemiya, G. Fei and Y. Sukeyasu, "2-D transient soil-surface foundation interaction and wave propagation by time domain BEM", *Earthquake Engineering and Structural Dynamics*, vol. 23, no. 9, pp. 931-945, 1994.

[171] H. Takemiya and K. Goda, "Prediction of ground vibration induced by high-speed train operation", *Proceedings of ICSV5, December 15-18, 1997, Adelaide, South Australia*, vol. 5, pp. 2681-2688, paper no. 354, International Institute of Acoustics and Vibration, Adelaide, Australia, 1997 (on CD-ROM).

[172] D.J. Thompson, W.J. van Vliet and J.W. Verheij, "Developments of the indirect method for measuring the high frequency dynamic stiffness of resilient elements", *Journal of Sound and Vibration*, vol. 213, no. 1, pp. 169-188, 1998.

[173] R.M. Thornely-Taylor, "Comparison between results of numerical modelling of railway tunnel vibration and field measurements", November 1997 (unpublished).

[174] S. Timoshenko and J.N. Goodier, *Theory of Elasticity*, 3rd ed., McGraw-Hill, New York, 1970.

[175] S. Timoshenko and S. Woinowsky-Krieger, *Theory of Plates and Shells*, 2nd ed., McGraw-Hill, New York, 1959.

[176] T. Triantafyllidis and B. Prange, "Mitgeführte Biegelinie beim Hochgeschwindigkeitszug 'ICE' – Teil I: Theoretische Grundlagen [Live deflection line of the railway track caused by the high-speed train 'ICE' – Part I: Theoretical model]", *Archive of Applied Mechanics*, vol. 64, no. 3, pp. 154-168, 1994.

[177] T. Triantafyllidis and B. Prange, "Mitgeführte Biegelinie beim Hochgeschwindigkeitszug 'ICE' – Teil II: Vergleich zwischen theoretischen und experimentellen Ergebnissen [Live deflection line of the railway track caused by the high-speed train 'ICE' – Part II: Comparison between theoretical and experimental results]", *Archive of Applied Mechanics*, vol. 64, no. 3, pp. 169-179, 1994.

[178] A. Trochides, "Ground-borne vibrations in buildings near subways", *Applied Acoustics*, vol. 32, no. 4, pp. 289-296, 1991.

[179] A. Tuchinda, "Underground Vibration", 4th-year project report, Department of Engineering, University of Cambridge, April 1998.

[180] G. Volberg, "Propagation of ground vibrations near railway tracks", *Journal of Sound and Vibration*, vol. 87, no. 2, pp. 371-376, 1983.

[181] A.S. Volmir, *Nonlinear Dynamics of Plates and Shells*, Nauka, Moscow, 1972 (in Russian).

[182] P.H. Waarts and W.M.G. Courage, "Traffic loads on bridges – dynamic amplification factors on parts of bridges" in Augusti, Borri and Spinelli (eds.), *Structural Dynamics – EURODYN'96*, Balkema, Rotterdam, Netherlands, 1996, pp. 795-800.

[183] R.-T. Wang and T.-Y. Lin, "Random vibration of multi-span Timoshenko beam due to a moving load", *Journal of Sound and Vibration*, vol. 213, no. 1, pp. 127-138, 1998.

[184] T.-L. Wang and D. Huang, "Cable-stayed bridge vibration due to road surface roughness", *Journal of Structural Engineering*, vol. 118, no. 5, pp. 1354-1374, 1992.

[185] G.N. Watson, *A Treatise on the Theory of Bessel Functions*, 2nd ed., Cambridge University Press, London, 1966.

[186] R. Wettschureck, "Vibration and structure-borne noise insulation by means of cellular polyurethane (PUR) elastomers in railway track applications", *Rail Engineering International Edition*, no. 2, pp. 7-14, 1995.

[187] R. Wettschureck, "Measures to reduce structure-borne noise emissions induced by above-ground, open railway lines", *Rail Engineering International Edition*, no. 1, pp. 12-16, 1997.

[188] R. Wettschureck and U.J. Kurze, "Insertion loss of ballast mats", *Acustica*, vol. 58, no. 3, pp. 177-182, 1985.

[189] W. White, S. Valliappan and I.K. Lee, "Unified boundary for finite dynamic models", *Journal of the Engineering Mechanics Division, Proceedings ASCE*, vol. 103, no. EM5, pp. 949-964, 1977.

[190] T.H. Wilmhurst, *Signal Recovery from Noise in Electronic Instrumentation*, Adam Hilger, Bristol, England, 1985.

[191] G.P. Wilson, H.J. Saurenman and J.T. Nelson, "Control of ground-borne noise and vibration", *Journal of Sound and Vibration*, vol. 87, no. 2, pp. 339-350, 1983.

[192] J.P. Wolf, *Foundation Vibration Analysis Using Simple Physical Models*, Prentice-Hall, Englewood Cliffs, New Jersey, USA, 1994.

[193] J.P. Wolf and G.R. Darbre, "Dynamic-stiffness matrix of soil by the boundary-element method: conceptual aspects", *Earthquake Engineering and Structural Dynamics*, vol. 12, no. 3, pp. 385-400, 1984.

[194] J.P. Wolf and G.R. Darbre, "Dynamic-stiffness matrix of soil by the boundary-element method: embedded foundation", *Earthquake Engineering and Structural Dynamics*, vol. 12, no. 3, pp. 401-416, 1984.

[195] J.P. Wolf and C. Song, "Dynamic-stiffness matrix in time domain of unbounded medium by infinitesimal finite element cell method", *Earthquake Engineering and Structural Dynamics*, vol. 23, no. 11, pp. 1181-1198, 1994.

[196] J.P. Wolf and C. Song, "Doubly asymptotic multi-directional transmitting boundary for dynamic unbounded medium-structure-interaction analysis", *Earthquake Engineering and Structural Dynamics*, vol. 24, no. 2, pp. 175-188, 1995.

[197] Y.-B. Yang and H.-H. Hung, "A parametric study of wave barriers for reduction of train-induced vibrations", *International Journal for Numerical Methods in Engineering*, vol. 40, no. 20, pp. 3729-3747, 1997.

[198] Y.-B. Yang, J.-D. Yau and L.-C. Hsu, "Vibration of simple beams due to trains moving at high speeds", *Engineering Structures*, vol. 19, no. 11, pp. 936-944, 1997.

[199] A. Yoshimura, T. Anami, Y. Okumura and M. Kamiyama, "A new method of repairing railway track irregularity using the restored waveform and its application", *Quarterly Report of the Railway Technical Research Institute (Japan)*, vol. 38, no. 1, pp. 13-18, 1997.

[200] O. Yoshioka, "Prediction analysis of train-induced ground vibrations using the equivalent excitation force", *Quarterly Report of the Railway Technical Research Institute (Japan)*, vol. 37, no. 4, pp. 216-224, 1996.

[201] O. Yoshioka and K. Ashiya, "Effects of masses and axle arrangement of rolling stock on train-induced ground vibrations", *Quarterly Report of the Railway Technical Research Institute (Japan)*, vol. 31, no. 3, pp. 145-152, 1990.

[202] W.C. Young, *Roark's Formulas for Stress and Strain*, 6th ed., McGraw-Hill, New York, 1989.

[203] C.-B. Yun, J.-M. Kim and C.-H. Hyun, "Axisymmetric elastodynamic infinite elements for multi-layered half-space", *International Journal for Numerical Methods in Engineering*, vol. 38, no. 22, pp. 3723-3743, 1995.

[204] A. Zach and G. Rutishauser, "Measures against structure borne noise and vibrations: Experience from projects carried out by Swiss Federal Railways (SBB).", report no. DT 217, *Question D 151: Vibrations transmitted through the ground*, Office for Research and Experiments of the International Union of Railways, Utrecht, Netherlands, April 1989.

[205] W. Zhai and Z. Cai, "Dynamic interaction between a lumped mass vehicle and a discreetly supported continuous rail track", *Computers and Structures*, vol. 63, no. 5, pp. 987-997, 1997.

[206] H.S. Zibdeh and R. Rackwitz, "Response moments of an elastic beam subjected to Poissonian moving loads", *Journal of Sound and Vibration*, vol. 188, no. 4, pp. 479-495, 1995.

Appendix A

BOUNDARY-CONDITION MATRICES FOR DOUBLE-BEAM UNIT

If the 8x8 matrices [**M**] and [**N**] of equations (3.6) in Chapter 3 are partitioned as follows

$$[\mathbf{M}] = \begin{bmatrix} [\mathbf{M}_{11}] & [\mathbf{M}_{12}] \\ [\mathbf{M}_{21}] & [\mathbf{M}_{22}] \end{bmatrix} \quad \text{and} \quad [\mathbf{N}] = \begin{bmatrix} [\mathbf{N}_{11}] & [\mathbf{N}_{12}] \\ [\mathbf{N}_{21}] & [\mathbf{N}_{22}] \end{bmatrix}$$

then each 4x4 submatrix is as given below. The eigenvector components are defined by $\mathbf{V}_1 = \{V_{11} \quad V_{12}\}^{\mathrm{T}}$ and $\mathbf{V}_2 = \{V_{21} \quad V_{22}\}^{\mathrm{T}}$.

$$[\mathbf{M}_{11}] = \begin{bmatrix} \{1 & 1 & 1 & 1\}V_{11} \\ \{\alpha_1 & i\alpha_1 & -\alpha_1 & -i\alpha_1\}V_{11} \\ \{1 & 1 & 1 & 1\}V_{12} \\ \{\alpha_1 & i\alpha_1 & -\alpha_1 & -i\alpha_1\}V_{12} \end{bmatrix}$$

$$[\mathbf{M}_{12}] = \begin{bmatrix} \{1 & 1 & 1 & 1\}V_{21} \\ \{\alpha_2 & i\alpha_2 & -\alpha_2 & -i\alpha_2\}V_{21} \\ \{1 & 1 & 1 & 1\}V_{22} \\ \{\alpha_2 & i\alpha_2 & -\alpha_2 & -i\alpha_2\}V_{22} \end{bmatrix}$$

$$[\mathbf{M}_{21}] = \begin{bmatrix} \{e^{\alpha_1 L} & e^{i\alpha_1 L} & e^{-\alpha_1 L} & e^{-i\alpha_1 L}\}V_{11} \\ \{\alpha_1 e^{\alpha_1 L} & i\alpha_1 e^{i\alpha_1 L} & -\alpha_1 e^{-\alpha_1 L} & -i\alpha_1 e^{-i\alpha_1 L}\}V_{11} \\ \{e^{\alpha_1 L} & e^{i\alpha_1 L} & e^{-\alpha_1 L} & e^{-i\alpha_1 L}\}V_{12} \\ \{\alpha_1 e^{\alpha_1 L} & i\alpha_1 e^{i\alpha_1 L} & -\alpha_1 e^{-\alpha_1 L} & -i\alpha_1 e^{-i\alpha_1 L}\}V_{12} \end{bmatrix}$$

$$[\mathbf{M}_{22}] = \begin{bmatrix} \{ e^{\alpha_2 L} & e^{i\alpha_2 L} & e^{-\alpha_2 L} & e^{-i\alpha_2 L} \} V_{21} \\ \{ \alpha_2 e^{\alpha_2 L} & i\alpha_2 e^{i\alpha_2 L} & -\alpha_2 e^{-\alpha_2 L} & -i\alpha_2 e^{-i\alpha_2 L} \} V_{21} \\ \{ e^{\alpha_2 L} & e^{i\alpha_2 L} & e^{-\alpha_2 L} & e^{-i\alpha_2 L} \} V_{22} \\ \{ \alpha_2 e^{\alpha_2 L} & i\alpha_2 e^{i\alpha_2 L} & -\alpha_2 e^{-\alpha_2 L} & -i\alpha_2 e^{-i\alpha_2 L} \} V_{22} \end{bmatrix}$$

$$[\mathbf{N}_{11}] = \begin{bmatrix} EI_1 \{ (\alpha_1)^3 & (i\alpha_1)^3 & (-\alpha_1)^3 & (-i\alpha_1)^3 \} V_{11} \\ -EI_1 \{ (\alpha_1)^2 & (i\alpha_1)^2 & (-\alpha_1)^2 & (-i\alpha_1)^2 \} V_{11} \\ EI_2 \{ (\alpha_1)^3 & (i\alpha_1)^3 & (-\alpha_1)^3 & (-i\alpha_1)^3 \} V_{12} \\ -EI_2 \{ (\alpha_1)^2 & (i\alpha_1)^2 & (-\alpha_1)^2 & (-i\alpha_1)^2 \} V_{12} \end{bmatrix}$$

$$[\mathbf{N}_{12}] = \begin{bmatrix} EI_1 \{ (\alpha_2)^3 & (i\alpha_2)^3 & (-\alpha_2)^3 & (-i\alpha_2)^3 \} V_{21} \\ -EI_1 \{ (\alpha_2)^2 & (i\alpha_2)^2 & (-\alpha_2)^2 & (-i\alpha_2)^2 \} V_{21} \\ EI_2 \{ (\alpha_2)^3 & (i\alpha_2)^3 & (-\alpha_2)^3 & (-i\alpha_2)^3 \} V_{22} \\ -EI_2 \{ (\alpha_2)^2 & (i\alpha_2)^2 & (-\alpha_2)^2 & (-i\alpha_2)^2 \} V_{22} \end{bmatrix}$$

$$[\mathbf{N}_{21}] = \begin{bmatrix} -EI_1 \{ (\alpha_1)^3 e^{\alpha_1 L} & (i\alpha_1)^3 e^{i\alpha_1 L} & (-\alpha_1)^3 e^{-\alpha_1 L} & (-i\alpha_1)^3 e^{-i\alpha_1 L} \} V_{11} \\ EI_1 \{ (\alpha_1)^2 e^{\alpha_1 L} & (i\alpha_1)^2 e^{i\alpha_1 L} & (-\alpha_1)^2 e^{-\alpha_1 L} & (-i\alpha_1)^2 e^{-i\alpha_1 L} \} V_{11} \\ -EI_2 \{ (\alpha_1)^3 e^{\alpha_1 L} & (i\alpha_1)^3 e^{i\alpha_1 L} & (-\alpha_1)^3 e^{-\alpha_1 L} & (-i\alpha_1)^3 e^{-i\alpha_1 L} \} V_{12} \\ EI_2 \{ (\alpha_1)^2 e^{\alpha_1 L} & (i\alpha_1)^2 e^{i\alpha_1 L} & (-\alpha_1)^2 e^{-\alpha_1 L} & (-i\alpha_1)^2 e^{-i\alpha_1 L} \} V_{12} \end{bmatrix}$$

$$[\mathbf{N}_{22}] = \begin{bmatrix} -EI_1 \{ (\alpha_2)^3 e^{\alpha_2 L} & (i\alpha_2)^3 e^{i\alpha_2 L} & (-\alpha_2)^3 e^{-\alpha_2 L} & (-i\alpha_2)^3 e^{-i\alpha_2 L} \} V_{21} \\ EI_1 \{ (\alpha_2)^2 e^{\alpha_2 L} & (i\alpha_2)^2 e^{i\alpha_2 L} & (-\alpha_2)^2 e^{-\alpha_2 L} & (-i\alpha_2)^2 e^{-i\alpha_2 L} \} V_{21} \\ -EI_2 \{ (\alpha_2)^3 e^{\alpha_2 L} & (i\alpha_2)^3 e^{i\alpha_2 L} & (-\alpha_2)^3 e^{-\alpha_2 L} & (-i\alpha_2)^3 e^{-i\alpha_2 L} \} V_{22} \\ EI_2 \{ (\alpha_2)^2 e^{\alpha_2 L} & (i\alpha_2)^2 e^{i\alpha_2 L} & (-\alpha_2)^2 e^{-\alpha_2 L} & (-i\alpha_2)^2 e^{-i\alpha_2 L} \} V_{22} \end{bmatrix}$$

Appendix B

SHELL EQUATIONS AND COEFFICIENT MATRICES FOR CYLINDRICAL SHELL & ELASTIC CONTINUUM

B1. Volmir's Shell Equations

The general dynamic shell equations as presented by Volmir [181] are given below. Consideration of dynamic equilibrium in the *x*, *y* and *z* directions yields equations (B.1), (B.2) and (B.3) respectively. The nomenclature is the same as in Chapter 4 with the addition of k_x and k_y, the principal curvatures of the shell. For a cylindrical shell $k_x = 0$ and $k_y = 1/a$. Noting also that $\partial y = a\partial\theta$, (B.1) to (B.3) can be simplified to equations (4.1) – (4.3).

$$\left(1 + \frac{h^2}{12}k_x k_y\right)\frac{\partial^2 u}{\partial x^2} + \frac{(1-\nu)}{2}\left[1 + \frac{h^2}{12}\left(k_y{}^2 - 3k_x k_y + 3k_x{}^2\right)\right]\frac{\partial^2 u}{\partial y^2} + \frac{(1+\nu)}{2}\left(1 + \frac{h^2}{12}k_x k_y\right)\frac{\partial^2 v}{\partial x \partial y}$$
$$+ k_y \frac{h^2}{12}\frac{\partial^3 w}{\partial x^3} + \frac{h^2}{12}\left(k_x \frac{(3-\nu)}{2} - k_y \frac{(1-\nu)}{2}\right)\frac{\partial^3 w}{\partial x \partial y^2} - \left(k_x + \nu k_y\right)\frac{\partial w}{\partial x} \qquad \text{(B.1)}$$
$$+ \frac{(1-\nu^2)}{Eh}q_x - \rho\frac{(1-\nu^2)}{E}\frac{\partial^2 u}{\partial t^2} = 0$$

$$\frac{(1+\nu)}{2}\left(1 + \frac{h^2}{12}k_x k_y\right)\frac{\partial^2 u}{\partial x \partial y} + \left(1 + \frac{h^2}{12}k_x k_y\right)\frac{\partial^2 v}{dy^2} + \frac{(1-\nu)}{2}\left[1 + \frac{h^2}{12}\left(k_x{}^2 - 3k_x k_y + 3k_y{}^2\right)\right]\frac{\partial^2 v}{\partial x^2}$$
$$+ \frac{h^2}{12}\left(k_y \frac{(3-\nu)}{2} - k_x \frac{(1-\nu)}{2}\right)\frac{\partial^3 w}{\partial x^2 \partial y} + k_x \frac{h^2}{12}\frac{\partial^3 w}{\partial y^3} - \left(k_y + \nu k_x\right)\frac{\partial w}{\partial y} \qquad \text{(B.2)}$$
$$+ \frac{(1-\nu^2)}{Eh}q_y - \rho\frac{(1-\nu^2)}{E}\frac{\partial^2 v}{\partial t^2} = 0$$

$$
\begin{aligned}
& k_y \frac{h^2}{12}\frac{\partial^3 u}{\partial x^3} + \frac{h^2}{12}\left(k_x\frac{(3-\nu)}{2} - k_y\frac{(1-\nu)}{2}\right)\frac{\partial^3 u}{\partial x\partial y^2} + \frac{h^2}{12}\left(k_y\frac{(3-\nu)}{2} - k_x\frac{(1-\nu)}{2}\right)\frac{\partial^3 v}{\partial x^2\partial y} \\
& + k_x\frac{h^2}{12}\frac{\partial^3 v}{\partial y^3} - \left(k_x + \nu k_y\right)\frac{\partial u}{\partial x} - \left(k_y + \nu k_x\right)\frac{\partial v}{\partial y} + \left({k_x}^2 + 2\nu k_x k_y + {k_y}^2\right)w \\
& + \frac{h^2}{12}\left(k_x - k_y\right)\left({k_x}^3 - {k_y}^3\right)w + \frac{h^2}{12}\nabla^4 w + \frac{h^2}{6}k_x\left(k_x - k_y\right)\frac{\partial^2 w}{\partial x^2} + \frac{h^2}{6}k_y\left(k_y - k_x\right)\frac{\partial^2 w}{\partial y^2} \\
& - \frac{(1-\nu^2)}{Eh}q_z + \rho\frac{(1-\nu^2)}{E}\frac{\partial^2 w}{\partial t^2} = 0
\end{aligned}
\tag{B.3}
$$

B2. Coefficients for the Cylindrical Shell

The elements of the matrix [**A**] used in equation (4.6) to calculate the displacements of the cylindrical shell are given below. These coefficients are the full ones derived from the Volmir [181] or Flügge [57] shell equations. The terms in these which are additional to those in the coefficients derived from the simplified shell theory used by Timoshenko and Woinowsky-Krieger [175] are double-underlined.

$$a_{11} = \frac{\rho a(1-\nu^2)}{E}\omega^2 - a\xi^2 - \frac{(1-\nu)}{2a}n^2 - \underline{\underline{\frac{(1-\nu)}{2a}\frac{h^2}{12a^2}n^2}}$$

$$a_{12} = \frac{(1+\nu)}{2}i\xi n$$

$$a_{13} = -\nu i\xi + \underline{\underline{\frac{h^2}{12}(i\xi)^3}} + \underline{\underline{\frac{h^2}{12a^2}\frac{(1-\nu)}{2}i\xi n^2}}$$

$$a_{21} = -\frac{(1+\nu)}{2}i\xi n$$

$$a_{22} = \frac{\rho a(1-\nu^2)}{E}\omega^2 - \frac{a(1-\nu)}{2}\xi^2 - \frac{1}{a}n^2 - \underline{\underline{\frac{a(1-\nu)}{2}\frac{h^2}{4a^2}\xi^2}}$$

$$a_{23} = \frac{1}{a}n + \underline{\underline{\frac{h^2}{12}\frac{(3-\nu)}{2a}\xi^2 n}}$$

$$a_{31} = \nu i\xi - \underline{\underline{\frac{h^2}{12}(i\xi)^3}} - \underline{\underline{\frac{h^2}{12a^2}\frac{(1-\nu)}{2}i\xi n^2}}$$

$$a_{32} = \frac{1}{a}n + \underline{\underline{\frac{h^2}{12a}\frac{(3-\nu)}{2}\xi^2 n}}$$

$$a_{33} = \frac{\rho a(1-\nu^2)}{E}\omega^2 - \frac{h^2}{12}\left(a\xi^4 + \frac{2}{a}\xi^2 n^2 + \frac{1}{a^3}n^4\right) - \frac{1}{a} + \underline{\underline{\frac{h^2}{6a^3}n^2}} - \underline{\underline{\frac{h^2}{12a^3}}}$$

B3. Coefficients for the Elastic Continuum

The elements of the matrix [**U**] used to determine the displacement components of the continuum in equations (4.20) are:

$$u_{11} = \frac{n}{r} I_n(\alpha r) + \alpha I_{n+1}(\alpha r)$$

$$u_{12} = \frac{n}{r} K_n(\alpha r) - \alpha K_{n+1}(\alpha r)$$

$$u_{13} = i\xi I_{n+1}(\beta r)$$

$$u_{14} = i\xi K_{n+1}(\beta r)$$

$$u_{15} = \frac{n}{r} I_n(\beta r)$$

$$u_{16} = \frac{n}{r} K_n(\beta r)$$

$$u_{21} = -\frac{n}{r} I_n(\alpha r)$$

$$u_{22} = -\frac{n}{r} K_n(\alpha r)$$

$$u_{23} = i\xi I_{n+1}(\beta r)$$

$$u_{24} = i\xi K_{n+1}(\beta r)$$

$$u_{25} = -\frac{n}{r} I_n(\beta r) - \beta I_{n+1}(\beta r)$$

$$u_{26} = -\frac{n}{r} K_n(\beta r) + \beta K_{n+1}(\beta r)$$

$$u_{31} = i\xi I_n(\alpha r)$$

$$u_{32} = i\xi K_n(\alpha r)$$

$$u_{33} = -\beta I_n(\beta r)$$

$$u_{34} = \beta K_n(\beta r)$$

$$u_{35} = 0$$

$$u_{36} = 0$$

The elements of the matrix [**T**] used to determine the stress components of the continuum in equations (4.20) are:

$$t_{11} = \left(2\mu\frac{(n^2-n)}{r^2} - \lambda\xi^2 + (\lambda+2\mu)\alpha^2\right)I_n(\alpha r) - 2\mu\frac{\alpha}{r}I_{n+1}(\alpha r)$$

$$t_{12} = \left(2\mu\frac{(n^2-n)}{r^2} - \lambda\xi^2 + (\lambda+2\mu)\alpha^2\right)K_n(\alpha r) + 2\mu\frac{\alpha}{r}K_{n+1}(\alpha r)$$

$$t_{13} = 2\mu i\xi\beta I_n(\beta r) - 2\mu i\xi\frac{(n+1)}{r}I_{n+1}(\beta r)$$

$$t_{14} = -2\mu i\xi\beta K_n(\beta r) - 2\mu i\xi\frac{(n+1)}{r}K_{n+1}(\beta r)$$

$$t_{15} = 2\mu\frac{(n^2-n)}{r^2}I_n(\beta r) + 2\mu\frac{n}{r}\beta I_{n+1}(\beta r)$$

$$t_{16} = 2\mu\frac{(n^2-n)}{r^2}K_n(\beta r) - 2\mu\frac{n}{r}\beta K_{n+1}(\beta r)$$

$$t_{21} = -2\mu\frac{(n^2-n)}{r^2}I_n(\alpha r) - 2\mu\frac{n}{r}\alpha I_{n+1}(\alpha r)$$

$$t_{22} = -2\mu\frac{(n^2-n)}{r^2}K_n(\alpha r) + 2\mu\frac{n}{r}\alpha K_{n+1}(\alpha r)$$

$$t_{23} = \mu i\xi\beta I_n(\beta r) - 2\mu i\xi\frac{(n+1)}{r}I_{n+1}(\beta r)$$

$$t_{24} = -\mu i\xi\beta K_n(\beta r) - 2\mu i\xi\frac{(n+1)}{r}K_{n+1}(\beta r)$$

$$t_{25} = \left(-2\mu\frac{(n^2-n)}{r^2} - \mu\beta^2\right)I_n(\beta r) + 2\mu\frac{\beta}{r}I_{n+1}(\beta r)$$

$$t_{26} = \left(-2\mu\frac{(n^2-n)}{r^2} - \mu\beta^2\right)K_n(\beta r) - 2\mu\frac{\beta}{r}K_{n+1}(\beta r)$$

$$t_{31} = 2\mu i\xi\frac{n}{r}I_n(\alpha r) + 2\mu i\xi\alpha I_{n+1}(\alpha r)$$

$$t_{32} = 2\mu i\xi\frac{n}{r}K_n(\alpha r) - 2\mu i\xi\alpha K_{n+1}(\alpha r)$$

$$t_{33} = -\mu\frac{n}{r}\beta I_n(\beta r) - \mu(\xi^2+\beta^2)I_{n+1}(\beta r)$$

$$t_{34} = \mu\frac{n}{r}\beta K_n(\beta r) - \mu(\xi^2+\beta^2)K_{n+1}(\beta r)$$

$$t_{35} = \mu i\xi\frac{n}{r}I_n(\beta r)$$

$$t_{36} = \mu i\xi \frac{n}{r} K_n(\beta r)$$

$$t_{41} = \left(-2\mu \frac{(n^2-n)}{r^2} + \lambda(\alpha^2-\xi^2)\right) I_n(\alpha r) + 2\mu \frac{\alpha}{r} I_{n+1}(\alpha r)$$

$$t_{42} = \left(-2\mu \frac{(n^2-n)}{r^2} + \lambda(\alpha^2-\xi^2)\right) K_n(\alpha r) - 2\mu \frac{\alpha}{r} K_{n+1}(\alpha r)$$

$$t_{43} = 2\mu i\xi \frac{(n+1)}{r} I_{n+1}(\beta r)$$

$$t_{44} = 2\mu i\xi \frac{(n+1)}{r} K_{n+1}(\beta r)$$

$$t_{45} = -2\mu \frac{(n^2-n)}{r^2} I_n(\beta r) - 2\mu \frac{n}{r} \beta I_{n+1}(\beta r)$$

$$t_{46} = -2\mu \frac{(n^2-n)}{r^2} K_n(\beta r) + 2\mu \frac{n}{r} \beta K_{n+1}(\beta r)$$

$$t_{51} = -2\mu i\xi \frac{n}{r} I_n(\alpha r)$$

$$t_{52} = -2\mu i\xi \frac{n}{r} K_n(\alpha r)$$

$$t_{53} = \mu \frac{n}{r} \beta I_n(\beta r) - \mu\xi^2 I_{n+1}(\beta r)$$

$$t_{54} = -\mu \frac{n}{r} \beta K_n(\beta r) - \mu\xi^2 K_{n+1}(\beta r)$$

$$t_{55} = -\mu i\xi \frac{n}{r} I_n(\beta r) - \mu i\xi\beta I_{n+1}(\beta r)$$

$$t_{56} = -\mu i\xi \frac{n}{r} K_n(\beta r) + \mu i\xi\beta K_{n+1}(\beta r)$$

$$t_{61} = \left(\lambda\alpha^2 - (\lambda+2\mu)\xi^2\right) I_n(\alpha r)$$

$$t_{62} = \left(\lambda\alpha^2 - (\lambda+2\mu)\xi^2\right) K_n(\alpha r)$$

$$t_{63} = -2\mu i\xi\beta I_n(\beta r)$$

$$t_{64} = 2\mu i\xi\beta K_n(\beta r)$$

$$t_{65} = 0$$

$$t_{66} = 0$$

Appendix C

ROW AND COLUMN NORMALISATION

Kreyszig [112] discusses some of the issues surrounding the numerical of solution of systems of linear equations using matrix methods. A system is ill-conditioned if small changes in the coefficients cause large changes in the computed solution; such small changes can be introduced by round-off errors. The matrix representing the system can be singular to machine working precision if it is very ill-conditioned. One way a matrix becomes ill-conditioned is when the relative scale of its largest to smallest elements is many orders of magnitude. The condition of a badly-scaled matrix can be improved by row or column normalisation. Row normalisation divides each row by the magnitude of its maximum element, ensuring that the maximum magnitude in any row of the normalised matrix is then unity, reducing the overall numerical range of the elements. Column normalisation does the same thing over the columns of the matrix. As an example, consider the 3×3 system of linear equations described by

$$\begin{bmatrix} a_{11} & a_{12} & a_{13} \\ a_{21} & a_{22} & a_{23} \\ a_{31} & a_{32} & a_{33} \end{bmatrix} \begin{Bmatrix} x_1 \\ x_2 \\ x_3 \end{Bmatrix} = \begin{Bmatrix} c_1 \\ c_2 \\ c_3 \end{Bmatrix} \tag{C.1}$$

where the object is to solve for the variables $\{x_1 \quad x_2 \quad x_3\}^{\mathrm{T}}$. If row normalisation is applied to this system, (C.1) becomes

$$\begin{bmatrix} a_{11}/m_1 & a_{12}/m_1 & a_{13}/m_1 \\ a_{21}/m_2 & a_{22}/m_2 & a_{23}/m_2 \\ a_{31}/m_3 & a_{32}/m_3 & a_{33}/m_3 \end{bmatrix} \begin{Bmatrix} x_1 \\ x_2 \\ x_3 \end{Bmatrix} = \begin{Bmatrix} c_1/m_1 \\ c_2/m_2 \\ c_3/m_3 \end{Bmatrix} \tag{C.2}$$

where m_1, m_2 and m_3 are the absolute row maxima of the matrix in (C.1). If column normalisation is applied to the system, (C.1) becomes

$$\begin{bmatrix} a_{11}/n_1 & a_{12}/n_2 & a_{13}/n_3 \\ a_{21}/n_1 & a_{22}/n_2 & a_{23}/n_3 \\ a_{31}/n_1 & a_{32}/n_2 & a_{33}/n_3 \end{bmatrix} \begin{Bmatrix} x_1 n_1 \\ x_2 n_2 \\ x_3 n_3 \end{Bmatrix} = \begin{Bmatrix} c_1 \\ c_2 \\ c_3 \end{Bmatrix} \tag{C.3}$$

where n_1, n_2 and n_3 are the absolute column maxima of the matrix in (C.1).

If the row maxima all fall in different columns, then row normalisation by itself will also achieve column normalisation, as the row-normalised matrix of (C.2) will also have a single element of unit magnitude in each column with all other magnitudes less than unity, so that the column normalisation of (C.3) will not change any values. Similarly, column normalisation alone will also achieve row normalisation if the column maxima all fall in different rows. Generally, however, these special cases will not occur, leaving some columns (or some rows) unnormalised after only one operation. Thus row normalisation followed by column normalisation (or vice versa) scales the original matrix as well or better than either procedure alone.

If the matrix of (C.1) is optimally scaled by performing row then column normalisation, the scaling effect of (C.2) then (C.3) must be accounted for in the solution. The original solution $\{x_1 \quad x_2 \quad x_3\}^{\mathrm{T}}$ sought is thus

$$\begin{Bmatrix} x_1 \\ x_2 \\ x_3 \end{Bmatrix} = \begin{bmatrix} 1/n_1' & 0 & 0 \\ 0 & 1/n_2' & 0 \\ 0 & 0 & 1/n_3' \end{bmatrix} \cdot \begin{bmatrix} a_{11}/m_1 n_1' & a_{12}/m_1 n_2' & a_{13}/m_1 n_3' \\ a_{21}/m_2 n_1' & a_{22}/m_2 n_2' & a_{23}/m_2 n_3' \\ a_{31}/m_3 n_1' & a_{32}/m_3 n_2' & a_{33}/m_3 n_3' \end{bmatrix}^{-1} \begin{Bmatrix} c_1/m_1 \\ c_2/m_2 \\ c_3/m_3 \end{Bmatrix} \tag{C.4}$$

where n_1', n_2' and n_3' are the absolute column maxima of the row-normalised matrix in (C.2). Numerically, Gaussian elimination would be used instead of the matrix inverse in (C.4).

Matlab has a function RCOND which returns a reciprocal condition estimator. RCOND is near 1.0 for well-conditioned matrices and near 0.0 for ill-conditioned ones. The matrix in equation (4.42), used to calculate tunnel and soil displacements, typically has RCOND values of the order of 10^{-21} (which is singular to working precision) before any normalisation, 10^{-11} after either row or column normalisation alone, and 10^{-3} after both row and column normalisation, for the parameters of Table 4.3. Thus the matrix scaling scheme of (C.4) is most suitable for overcoming the numerical difficulties encountered in this situation.